

2000-11-20
25323
AIRCRAFT INTERIOR NOISE REDUCTION
BY ALTERNATE RESONANCE TUNING

PROGRESS REPORT FOR THE PERIOD ENDING
DECEMBER, 1990
FINAL PROGRESS REPORT

NASA RESEARCH GRANT # NAG-1-722

Prepared for:

STRUCTURAL ACOUSTICS BRANCH
NASA LANGLEY RESEARCH CENTER

Prepared by:

Dr. James A. Gottwald
Dr. Donald B. Bliss

Department of Mechanical Engineering
and Materials Science

DUKE UNIVERSITY
DURHAM, NC 27705

(NASA-CR-135453) AIRCRAFT INTERIOR NOISE
REDUCTION BY ALTERNATE RESONANCE TUNING
Final Progress Report, period ending Dec.
1990 (Duke Univ.) 215 p

CSCL 20A

N91-26289

Unclass

03/71 0025633

Abstract

Existing interior noise reduction techniques for aircraft fuselages perform reasonably well at higher frequencies, but are inadequate at lower frequencies, particularly with respect to the low blade passage harmonics with high forcing levels found in propeller aircraft. This research focuses on a noise control method which considers aircraft fuselages lined with panels alternately tuned to frequencies above and below the frequency that must be attenuated. Adjacent panels would oscillate at equal amplitude, to give equal source strength, but with opposite phase. Provided these adjacent panels are acoustically compact, the resulting cancellation causes the interior acoustic modes to become cutoff, and therefore be non-propagating and evanescent. This interior noise reduction method, called *Alternate Resonance Tuning* (ART), is described in this thesis both theoretically and experimentally.

Problems presented herein deal with tuning single paneled wall structures for optimum noise reduction using the ART tuning methodology, and three theoretical problems are analyzed. The first analysis is a three dimensional, full acoustic solution for tuning a panel wall composed of repeating sections with four different panel tunings within that section, where the panels are modeled as idealized spring-mass-damper systems. The second analysis is a two dimensional, full acoustic solution for a panel geometry influenced by the effect of a propagating external pressure field such as that which might be associated with propeller passage by a fuselage. To reduce the analysis complexity, idealized spring-mass-damper panels are again employed. The final theoretical analysis presents the general four panel problem with real panel sections, where the effect of higher structural modes is discussed. Results from an experimental program highlight real applications of the ART concept and show the effectiveness of the tuning on real structures.

Acknowledgements

The authors gratefully acknowledge the support of the Structural Acoustics Branch of the NASA Langley Research Center. In particular, we wish to thank Dr. Kevin P. Shepherd, contract monitor, for his assistance throughout the duration of this project.

Table of Contents

Title page	i
Abstract	ii
Acknowledgements	iii
Table of Contents	iv
List of Figures	vii
List of Tables	xix
List of Symbols and Abbreviations	xx
Chapter 1: The General Noise Problem and Alternate Resonance Tuning	1
1.1 Introduction	1
1.2 Review of the Literature	2
1.3 Alternate Resonance Tuning	8
Chapter 2: The Four Panel Problem	12
2.1 Introduction	12
2.2 Acoustic Branch Analysis	16
2.2.1 Nondimensionalization	22
2.2.2 Branch Analysis Results	24
2.3 The Full Four Panel Analysis	26
2.4 Analytical Results	35
2.4.1 Two Panel Results and Discussion	35
2.4.2 Averaged Noninteracting Noise Reduction	37
2.4.3 Four Panel Results and Discussion	39
2.4.4 Mass Ratio Optimization	42

2.4.5 Model Parameter Studies	48
Chapter 3: External Pressure Field Modeling	59
3.1 Introduction	59
3.2 Analysis Derivation	59
3.2.1 Noise Reduction Calculation	68
3.2.2 Nondimensionalization	69
3.2.3 Numerical Solution Procedure	69
3.2.4 Results Verification	71
3.3 Analytical Results	72
3.3.1 Case Study Inputs	72
3.3.2 Mode Convergence Study	74
3.3.3 Comparison of ART and Identical Tunings	78
3.3.4 Model Parameter Studies	89
3.3.5 Pressure and Noise Reduction Mapping	95
3.3.6 Comparison to the Two Panel Model	107
3.3.7 Miscellaneous Results	107
Chapter 4: The General ART Panel Analysis	120
4.1 Introduction	120
4.2 Analysis Derivation	120
4.3 Recovering Some Familiar Results From the General Real Panel Analysis	130
4.4 Structural Branch Analysis	134
4.5 Structural Branch Analysis Results	143
4.5.1 Mode Study and Comparison of ART and Identical Panels	143
4.5.2 Parameter Studies	148
Chapter 5: Experimental Confirmation of the ART Concept	154
5.1 Introduction	154
5.2 Experimental Setup	154
5.3 Single Panel Wall Noise Reduction Measurements	157
5.4 Double Panel Wall Noise Reduction Measurements With One Identical Wall	165

	and One ART Wall	
5.5	Double Panel Wall Noise Reduction Measurements With Two ART Walls	168
5.6	Double Panel Wall Noise Reduction Measurements With Nonuniform Panel Size	171
5.7	Noise Reduction Measurements With Real Panel ART Walls	174
Chapter 6: Summary and Conclusions		179
6.1	Introduction	179
6.2	The Four Panel Problem	179
6.3	External Pressure Field Modeling	181
6.4	The General ART Panel Analysis	182
6.5	Experimental Confirmation of the ART Concept	183
6.6	Future Effort in Alternate Resonance Tuning	185
References		187

List of Figures

Figure	Title	Page
1.2.1	Exterior fuselage sound pressure level spectra measured 63.5 cm behind the propeller plane with and without the propfan on a Gulfstream II aircraft (reproduced from Kuntz and Prydz).	4
1.2.2	Cabin sound pressure level spectra measured in the prop plane with and without the propfan (reproduced from Kuntz and Prydz).	4
1.2.3	Experimental data for the first 40 harmonics of the blade passage frequency taken from 1/4 scale model tests, including a comparison to predicted levels by the noise prediction program WOPWOP (reproduced from Brentner).	5
1.2.4	Distribution of acoustic treatments for noise control in an aircraft fuselage (reproduced from Vaicaitis and Mixson).	7
1.2.5	Measurement of noise transmitted into untreated fuselage compared with prediction of noise transmitted into treated fuselage (reproduced from Vaicaitis and Mixson).	7
1.3.1	Amplitude and phase relations of adjacent panels for ART tuning.	10
2.1.1	Panel wall layout with analysis subsection highlighted with thickened line. Note periodicity assumed in the wall construction.	13
2.1.2	Arrangement possibilities for the four panel analysis configuration.	14
2.1.3	Extraction of the panel wall subsystem and incorporation into a duct.	15
2.2.1	Schematic of analysis configuration placed in the duct.	17
2.2.2	Equivalent branch analysis schematic.	18
2.2.3	Typical nondimensional impedance versus nondimensional frequency with components as noted.	19

2.2.4a	Branch analysis pressure ratio results for identical panels and ART tuned panels. Values for the nondimensional parameters are as shown in Table 2.2.1.	25
2.2.4b	Branch analysis noise reduction results for identical and ART tuned panels. Values for the nondimensional parameters are as shown in Table 2.2.1.	25
2.4.1	ART and identical two panel noise reduction prediction with apparent mass plotted versus nondimensional frequency. Values for the nondimensional parameters are as shown in Table 2.2.1.	36
2.4.2	Detail of the branch analysis and full theory noise reduction predictions around the ART cancellation frequency. Remainder of noise reduction calculation is essentially the same.	36
2.4.3	Theoretical phase difference in degrees between the ART panels with apparent mass as a function of nondimensional frequency.	38
2.4.4	Panel velocity relationships from two panel theory with apparent mass.	38
2.4.5	Averaged Noninteracting Noise Reduction (ANNR) schematic.	39
2.4.6	Two panel ART noise reduction plotted with Averaged Noninteracting Noise Reduction (ANNR) with apparent mass.	40
2.4.7a	Four panel ART pressure ratio (P_t/P_I) plotted against identical panels pressure ratio with apparent mass.	41
2.4.7b	Four panel ART and identical panels noise reduction predictions with apparent mass.	41
2.4.8	Four panel ART noise reduction prediction with apparent mass plotted against Averaged Noninteracting Noise Reduction (ANNR).	43
2.4.9	Noise reduction prediction using the ART four panel theory with and without apparent mass modes as indicated above.	43
2.4.10a	Four panel theory with and without compensated mass ratios. Note shift of peak ART cancellation frequencies and slight increase in noise reduction for compensated system. Values are as shown in Table 2.2.1.	45

2.4.10b	Full four panel theory with parameters changed as shown above. Other parameters equivalent to Figure 2.4.10a.	45
2.4.10c	Comparison of mass ratios for noncompensated and compensated predictions with varying panel size and apparent mass loading.	47
2.4.11	Magnitude of apparent mass sums versus nondimensional frequency showing increased coupling at higher frequencies.	48
2.4.12	Parameter studies with the four panel model varying the panel damping ratios as indicated above. Nonadjusted parameter values remain as listed in Table 2.2.1.	49
2.4.13	Parameter studies with the four panel model varying sound propagation speed via the parameter $\omega_r H/c$. The effective sound speeds are shown in the legend.	49
2.4.14a	Parameter studies with the four panel model varying the panel aspect ratio W/H as shown above. Effective panel widths are shown in the legend.	51
2.4.14b	Detail of highest ART cancellation frequency increase as effective mass loading decreases due to panel aspect ratio change.	51
2.4.15a	Parameter studies with the four panel model varying the apparent mass loading parameter as indicated above. Panel aspect ratio $W/H = 1.0$.	52
2.4.15b	Parameter studies with the four panel model varying the apparent mass loading parameter as indicated above. Panel aspect ratio $W/H = 0.25$.	52
2.4.16	Parameter studies with the two panel model varying the higher panel natural frequency as indicated above to increase the noise reduction bandwidth. Nonadjusted parameter values remain as shown in Table 2.2.1.	53
2.4.17a	Parameter studies with the four panel model varying the real part of the nondimensional termination impedance Z_b as indicated above.	55
2.4.17b	Parameter studies with the four panel model varying the real part of the nondimensional termination impedance Z_b as indicated above.	55

2.4.18a	Parameter studies with the four panel model for high values of damping as indicated.	56
2.4.18b	High damping comparison ($\zeta = 0.4$) of ANNR and ART noise reduction predictions.	56
2.4.19a	Comparison of tuning methodologies for the four panel model using the 3 patterns indicated above.	58
2.4.19b	Enlargement of noise reduction results around ART cancellation nondimensional frequency = 3.0 to highlight subtle differences between tuning strategies. Patterns as in Figure 2.1.2.	58
3.1.1	Front view of aircraft fuselage showing relative locations of propeller and panels in the propeller plane. Dimensions for aircraft used in computational cases are given in Table 3.1.1.	60
3.2.1	External pressure field modeling schematic.	61
3.3.1a	Prediction of noise reduction moving away from panel barrier for the long wavelength case without external sweep. Number of modes in calculation varied as shown in legend.	76
3.3.1b	Prediction of noise reduction moving away from panel barrier for the short wavelength case without external sweep. Number of modes in calculation varied as shown in legend.	76
3.3.2a	Prediction of noise reduction moving away from panel barrier for the long wavelength case with external sweep. Number of modes in calculation varied as shown in legend.	77
3.3.2b	Prediction of noise reduction moving away from panel barrier for the short wavelength case with external sweep. Number of modes in calculation varied as shown in legend.	77
3.3.3a	Acoustic pressure ratio p_t/p_E moving away from the panel barrier for the long and short wavelength cases with external sweep. 32 acoustic modes are used in the solution.	79
3.3.3b	Acoustic pressure ratio p_t/p_E moving away from the panel barrier for the long and short wavelength cases without external sweep. 32 acoustic modes are used in the solution.	79

3.3.4a	Pressure ratio p_t/p_E calculation for two panel ART tuned and identical panels with long wavelength external sweep calculated at location A in Figure 3.2.1.	80
3.3.4b	Pressure ratio p_t/p_E calculation for two panel ART tuned and identical panels with short wavelength external sweep calculated at location A in Figure 3.2.1.	80
3.3.5a	Noise reduction calculation for two panel ART tuned and identical panels with long wavelength external sweep calculated at location A in Figure 3.2.1.	82
3.3.5b	Noise reduction calculation for two panel ART tuned and identical panels with short wavelength external sweep calculated at location A in Figure 3.2.1.	82
3.3.6a	Phase difference between panels 3 and 4 as a function of nondimensional frequency for the long sweep wavelength case.	83
3.3.6b	Phase difference between panels 3 and 4 as a function of nondimensional frequency for the short sweep wavelength case.	83
3.3.7a	Velocity relationships for panels 3 and 4 as a function of nondimensional frequency for the long sweep wavelength case.	85
3.3.7b	Velocity relationships for panels 3 and 4 as a function of nondimensional frequency for the short sweep wavelength case.	85
3.3.8a	Averaged noninteracting noise reduction for identical panels and two panel ART noise reduction prediction for long sweep wavelength case calculated at location A in Figure 3.2.1.	86
3.3.8b	Averaged noninteracting noise reduction for identical panels and two panel ART noise reduction prediction for short sweep wavelength case calculated at location A in Figure 3.2.1.	86
3.3.9a	Relative comparison of the first 21 modal contributions to noise reduction in the long sweep wavelength case at the ART design frequency. Note that the comparison is logarithmic.	87
3.3.9b	Relative comparison of the first 21 modal contributions to noise reduction in the short sweep wavelength case at the ART design frequency. Note that the comparison is logarithmic.	87

3.3.10a	Parameter studies with two panel tuning varying the higher panel natural frequency as indicated above to increase the noise reduction bandwidth in the long wavelength sweep case.	90
3.3.10b	Parameter studies with two panel tuning varying the higher panel natural frequency as indicated above to increase the noise reduction bandwidth in the short wavelength sweep case.	90
3.3.11a	Parameter studies with the two panel model varying the panel damping ratio as indicated above in the long wavelength sweep case.	91
3.3.11b	Parameter studies with the two panel model varying the panel damping ratio as indicated above in the short wavelength sweep case.	91
3.3.12a	Parameter studies with the two panel model varying the panel apparent mass loading as indicated above in the long wavelength sweep case.	93
3.3.12b	Parameter studies with the two panel model varying the panel apparent mass loading as indicated above in the short wavelength sweep case.	93
3.3.13a	Noise reduction calculation for two panel ART tuned panel array and long sweep wavelength with $A = 1$ and $A = 2$. Noticeable difference occurs only at resonance frequencies.	94
3.3.13b	Noise reduction calculation for two panel ART tuned panel array and short sweep wavelength with $A = 1$ and $A = 2$. Noticeable difference occurs only at resonance frequencies.	94
3.3.14a	Forward and reverse sweep direction noise reduction calculation for two panel ART tuning with long wavelength external sweep calculated at Location A.	96
3.3.14b	Forward and reverse sweep direction noise reduction calculation for two panel ART tuning with short wavelength external sweep calculated at Location A.	96
3.3.15a	Pressure map for the ART tuned panel array at the maximum ART noise reduction frequency $\omega = 1.00$ in the long sweep wavelength case.	98

3.3.15b	Pressure map for the ART tuned panel array at the maximum ART noise reduction frequency $\omega = 1.03$ in the short sweep wavelength case.	99
3.3.16a	Noise reduction map for the ART tuned panel array at the maximum ART noise reduction frequency $\omega = 1.00$ in the long sweep wavelength case.	100
3.3.16b	Noise reduction map for ART tuned panel array at the maximum ART noise reduction frequency $\omega = 1.03$ in the short sweep wavelength case.	101
3.3.16c	Noise reduction map for the ART tuned panel array at the maximum ART noise reduction frequency $\omega = 1.00$ for the long wavelength parameters without external pressure sweep.	102
3.3.16d	Noise reduction map for the ART tuned panel array at the maximum ART noise reduction frequency $\omega = 1.03$ for the short wavelength parameters without external pressure sweep.	103
3.3.17a	Cross sectional noise reduction predictions at indicated X locations for the long wavelength sweep case.	105
3.3.17b	Cross sectional noise reduction predictions at indicated X locations for the short wavelength sweep case.	105
3.3.17c	Cross sectional noise reduction predictions at indicated X locations for the long wavelength sweep parameters without external sweep.	106
3.3.17d	Cross sectional noise reduction predictions at indicated X locations for the short wavelength sweep parameters without external sweep.	106
3.3.18a	Far field (5 duct widths) noise reduction predictions for the Chapter 2 model (with decay of higher modes) plotted with the Chapter 3 model including all modal contributions for the 2 panel configuration.	108
3.3.18b	Near field (1 panel width) noise reduction predictions for the Chapter 2 model (with decay of higher modes) plotted with the Chapter 3 model including all modal contributions for the 2 panel configuration.	108
3.3.19a	Far field (5 duct widths) noise reduction predictions for the Chapter 2 model (with decay of higher modes) plotted with the Chapter 3 model including all modal contributions for the 8 panel configuration.	109

3.3.19b	Near field (1 panel width) noise reduction predictions for the Chapter 2 model (with decay of higher modes) plotted with the Chapter 3 model including all modal contributions for the 8 panel configuration.	109
3.3.20a	High damping ratio noise reduction prediction for the long wavelength sweep case compared to the averaged noninteracting noise reduction prediction.	110
3.3.20b	High damping ratio noise reduction prediction for the short wavelength sweep case compared to the averaged noninteracting noise reduction prediction.	110
3.3.21a	Noise reduction calculation at Location A for detuned panel properties in the long wavelength external sweep case.	112
3.3.21b	Noise reduction calculation at Location A for detuned panel properties in the short wavelength external sweep case.	112
3.3.22a	Modelling a panel wall irregularity for the long sweep wavelength case.	114
3.3.22b	Modelling a panel wall irregularity for the short sweep wavelength case.	114
3.3.22c	Cross sectional noise reduction predictions at indicated X locations for the long wavelength sweep case with tuning irregularities. Calculation at $\omega_{ART} = 1.0$.	115
3.3.22d	Cross sectional noise reduction predictions at indicated X locations for the short wavelength sweep case with tuning irregularities. Calculation at $\omega_{ART} = 1.0$.	115
3.3.23a	Comparison of noise reduction predictions with two apparent mass loading values for the long wavelength parameters sweep case.	117
3.3.23b	Comparison of noise reduction predictions with two apparent mass loading values for the short wavelength parameters sweep case.	117
3.3.24a	Noise reduction calculation for four panel ART tuned and identical panels with long wavelength external sweep calculated at location A in Figure 3.2.1.	118
3.3.24b	Noise reduction calculation for four panel ART tuned and identical panels with short wavelength external sweep calculated at location A in Figure 3.2.1.	118

4.2.1	Configuration for ART real panel analysis.	121
4.4.1	Dissymmetry of apparent mass loadings (generalized forces) with the inclusion of higher structural modes in the real panel analysis.	135
4.4.2	Qualitative apparent mass differences for flat, pinned, and clamped mode shapes.	136
4.4.3	Frequency parameters, amplitude coefficients, and schematic mode shape configurations showing modal lines for clamped modes determined by Young (reproduced from Leissa).	142
4.5.1	Noise reduction predictions for ART and identical panels using 1 structural mode and panel mode shapes as indicated.	144
4.5.2	Noise reduction predictions for ART and identical panels using 2 structural modes and panel mode shapes as indicated.	144
4.5.3	Noise reduction predictions for ART and identical panels using 3 structural modes and panel mode shapes as indicated.	146
4.5.4	Noise reduction predictions for ART and identical panels using 4 structural modes and panel mode shapes as indicated.	146
4.5.5	Noise reduction predictions for ART and identical panels using 5 structural modes and panel mode shapes as indicated.	147
4.5.6	Noise reduction predictions for ART and identical panels using 6 structural modes and panel mode shapes as indicated.	147
4.5.7	ANNR and ART noise reduction predictions using 2 structural modes and panel mode shapes as indicated.	148
4.5.8a	Parameter studies varying the panel apparent mass loading as indicated for 2 structural modes with pinned mode shapes.	149
4.5.8b	Parameter studies varying the panel apparent mass loading as indicated for 2 structural modes with clamped mode shapes.	149

4.5.9a	Parameter studies varying the panel damping as indicated for 2 structural modes with pinned mode shapes.	150
4.5.9b	Parameter studies varying the panel damping as indicated for 2 structural modes with clamped mode shapes.	150
4.5.10a	Parameter studies varying the ART noise reduction bandwidth by increasing the higher panel natural frequency for 2 structural modes with pinned mode shapes.	151
4.5.10b	Parameter studies varying the ART noise reduction bandwidth by increasing the higher panel natural frequency for 2 structural modes with clamped mode shapes.	151
4.5.11a	Parameter studies varying duct termination impedance as indicated for 2 structural modes with pinned mode shapes.	152
4.5.11b	Parameter studies varying duct termination impedance as indicated for 2 structural modes with pinned mode shapes.	152
5.2.1	Overall experimental setup showing general microphone positions, test section location, and processing equipment.	155
5.3.1	Single wall panel array test sections.	158
5.3.2	Experimental noise reduction measurement with 2 ART tuned panels and two identical panels.	159
5.3.3	Measured phase difference between two ART panels used to generate ART data shown in Figure 5.3.2.	159
5.3.4	Two panel ART noise reduction measurement plotted with two panel ANNRR calculation.	161
5.3.5	ART noise reduction measurements with two panel setup varying panel natural frequencies as shown.	161
5.3.6	Four panel noise reduction measurement.	162
5.3.7	Experimental noise reduction falloff setup showing duct, upstream microphone, and cart microphone setup. Note coordinate system location just below ART panel array. Cross sectional view of duct at panel array shows relative microphone position in the duct.	163

5.3.8	Difference between upstream microphone and cart microphone levels as a function of distance down the duct for the two panel ART array. Measurement is taken as shown in Figure 5.3.7.	164
5.3.9	Falloff measured away from the panel wall array with the cart microphone. The falloff in decibels is referenced to the sound pressure level just downstream of the panel wall.	164
5.4.1	Double wall test section with identical panels upstream and ART tuned or identical panels downstream. Midstream microphone located as shown.	166
5.4.2	Experimental noise reduction measurement in the double wall setup with four identical panels and identical panels upstream and ART tuned panels downstream with the 7" coupling.	167
5.4.3	Phase difference between ART tuned panels used to generate noise reduction data in Figure 5.4.2.	167
5.4.4	Noise reduction measurements for ART tuned panels downstream and identical panels upstream with coupling separation distances as shown.	168
5.5.1	Double wall test sections with ART panels upstream and downstream. Note difference between inline and opposed ART configurations. Midstream microphone located as shown in Figure 5.4.1.	169
5.5.2	Experimental noise reduction measurements for inline and opposed double ART walls.	170
5.5.3	Experimental noise reduction results for inline double ART walls with coupler spacings as shown.	170
5.5.4	Experimental noise reduction results for opposed double ART walls with coupler spacings as shown.	171
5.6.1	Double wall test section with nonuniform panel sizes. ART or identical panels are placed on downstream panel. Midstream microphone is placed on duct centerline and equidistant from each panel array.	172
5.6.2	Experimental noise reduction comparison between uniform and ART panel arrangements for the 1" coupling.	173

5.6.3	Noise reduction data from double wall nonuniform panel size experiments with coupling spacings as shown.	173
5.7.1	Plan view of real panel wall test configuration. Noise reduction measurements are made using both single panel and double panel ducts.	175
5.7.2	Experimental noise reduction measurement comparison for a single 1/64" unaltered Bakelite panel and mass-altered Bakelite panel.	176
5.7.3	Experimental noise reduction measurement with two panel ART setup with unaltered 1/64" Bakelite panel and 1/64" mass-altered Bakelite panel.	176
6.6.1	Multi-walled model for future investigation.	186

List of Tables

Figure	Title	Page
2.2.1	Base nondimensional parameter components and values for the four panel and two panel models.	23
3.3.1	Long and short wavelength sweep input parameters representing the Gulfstream Aerospace Commander 695A and the Gulfstream II. Unlisted parameters are as given in Table 2.2.1, "Compensated Two Panel Model".	73
3.3.2	Mode turn-on frequencies below $\omega = 5.0$ for the long and short wavelength sweep parameters.	74
3.3.3	Panel detuned parameter values used in Figure 3.3.22.	113

List of Symbols and Abbreviations

A	acoustic pressure and velocity coefficient
A	hydrodynamic loading consideration (Chapter 3 only)
A_A	duct area on side A
A_B	duct area on side B
A_i	branch i panel area
A_{ij}	area of panel ij in four panel analysis
$A_{pq}^{\alpha\beta}$	modal amplitude for mode pq of panel $\alpha\beta$
ANNR	averaged noninteracting transmission loss
AR	panel aspect ratio W/H
B	acoustic pressure and velocity coefficient
BPF	blade passage frequency
C_{area}	dimensionless area coefficients
C_{kl}^{ij}	influence coefficients
C_{mass}	dimensionless mass coefficient
c	sound speed
c_e	pressure sweep trace speed
D	propeller diameter
d	propeller tip to fuselage clearance
dB	decibels
e	~ 2.71828
F_{ij}^{kl}	force on panel ij due to panel kl
H	panel height
Hz	frequency in Hertz
h	overall height for 2D pressure sweeping duct configuration
k	acoustic wavenumber
k_e	exterior forcing pressure field wavenumber
k_n	modal wavenumbers
$k_{m\ n}$	modal wavenumbers
L_M	length to microphone from coordinate system location
L	length to panel array from coordinate system
M	mass per unit area

M_i	two panel mass for panel i
M_{pq}^{ij}	panel ij mode pq mass
M_{pq}^{ij}	Lagrangian representation of panel ij, mode pq dynamics
MR_i	two panel mass ratio for panel i
MR_{ij}	four panel mass ratio for panel ij
m_a	hydrodynamic mass
N	number of panels in repeating paneled system
NR	noise reduction in decibels
P_A	pressure on side A of panel wall
P_0	pressure due to 1 dimensional acoustic mode (acoustic mode "zero" pressure)
P_E	amplitude of exterior forcing field pressure
P_{EX}	overall exterior pressure forcing
P_I	incident exterior pressure at panel wall
P_M	acoustic pressure at microphone location
P_R	exterior reflected pressure at panel wall
p	general acoustic pressure
p_{ij}	pressure on panel ij
P_r	downstream pressure reflected from termination impedance
P_t	transmitted pressure downstream from panel barrier
Q	number of panels for sweeping analysis
$Q_E^{\alpha\beta}$	generalized external force on panel $\alpha\beta$
Q_m	generalized force due to motion
$Q_{mpq}^{ab,ij}$	generalized force due to motion of panel ij on panel $\alpha\beta$, mode pq
$Q_{pq}^{\alpha\beta}$	generalized force on panel $\alpha\beta$, mode pq
R_i	damping constant for panel i for two panel models
R_{ij}	damping constant for panel ij for four panel models
S_i	stiffness constant for panel i for two panel models
S_{ij}	stiffness constant for panel ij for four panel models
S_1	panel size to sound speed parameter (see Table 2.2.1)
S_2	apparent mass loading parameter (see Table 2.2.1)

S_3	ratio of microphone position to panel size (see Table 2.2.1)
S_4	ratio of duct length to panel size (see Table 2.2.1)
S_5	ratio of entire duct cross sectional area to individual panel area (see Table 2.2.1)
S_6	ratio of 2π *panel height to external propagating pressure wavelength (see Table 3.3.1)
S_n	cutoff pressure mode summations
s	fuselage skin thickness
t	time
U_{ij}	panel velocities
u_{ij}	velocity boundary conditions
u,v,w	acoustic velocity components
W	panel width
Z_b	duct termination impedance
Z_{ei}	equivalent net mechanical impedance of panel i
Z_{ij}	mechanical impedance of panel ij
Z_m	mechanical impedance
α	Young's eigenfunction parameter
χ	Young's mode shape
ϵ	Young's eigenfunction parameter
Φ	panel velocity mode shape
ϕ_{pq}^{ij}	panel ij mode pq shape
λ_e	external pressure propagation wavelength
π	~ 3.1415926
ρ_o	air density
ω	nondimensional frequency
ω_{ART}	nondimensional frequencies for greatest noise reduction
ω_i	natural frequency
$\omega_{npq}^{\alpha\beta}$	natural frequency for mode pq of panel $\alpha\beta$
ω_r	reference frequency for nondimensionalization
ξ_w	wall displacement
Ψ_{ij}	spatial dependence of acoustic modal function

ζ_i damping ratio
 $\zeta_{npq}^{\alpha\beta}$ damping ratio for mode pq of panel $\alpha\beta$

Chapter 1

The General Noise Problem and Alternate Resonance Tuning

Section 1.1: Introduction

Existing noise reduction techniques for paneled structures perform reasonably well at higher frequencies, but are less effective at lower frequencies, particularly if the low frequency noise problem has high forcing levels such as those found in helicopter or propeller aircraft. This research effort focuses on a method which considers enclosures lined with panels alternately tuned to frequencies above and below the frequency that must be attenuated. Adjacent panels would oscillate at equal amplitude, to give equal source strength, but with opposite phase. If these adjacent panels are acoustically compact, the resulting cancellation causes the interior acoustic modes to become cutoff, and therefore be non-propagating and evanescent. This noise reduction method, called *Alternate Resonance Tuning* (ART), has potential application to reducing interior noise in a variety of structures. As mentioned previously, one particularly appropriate application is in aircraft fuselages. With some minor modifications, the method might also be applied to a variety of noise problems in other areas, such as road and wind noise in

automobiles, flow and fan noise in heating and air conditioning ducts, and noisy discrete frequency components in household appliances.

The ART technique is a procedure intended to reduce low frequency noise within an enclosure. A paneled wall could be constructed of, or lined with, a series of special panels which would allow the designer to control the wavenumber spectrum of the wall motion, thus controlling the interior sound field. By judicious tuning of the structural response of individual panels, wavelengths inside the enclosure can be reduced to the order of the panel size, thus causing low frequency interior acoustic modes to be cutoff provided these panels are sufficiently small. By cutting off the acoustic modes in this manner, a significant reduction of interior noise at lower frequencies should be achieved.

Current aircraft fuselage noise control treatments have already demonstrated that the mass and stiffness of individual panels can be altered. This research effort demonstrates that panel resonance frequencies can be manipulated to achieve the ART effect. Application of this concept might involve the modification of existing structural panels or development of a new design for enclosure interior trim panels. Although complete acoustic cutoff will not be achievable in practice, an approximate cancellation should still substantially reduce the interior noise levels at the particular frequency of interest. It is important to note that the ART method utilizes the flexibility and dynamic behavior often found in these structures to good advantage, although these properties are not normally beneficial in noise control.

Section 1.2: Review of the Literature

A survey of the current state-of-the-art in noise measurements and noise reduction techniques associated with

paneled structures provides insight for the problems found in these structures. The following is not intended as a complete literature review but rather a survey of work related to the definition of the noise problem in paneled structures (especially aircraft applications) and existing techniques for noise reduction in those structures. Low frequency sound transmission of propeller near-field pressure, radiated noise, and structural vibration through the aircraft fuselage are important sources of interior noise for propeller aircraft. Test results of interior noise measurements on actual aircraft, such as those conducted by Kuntz and Prydz¹ and Wilby and Wilby², confirm the presence of high noise levels outside and inside the fuselage. Figure 1.2.1 (reproduced from Kuntz and Prydz) shows sound pressure level spectra measured outside the fuselage behind the propeller plane with and without the propfan in place. Figure 1.2.2 (also reproduced from Kuntz and Prydz) shows the resulting interior cabin spectra measured with and without the propfan. There remains a definite need to reduce the interior noise due to this discrete, low frequency noise source. The ongoing development of advanced turboprop aircraft technology for commercial use (spurred forward by fuel savings claims of 35% for a contrarotating propfan over a conventional turbofan³) underscores the need for a solution to this noise problem. The first few propeller blade passage harmonics are difficult to reduce because of their low frequency and high forcing levels. Low frequency acoustic transmission is particularly difficult to block or absorb given the weight and wall thickness constraints imposed by fuselage construction techniques. Fuselage panels are necessarily thin and flexible and are often lightly damped, with resonance frequencies in the same range as the blade passage harmonics. Helicopters suffer from similar discrete low frequency noise problems, where the blade passage frequencies are even lower (and hence, harder to control) than that found in propeller driven aircraft, as shown in Figure 1.2.3 (reproduced from Brentner).⁴

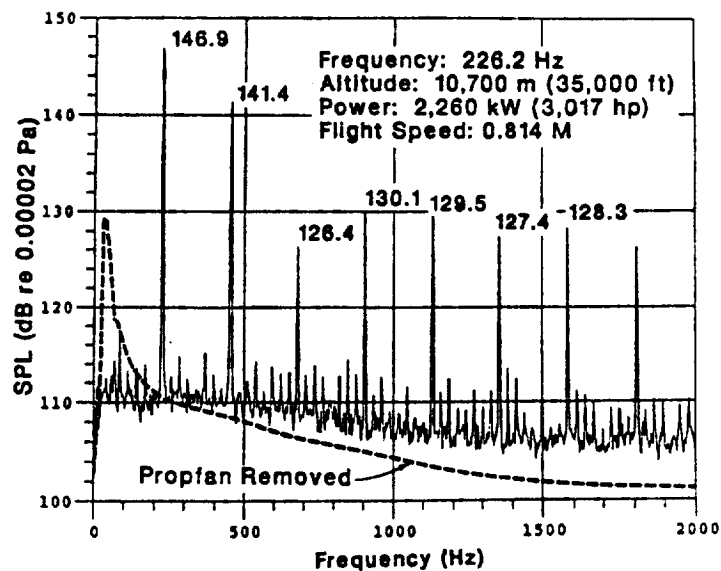


Figure 1.2.1: Exterior fuselage sound pressure spectra measured 63.5 cm behind the propeller plane with and without the propfan on a Gulfstream II aircraft (reproduced from Kuntz and Prydz).

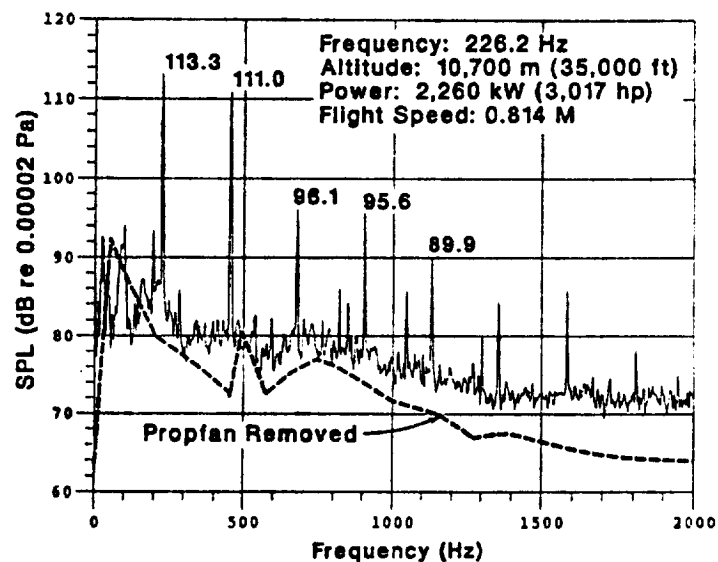


Figure 1.2.2: Cabin sound pressure level spectra measured in the prop plane with and without the propfan (reproduced from Kuntz and Prydz).

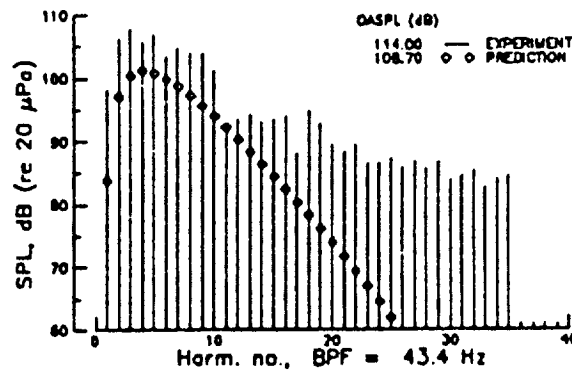


Figure 1.2.3: Experimental data for the first 40 harmonics of the blade passage frequency taken from 1/4 scale model tests, including a comparison to predicted levels by the noise prediction program WOPWOP (reproduced from Brentner).

Although not mentioned as often as discrete noise sources, broadband noise can also play a role in fuselage interior sound levels at low speed, low power operating conditions, as reported by Knowles.⁵

An additional and extensive review of the subject of propeller-driven aircraft interior noise is given by Mixson and Powell.⁶ The more specific topic of noise transmission through aircraft panels is reviewed by Vaicaitis, Grosveld, and Mixson.⁷ A current methodology to predict the performance of acoustic treatments installed in an actual aircraft fuselage is given by Heitman and Mixson.⁸ These papers show the complexity of the interior noise problem and demonstrate the degree of success of current acoustic treatment methods. In the detailed design of an interior noise treatment, as described by Vaicaitis and Mixson⁹, panels have had alterations in mass, stiffness, and damping, and

fuselage walls have been filled with multi-layered absorptive materials. Figure 1.2.4 (reproduced from Vaicaitis and Mixson) displays the breadth and complexity of such acoustic treatments. It has been found most effective to utilize different treatment combinations depending on the specific panel or panel region involved. Considerable noise reduction has been achieved over most of the frequency spectrum by careful application of these standard methods. However, additional improvement is still required at the lowest harmonics of blade passage frequency, where even sophisticated multi-layer wall treatments are not adequate. Figure 1.2.5 (also reproduced from Vaicaitis and Mixson) shows a comparison of measured noise levels in an untreated aircraft and a prediction of noise levels after acoustic treatment has been applied. Note that little improvement is realized below about 200 Hertz.

Beyond the implementation of these basic noise reduction techniques (adding mass, stiffness, structural damping, and absorptive material), several other approaches specifically applicable to this problem have been previously put forth, or are currently being investigated. These include the careful design of the periodic structural members of the fuselage and the concept of intrinsic structural tuning.^{10,11,12} Another approach involves the use of a large number of sharply tuned Helmholtz resonators embedded within the fuselage wall.^{13,14} Other techniques include direct consideration of the propeller as a noise source. One such possibility is the reduction of propeller noise by controlling the phasing of multiple propellers.⁶ Another promising area of current research is the use of active noise control.^{15,16} This method seeks to achieve cancellation of certain acoustic modes in the cabin enclosure by the introduction of additional canceling acoustic sources. These sources are intended to actively adjust their properties to achieve the desired effect.

There is a clear need for a new method to reduce discrete, low frequency propeller generated interior noise. Such a method

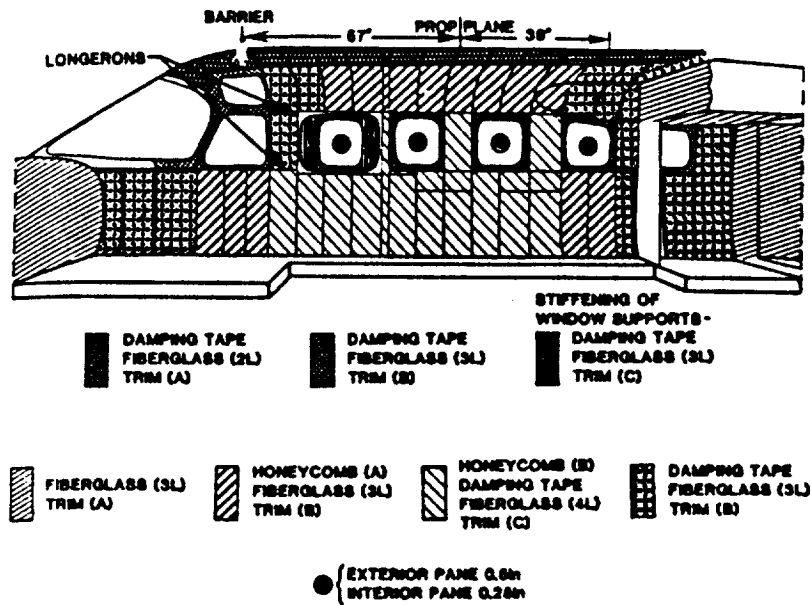


Figure 1.2.4: Distribution of acoustic treatments for noise control in an aircraft fuselage (reproduced from Vaicaitis and Mixson).

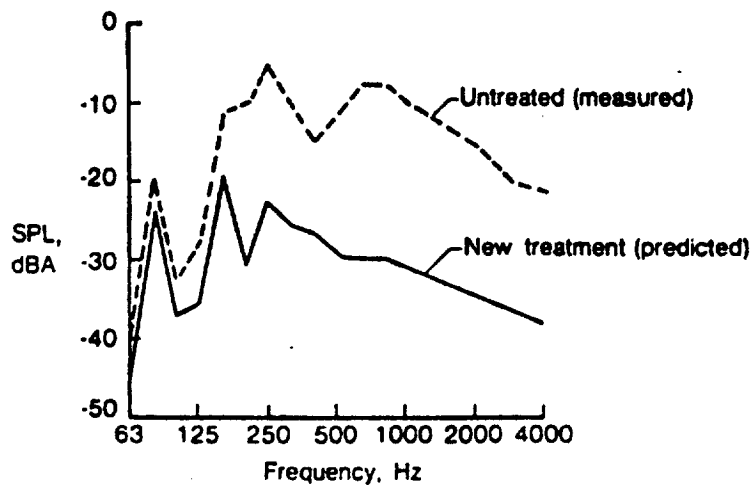


Figure 1.2.5: Measurement of noise transmitted into untreated fuselage compared with prediction of noise transmitted into treated fuselage (reproduced from Vaicaitis and Mixson).

must successfully coexist with the noise reduction methods already demonstrated to work well at higher frequency, and must also function within the constraints imposed by fuselage construction techniques. It would be highly desirable to have a method that does not entail a significant weight penalty, does not require precise tuning, and is relatively robust in terms of variations in operating conditions and environment. Alternate Resonance Tuning (ART) is a novel approach to low frequency noise reduction that appears to satisfy these constraints and still be compatible with current noise reduction techniques. This new approach could be implemented on existing fuselage structures. Even greater effectiveness may be achieved with structures intentionally designed to utilize this method, such as future turboprop designs or state-of-the-art fuselage trim panels and liners.

Section 1.3: Alternate Resonance Tuning

The concept of Alternate Resonance Tuning was developed at Duke University by Dr. Donald B. Bliss in 1986.¹⁷ Many noise control methods depend heavily on the addition of structural damping as a means to reduce the motion of surfaces which radiate noise. ART relies instead on designing paneled structures which use acoustic cutoff as a means to couple poorly to the acoustic fields within an enclosure. The method therefore allows surfaces to move, but in a motion which is prescribed by the designer. Additional damping is not required to improve noise reduction performance in a structure provided the structure follows the criteria outlined below.

Consider a low frequency noise source, such as a propeller blade passage harmonic, that needs to be suppressed in the fuselage interior. The forcing frequency will be fixed by the characteristics of the noise source, and the wavelength will typically be large compared to most fuselage construction features; for example, panel sizes, frame spacings, and so forth. The

characteristics of the interior sound field depend on the possible modes of motion of the interior wall surfaces. The fuselage walls could be constructed using a series of panels. These may be panels normally used in fuselage construction, or a special panel structure can be introduced on the interior walls. The paneled structure of the fuselage walls allows the opportunity to control the wavenumber spectrum of the wall motion and thereby control the behavior of the interior sound field. Specifically, by judicious tuning of the structural response of the individual panels, the wavenumber spectrum of the interior wall motion can be reduced to the order of the panel size. At low frequency, physically reasonable panel sizes correspond to wavelengths for which interior acoustic modes are cutoff; i.e., the modes are evanescent and nonpropagating. Achieving cutoff will produce a dramatic reduction in interior noise levels at the propeller blade passage harmonic.

To achieve cutoff, the panels must be smaller than the acoustic wavelength at the frequency in question; namely, the adjacent panels must be acoustically compact. Furthermore, the motion of adjacent panels must be out of phase and have equal and opposite acoustic source strength. For equal size panels, it is thus necessary for adjacent panels to execute equal and opposite motions. Figure 1.3.1 shows qualitatively the velocity magnitude and phase relationships for the lowest modes of two appropriately tuned panels. To achieve this condition, the adjacent panels must be tuned to have resonance frequencies alternately above and below the frequency to be attenuated. For this reason the method is called *Alternate Resonance Tuning* (ART). Although complete acoustic cutoff will not be achieved in practice, an approximate cancellation will still substantially reduce interior noise levels at and around the particular frequency of interest.

It is important to note that the ART method utilizes the flexibility and dynamic behavior of the structure to good advantage, although these properties are not normally beneficial in

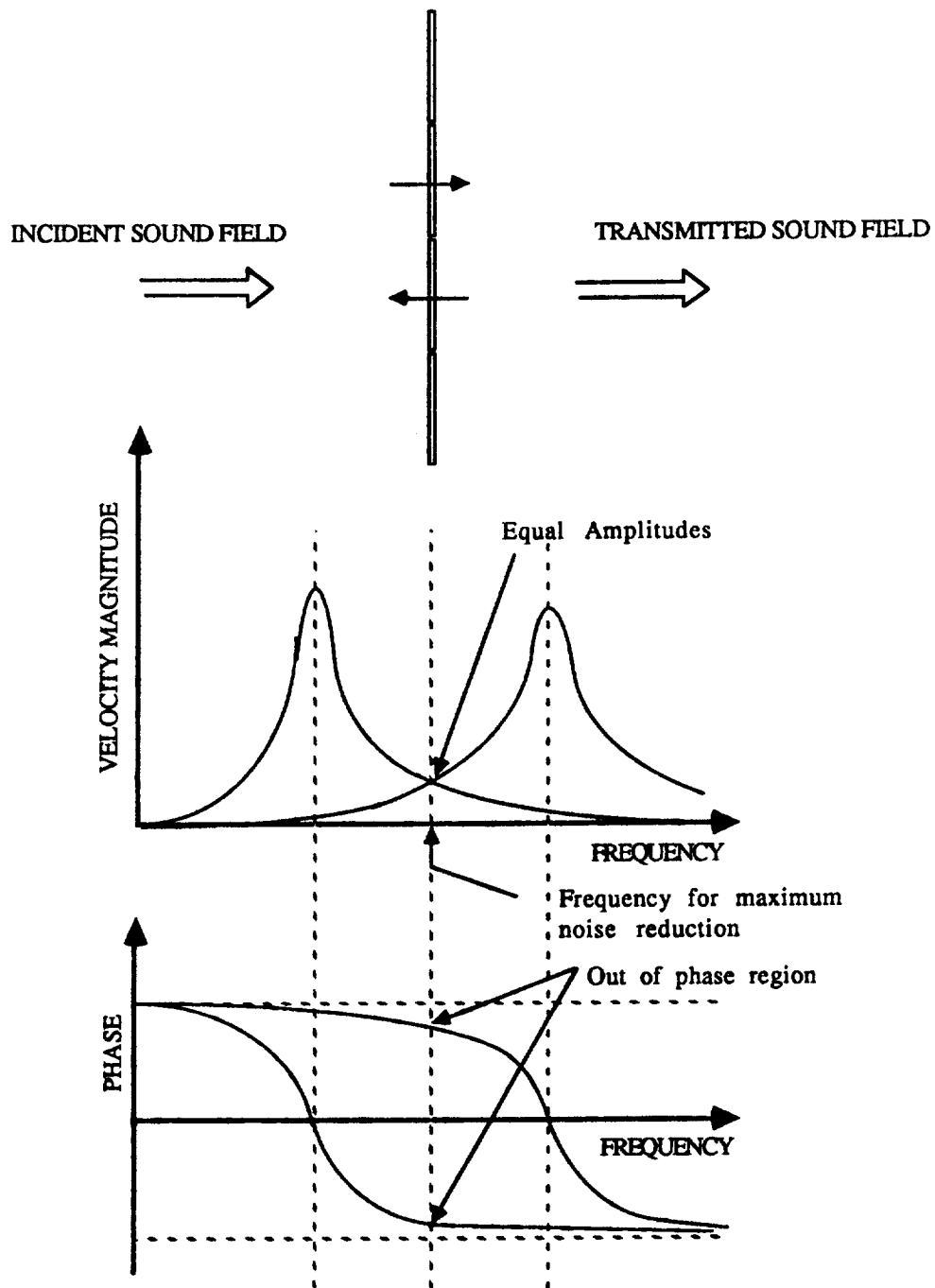


Figure 1.3.1: Amplitude and phase relations for adjacent panels for ART tuning.

noise control. Whereas traditional noise control methods focus on reducing the amplitude of wall motion, the ART method focuses on controlling the shape of the wall motion to break the coupling to the acoustic interior. Interestingly, the ART method tends to work better with less damping, since more perfectly out-of-phase panel motions can be achieved. Transmission loss is obtained by reflecting the incident sound field, although the individual panels are neither massive nor stiff.

Chapter 2

The Four Panel Problem

Section 2.1: Introduction

Many paneled structures are composed of a finite number of elements or building blocks which are grouped together into a repeating pattern which covers a structure over a desired area. Some familiar examples, as noted in Chapter 1, might include an aircraft fuselage with panels applied over ribs and stringers, a paneled wall on a railroad car or passenger vehicle, a noise reducing divider in a building between noisy equipment rooms and quiet office areas, and a heating/ventilation duct. The theoretical models presented in this chapter consider sound transmission through such a wall of panels, as shown in Figure 2.1.1. A wall of infinite extent composed of idealized spring-mass-damper panels is arranged in a periodic pattern. Note that these idealized panels are assumed to have a flat, rigid panel element. Sound waves are assumed to strike the wall at normal incidence and the acoustic transmission is calculated in terms of the dynamic properties of the panels. In addition, the analysis considers placement of a parallel barrier beyond the panel wall of specified acoustic impedance to simulate reflections within an enclosure. The panel wall itself is subdivided into identical blocks of panels; within each block the analysis allows for four panels with varying dynamic properties. By adjusting the panel dimensions (wavelengths must be long compared to the panel dimensions) and

11	12	11	12	11	12	11	12	11	12
21	22	21	22	21	22	21	22	21	22
11	12	11	12	11	12	11	12	11	12
21	22	21	22	21	22	21	22	21	22
11	12	11	12	11	12	11	12	11	12
21	22	21	22	21	22	21	22	21	22
11	12	11	12	11	12	11	12	11	12
21	22	21	22	21	22	21	22	21	22
11	12	11	12	11	12	11	12	11	12
21	22	21	22	21	22	21	22	21	22
11	12	11	12	11	12	11	12	11	12
21	22	21	22	21	22	21	22	21	22

Figure 2.1.1: Panel wall layout with analysis subsection highlighted with thickened line. Note periodicity assumed in the wall construction. Panels are labeled in matrix-like notation.

choosing different dynamical properties for the panels, a variety of one, two, and three dimensional physical configurations may be simulated as shown in Figure 2.1.2. The actual number of degrees of freedom depends on the nature of the velocities of the fluid close to the surface of the panel array. In Figure 2.1.2, the first three dimensional pattern will have a horizontal velocity as fluid sloshes back and forth between panels 1 and 2 and panels 3 and 4. A vertical velocity is created by similar vibration of panels 1 and 3 and panels 2 and 4. All panels produce fluid motion in a direction perpendicular to the page by virtue of their oscillation. The paneled pattern in Figure 2.1.2 repeats indefinitely on the wall, and the analysis proceeds with a repeating portion of the four panel geometry extracted and placed in a duct, as shown in Figure 2.1.3.

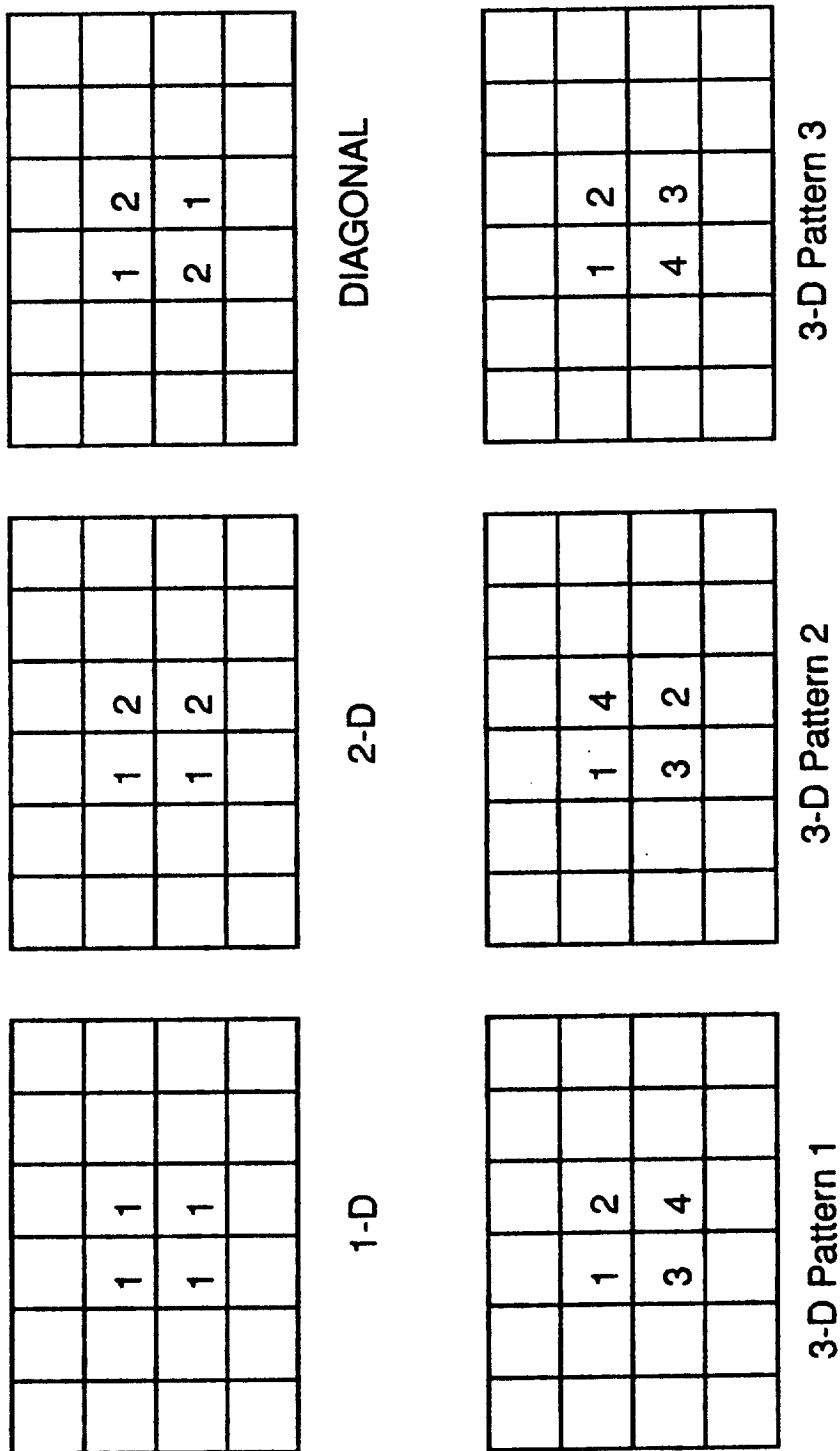


Figure 2.1.2: Arrangement possibilities for the four panel analysis configuration.

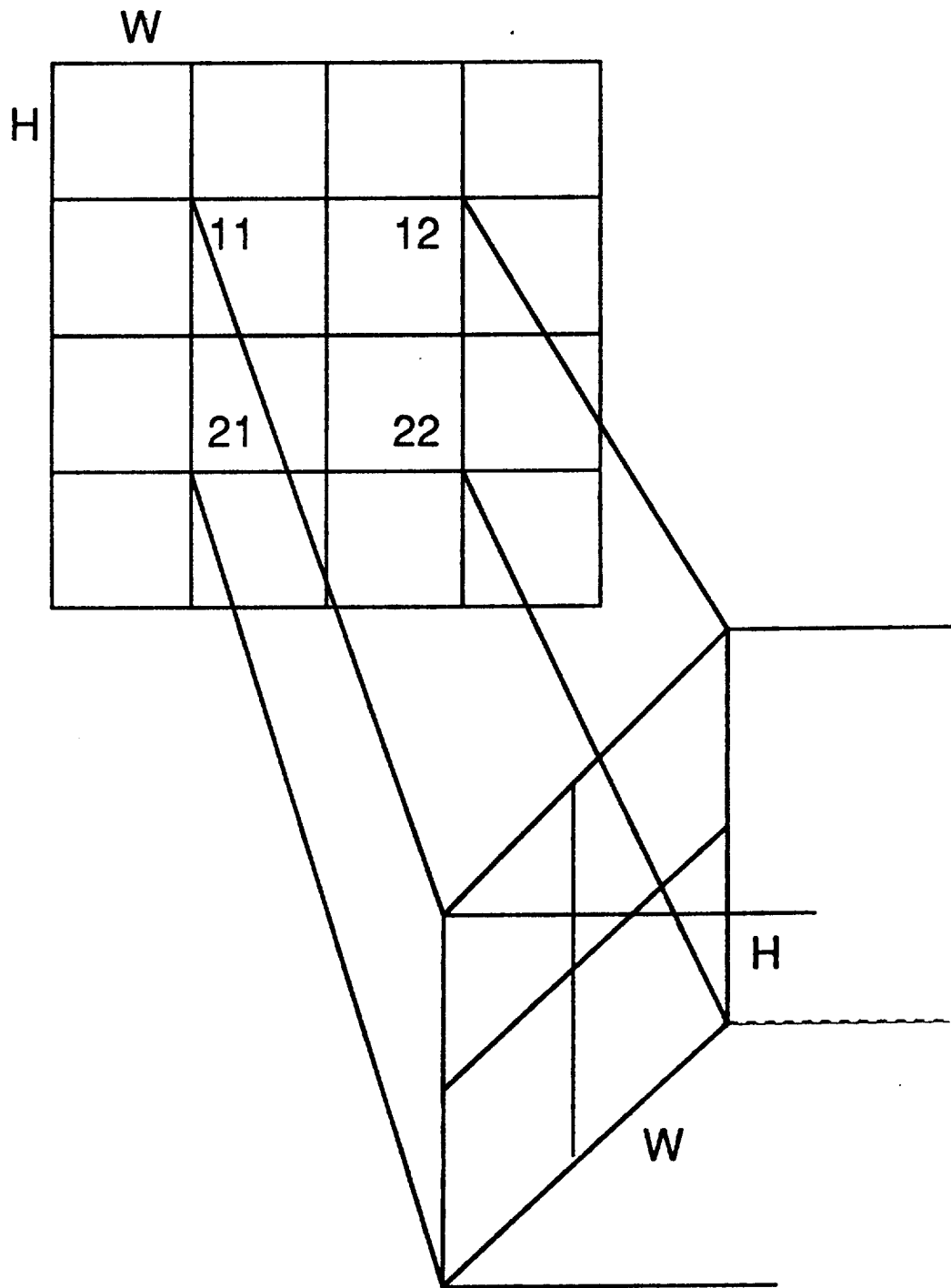


Figure 2.1.3: Extraction of the panel wall subsystem and incorporation into a duct.

Section 2.2: Acoustic Branch Analysis

The acoustic branch analysis technique is a quasi one-dimensional treatment which provides a fairly easy method for obtaining approximate solutions for the behavior of a system as shown schematically in Figure 2.2.1. Additionally, this method provides simple results with which more elaborate analyses may be checked. A brief derivation of the branch analysis result will introduce terminology, acoustics results, and nondimensionalization which will be applied to a variety of problems throughout this work.

With respect to Figures 2.2.1 and 2.2.2, capital subscripts are applied to pressures on the exterior side of the paneled structure, while small subscripts are applied to pressures on the interior. Note that P_I is the uniform normal incident pressure applied to the panels, and P_R is the reflected exterior pressure amplitude. Similarly, P_t is the pressure transmitted through the structure and present on the downstream side, and P_r is the pressure amplitude of the reflected wave from the termination impedance Z_B . All pressures are complex quantities. Other alternative pressure variables apply for different analysis purposes; P_A is the net effective exterior pressure at point A, while P_B is the net effective interior pressure at point B on the downstream (right of the panel barrier) side. The duct is of length L from panel barrier to termination impedance, with a coordinate system located as shown in Figure 2.2.2. The analysis will solve for the noise reduction which occurs across the panel barrier. This is equivalent to the sound pressure level difference in decibels which microphones would read at locations M_1 and M_2 ; a positive noise reduction is indicated by a lower sound pressure level at position M_2 . The acoustic loading due to the cutoff modes (inertance or apparent mass effects) acting on the panels is neglected in the branch analysis, which significantly simplifies the results. Essentially, the incident acoustic field is split into separate branches, one for each

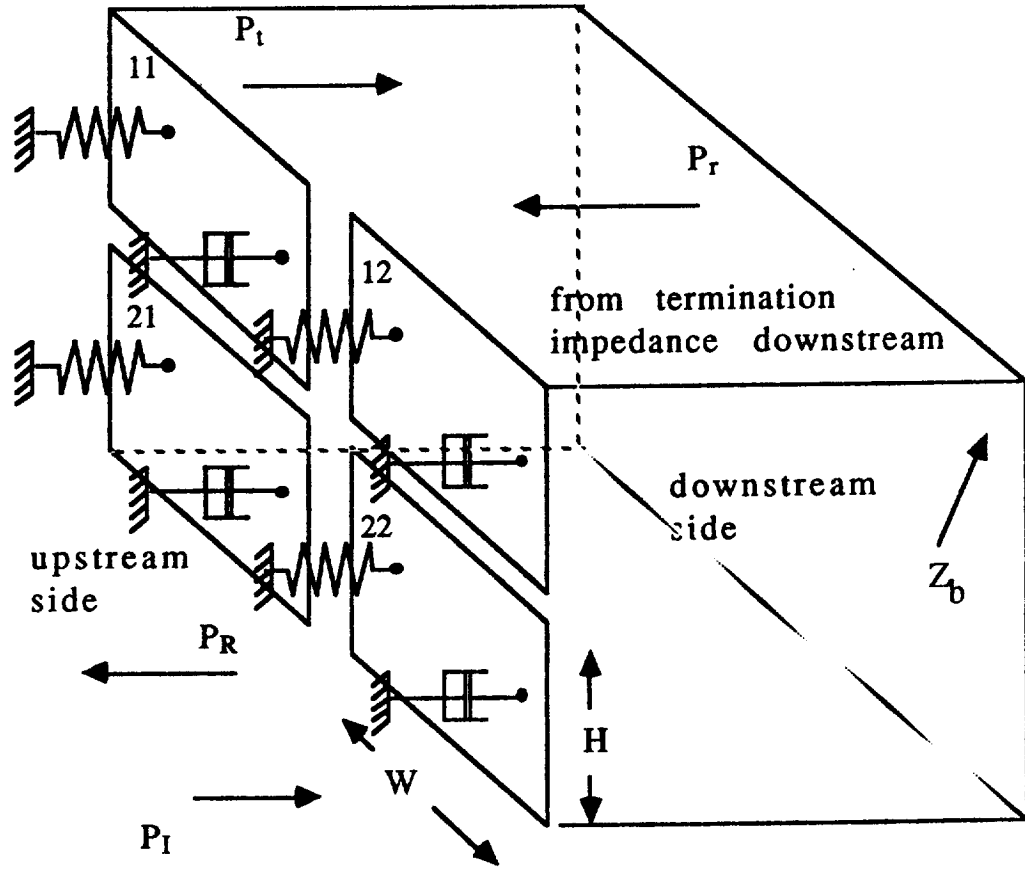


Figure 2.2.1: Schematic of analysis configuration placed in the duct.

panel as shown in Figure 2.2.2, and these branches are rejoined on the other side of the panel barrier. At each branch junction pressure and flow continuity conditions are applied. Shape details of the individual branches do not affect the results; therefore, a coordinate system in the plane of the panel barrier is not required for this analysis.

For the branched panel barrier, note that duct areas on both sides on the panel barrier are the same; that is,

$$A_A = A_B = \sum_{i=1}^N A_i \quad (2.2.1)$$

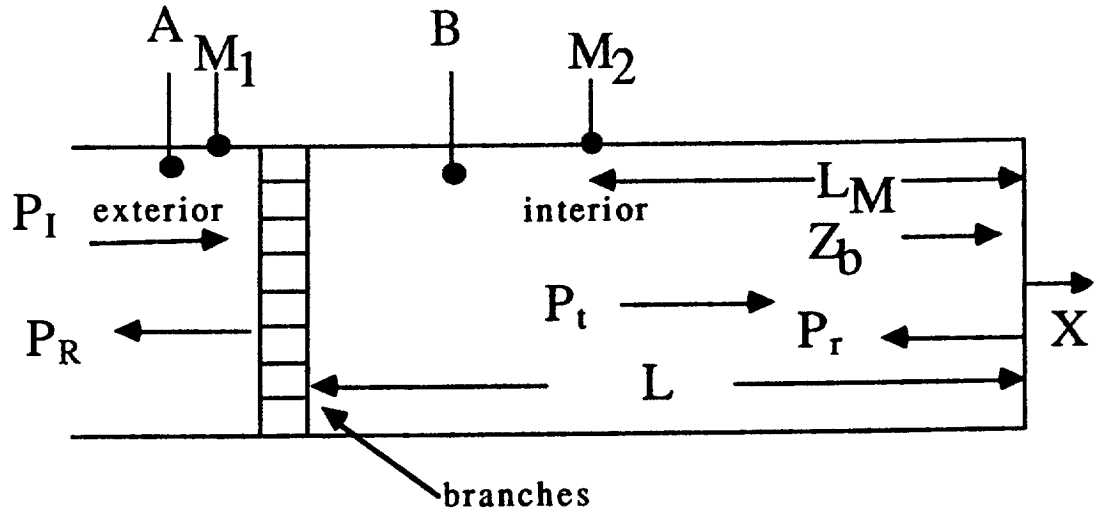


Figure 2.2.2: Equivalent branch analysis schematic.

where the subscripts denote upstream (A) or downstream (B) position with respect to the panel wall barrier. N is the total number of branches considered, or 4 for this analysis. A one dimensional continuity equation may then be written as

$$U_0^A e^{i\omega t} A_A = U_0^B e^{i\omega t} A_B = \sum_{i=1}^N U_i e^{i\omega t} A_i \quad (2.2.2)$$

The zero subscript on velocities U represents the one dimensional acoustic mode, or the "zero mode". Let Z_{mi} denote the mechanical impedance of the i^{th} panel. This mechanical impedance is of the form

$$Z_{mi} = R_i + i \left(M_i \omega + \frac{S_i}{\omega} \right) \quad (2.2.3)$$

where R_i is the panel damping constant, M_i is the panel mass, and S_i is the panel stiffness. Figure 2.2.3 shows a typical

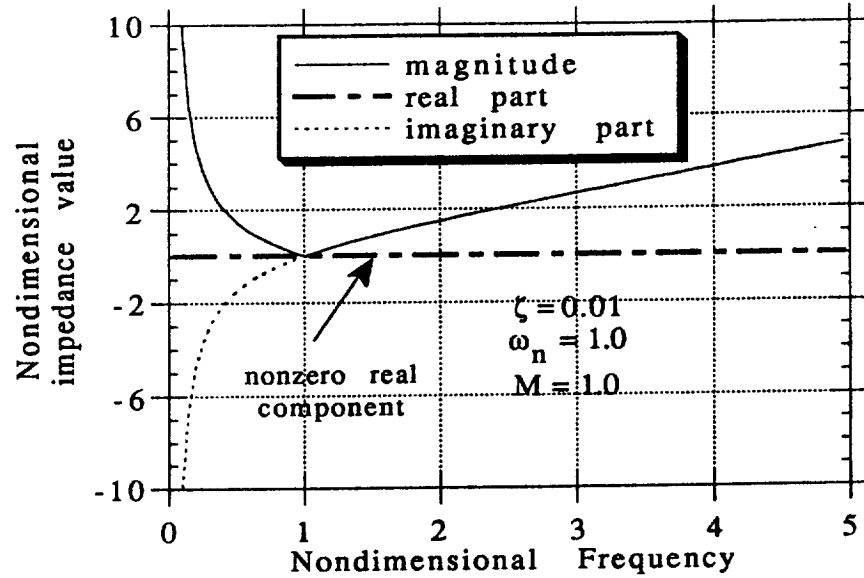


Figure 2.2.3: Typical nondimensional impedance versus nondimensional frequency with components as noted. Low damping yields small but nonzero real component of the impedance.

nondimensional impedance versus frequency plot. Note that the magnitude of the nondimensional impedance approaches a minimum at the panel nondimensional natural frequency, and that the real part of this impedance is frequency independent. Invoking the definition of mechanical impedance along with a simple force balance on the panel barrier yields

$$U_i Z_{m_i} = F_i = (P_0^A - P_0^B) A_i \quad (2.2.4)$$

Solving Equation (2.2.4) for U_i and inserting into Equation (2.2.2) yields

$$U_0^B A_B = (P_0^A - P_0^B) \sum_{i=1}^N \frac{A_i^2}{Z_{m_i}} \quad (2.2.5)$$

Taking advantage of the fact that $A_A = A_B$ and

$$U_0^B = \frac{P_0^B}{Z_0^B}$$

the following relationship may be obtained.

$$\frac{P_0^B}{Z_0^B} A_A = (P_0^A - P_0^B) \sum_{i=1}^N \frac{A_i^2}{Z_{m_i}} \quad (2.2.6)$$

Here Z_0^B refers to the acoustic impedance looking downstream from the panel barrier. A derivation of this acoustic impedance Z_0^B at the point $X = -L$ begins by assuming right and left traveling pressure and velocity expressions given by

$$p(x,t) = A e^{i(\omega t - kx)} + B e^{i(\omega t + kx)} \quad (2.2.7a)$$

$$u(x,t) = \frac{A}{\rho c} e^{i(\omega t - kx)} - \frac{B}{\rho c} e^{i(\omega t + kx)} \quad (2.2.7b)$$

Standard acoustic impedance at x and t is defined as

$$Z_b = \frac{p(x,t)}{u(x,t)} \quad (2.2.8)$$

At $x = 0$, the following classic result is obtained after substitution into Equations (2.2.7).

$$\frac{B}{A} = \frac{Z_b - \rho c}{Z_b + \rho c} \quad (2.2.9)$$

Substitution into (2.2.7) for $X = -L$ followed by substitution of (2.2.7a) and (2.2.7b) into (2.2.8), coupled with the use of (2.2.9) and some manipulation produces

$$Z_0^B = \rho_0 c \frac{Z_b \cos kL + i\rho_0 c \sin kL}{\rho_0 c \cos kL + iZ_b \sin kL} \quad (2.2.10)$$

Equation (2.2.6) may be then solved for the ratio of downstream to upstream pressures adjacent to the panel barrier in Figure 2.2.2 as

$$\frac{P_0^B}{P_0^A} = \frac{\sum_{i=1}^N \frac{A_i^2}{Z_{m_i}}}{\frac{A_A}{Z_0^B} + \sum_{i=1}^N \frac{A_i^2}{Z_{m_i}}} \quad (2.2.11)$$

However, it is more useful to determine the effective pressure at the microphone location $-L_M$; in this manner, the analysis will yield results which are equivalent to a microphone reading in decibels at position $-L_M$. Note that

$$\frac{P_M^B}{P_0^A} = \frac{P_0^B}{P_0^A} \frac{P_M^B}{P_0^B} \quad (2.2.12)$$

where

$$\frac{P_M^B}{P_0^B} = \frac{Z_b \cos k[L - L_M] + i\rho_0 c \sin k[L - L_M]}{Z_b \cos kL + i\rho_0 c \sin kL} \quad (2.2.13)$$

Equation (2.2.13) is obtained in a similar manner as was Equation (2.2.10). Equation (2.2.12) may then be directly turned into a noise reduction in decibels as

$$NR = -10 \log \left| \frac{P_0^B}{P_0^A} \right|^2 - 10 \log \left| \frac{P_M^B}{P_0^B} \right|^2 \quad (2.2.14)$$

A similar methodology can determine the ratio of transmitted to incident pressure as

$$\frac{P^t}{P^I} = \frac{(Z_b + \rho c)}{Z_b} \left(\frac{Z_0^B}{Z_0^A + \rho c} \right) \quad (2.2.15)$$

where

$$Z_0^A = Z_0^B + \frac{A_A}{\sum_{i=1}^N \frac{A_i^2}{Z_i}} \quad (2.2.16)$$

Here Z_0^A is the impedance on the left hand side of the panel assembly. Equation (2.2.12) may be applied for any number of panels to obtain closed form dimensional results. For example, for 2 panels and an anechoic termination,

$$\frac{P_t}{P_I} = \frac{Z_1 + Z_2}{Z_1 + Z_2 + \frac{Z_1 Z_2}{\rho_0 c W H}} \quad (2.2.17)$$

For four panels and an anechoic termination,

$$\frac{P_t}{P_I} = \frac{Z_1 Z_2 Z_3 + Z_2 Z_3 Z_4 + Z_3 Z_4 Z_1 + Z_4 Z_1 Z_2}{Z_1 Z_2 Z_3 + Z_2 Z_3 Z_4 + Z_3 Z_4 Z_1 + Z_4 Z_1 Z_2 + \frac{Z_1 Z_2 Z_3 Z_4}{2 \rho_0 c W H}} \quad (2.2.18)$$

Section 2.2.1: Nondimensionalization

Nondimensionalization of the general results presented above makes use of the nondimensional groupings shown in Table 2.2.1 below. Typical numerical values are based on a square aluminum panel of length 12" on each side and 1/16" thick. Note that noncompensated mass ratios place the ART design frequencies (the frequencies of maximum noise reduction) at $\omega = 1.0$ (two

Table 2.2.1: Base nondimensional parameter components and values for the four panel and two panel models.

PARAMETER		NONCOMPENSATED				COMPENSATED			
name	definition	grouping	2 panel	4 panel	2 panel	4 panel	2 panel	4 panel	2 panel
$\overline{\omega_{ART}}$	ART design frequencies	$\frac{\omega_{ART}}{\omega_{ref}}$	1.0	1.0 2.0 3.0	1.0	1.0	1.0	1.0 2.0 3.0	
MR_{ij}	mass ratios	$\frac{mass_{ij}}{mass_{11}}$	1.0 0.6	1.0 0.925 0.757 0.409	1.0 0.680	1.0	1.0	1.0 0.929 0.841 0.620	
S_1	panel size to sound speed	$\frac{\omega_{ref} H}{c}$	0.56	0.56	0.56	0.56	0.56	0.56	
S_2	apparent mass loading	$\frac{\rho_o H^3}{m_{11}}$	0.09	0.09	0.09	0.09	0.09	0.09	
S_3	microphone position to panel size	$\frac{L_M}{H}$	7.0	7.0	7.0	7.0	7.0	7.0	
S_4	duct length to panel size	$\frac{L}{H}$	10.0	10.0	10.0	10.0	10.0	10.0	
ζ	damping ratio	$\frac{R}{2\sqrt{SM}}$	0.01	0.01	0.01	0.01	0.01	0.01	
$\overline{\omega_n}$	natural frequency	$\frac{\omega_n}{\omega_{ref}}$	0.5 1.5	0.5 1.5 2.5 3.5	0.5 1.5	0.5 1.5	0.5 1.5	0.5 1.5 2.5 3.5	
AR	aspect ratio	$\frac{W}{H}$	1.0	1.0	1.0	1.0	1.0	1.0	
U_{ij}	panel ij velocity	U_{ijpc}/P_1	solved for	solved for	solved for	solved for	solved for	solved for	
Z_b	termination impedance	$\frac{Z_b}{\rho_o c}$	1.0 + i0	1.0 + i0	1.0 + i0	1.0 + i0	1.0 + i0	1.0 + i0	

panel model) and $\omega = 1.0, 2.0,$ and 3.0 (four panel model) for the branch analysis without apparent mass. Compensated mass ratios place the ART design frequencies at the same frequencies but are compensated to include the effect of apparent mass loading, which will be discussed in detail later. Much of the analysis results presented in this work will use similar nondimensional groupings.

Section 2.2.2: Branch Analysis Results

Figure 2.2.4a presents the transmitted nondimensional pressure ratio p_t/p_I for both identical and ART tuned panels. For identical panels with a natural frequency of 1.0 , note that the pressure ratio approaches a value of 1.0 at the natural frequency. (In the limit of no damping, this pressure ratio would be exactly 1.0 at the natural frequency.) However, ART tuned panels show pressure ratios much less than 1.0 between the two panel natural frequencies of 0.5 and 1.5 . Both results approach the same limiting values at very low and very high frequencies. Figure 2.2.4b presents noise reduction results in decibels (dB) for the same configuration. Both identical and ART tuned panels show stiffness dominated noise reduction behavior (-6 dB/octave) at low frequencies and mass dominated noise reduction behavior ($+6$ dB/octave) at high frequencies.

As mentioned earlier, this technique provides simple results to check more complicated analyses. While apparent mass effects are not included (and are an important part of the general solution of the problem), the branch analysis represents the easiest analytical way to obtain quantitative results.

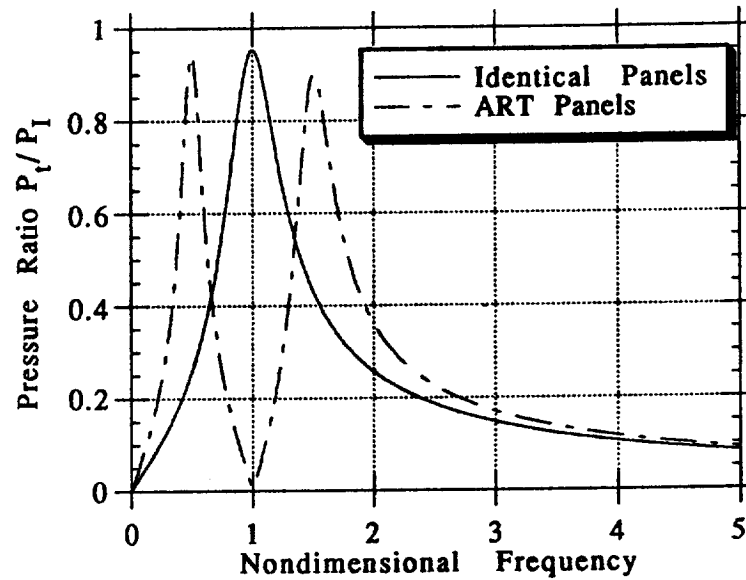


Figure 2.2.4a: Branch analysis pressure ratio results for identical panels and ART tuned panels. Values for the nondimensional parameters are as shown in Table 2.2.1.

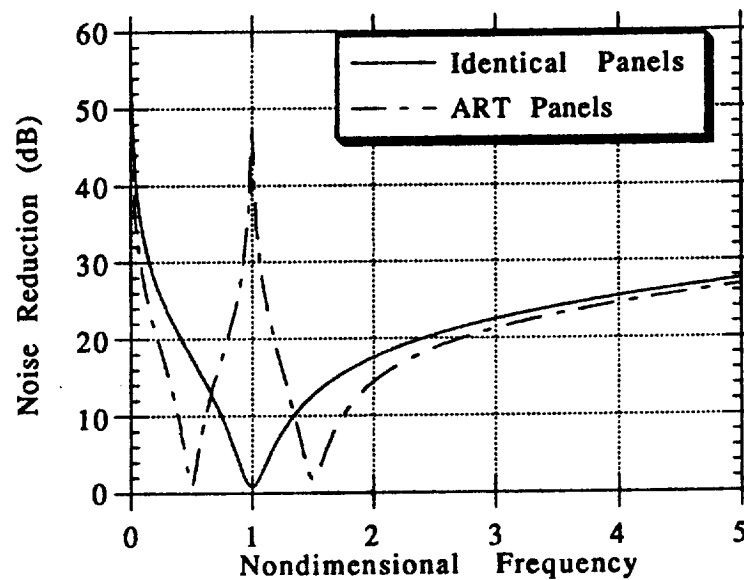


Figure 2.2.4b: Branch analysis noise reduction results for identical and ART tuned panels. Values for the nondimensional parameters are as shown in Table 2.2.1.

Section 2.3: The Full Four Panel Analysis

This section presents the analysis of an idealized wall composed of multi-panel ART subsystems. The set of N panels in each subsystem grouping is assumed to repeat periodically along the paneled wall. As mentioned in Chapter 1, if each ART subsystem contains N panels tuned to N different resonance frequencies, there can occur $N-1$ frequencies where the panels produce acoustic cutoff of the transmitted sound field. This fact demonstrates the possibility of canceling several propeller blade passage harmonics in an aircraft application, as demonstrated in Figures 1.2.1 and 1.2.2, for example.

An infinite wall of panels composed of identical panel subsystems which repeat periodically in all directions is shown in Figure 2.1.1. The coordinate system is now located in the center of the panel grouping, and the panels are labeled in the matrix-like subscript notation as shown in Figure 2.1.1 and Figure 2.2.1. Note that this is the same analysis configuration used in the branch analysis described in Section 2.2.2, except for the coordinate system location. Suppose each panel subsystem contains four rectangular panels, with each panel having height H and width W , as shown in Figure 2.2.1. As before, each of the four panels can have different dynamic properties; however, other cases involving subsystems with one, two, or three panels can be recovered by defining various combinations of the panels to have identical dynamic properties.

The analysis of normal incidence acoustic transmission through such a paneled wall has been accomplished using a number of analytical methods. The most efficient method first considers the forces associated with the motion of a single panel in each subsystem with the other panels held fixed. The corresponding forces associated with the other panels can be deduced from the symmetries of the problem. The general acoustic field for arbitrary panel motions can then be constructed

using superposition. The dynamics equation for each panel determines the relationship between the acoustic pressure on each panel and the resulting panel velocity. For simplicity, as in the branch analysis, the panel dynamics are modeled in terms of the impedance of an equivalent spring-mass-damper system as previously described by Equation (2.2.3).

The acoustic pressure $p(x,y,z)e^{i\omega t}$ satisfies the reduced wave equation

$$\nabla^2 p + (\omega/c)^2 p = 0 \quad (2.3.1)$$

The acoustic velocity vector is $[u(x,y,z)\mathbf{i} + v(x,y,z)\mathbf{j} + w(x,y,z)\mathbf{k}] e^{i\omega t}$. The x-component of the acoustic momentum equation is

$$i\omega u = -\frac{1}{\rho} \frac{\partial p}{\partial x} \quad (2.3.2)$$

Therefore the velocity component $u(x,y,z)$ can also be shown to satisfy the wave equation

$$\nabla^2 u + (\omega/c)^2 u = 0 \quad (2.3.3)$$

Now consider the motion of the panel denoted by "12" located in the first quadrant, as shown in Figure 2.2.1, with the other panels held fixed. The panel velocity mode shape is given by $\Phi(y,z)$. With the other panels held fixed, the velocity boundary condition on the panel wall ($x = 0$) for the acoustic field is given by

$$\Phi(y, z) = \begin{cases} \phi(y, z) & \text{for } 0 \leq y \leq W \text{ and } 0 \leq z \leq H \\ 0 & \text{for } -W \leq y \leq 0 \text{ and/or } -H \leq z \leq 0 \end{cases} \quad (2.3.4)$$

Since the panel subsystems are identical, $\Phi(y, z) = \Phi(y + 2W, z) = \Phi(y, z + 2H) = \Phi(y + 2W, z + 2H)$. The periodic function $\Phi(y, z)$ can be represented by a Fourier series of the form

$$\Phi(y, z) = a_{00} + \sum_{m=1}^{\infty} \sum_{n=1}^{\infty} a_{mn} \sin\left(\frac{m\pi y}{H}\right) \sin\left(\frac{n\pi z}{W}\right) \quad (2.3.5)$$

For the present analysis, the panels are assumed to move as rigid spring-mass-damper panels; therefore, $\phi(y, z) = \text{constant} = 1.0 \cdot U_{12}$. The Fourier series for the velocity boundary condition then takes the form

$$\begin{aligned} u_{12}(0, x, y) = & \frac{U_{12}}{4} + \frac{U_{12}}{\pi} \sum_{n=1}^{\infty} \frac{1}{(2n-1)} \sin \frac{(2n-1)\pi y}{W} \\ & + \frac{U_{12}}{\pi} \sum_{m=1}^{\infty} \frac{1}{(2m-1)} \sin \frac{(2m-1)\pi z}{H} \\ & + \frac{U_{12}}{\pi^2} \sum_{m=1}^{\infty} \sum_{n=1}^{\infty} \frac{4}{(2n-1)(2m-1)} \sin \frac{(2n-1)\pi y}{W} \sin \frac{(2m-1)\pi z}{H} \end{aligned} \quad (2.3.6)$$

Since $u(x, y, z)$ satisfies the wave equation subject to the boundary condition $u_{12}(0, y, z)$ given above, the solution is

$$\begin{aligned} u_{12}(0, x, y) = & \frac{U_{12}}{4} e^{-k_{00}x} + \frac{U_{12}}{\pi} \sum_{n=1}^{\infty} \frac{1}{(2n-1)} \sin \frac{(2n-1)\pi y}{W} e^{-k_{0n}x} \\ & + \frac{U_{12}}{\pi} \sum_{m=1}^{\infty} \frac{1}{(2m-1)} \sin \frac{(2m-1)\pi z}{H} e^{-k_{m0}x} \\ & + \frac{U_{12}}{\pi^2} \sum_{m=1}^{\infty} \sum_{n=1}^{\infty} \frac{4}{(2n-1)(2m-1)} \sin \frac{(2n-1)\pi y}{W} \sin \frac{(2m-1)\pi z}{H} e^{-k_{mn}x} \end{aligned} \quad (2.3.7)$$

The wave numbers in this expression are given by

$$k_{00} = k = \frac{\omega}{c} \quad (2.3.8a)$$

$$k_{0n} = \sqrt{\left[\frac{(2n-1)\pi}{W}\right]^2 - \left[\frac{\omega}{c}\right]^2} \quad (2.3.8b)$$

$$k_{m0} = \sqrt{\left[\frac{(2m-1)\pi}{H}\right]^2 - \left[\frac{\omega}{c}\right]^2} \quad (2.3.8c)$$

$$k_{mn} = \sqrt{\left[\frac{(2m-1)\pi}{H}\right]^2 + \left[\frac{(2n-1)\pi}{W}\right]^2 - \left[\frac{\omega}{c}\right]^2} \quad (2.3.8d)$$

Note that the panels are assumed to be acoustically compact and that only the one-dimensional mode propagates; thus $\omega H/c$ and $\omega W/c < \pi$.

The x-component of the momentum equation can then be integrated to obtain the corresponding pressure solution

$$\begin{aligned} p(0,x,y) = & \frac{\rho c U_{12}}{4} e^{-ik_{00}x} + \frac{i\omega \rho U_{12}}{\pi} \sum_{n=1}^{\infty} \frac{1}{(2n-1)k_{0n}} \sin \frac{(2n-1)\pi y}{W} e^{-k_{0n}x} \\ & + \frac{i\omega \rho U_{12}}{\pi} \sum_{m=1}^{\infty} \frac{1}{(2m-1)k_{m0}} \sin \frac{(2m-1)\pi z}{H} e^{-k_{m0}x} \\ & - \frac{i\omega \rho U_{12}}{\pi^2} \sum_{m=1}^{\infty} \sum_{n=1}^{\infty} \frac{4}{(2n-1)(2m-1)k_{mn}} \sin \frac{(2n-1)\pi y}{W} \sin \frac{(2m-1)\pi z}{H} e^{-k_{mn}x} \end{aligned} \quad (2.3.9)$$

The next step in the derivation is to determine the forces on each panel in the array due to the motion of panel 12 by integrating the pressure expression over each panel surface. Let F_{ij}^{kl} be the force on panel ij due to the motion of panel kl . Then

$$F_{ij}^{12} = 2 \iint_{A_{12}} p_{12}(0+,y,z) dy dz \quad (2.3.10)$$

where A_{12} indicates the surface of panel 12 (referring to Figure 2.2.1); the factor of two in front of the integral accounts for radiation from both sides of the panel. Carrying out the integrations for the forces induced on each panel by the motion of panel 12 yields

$$F_{12}^{12} = 2\rho cWH \left[\frac{1}{4} + S_n + S_m + S_{mn} \right] U_{12} \equiv C_S U_{12} \quad (2.3.11a)$$

$$F_{11}^{12} = 2\rho cWH \left[\frac{1}{4} - S_n + S_m - S_{mn} \right] U_{12} \equiv C_W U_{12} \quad (2.3.11b)$$

$$F_{22}^{12} = 2\rho cWH \left[\frac{1}{4} + S_n - S_m - S_{mn} \right] U_{12} \equiv C_H U_{12} \quad (2.3.11c)$$

$$F_{21}^{12} = 2\rho cWH \left[\frac{1}{4} - S_n - S_m + S_{mn} \right] U_{12} \equiv C_D U_{12} \quad (2.3.11d)$$

where

$$S_n = \frac{2ik}{\pi^2} \sum_{n=1}^{\infty} \frac{1}{(2n-1)^2 k_{0n}} \quad (2.3.12a)$$

$$S_m = \frac{2ik}{\pi^2} \sum_{m=1}^{\infty} \frac{1}{(2m-1)^2 k_{m0}} \quad (2.3.12b)$$

$$S_{mn} = \frac{16ik}{\pi^4} \sum_{n=1}^{\infty} \sum_{m=1}^{\infty} \frac{1}{(2n-1)^2 (2m-1)^2 k_{mn}} \quad (2.3.12c)$$

Problem symmetry and superposition now allow these results to be generalized to the case where all panels are in motion. Let F_{ij} be the total force on panel ij due to the motion of all other panels. In general, it can be deduced that

$$F_{ij} = U_{11}C_{11}^{ij} + U_{12}C_{12}^{ij} + U_{21}C_{21}^{ij} + U_{22}C_{22}^{ij} \quad (2.3.13)$$

The coefficients C_{kl}^{ij} are related as

$$C_{11}^{11} = C_{12}^{12} = C_{21}^{21} = C_{22}^{22} = C_S \quad (2.3.14a)$$

$$C_{11}^{12} = C_{12}^{11} = C_{21}^{22} = C_{22}^{21} = C_W \quad (2.3.14b)$$

$$C_{11}^{22} = C_{12}^{21} = C_{21}^{12} = C_{22}^{11} = C_D \quad (2.3.14c)$$

$$C_{11}^{21} = C_{12}^{22} = C_{21}^{11} = C_{22}^{12} = C_H \quad (2.3.14d)$$

Therefore, the acoustic forces due to panel motion can be written as

$$F_{11} = U_{11}C_S + U_{12}C_W + U_{21}C_H + U_{22}C_D \quad (2.3.15a)$$

$$F_{12} = U_{11}C_W + U_{12}C_S + U_{21}C_D + U_{22}C_H \quad (2.3.15b)$$

$$F_{21} = U_{11}C_H + U_{12}C_D + U_{21}C_S + U_{22}C_W \quad (2.3.15c)$$

$$F_{22} = U_{11}C_D + U_{12}C_H + U_{21}C_W + U_{22}C_S \quad (2.3.16d)$$

In the complete problem, acoustic forces also arise from a pressure wave striking the panel barrier at normal incidence. By the principle of superposition, the wall can be treated as rigid when including the effect of this incident pressure. The resulting wall motion, actually in response to this pressure wave, can be treated separately using the solution developed above. The appropriate wall response due to this forcing is then found by analyzing the dynamics of the panels; the latter is contained in the panel velocities. The right traveling incident wave, striking the panels at

$x = 0$ - and reflecting as if from a rigid wall, has amplitude P_I . The corresponding pressure field is $2P_I \cos(kx) e^{i\omega t}$, where the factor of 2 accounts for double amplitude due to the reflection from a perfectly rigid wall, and the resultant pressure is the real part of the complex pressure and harmonic in time. Note that adding the previous pressure field solution due to panel motion corrects the reflected pressure to its actual value and accounts for the transmitted wave. The force exerted by the incident wave and its perfect reflection on each panel is $2P_I WH$. The net acoustic force on a given panel is therefore

$$F_{Net,ij} = F_{ij} + 2P_I WH \quad (2.3.17)$$

The above results are used in the force balance equations for the panel motion. Suppose each panel is modeled as a spring-mass-damper system of mass M_{ij} connected to a rigid frame by a spring constant S_{ij} and a damper R_{ij} . The net force and velocity of each panel are related through the mechanical impedance Z_{ij} as

$$F_{Nij} = Z_{ij} U_{ij} = \left[R_{ij} + i \left(\omega M_{ij} - \frac{S_{ij}}{\omega} \right) \right] U_{ij} \quad (2.3.18)$$

Writing out this equation for each of the four panels yields a system of coupled equations for the panel velocities

$$\begin{bmatrix} (Z_{11} + C_S) & C_W & C_H & C_D \\ C_W & (Z_{12} + C_S) & C_D & C_H \\ C_H & C_D & (Z_{21} + C_S) & C_W \\ C_D & C_H & C_W & (Z_{22} + C_S) \end{bmatrix} \begin{bmatrix} U_{11} \\ U_{12} \\ U_{21} \\ U_{22} \end{bmatrix} = \begin{bmatrix} 2P_I WH \\ 2P_I WH \\ 2P_I WH \\ 2P_I WH \end{bmatrix} \quad (2.3.19)$$

In general, it is necessary to solve this equation numerically. However, one closed form result for the full problem will be mentioned later.

Having solved the governing equations for the panel velocities, the pressures upstream and downstream can be computed and the noise reduction across the wall can be determined. It is readily shown by superimposing the earlier results for the motion of a single panel that the net transmitted one-dimensional pressure wave ($x > 0$) is given by

$$p_{1-D}(x,y,z) = P_t e^{i(\omega t - kx)} = \frac{\rho c}{4} [U_{11} + U_{12} + U_{21} + U_{22}] e^{i(\omega t - kx)} \quad (2.3.20)$$

Similarly, the one-dimensional wave field on the incident side ($x < 0$) is given by

$$p_{1-D}(x,y,z) = 2P_I \cos(kx) e^{i\omega t} - \frac{\rho c}{4} [U_{11} + U_{12} + U_{21} + U_{22}] e^{i(\omega t - kx)} \quad (2.3.21)$$

These expressions can be used to determine the noise reduction across a paneled wall. Note that the above expressions do not include the higher pressure modes in the near field of the wall. These modes are less important from a noise standpoint because they decay exponentially and are nonpropagating; the effect of these modes has been included in the solution for the panel motions.

As mentioned earlier, certain relatively simple closed form solutions can be obtained for special cases of the above analysis. One such case involves a panel subsystem with only two types of panels. Consider the particular case of two-dimensional panels of height H with unit width. After considerable work it is possible to show that the ratio of transmitted pressure to incident pressure takes the form

$$\frac{P_t}{P_I} = \frac{(Z_{e1} + Z_{e2})}{(Z_{e1} + Z_{e2}) + \frac{Z_{e1}Z_{e2}}{\rho c H} - i \frac{\omega m_a}{2\rho c H} (Z_{e1} + Z_{e2})} \quad (2.3.22)$$

where $Z_{e1} = Z_1 + i\omega m_a$ and $Z_{e2} = Z_2 + i\omega m_a$ are equivalent net mechanical impedances, with the impedances Z_1 and Z_2 being the mechanical impedances of the two types of panels. The quantity m_a is analogous to an equivalent hydrodynamic mass associated with the higher order evanescent pressure modes produced by the out-of-phase components of panel motion, and may be expressed as

$$m_a = \frac{16\rho c H}{\pi^2 \omega} \sum_{n=1}^{\infty} \frac{1}{(2n-1)^2} \left[\left(\frac{[2n-1]\pi c}{2\omega H} \right)^2 - 1 \right]^{-1/2} \quad (2.3.23)$$

Note that Equation (2.3.22), with $m_a = 0$ recovers the branch analysis result for a two panel system. The four panel model will effectively yield this result when neighboring panels are designed with the same dynamical properties.

Section 2.4: Analytical Results

Section 2.4.1: Two Panel Results and Discussion

Figure 2.4.1 shows a noise reduction prediction in decibels plotted against nondimensional frequency for identical and ART tuned panels. Parameters are as shown in Table 2.2.1 under "Noncompensated 2 Panel Model". (Panel mass compensation is addressed later in this section.) These parameters correspond to square aluminum panels measuring 12" on a side, having a thickness of 1/16". As with the branch analysis, both panel systems show similar stiffness dominated noise reduction behavior at low frequencies (-6 dB/octave) and mass dominated noise reduction behavior (+6 dB/octave) at high frequencies. At a panel natural frequency, that particular panel will appear acoustically transparent in the limit of zero damping. Between the frequencies of 0.8 and 1.2, the ART contribution to noise reduction is greater than 20 dB. This result differs only slightly from the branch analysis result in that the peak ART noise reduction frequency has decreased slightly, as shown in more detail in Figure 2.4.2. This is due to the additional mass loading of the fluid surrounding the panels. From a practical viewpoint, the frequency regime around $\omega = 1.0 \pm 0.2$ indicates a fairly large noise reduction bandwidth; that is, a frequency regime where the noise reduction is greater than a certain amount (in this example, about 20 dB). This fact may be of value in reducing large sound levels at slightly varying frequencies; for example, a slightly varying propeller blade passage frequency due to propeller gust loading. The large noise reduction bandwidth phenomenon also indicates the robust nature of this tuning method.

The solution of the governing equations for panel complex velocities permits the extraction of phase data for the individual panels. Figure 2.4.3 shows the theoretical phase difference between the two ART tuned panels including apparent mass as a

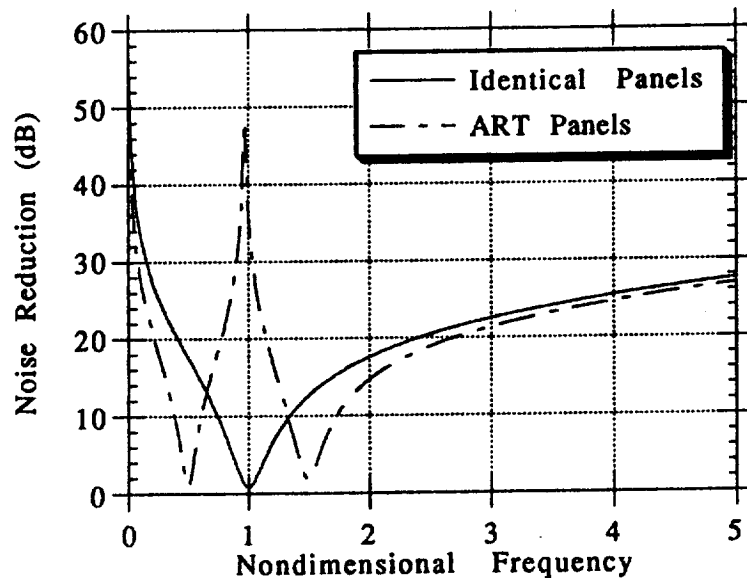


Figure 2.4.1: ART and identical two panel noise reduction prediction with apparent mass plotted versus nondimensional frequency. Values for the nondimensional parameters are as shown in Table 2.2.1.

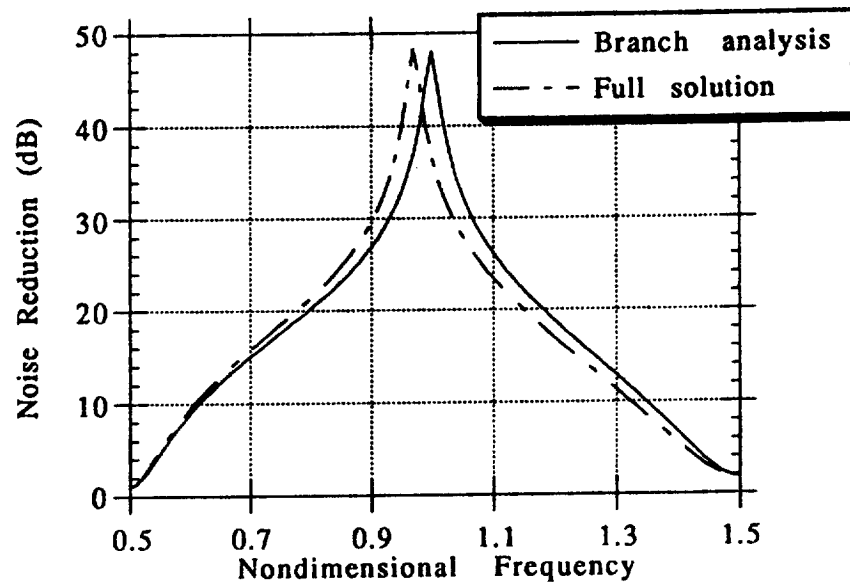


Figure 2.4.2: Detail of the branch analysis and full theory noise reduction predictions around the ART cancellation frequency. Remainder of noise reduction calculation is essentially the same.

function of nondimensional frequency. Here, the damping ratio has been fixed to 0.01, and as a result of this low damping, much of the frequency domain between the natural frequencies $0.5 < \omega < 1.5$ shows almost perfect out-of-phase behavior. Figure 2.4.4 shows panel velocity magnitude relationships, where the velocity magnitude is relative to a constant amplitude of incident pressure P_I . (This differs qualitatively from the concept of Figure 1.3.1, where panel velocities are sketched relative to constant forcing.) The panel velocity magnitudes are equivalent at just below $\omega = 1.0$, which corresponds to the "ART design frequency", or ω_{ART} . However, as shown by Figure 2.4.1, significant noise reduction can occur at nondimensional frequencies where the panel velocity magnitudes are somewhat different. Figure 2.4.4 indicates that the panel motions are coupled to the surrounding pressure field in a frequency dependent manner. Note that at the individual panel resonances, the non-resonance panel velocity is at a minimum. Again, at a natural frequency, a panel will appear almost acoustically transparent, and nearly all of the sound transmission will occur through that panel.

Section 2.4.2: Averaged Noninteracting Noise Reduction

In order to observe the true contribution of out-of-phase motion to noise reduction across the panel configuration, it is necessary to compare the ART data to an idealized case where only uniform panels are used, and the resulting acoustic fields do not interact, as shown in Figure 2.4.5. This comparison allows the mass law and stiffness law effects associated with moving the panel resonance frequencies apart to be separated from the effects of acoustic cancellation or cutoff which are central to the ART concept. Such an averaged noninteracting noise reduction (ANNR) may be derived for N panels as

$$(NR)_{ANNR}(\omega) = 10 \log(N) - \sum_{i=1}^N 10^{-(NR)_i(\omega)/10} \quad (2.4.1)$$

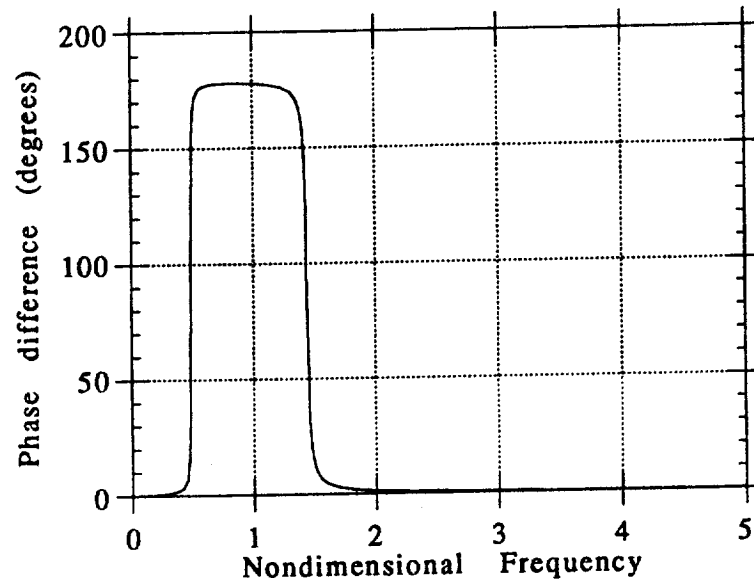


Figure 2.4.3: Theoretical phase difference in degrees between the ART panels with apparent mass as a function of nondimensional frequency.

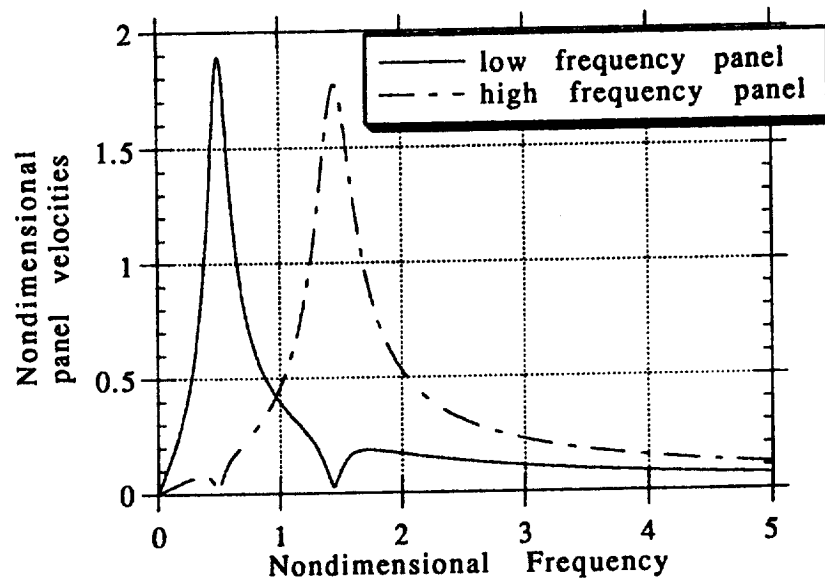


Figure 2.4.4: Panel velocity relationships from two panel theory with apparent mass.

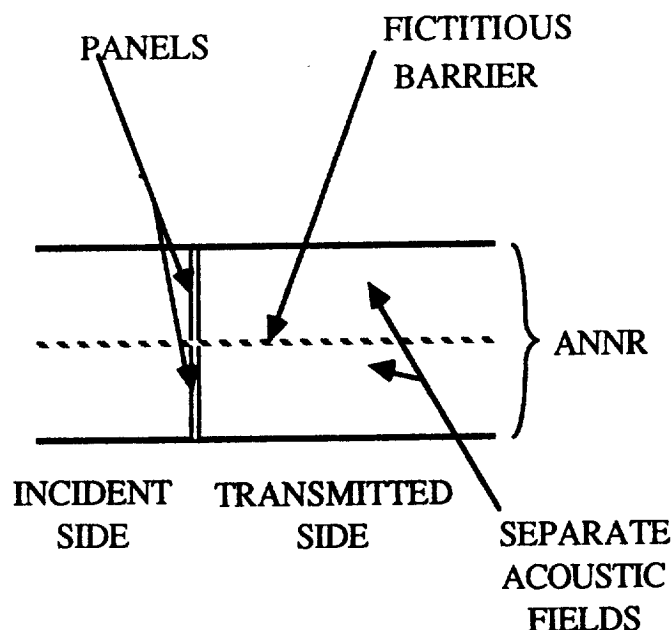


Figure 2.4.5: Averaged Noninteracting Noise Reduction (ANNR) schematic.

Figure 2.4.6 shows the two panel ART noise reduction plotted with the ANNR result. Note that the ANNR result is intuitively satisfying, since its behavior is stiffness and mass dominated at low and high frequencies. ANNR also reaches a minimum at resonance frequencies, and this noise reduction minimum for identical panels is slightly better than the ART minimum since ANNR has another set of panels (the higher resonance frequency set) contributing to the noise reduction effort. However, ART still indicates a true maximum noise reduction increase of 20 dB or more between the panel natural frequencies, depending on the desired size of the noise reduction bandwidth.

Section 2.4.3: Four Panel Results and Discussion

Figure 2.4.7a shows the pressure ratio p_t/p_I for both identical panels tuned to $\omega_n = 1.0$ and ART panels tuned to $\omega_n = 0.5, 1.5, 2.5,$ and 3.5 . Other parameters are as listed in Table 2.2.1. All previous comments with respect to pressure maxima and

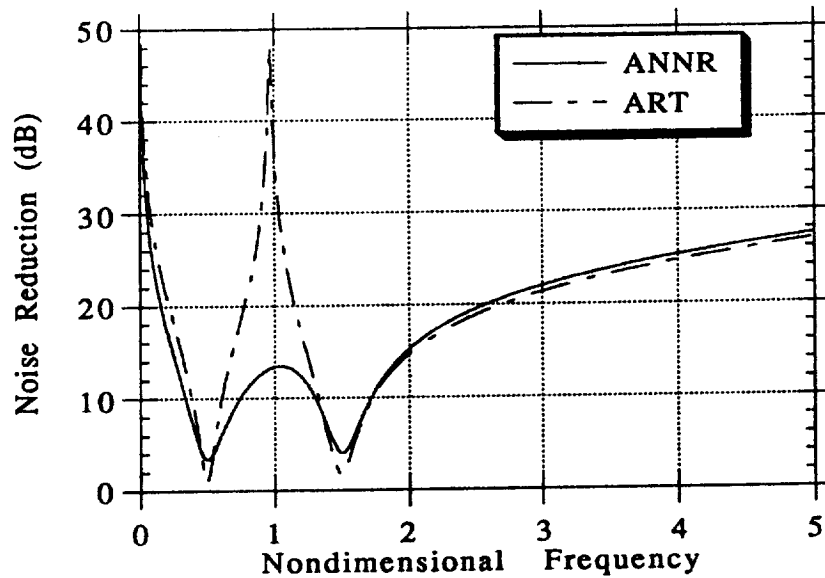


Figure 2.4.6: Two panel ART noise reduction plotted with Averaged Noninteracting Noise Reduction (ANNR) with apparent mass.

minima, mass and stiffness domination, and acoustic transparency apply here. However, Figure 2.4.7a demonstrates the ability of an ART tuned panel array with four different panel tunings to cancel three frequencies. (Measurements by Woodward on a scale model SR-7A high speed propeller have shown that the tonal content of the propeller noise spectra was typically limited to the first three harmonics, with higher tone orders either not present or masked by broadband background noise probably produced by the flow over the microphone.¹⁸⁾ Figure 2.4.7b shows the equivalent data as a noise reduction in decibels. Again, note the fairly wide bandwidth of noise reduction at 20 dB, indicating the robustness of the tuning method. With four panels, the apparent mass loading becomes more important, especially with respect to the higher natural frequency panel since this panel has the lowest mass. The lowest ART cancellation frequency displays the greatest noise reduction simply because these lower frequencies are more cutoff due to their longer wavelengths; restated, the panels are more

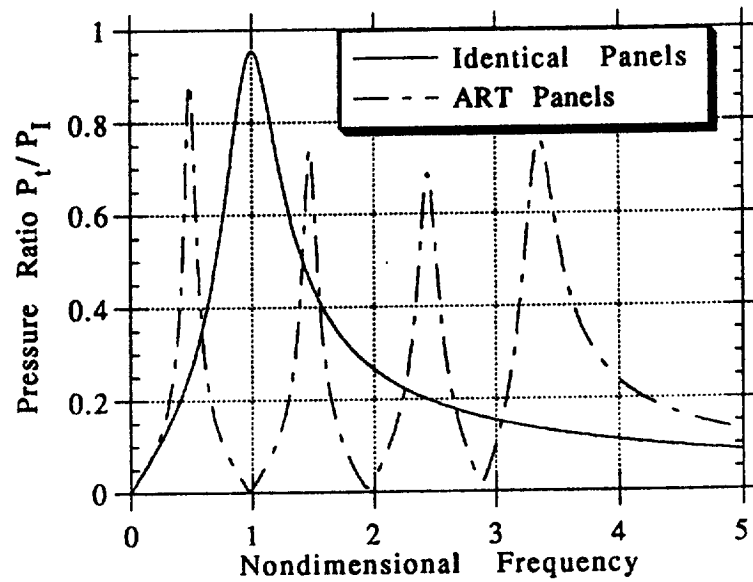


Figure 2.4.7a: Four panel ART pressure ratio P_t/P_I plotted against identical panels pressure ratio with apparent mass.

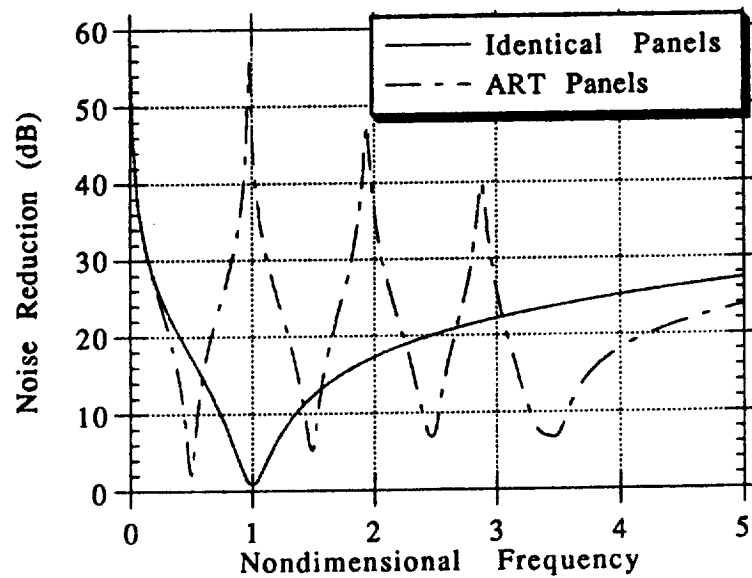


Figure 2.4.7b: Four panel ART and identical panels noise reduction predictions with apparent mass.

acoustically compact at lower frequencies. Figure 2.4.8 shows the same ART configuration plotted with the ANNR results for four panels, showing a true maximum gain in noise reduction of at least 15 dB at $\omega_{ART} = 3.0$ and at least 20 dB at $\omega_{ART} = 1.0$ over the identically tuned system.

Section 2.4.4: Mass Ratio Optimization

Figure 2.4.9 shows the ART four panel model results plotted with and without the apparent mass loadings. Note that the data without apparent mass is equivalent to the branch analysis results discussed earlier and presented in closed form via Equation (2.2.18). Both calculations have input data which should set the ART cancellation frequencies at $\omega_{ART} = 1.0, 2.0$, and 3.0 . However, in the case of the simulation with apparent mass, the additional loading of the fluid surrounding the panel adds mass, and thereby reduces the natural frequencies of the combined panel/fluid system. It is generally desired to place the maximum ART cancellation frequencies at specific values in order to attenuate harmonics of the fundamental frequency, or to be able to control precisely the frequencies at which noise reduction will occur. This can be accomplished by altering the panel natural frequency, stiffness, or mass. Mass ratio (that is, the ratio of any panel mass to a reference panel mass in the panel array) optimization is chosen because this method is successful in laboratory simulations. Iteration of the four panel theory via a multi-dimensional Newton-Raphson method with equations of the form

$$(\omega_{desired}^{ART} - \omega_{current}^{ART}) =$$

$$\Delta\omega_{ARTi} = \sum_{j=1}^3 \frac{\partial \left[\frac{P_i}{P_{Ij}} \right]}{\partial (MR)_j} d(MR)_j \quad (2.4.2)$$

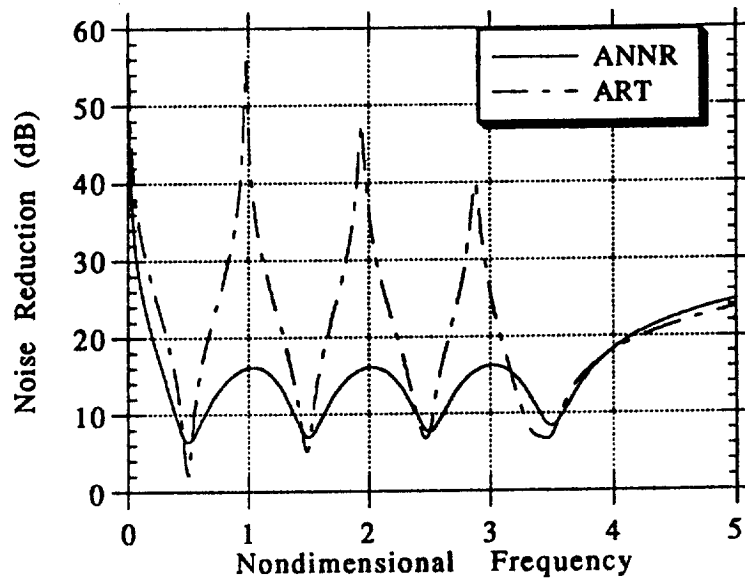


Figure 2.4.8: Four panel ART noise reduction prediction with apparent mass plotted against Averaged Noninteracting Noise Reduction (ANNR).

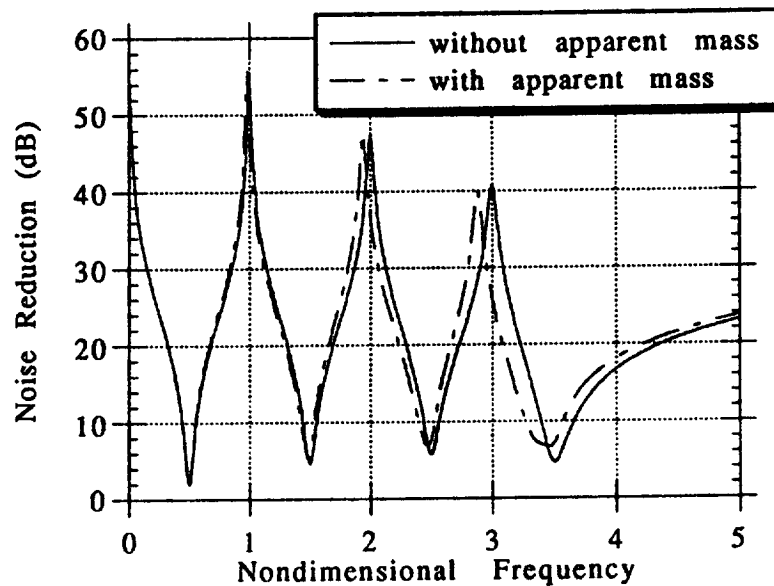


Figure 2.4.9: Noise reduction prediction using the ART four panel theory with and without apparent mass modes as indicated above.

yields three equations with three unknowns, one for each mass ratio. The mass of panel 11 is held fixed at 1.0, and the numerical solutions to Equation (2.4.2) are the adjustments to the current mass ratios MR_{ij} to bring the ART maximum cancellation frequencies closer to the desired value. Equation (2.4.2) is iterated until convergence within 0.001 nondimensional frequency is met.

Of particular interest in this problem is the efficient location of a minimum of a function within specified bracketing limits. The four panel pressure ratio plotted in Figure 2.4.7a shows an approximately parabolic and well-behaved function which is at a minimum when noise reduction is at a maximum. Brent's method provides an effective and quick scheme for finding minima in such situations.¹⁹ Parabolic interpolation using three points is attempted first, using the panel natural frequencies which bound the minimum and a midpoint between them as initial guesses. If the parabolic steps become nonconvergent in finding a minimum, the routine switches to a golden section search. In the worst case, the routine alternates between these two methods until a suitable minimum is found. In practice, this method found a pressure ratio minimum between panel natural frequencies in about five to ten attempts, and generally found the optimum mass ratios after three to five iterations of Equation (2.4.2). The initial guesses for the mass ratio values were obtained using *MACSYMA* to solve three of the four Equations (2.3.19) with $C_S = C_W = C_H = C_D = 0.0$, and freezing the mass ratio of panel 11 at 1.0.

Figure 2.4.10a shows the full four panel theory with and without compensated mass ratios. Note that the peak ART noise reduction values align to $\omega_{ART} = 1.0, 2.0$, and 3.0 , and the peak noise reduction values increase. To further show the sensitivity of the four panel theory on panel size and apparent mass, Figure 2.4.10b shows noise reduction prediction data for panels similar to the type used in the laboratory confirmation experiments (see Chapter 5). Here, the panel is assumed to be square and 4" on each side, and the panel mass is approximately 1 gram. Apparent mass

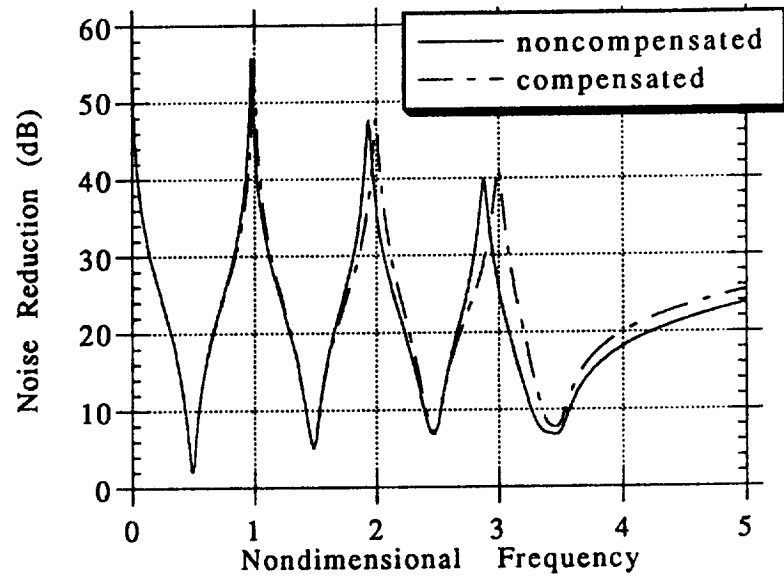


Figure 2.4.10a: Four panel theory with and without compensated mass ratios. Note shift of peak ART cancellation frequencies and slight increase in noise reduction for compensated system. Values are as shown in Table 2.2.1.

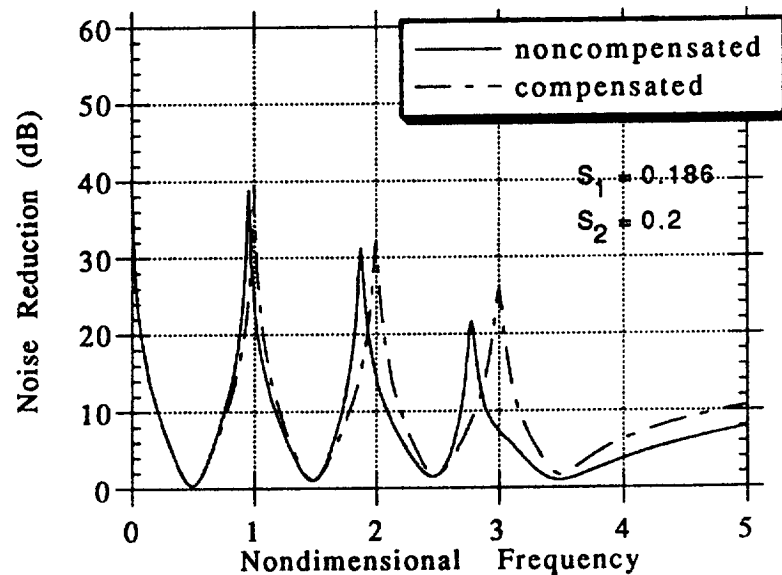


Figure 2.4.10b: Full four panel theory with parameters changed as shown above. Other parameters equivalent to Figure 2.4.10a.

effects are consequently much more evident, as the uncompensated ART data shows that the peak noise reduction frequencies have severely dropped due to a higher apparent mass/panel mass ratio. Figure 2.4.10c shows a comparison of the values of the mass ratios for the previous two figures. Both noncompensated noise predictions begin with the same panel mass ratios. The compensated mass ratio values are then compared in the legend. As the panels with the higher natural frequencies and smaller size are less massive, the mass ratio optimization procedure compensates by adding more mass to the smaller and/or lighter panels.

Finally, Figure 2.4.11 shows the magnitude of the nondimensionalized apparent mass sums as a function of nondimensional frequency for the standard parameters as shown in Table 2.2.1. Note that panels horizontally adjacent and vertically adjacent have the same apparent mass contributions to the governing Equations (2.3.19); that is, $C_W = C_H$. Equivalently, from Equation (2.3.12), S_n and S_m are identical. This again is a consequence of the symmetry of the problem. The apparent mass sums shown in Figure 2.4.11 are the coupling terms appearing on the off-diagonal elements of the linear system denoted by Equation (2.3.19); their contribution to the full problem by coupling panel motions to the surrounding pressure field increases as frequency increases. Also, note that adjacent panels produce stronger coupling through the apparent mass than diagonal panels. This phenomenon is readily explained by the perimeters matching along a line for adjacent panel boundaries and only matching at a point for diagonal panels. Adjacent panels slosh fluid from each to the other, and are thus more highly loaded than panels meeting at just a point. In the latter case, much less surrounding fluid is shared by diagonal panels in the sloshing motion.

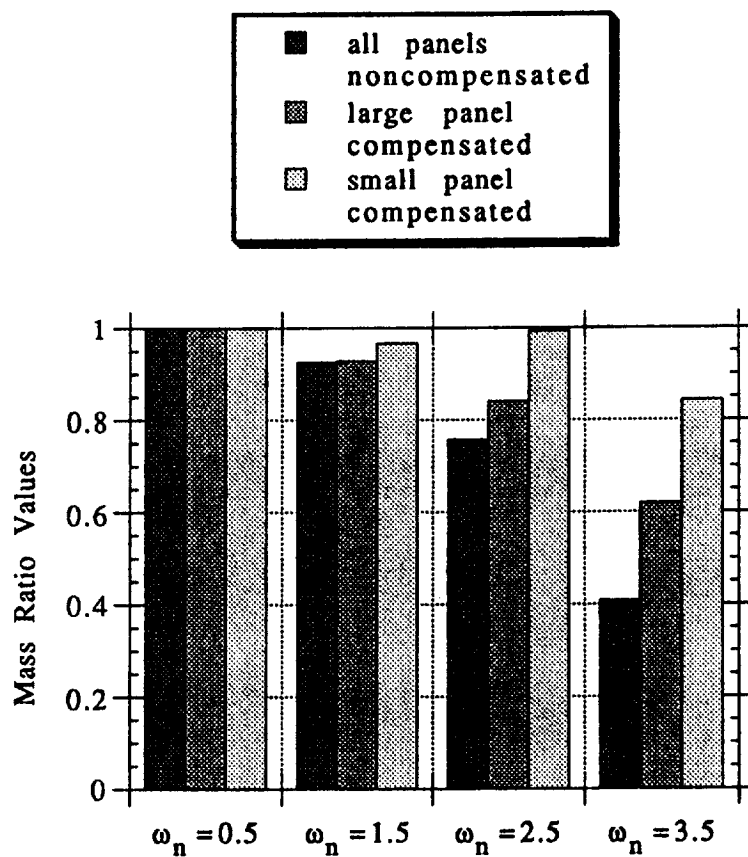


Figure 2.4.10c: Comparison of mass ratios for noncompensated and compensated predictions with varying panel size and apparent mass loading.

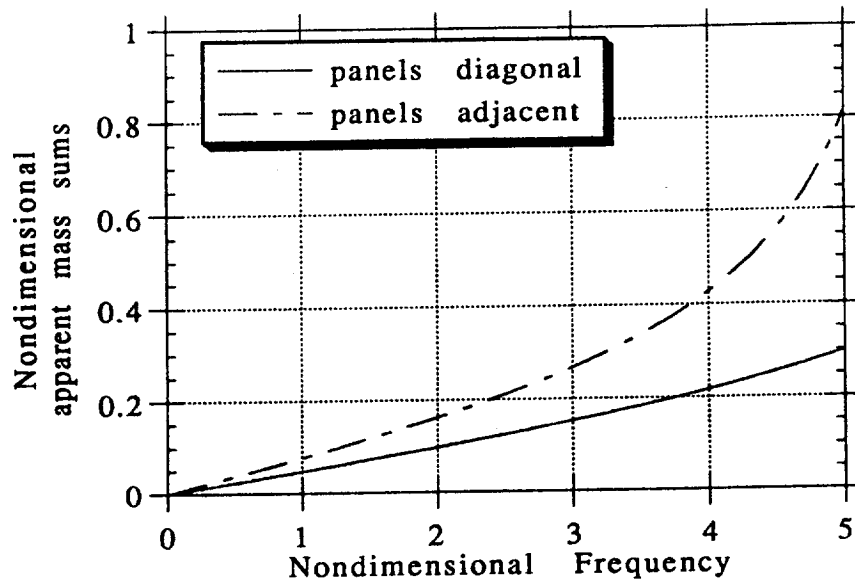


Figure 2.4.11: Magnitude of apparent mass sums versus nondimensional frequency showing increased coupling at higher frequencies.

Section 2.4.5: Model Parameter Studies

Having established the basic acoustic behavior of the four panel system with identical and ART tuned panels, parameter studies with the ART tuned system can establish performance expectations over a wide range of conditions. Figure 2.4.12 shows the effect of varying panel damping on the ART model. Increasing panel damping ratios reduces the peak ART noise reduction values and increases the minimum noise reduction at the panel resonances. In effect, adding more damping makes the system less acoustically transparent at resonances. However, Figure 2.4.12 clearly shows that a comfortable noise reduction bandwidth of about 20 dB can still be maintained around the ART design frequencies ± 0.2 nondimensional frequency. This is again an indication of the robust nature of the method.

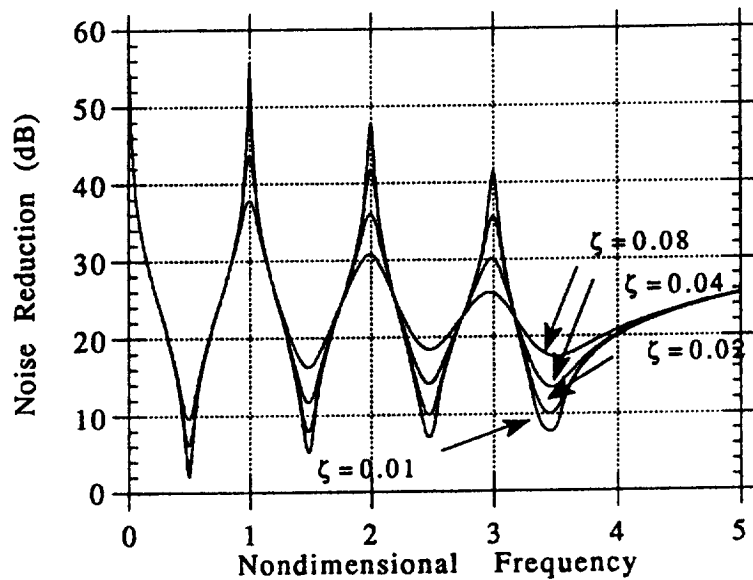


Figure 2.4.12: Parameter studies with the four panel model varying the panel damping ratios as indicated above. Nonadjusted parameter values remain as listed in Table 2.2.1.

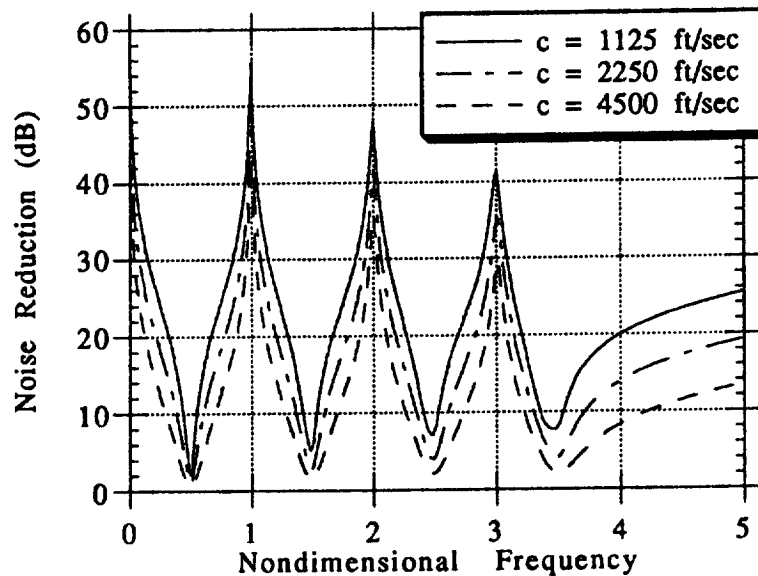


Figure 2.4.13: Parameter studies with the four panel model varying sound propagation speed via the parameter $\omega_r H/c$. The effective sound speeds are shown in the legend.

Figure 2.4.13 shows the effect of the variation of sound speed on the model. Increasing sound speed tends to reduce cutoff behavior and causes the ART cancellation peaks to become sharper. It is similar to variation of panel damping also in that minimum noise reductions at panel resonances decrease. Note that this is only an exercise in variation of a parameter in the computer code; physical panel systems under atmospheric loadings would not experience this degree of sound speed variation. It does indicate that different behavior might be expected if this tuning scheme were to be used in water, for example. However, the latter scenario would drastically increase the fluid loadings on the panels, and would require different analyses.

Figure 2.4.14a shows variation of the panel aspect ratio while holding apparent mass loading fixed. This is clearly a higher order effect, as shown in Figure 2.4.14b, which shows a detail of the frequency regime around the highest ART frequency. This behavior shows that as the panel becomes smaller, apparent mass loading plays only a small effect on the higher natural frequency panel, as shown in Figure 2.4.14b.

Figures 2.4.15a and 2.4.15b show more of the coupling between apparent mass and panel aspect ratio. Figure 2.4.15a shows variations in apparent mass loading by varying the density of the surrounding fluid from normal air density to eight times normal air density with a panel aspect ratio of 1.0. As can be expected, the less massive panels are more affected by the increased loading, and the noise reduction bandwidths begin to narrow with higher fluid loadings. The prediction for eight times normal air loading in Figure 2.4.15a even shows the emergence of an additional noise reduction peak at a frequency slightly above the highest ART cancellation peak. This might be viewed as a "spring-like" inertance effect of the fluid around the panel. Figure 2.4.15b shows the same variations in apparent mass loading on panels with $W/H = 0.25$, and the inertance effect is less prominent.

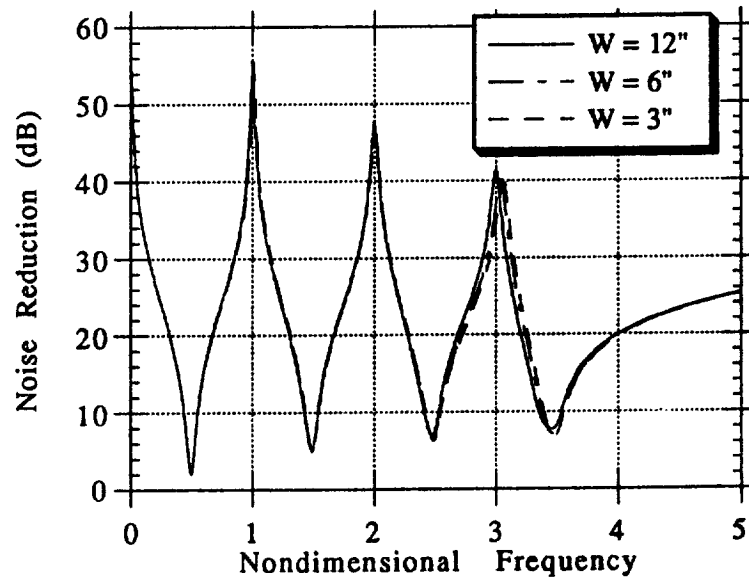


Figure 2.4.14a: Parameter studies with the four panel model varying the panel aspect ratio W/H as shown above. Effective panel widths are shown in the legend. Panel height remains at 12".

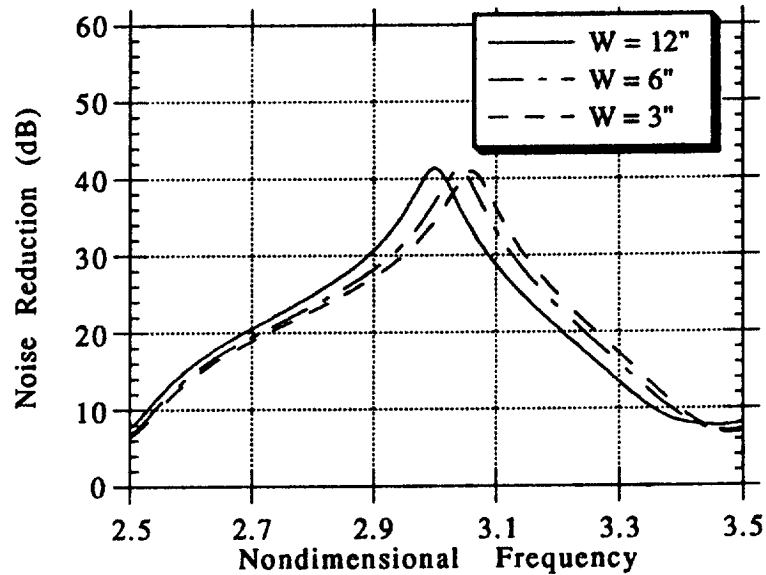


Figure 2.4.14b: Detail of highest ART cancellation frequency increase due to panel aspect ratio change.

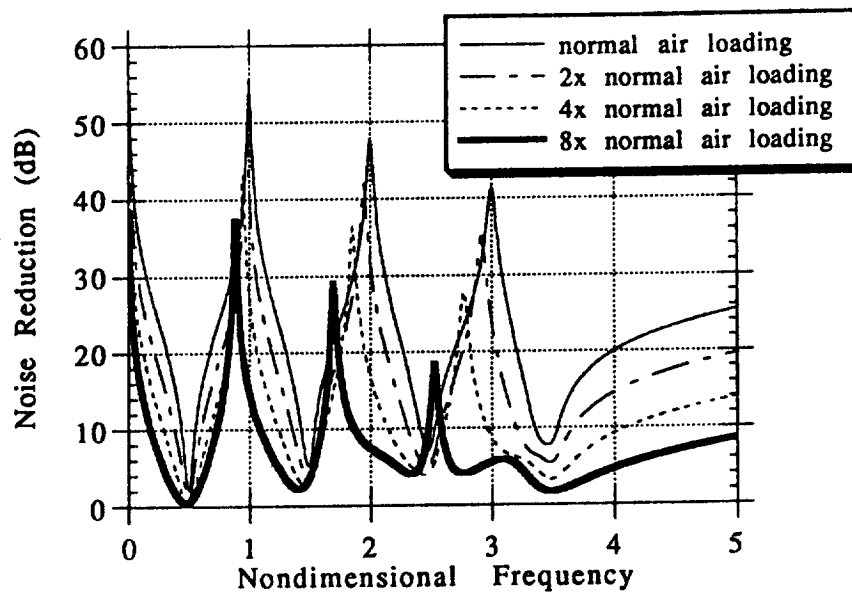


Figure 2.4.15a: Parameter studies with the four panel model varying the apparent mass loading parameter as indicated above. Panel aspect ratio $W/H = 1.0$.

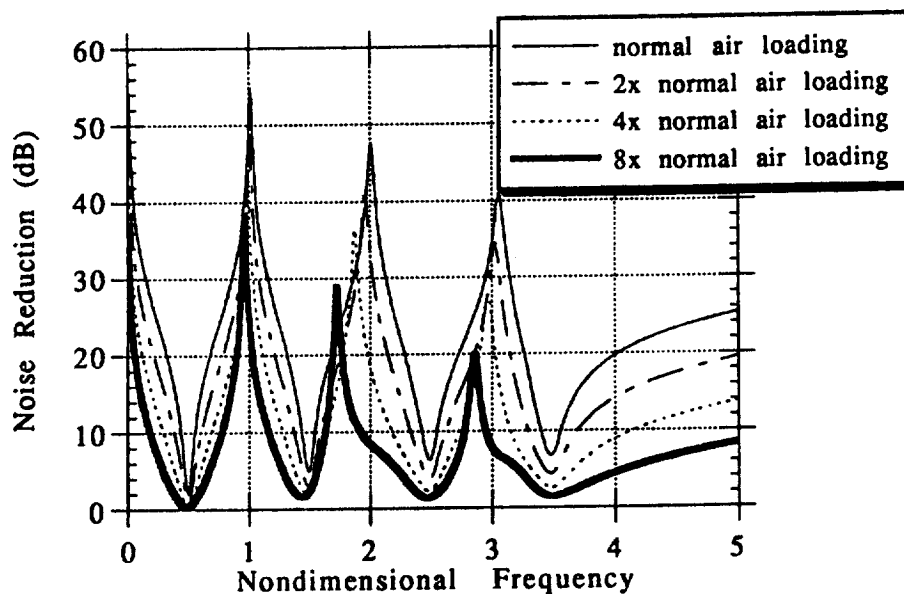


Figure 2.4.15b: Parameter studies with the four panel model varying the apparent mass loading parameter as indicated above. Panel aspect ratio $W/H = 0.25$.

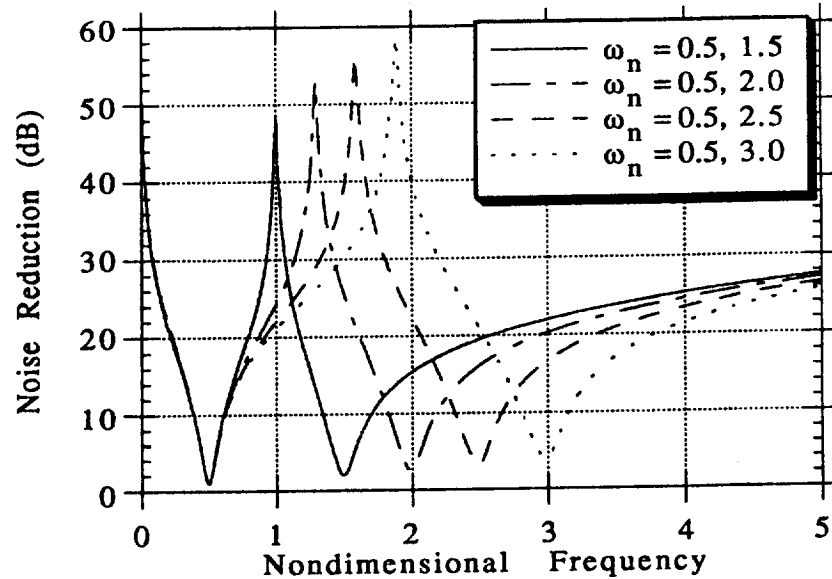


Figure 2.4.16: Parameter studies with the two panel model varying the higher panel natural frequency as indicated above to increase the noise reduction bandwidth. Nonadjusted parameter values remain as shown in Table 2.2.1.

Figure 2.4.16 shows how spreading the panel natural frequencies apart can effectively increase the noise reduction bandwidth. This application may hold promise for noise problems which are both narrowband and broadband, as mentioned by Knowles.²⁰

Figures 2.4.17a and b show the effect of variation in the termination impedance in the four panel model. Figure 2.4.17a varies the real portion of the termination impedance from anechoic ($Z_b = 1.0 + i0$) to ($Z_b = 8.0 + i0$) by successive doubling. Note that the duct is 10 panel widths long and the microphone is placed at a position 7 panel widths downstream. The noise reduction predictions now become contaminated by the reflected wave. However, the ART noise reduction peaks clearly remain intact, although the effect of “hardbox” frequencies can be seen, intertwined with the minima associated with panel natural frequencies. These hardbox frequencies are denoted by²¹

$$f_m = \frac{mc}{2L_{\text{duct}}} \quad (2.4.3)$$

where m is an integer. In nondimensional terms, Equation (2.4.3) becomes

$$\bar{\omega}_m = \frac{mc}{S_1 S_4} \quad (2.4.4)$$

For the parameters shown in Table 2.2.1, this means that noise reduction minima will occur at frequency multiples of 0.561 (as well as at panel natural frequencies), and close examination of Figure 2.4.17a shows this to be the case. However, an interesting feature of the ART method is its ability to work at a hardbox frequency; examination of both Figure 2.4.17a and b shows that while the hardbox frequency at $\omega = 2.80$ is visible, is still effectively attenuated in the surrounding frequency regime by the ART concept. Additionally, Figure 2.4.17b shows wider variations in the downstream termination impedance, from ($Z_b = 1.0 + i0$) to ($Z_b = 50.0 + i0$). However, any termination impedance equal to or harder than ($Z_b = 10.0 + i0$) looks essentially the same. However, care should still be exercised in this regard; placing a hardbox frequency exactly at an ART design frequency in a single panel wall-duct configuration will deteriorate performance unnecessarily.

Noise attenuation has been shown to be enhanced by increasing the panel damping in a structure.²² Figure 2.4.18a shows that while the ART concept is more effective at lower values of the damping constant ζ , it can still contribute to noise reduction in structures with higher damping. The noise reduction around the panel natural frequency regime $\pm 0.2\omega$ has remained nearly the same despite increased damping. Figure 2.4.18b compares a very highly damped ART noise prediction ($\zeta = 0.4$) to the ANNR noise prediction for uniform panels with the same damping; ART still outperforms uniform panels, as can clearly be seen. Note that the

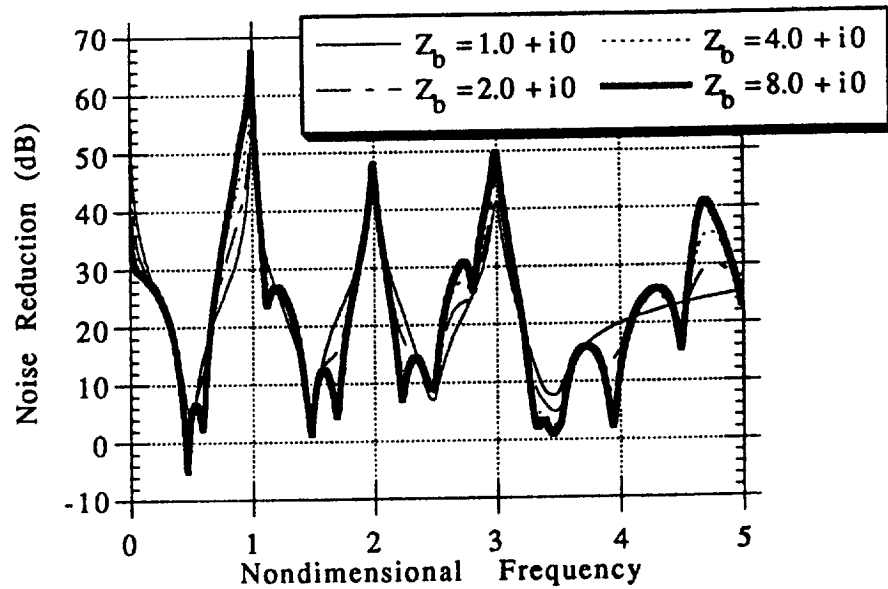


Figure 2.4.17a: Parameter studies with the four panel model varying the real part of the nondimensional termination impedance Z_b as indicated above.

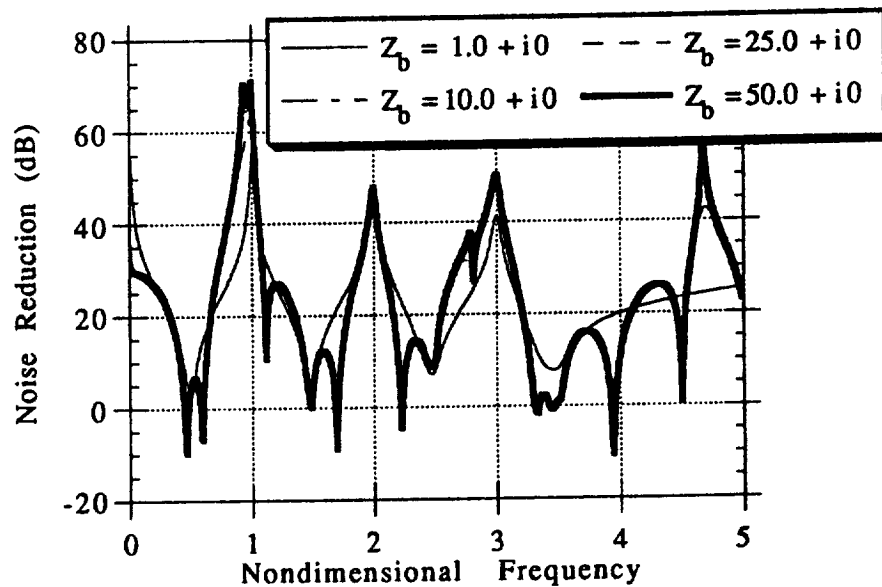


Figure 2.4.17b: Parameter studies with the four panel model varying the real part of the nondimensional termination impedance Z_b as indicated above.

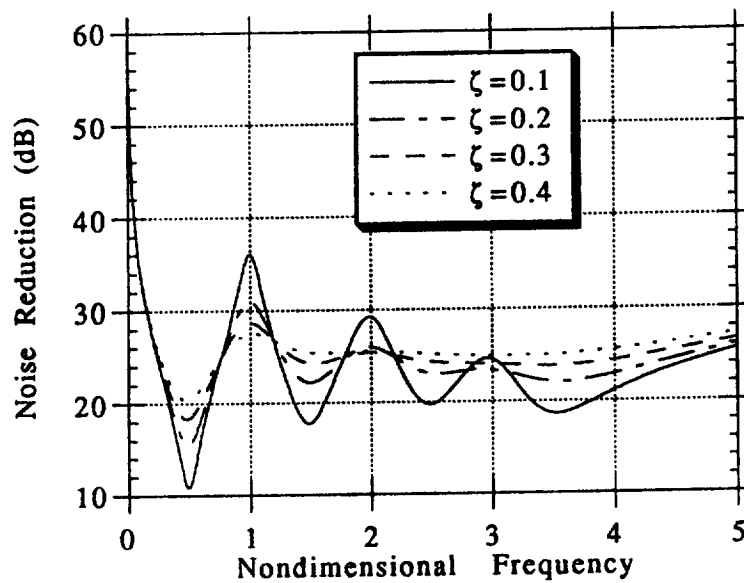


Figure 2.4.18a: Parameter studies with the four panel model for high values of damping as indicated.

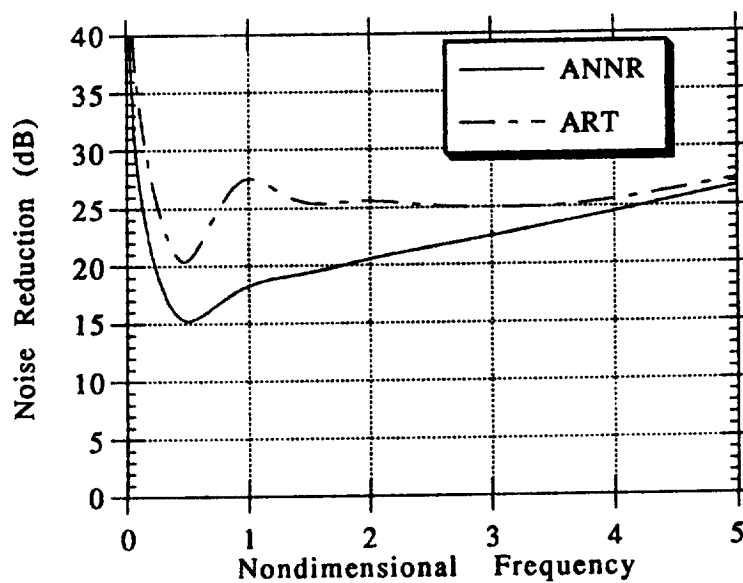


Figure 2.4.18b: High damping comparison ($\zeta=0.4$) of ANN and ART noise reduction predictions.

lowest frequency portion of the ANNR calculation occurs at the lowest panel natural frequency $\omega = 0.5$, another indication that low frequencies are the most difficult to attenuate. Figure 2.4.18b suggests that the ART concept might also be integrated with other noise reduction techniques such as increased damping.

Finally, Figures 2.4.19a and 2.4.19b show a comparison between tuning configurations as indicated in Figure 2.1.2. The data was generated by moving panel natural frequencies with their associated mass ratios to match the possible tuning patterns from Figure 2.1.2. Note that when apparent mass is compensated using panel mass ratio adjustment, the different systems behave in remarkably the same way. Only the highest ART cancellation frequency (due to the combination of lowest mass panel with the highest natural frequency) is affected in a noticeable way. Minor mass ratio compensation could clearly be done on any configuration, and effectively locate the noise reduction attenuation maximums at any frequency region desired.

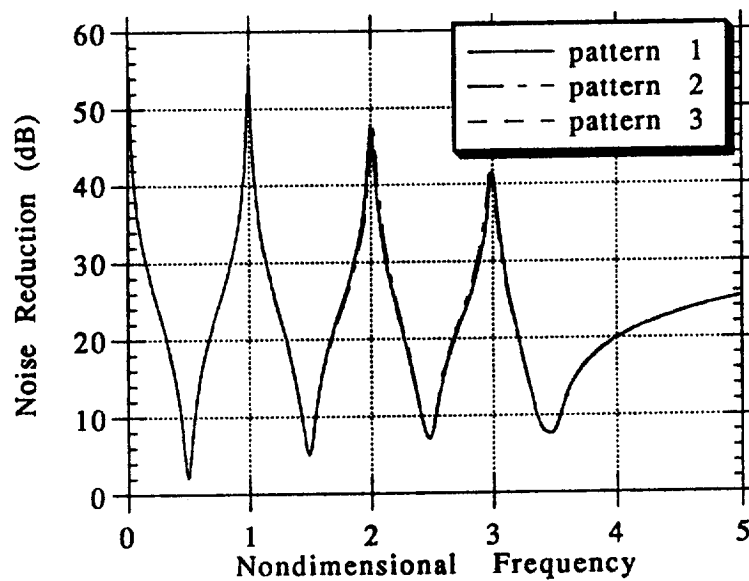


Figure 2.4.19a: Comparison of tuning methodologies for the four panel model using the 3 patterns indicated in Figure 2.1.2.

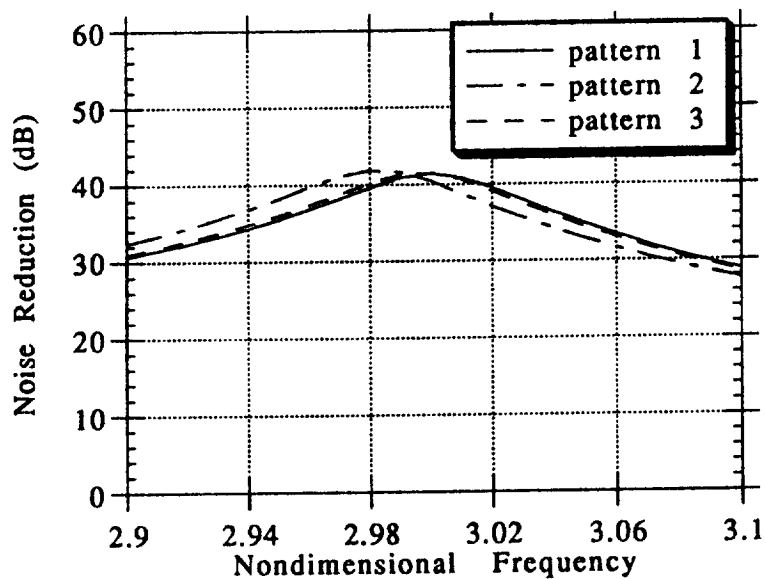


Figure 2.4.19b: Enlargement of noise reduction results around ART cancellation nondimensional frequency = 3.0 to highlight subtle differences between tuning strategies. Patterns as in Figure 2.1.2.

Chapter 3

External Pressure Field Modeling

Section 3.1: Introduction

The purpose of this investigation is to determine the effectiveness of the ART concept under an external propagating pressure field such as that which might be associated with propeller passage by an aircraft fuselage. Figure 3.1.1 shows a schematic representation of a typical aircraft cross section near the propeller plane. Associated with the motion of the propeller near the fuselage is a pressure wave which sweeps by the fuselage panels at some frequency and wavelength which is related to the engine operating speed and propeller characteristics. (Nallasamy, et. al., have shown experimentally that the measured acoustic pressure signal in the plane of the propeller is very closely sinusoidal at a number of blade pitch angles.²³) In general, the problem deals with modeling the interaction of fluid and structural components within the realm of ART tuning.

Section 3.2: Analysis Derivation

The physical schematic for the system is presented in Figure 3.2.1. The analysis configuration consists of a two-dimensional duct, where the position of the coordinate system is shown in the lower left hand side of the schematic. A linear array of Q panels, each of height H , is placed along the z axis at the location $x = 0$. For

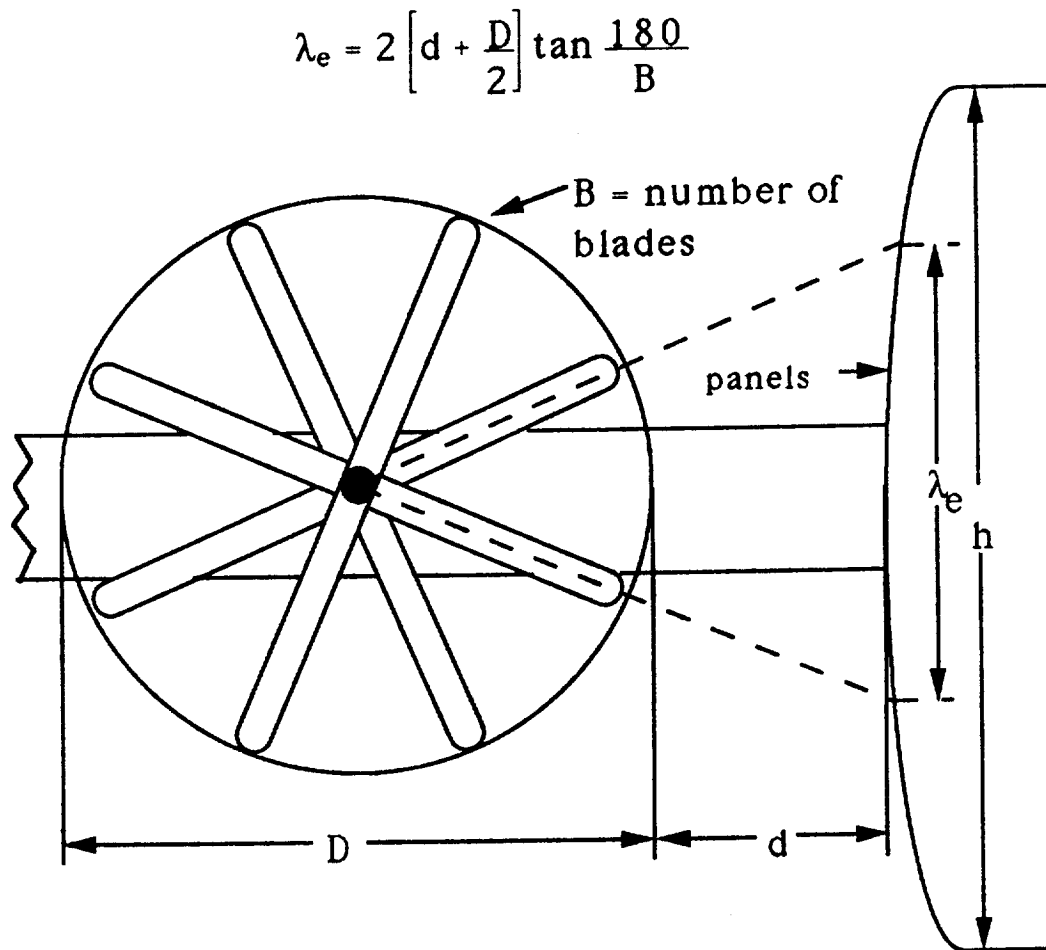


Figure 3.1.1: Front view of aircraft fuselage showing relative locations of propeller and panels in the propeller plane. Dimensions for aircraft used in computational cases are given in Table 3.1.1.

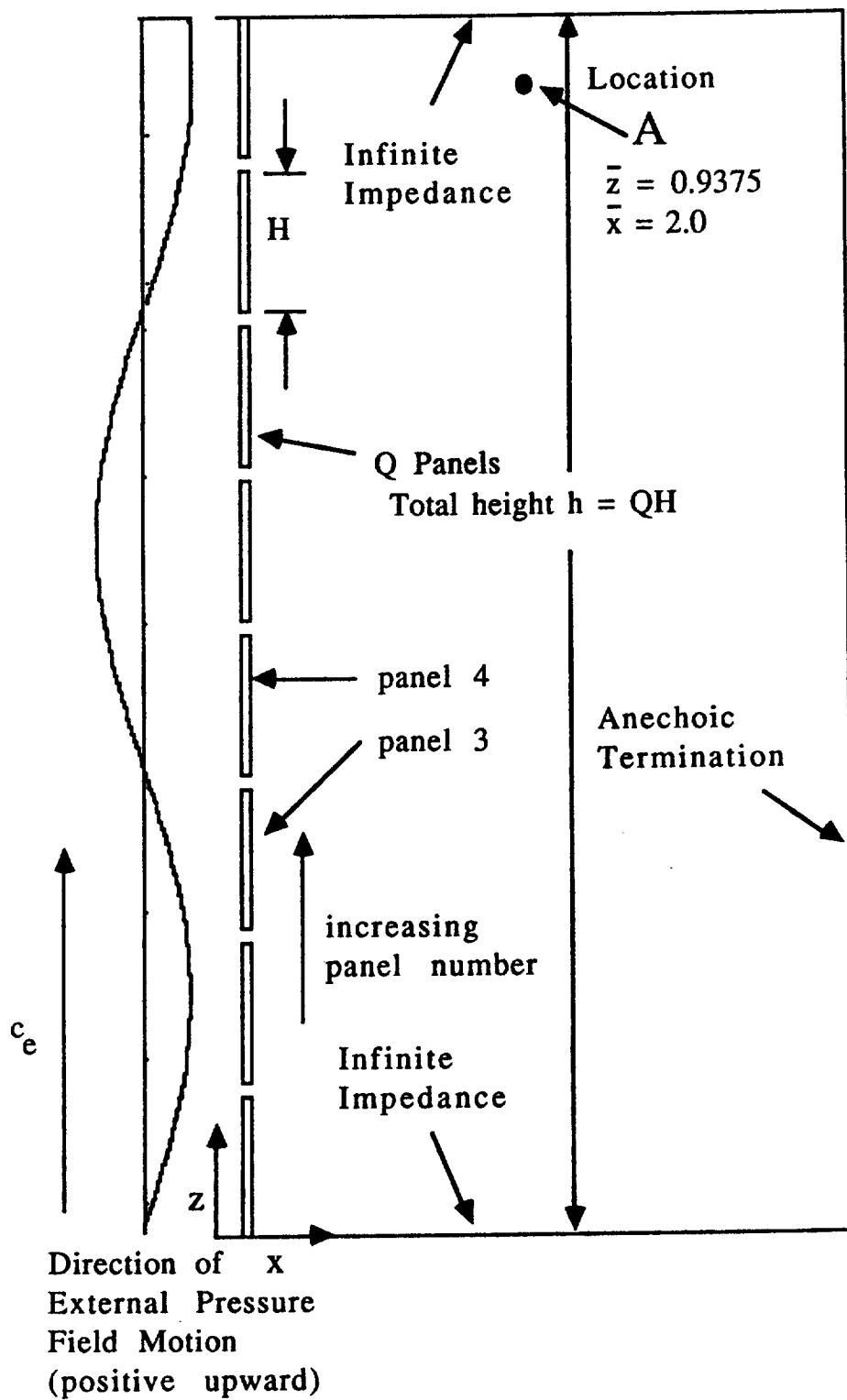


Figure 3.2.1: External pressure field modeling schematic

convenience, these panels are modeled as standard acoustic spring-mass-damper impedances. Note that these Q panels may be tuned in any manner. For example, a standard ART tuning of 2 panels per ART panel pair may be used (one panel has a low natural frequency, and the second panel has a high natural frequency) or more complex tuning arrangements may be used where n panels have n different tunings, where the only constraint is $n \leq Q$. The choice for the panel tuning methodology is not required at this point in the analysis. The termination impedance for the duct is considered to be anechoic. A propagating external pressure is present on the exterior side of the panel wall barrier (at $x = 0^-$) and is of the form

$$P_{ex} = P_e e^{i(\omega t - k_e z)} \quad (3.2.1)$$

This pressure is assumed to be sweeping past the panel array, as shown in Figure 3.2.1.

The analysis begins by considering that one panel of the Q total panels is raised on both the duct and an associated image duct. For the duct,

$$\begin{aligned} f(z) &= 0, QH \geq z \geq rH \\ f(z) &= 1, rH \geq z \geq (r-1)H \\ f(z) &= 0, (r-1)H \geq z \geq 0 \end{aligned} \quad (3.2.2)$$

where r is a panel counting integer $1 \leq r \leq Q$. Similarly, for the image duct

$$\begin{aligned} f(z) &= 0, 0 \geq z \geq -(r-1)H \\ f(z) &= 1, -(r-1)H \geq z \geq -rH \\ f(z) &= 0, -rH \geq z \geq -QH \end{aligned} \quad (3.2.3)$$

A Fourier series representation of these raised panels on both the duct and the image is then given by

$$f(z) = \frac{1}{Q} + \sum_{n=1}^{\infty} \left(\frac{4}{n\pi} \cos \left(\frac{n\pi}{Q} \left(r - \frac{1}{2} \right) \right) \sin \left(\frac{n\pi}{2Q} \right) \cos \left(\frac{n\pi z}{QH} \right) \right) \quad (3.2.4)$$

From hence forth, one need not consider the image duct in the analysis. The velocity representation for the raised panel on the duct is then assumed to be

$$\begin{aligned} u(0,z) &= 0, \quad QH \geq z \geq rH \\ u(0,z) &= U_r e^{i\omega t}, \quad rH \geq z \geq (r-1)H \\ u(0,z) &= 0, \quad (r-1)H \geq z \geq 0 \end{aligned} \quad (3.2.5)$$

Using the Fourier series representation in Equation (3.2.4) above, the general velocity u_r for panel r is then compactly written as

$$u_r(0,z,t) = U_r e^{i\omega t} \left(\frac{1}{Q} + \sum_{n=1}^{\infty} \left(\frac{4}{n\pi} \cos \left(\frac{n\pi}{Q} \left(r - \frac{1}{2} \right) \right) \sin \left(\frac{n\pi}{2Q} \right) \cos \left(\frac{n\pi z}{QH} \right) \right) \right) \quad (3.2.6)$$

The modal velocities $u_n(x,z)$ in the duct satisfy the linearized two-dimensional wave equation

$$\frac{\partial^2 u_n}{\partial x^2} + \frac{\partial^2 u_n}{\partial z^2} + k^2 u_n = 0 \quad (3.2.7)$$

where

$$u_0 = e^{ik_0 x} \quad \rightarrow \quad k_0 = \frac{\omega}{c} \quad (3.2.8)$$

and

$$u_n = e^{ik_n x} \quad \rightarrow \quad k_n = \sqrt{\frac{\omega^2}{c^2} - \left(\frac{n\pi}{QH} \right)^2} \quad (3.2.9)$$

Note that the mode zero velocity, denoted by Equation (3.2.8), always propagates. The higher modal velocities, denoted by u_n , contain the wavenumbers k_n ; some of the k_n are cut off, while the remainder propagate. The frequency of cut on for the n^{th} mode may be described as the solution to

$$\omega = c \left(\frac{n\pi}{QH} \right) \quad (3.2.10)$$

Similarly, at any given ω , the maximum propagating mode will be denoted by the numeric truncation of

$$n = \frac{\omega QH}{\pi c} \quad (3.2.11)$$

Mode numbers up to and including this truncated value for n will propagate. All higher modes will be cut-off. For convenience in the remainder of the derivation, the truncated value of n represented by Equation (3.2.11) will be denoted as n_{low} . Similarly, an integer value of n_{high} will be defined where $n_{\text{high}} = n_{\text{low}} + 1$.

The velocity contribution from the r^{th} single moving panel at any point in the duct is then denoted by

$$\begin{aligned} u_r(x, z, t) = & U_r e^{i\omega t} \frac{1}{Q} e^{-ik_0 x} \\ & + U_r e^{i\omega t} \left(\sum_{n=1}^{n_{\text{low}}} e^{-ik_n^p x} \left(\frac{4}{n\pi} \cos \left(\frac{n\pi}{Q} \left(r - \frac{1}{2} \right) \right) \sin \left(\frac{n\pi}{2Q} \right) \cos \left(\frac{n\pi z}{QH} \right) \right) \right. \\ & \left. + U_r e^{i\omega t} \left(\sum_{n=n_{\text{high}}}^{\text{MODES}-1} e^{-k_n^c x} \left(\frac{4}{n\pi} \cos \left(\frac{n\pi}{Q} \left(r - \frac{1}{2} \right) \right) \sin \left(\frac{n\pi}{2Q} \right) \cos \left(\frac{n\pi z}{QH} \right) \right) \right) \right) \end{aligned} \quad (3.2.12)$$

In this formulation, the modal wavenumber k_n is forced to be a positive real number at all times. Therefore, for propagating modes,

$$k_n^p = \sqrt{\frac{\omega^2}{c^2} - \left(\frac{n\pi}{QH}\right)^2} \quad (3.2.13)$$

while for cutoff modes,

$$k_n^c = \sqrt{\left(\frac{n\pi}{QH}\right)^2 - \frac{\omega^2}{c^2}} \quad (3.2.14)$$

Application of the momentum equation in the x direction

$$p(x,z,t) = -i\omega\rho \int u(x,z,t)dx \quad (3.2.15)$$

results in an expression denoting the pressure contribution by the r^{th} moving panel at any location in the duct. Specifically,

$$\begin{aligned} p_r(x,z,t) = & U_r e^{i\omega t} \frac{\rho}{Qc} e^{-ik_0 x} \\ & + U_r e^{i\omega t} \left(\sum_{n=1}^{n_{\text{low}}} \frac{\omega\rho}{k_n^p} e^{-ik_n^p x} \left(\frac{4}{n\pi} \cos\left(\frac{n\pi}{Q}\left(r - \frac{1}{2}\right)\right) \sin\left(\frac{n\pi}{2Q}\right) \cos\left(\frac{n\pi z}{QH}\right) \right) \right) \\ & + U_r e^{i\omega t} \left(\sum_{n=n_{\text{high}}}^{\text{MODES}-1} \frac{i\omega\rho}{k_n^c} e^{k_n^c x} \left(\frac{4}{n\pi} \cos\left(\frac{n\pi}{Q}\left(r - \frac{1}{2}\right)\right) \sin\left(\frac{n\pi}{2Q}\right) \cos\left(\frac{n\pi z}{QH}\right) \right) \right) \end{aligned} \quad (3.2.16)$$

Only the cut on pressure modes will contribute to the overall complex acoustic pressure far down the duct. In the panel array near-field, however, the resultant pressure is a combination of the cutoff evanescent modes and propagating modes.

Next, an expression is required to obtain the forces on each panel in the panel array. Conceptually, panel r will cause a force on panel s , where s is another panel counting integer operating over the same limits as r . The general sign convention shall be that a positive panel velocity will effect a negative panel force. Additionally, the effect of the external sweeping pressure must also be included. This may be expressed as

$$F_{rs} = -A \int_{\text{panel limits}} p(x=0+,z,t)dz + \int_{\text{panel limits}} P_{ex}dz \quad (3.2.17)$$

The variable $A = 1$ to account for hydrodynamic loading on only one side of the panel array; $A = 2$ allows for hydrodynamic contributions on both sides of the panels. Setting $A = 2$ and allowing only one acoustic mode to be present (the one dimensional mode) along with a long wavelength for the external pressure forcing allows the recovery of the branch analysis results presented in Chapter 2 as a check of both analysis and coding accuracy. If the external sweep forcing is assumed much greater than the hydrodynamic loading, it can be expected that the solutions for $A = 1$ or 2 will not differ greatly except at the panel natural frequency (in this general frequency regime the panel velocities are the greatest) and perhaps at the ART frequency, where the out-of-phase motion of the ART panel pairs causes a different hydrodynamic loading on the panels. Allowing $x = 0+$ in Equation (3.2.16) above and integrating along individual panel limits defined by s yields

$$\begin{aligned}
F_{rs} = & -AU_r e^{i\omega t} \frac{\rho\omega}{Qk_0} H \\
& -AU_r e^{i\omega t} \left(\sum_{n=1}^{n_{low}} \frac{\omega\rho}{k_n^p} \left(\frac{8QH}{(n\pi)^2} \cos\left(\frac{n\pi}{Q}\left(r - \frac{1}{2}\right)\right) \sin^2\left(\frac{n\pi}{2Q}\right) \cos\left(\frac{n\pi}{Q}\left(s - \frac{1}{2}\right)\right) \right) \right) \\
& -AU_r e^{i\omega t} \left(\sum_{n=n_{high}}^{MODES-1} \frac{i\omega\rho}{k_n^c} \left(\frac{8QH}{(n\pi)^2} \cos\left(\frac{n\pi}{Q}\left(r - \frac{1}{2}\right)\right) \sin^2\left(\frac{n\pi}{2Q}\right) \cos\left(\frac{n\pi}{Q}\left(s - \frac{1}{2}\right)\right) \right) \right)
\end{aligned}
\tag{3.2.18}$$

where use has been made of a standard trigonometric identity to simplify the expression. Note that the integration described above is a piecewise application of orthogonality. Next, the integration of the pressure term shown in Equation (3.2.1) is also considered over each panel in the array as

$$\int_{(r-1)H}^{rH} P_e e^{i(\omega t - k_e z)} = \frac{iP_e}{k_e} e^{i\omega t} (e^{-ik_e rH} (1 - e^{ik_e H})) \tag{3.2.19}$$

The following definitions may now be made for notational convenience.

$$B_{prop} = \left(\sum_{n=1}^{n_{low}} \frac{1}{k_n^p} \left(\frac{8}{(n\pi)^2} \cos\left(\frac{n\pi}{Q}\left(r - \frac{1}{2}\right)\right) \cos\left(\frac{n\pi}{Q}\left(s - \frac{1}{2}\right)\right) \sin^2\left(\frac{n\pi}{2Q}\right) \right) \right)
\tag{3.2.20}$$

$$B_{cut} = \left(\sum_{n=n_{high}}^{MODES-1} \frac{1}{k_n^c} \left(\frac{8}{(n\pi)^2} \cos\left(\frac{n\pi}{Q}\left(r - \frac{1}{2}\right)\right) \cos\left(\frac{n\pi}{Q}\left(s - \frac{1}{2}\right)\right) \sin^2\left(\frac{n\pi}{2Q}\right) \right) \right)
\tag{3.2.21}$$

The governing equations may then be expressed as

$$\frac{iP_e}{k_e} (e^{-ik_e r H} (1 - e^{ik_e H})) = U_r \left(A(\rho c H + \omega \rho Q H^2 B_{\text{prop}} + i\omega \rho Q H^2 B_{\text{cut}}) \right) + U_r Z_r \text{ (iff } r = s) \quad (3.2.22)$$

where the common factor of $e^{i\omega t}$ has been cancelled. As stated above in Equation (3.2.22), the term with velocity U_r multiplied by the panel mechanical impedance term Z_r is only added into the equation if $r = s$; i.e., if this coefficient in the matrix is on a diagonal term. Appropriate nondimensionalization then leads to a set of Q linear algebraic equations in the Q unknowns $U_r(\omega)$. When these $U_r(\omega)$ are known, they may be reinserted into Equation (3.2.16) above (also in the appropriately nondimensionalized form) to obtain the pressure at any point in the duct as a result of the motion of panel r . The total overall acoustic pressure at any location in the duct is then obtained simply by summing the Q contributions of Equation (3.2.16).

Section 3.2.1: Noise Reduction Calculation

Pressures on each side of the panel barrier contribute to the calculation of a nondimensional pressure ratio for the expression of a noise reduction in decibels at any location in the duct. Upstream incident pressure is a combination of the external sinusoidal forcing and the resultant loading from the apparent mass modes.

$$\begin{aligned} p_A &= p_{\text{EX}}(z,t) + p_r(x = 0-, z,t) \\ &= p_{\text{EX}}(z,t) - p_r(x = 0+, z,t) \end{aligned} \quad (3.2.23)$$

Transmitted pressure p_B is obtained by summing the Q contributions as given in Equation (3.2.16); together, p_A and p_B

form a pressure ratio of incident to transmitted pressure. The noise reduction in decibels is then denoted by

$$NR_{dB} = -20 \log \frac{P_B}{P_A} \quad (3.2.24)$$

Section 3.2.2: Nondimensionalization

Nondimensionalization of the general results presented above makes use of the nondimensional groupings as shown in Table 2.2.1 in Chapter 2. However, for this problem, a nondimensional velocity is defined as

$$\bar{U}_r = \frac{U_r \rho_o c}{P_E} \quad (3.2.25)$$

and a ratio of panel height to external wavelength nondimensional variable is defined as

$$S_6 = K_E H = \frac{2\pi H}{\lambda_e} \quad (3.2.26)$$

As in Chapter 2, the standard set of parameters considers a square aluminum panel 12" on each side. More discussion on the code input parameters is given in section 3.3.1.

Section 3.2.3: Numerical Solution Procedure

The numerical solution for the external pressure field modeling problem is accomplished in a two step procedure. The governing Equation (3.2.22) and its components are programed to allow for any number of panels to be included in the duct. Additionally, any number of panel impedances may be modeled in

any order, the latter being made possible by a definition of panel properties in a data input file. For a given value of nondimensional frequency ω , the arrays B_{prop} and B_{cut} are calculated. (Note that because these arrays contains the propagating and cutoff wavenumbers, Equations (3.2.20) and (3.2.21) are functions of ω .) Equation (3.2.22) is first solved for the complex nondimensional velocities U_r , and these velocities are written to a data file. A second program then calculates pressures according to Equation (3.2.16), and the total nondimensional pressure, as mentioned earlier, is the sum total of all contributions of Equation (3.2.16). This procedure was adopted to allow multiple calculations of nondimensional pressures and noise reductions in decibels at many locations in the duct without recalculating velocities; the velocity calculation generally is the most time consuming portion of the procedure. Knowledge of the panel velocities for a given set of input parameters (panel size, mass, natural frequencies, apparent mass loading, damping ratios, and external propagating pressure speed) allows the calculation of pressures and noise reduction levels at any location in the duct.

Two other programming issues are deserving of a short note. The numeric solution of the governing Equations (3.2.22) is first solved using LINPACK routines, which are available in the public domain; these routines are quite robust and check for matrix ill-conditioning. Given stable solutions for a number of cases, a faster matrix inversion routine was used; since the results obtained are identical, the faster solution routine is used for production runs. Also, given the desire to generate large amounts of data for a variety of panel configurations, a simple subroutine keeps track of all data inputs and file names for a given simulation. In this manner, all numeric "housekeeping" was computerized and no longer prone to human error.

Section 3.2.4: Results Verification

The computer models mentioned in Chapter 2 may be used as a base upon which comparisons for ART and identical panels may be made. In particular, solving the sweep problem numerically for two ART panels with 1 acoustic mode and $K_{EH} \rightarrow 0$ will recover the ART branch analysis results. (Note that K_{EH} cannot be set to exactly zero in the computer code; due to the formulation of the governing equations for the program, division by zero will result.) Additionally, the external pressure modeling computer program with many acoustic modes as input will be similar to the full 2 panel ART solution with apparent mass, except for results near frequencies where mode turn-on occurs. Also, this latter phenomenon can still be checked with an identical panels simulation using both the full 2 or 4 panel codes, as identical panels in a duct will produce the same noise reduction and nondimensional pressure results with and without apparent mass. Verification of the sweep problem results in this manner assures correct solutions and generates user confidence in the analysis and associated programs.

Section 3.3: Analytical Results

Section 3.3.1: Case Study Inputs

Data from two aircraft are used in case studies for the sweeping analysis. Both simulations include the use of eight aluminum panels 12" on each side to construct the total height for the duct (fuselage sidewall) model. Table 3.3.1 shows parameters representing the two aircraft; the first is a Gulfstream Aerospace Commander 695A aircraft, a high-wing business aircraft, as reported by Wilby and Wilby.²⁴ These input parameters will be referred to as the "long wavelength" case, due principally to the use of a three-bladed propeller. Additionally, this three-bladed propeller creates a low blade passage frequency, which is represented in the nondimensional parameter S_1 as shown in Table 3.3.1. Note here that the external sweep wavelength is about two and one-half times longer than the overall duct height. Table 3.3.1 also displays data from Kuntz and Prydz²⁵ representing a Gulfstream II aircraft modified for noise studies; this configuration will be referred to as the "short wavelength" case due to use of an eight-bladed propeller. The blade passage frequency of the latter case is correspondingly higher, as shown by the value of S_1 in Table 3.3.1 under the "short wavelength" category. In the latter example, the external wavelength is comparable to the duct height. The adjustment of the nondimensional parameter S_1 as shown places the lowest desired ART cancellation frequency at nondimensional frequency $\omega = 1.0$ (the blade passage frequency) for each configuration. Due to the use of different fundamental blade passage frequencies as nondimensional reference frequencies, mode cut on frequencies are quite different in the two cases presented. All mode turn-on frequencies below nondimensional frequency $\omega = 5.0$ are listed in Table 3.3.2. One additional area of difference noted in Table 3.3.1 is the fuselage skin thickness; the Gulfstream 695A fuselage skin thickness is

Table 3.3.1: Long and short wavelength sweep input parameters representing the Gulfstream Aerospace Commander 695A and the Gulfstream II. Unlisted parameters are as given in Table 2.2.1, "Compensated Two Panel Model".

	Gulfstream 695A Long wavelength case	Gulfstream II Short wavelength case
propeller RPM	1518 - 1591	1305 - 1778
B number of blades	3	8
BPF blade passage frequency	75.9 - 79.6	174 - 237 (225 Hz cruise)
h fuselage height	NA	7.9'
d (tip to fuselage clearance)	1.18'	5.55'
s (skin thickness)	0.063"	0.040"
D (propeller diameter)	8.82'	9.00'
λ_e (external pressure propagation wavelength)	19.36'	8.32'
S_1 $\frac{\omega_{ref} H}{c}$	0.434	1.257
S_2 $\frac{\rho_o H^3}{m_{11}}$	0.085	0.134
S_6 $K_e H$	0.3245	0.7547
ζ (panel damping ratios)	0.01	0.01
MR_i (panel mass ratios)	1.0, 0.6746	1.0, 0.7263
U_i (nondimensional panel velocities)	solved for	solved for
ω_n (panel natural frequencies)	0.5, 1.5	0.5, 1.5

0.0625", while the Gulfstream II fuselage skin thickness is 0.040". The thicker skin of the Gulfstream 695A is 50% more massive than the Gulfstream II; in order to keep the simulations representing realistic configurations, these data were left as is. However, Figure 3.3.23 shows the noise reduction predictions for the two aircraft with identical skin thicknesses for comparison.

Table 3.3.2: Mode turn-on frequencies below $\omega = 5.0$ for the long and short wavelength sweep parameters.

mode #	Gulfstream 695A Long wavelength case	Gulfstream II Short wavelength case
1	0.905	0.312
2	1.810	0.625
3	2.715	0.937
4	3.619	1.250
5	4.524	1.562
6		1.874
7		2.187
8		2.499
9		2.812
10		3.124
11		3.437
12		3.749
13		4.061
14		4.374
15		4.686
16		4.999

Section 3.3.2: Mode Convergence Study:

One important decision in numerically solving the governing Equations (3.2.22) with its constituent parts is the number of acoustic modes required to accurately represent a solution. Use of

too few modes will present incorrect results and perhaps hide some interesting phenomena. Inclusion of unneeded modes in the solution increases computation time unnecessarily. A simple way to determine this is to perform a mode convergence and fall-off study away from the panel barrier at the ART frequency. Near the panel barrier, even those modes which are cutoff will have an effect on the resultant pressure (recall that these modes need room in the X direction to decay) and as such are important to the calculation. Figures 3.3.1 and 3.3.2 show convergence fall off results, where the noise reduction is calculated at $z = 0.9375$ in Figure 3.2.1 along the X direction from just inside the panel barrier to a point 80 panel lengths downstream, far enough for all cut off modes to have decayed. Note that for comparison reasons, all falloff results are shown plotted on identical scales. Figure 3.3.1a and 3.3.1b show falloff results for the case without external pressure sweep. The long wavelength case presented in Figure 3.3.1a shows a uniformly oscillating noise reduction down the duct. For this configuration, only one mode is propagating at the ART nondimensional frequency $\omega = 1.0$, and this oblique wave bounces down the duct, adding and subtracting to the overall noise reduction level. Figure 3.3.1b shows the same calculation for the short wavelength case, where at the ART frequency three modes have turned on and cause a greater fluctuation in the noise reduction in the X direction. Figures 3.3.2a and 3.3.2b show the same calculation with the external sweep effect, where now the noise reduction variation has increased in the long wavelength parameters example due to the introduction of more oblique waves in the duct caused by the sweeping effect. The calculation in the short wavelength case remains qualitatively similar to the case without external sweep, except that the variation in noise reduction levels is now over a slightly narrower dynamic range. Figures 3.3.1 and 3.3.2 indicate that 16 modes generally resolves the noise reduction predictions well in the panel near-field for all

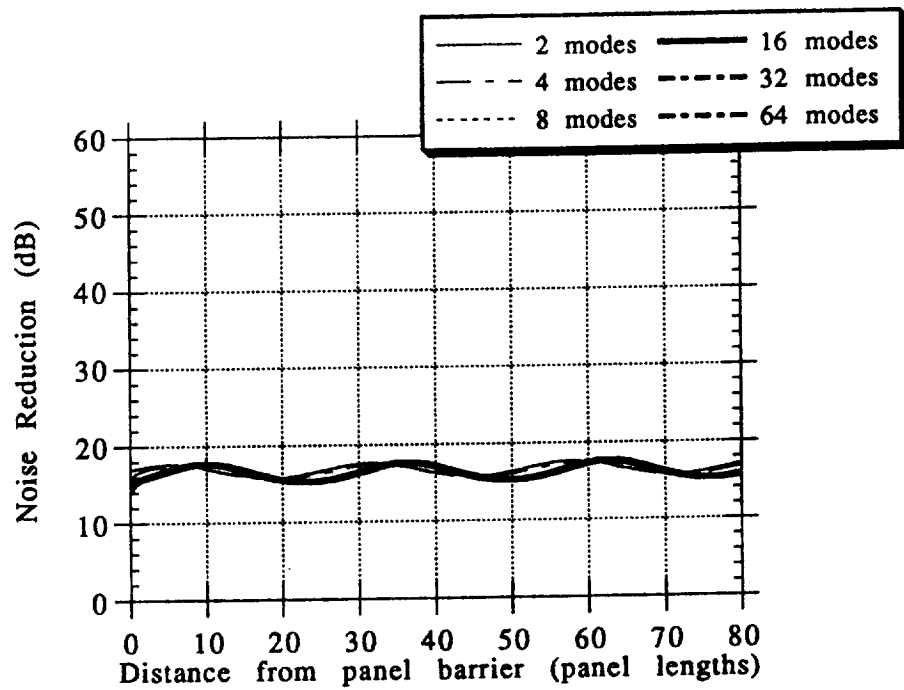


Figure 3.3.1a: Prediction of noise reduction moving away from panel barrier for the long wavelength case without external sweep. Number of modes in calculation as shown in legend.

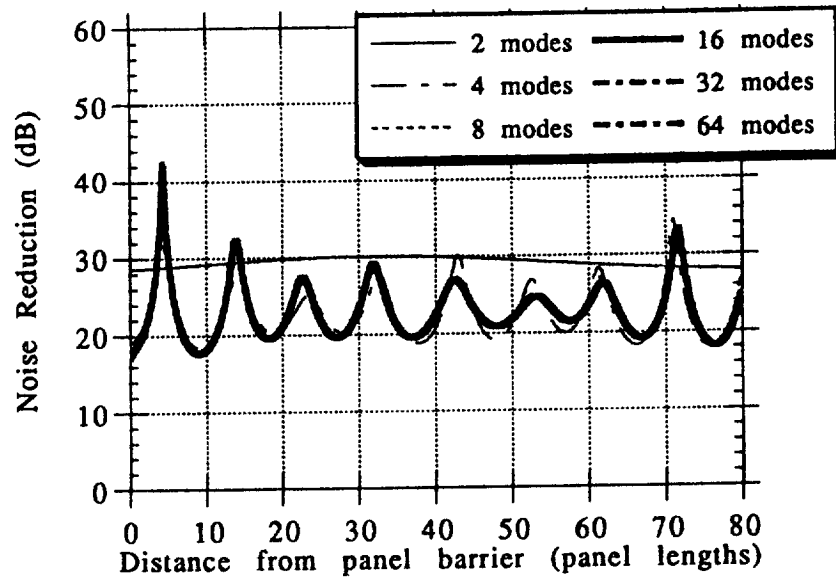


Figure 3.3.1b: Prediction of noise reduction moving away from panel barrier for the short wavelength case without external sweep. Number of modes in calculation as shown in legend.

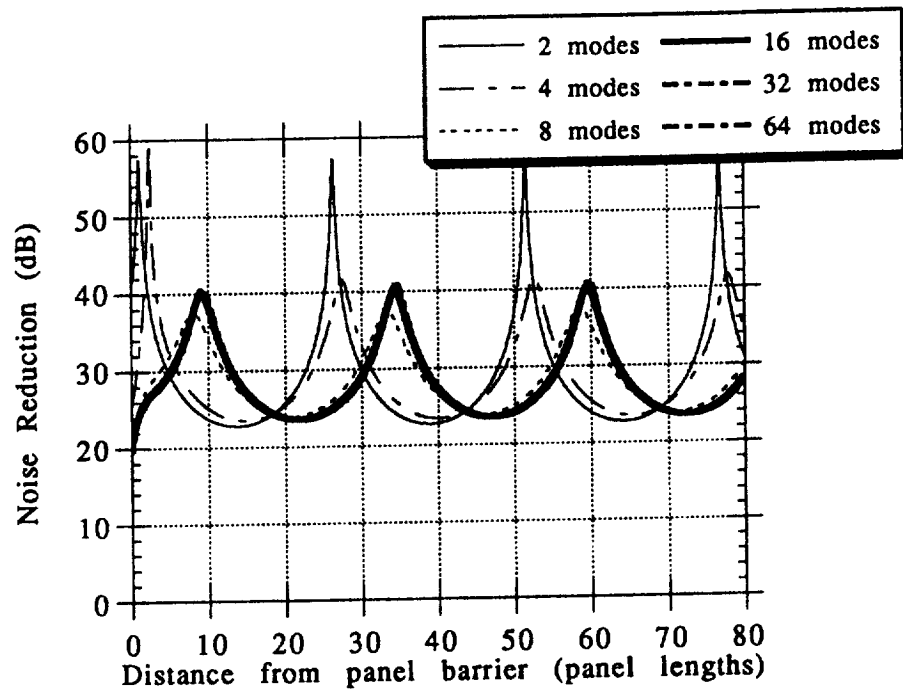


Figure 3.3.2a: Prediction of noise reduction moving away from panel barrier for the long wavelength case with external sweep. Number of modes in calculation as shown in legend.

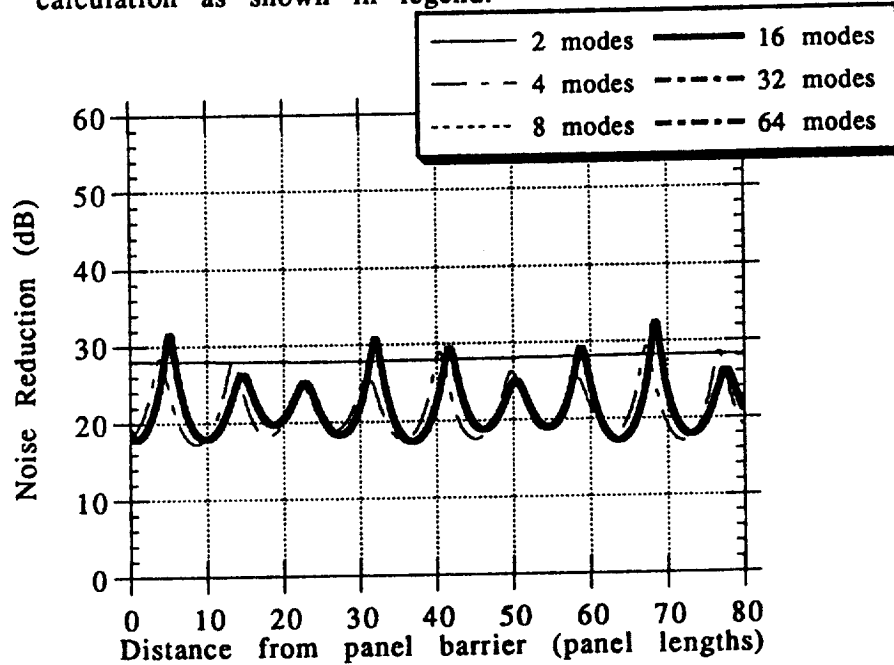


Figure 3.3.2b: Prediction of noise reduction moving away from panel barrier for the short wavelength case with external sweep. Number of modes in calculation as shown in legend.

cases; 32 modes were universally used in all calculations, and represents a conservative choice.

Figure 3.3.3a shows a comparison of the falloff of the pressure ratio p_t/p_E for 32 modes in the duct with external sweep in the X direction at height $z = 0.9375$ for both sets of input data. In both cases, the pressure ratio is relatively large near the panel barrier due to the effect of cutoff modes. As mentioned previously, in the long wavelength case the pressure ratio uniformly rises and falls down the duct due to the interaction of the one cut on mode with the one dimensional mode. The short sweep calculation shows more variation due to the increased number of propagating modes. Figure 3.3.3b shows similar calculations without the effect of external sweep. Again the long sweep case shows a uniform variation as the calculation point moves down the duct, and the short wavelength case is less regular. Figures 3.3.3a and b predict that the long sweep parameters function more effectively to reduce the transmitted pressure ratio in the cases with external sweep; without the effect of the external sweep, the short wavelength parameters function better.

Section 3.3.3: Comparison of ART and Identical Tunings

Figure 3.3.4a shows pressure ratio p_t/p_E for ART tuned and identically tuned panels calculated as a function of frequency at location A ($x = 2.0$, $z = 0.9375$) in the duct as shown in Figure 3.2.1 for the long wavelength parameters. This location is two panel widths downstream in the X direction, and at a vertical position of just under 94% duct height in the Z direction. Identically tuned panels have a large transmitted pressure ratio at nondimensional frequency = 0.8; this frequency is below the nondimensional resonance frequency of 1.0 due to the loading of the apparent mass modes and corresponds to a resonance of the combined panel-fluid system. At this resonance frequency, the entire panel

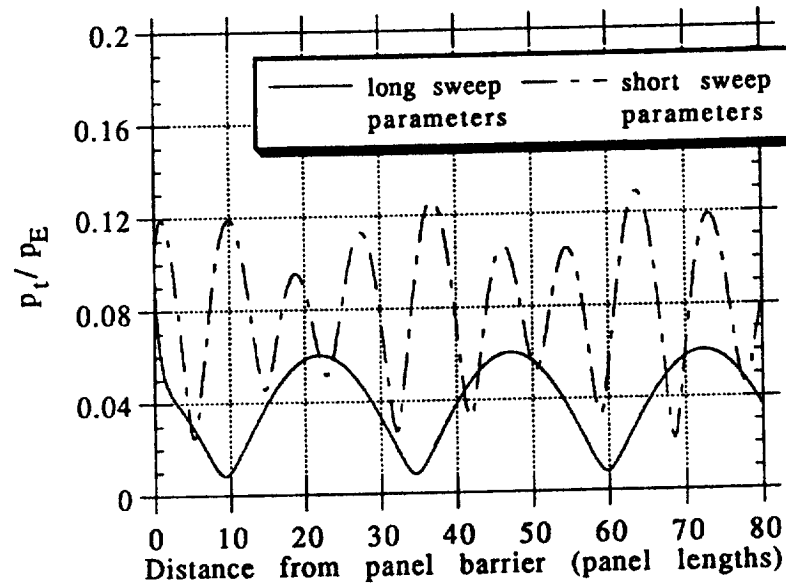


Figure 3.3.3a: Acoustic pressure ratio p_t/p_E prediction moving away from the panel barrier for the long and short wavelength cases with external sweep. 32 acoustic modes are used in the solution.

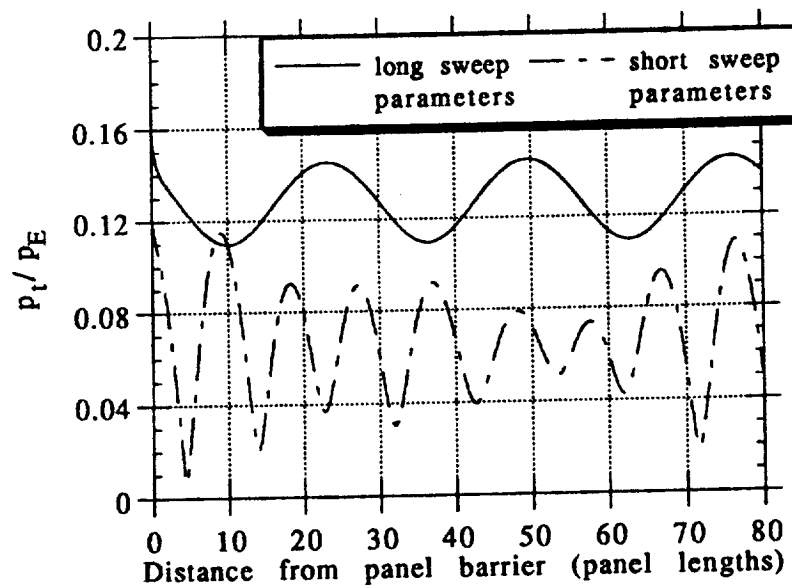


Figure 3.3.3b: Acoustic pressure ratio p_t/p_E prediction moving away from the panel barrier for the long and short wavelength cases without external sweep. 32 acoustic modes are used in the solution.

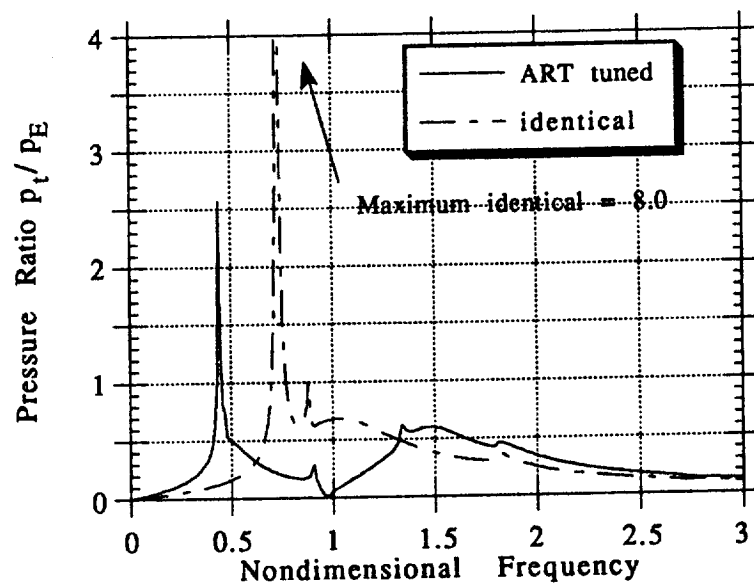


Figure 3.3.4a: Pressure ratio p_t/p_E calculation for two panel ART tuned and identical panels with long wavelength external sweep calculated at Location A in Figure 3.2.1.

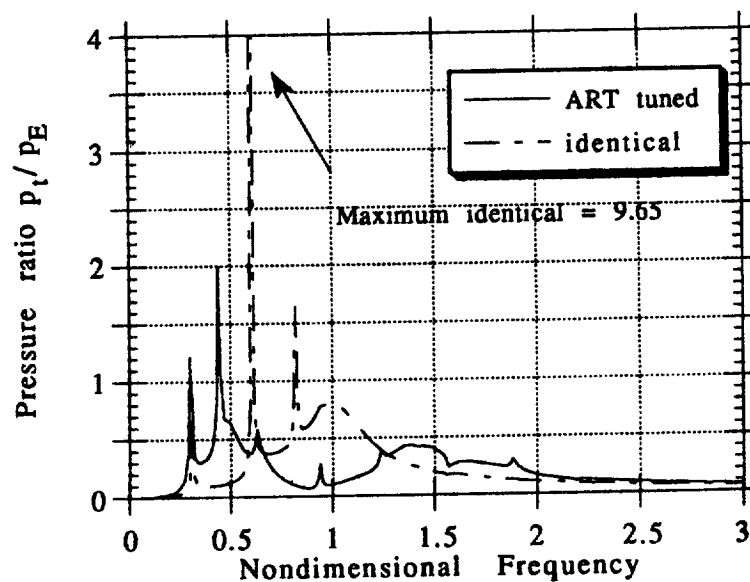


Figure 3.3.4b: Pressure ratio p_t/p_E calculation for two panel ART tuned and identical panels with short wavelength external sweep calculated at Location A in Figure 3.2.1.

barrier moves in an approximately uniform motion (with the exception of the phase variation from panel to panel as a result of the external sweep) with large panel velocities. ART panels have pressure ratio maximums at nondimensional frequencies of 0.5 and 1.5 which are much less, since now two resonance frequencies are present in the system. Minor perturbations can be seen near mode cut on frequencies. Figure 3.3.4b displays results for the short wavelength case study; much similarity to the long wavelength case is observed with the additional effects of more mode cut ons.

Figures 3.3.5a and 3.3.5b show noise reduction calculations for ART and identically tuned panels at the same location in the duct for the long and short wavelength case studies, respectively. Low frequencies exhibit the usual stiffness dominated behavior, and high frequencies show typical mass dominated behavior. As can be expected, noise reduction is low at panel natural frequencies, and high at the ART design frequency of 1.0. The effects of mode cut on can be seen. The long wavelength parameters tend to show somewhat better noise reduction performance because the ART design frequency is lower and the panel sizes are shorter compared to the acoustic forcing wavelengths; that is, the longer wavelength case is effectively more cutoff.

Figure 3.3.6a shows the phase difference between panels 3 and 4 as indicated in Figure 3.2.1 for the long wavelength case.* At low frequencies, the phase difference corresponds to that associated with the external forcing. (Note that the external wavelength of 19.36' for the long wavelength case divided into

* Phase difference between panels is calculated from complex velocities obtained from the solution of Equations (3.2.22). At each frequency, the sign of the velocity components is checked and a panel phase angle relative to the forcing ϕ is calculated using the relationship $\phi = \arctan(U_{\text{imaginary}}/U_{\text{real}})$. Successive phase shifts may add multiples of 2π to this phase angle difference which do not appear in Figures 3.3.6a and 3.3.6b.

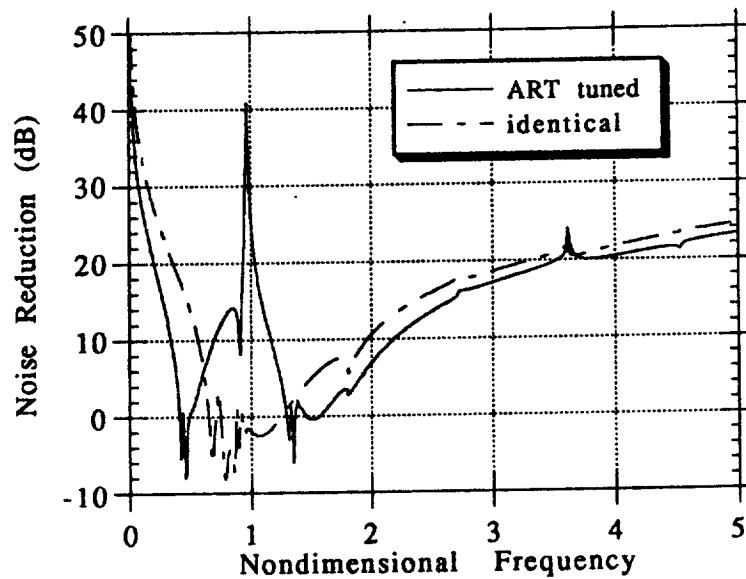


Figure 3.3.5a: Noise reduction calculation for two panel ART tuned and identical panels with long wavelength external sweep calculated at Location A in Figure 3.2.1.

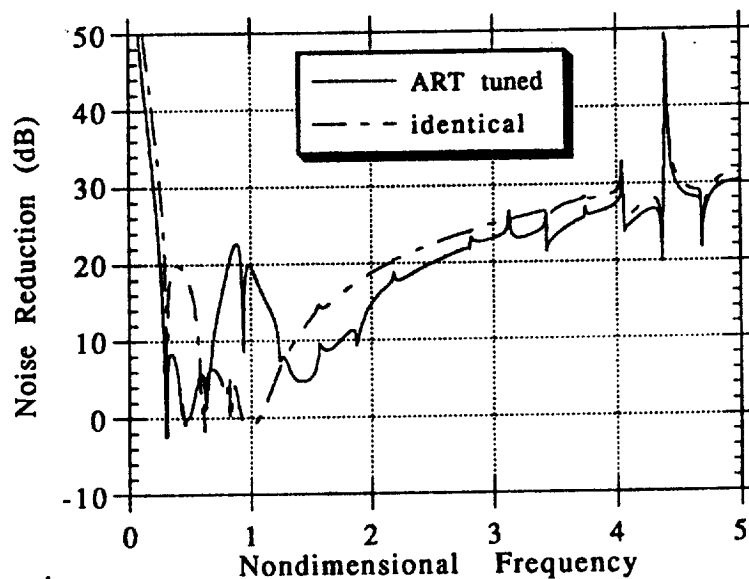


Figure 3.3.5b: Noise reduction calculation for two panel ART tuned and identical panels with short wavelength external sweep calculated at Location A in Figure 3.2.1.

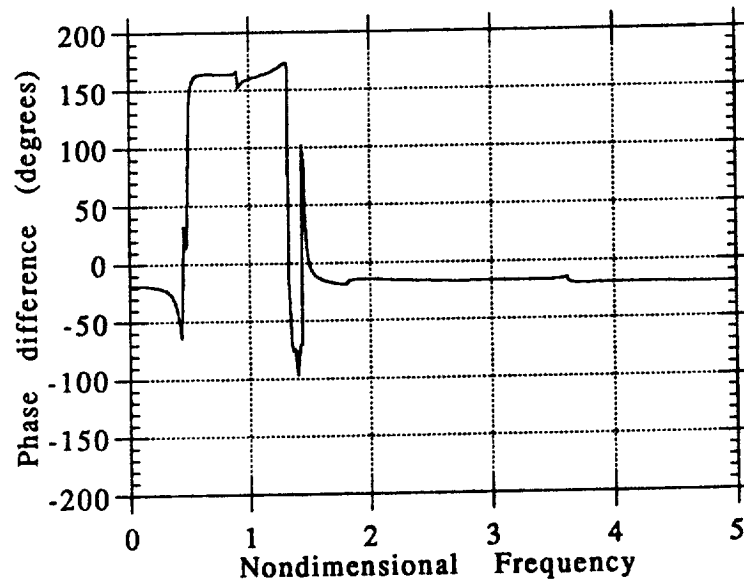


Figure 3.3.6a: Phase difference between panels 3 and 4 as a function of nondimensional frequency for the long sweep wavelength case.

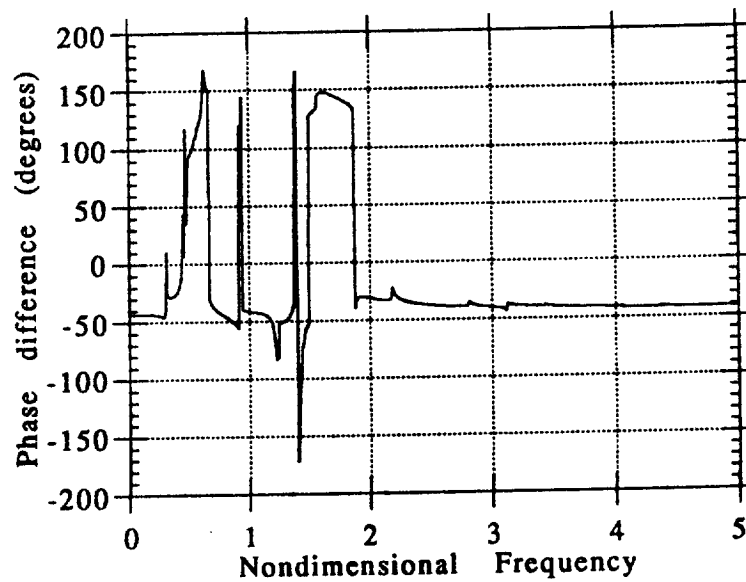


Figure 3.3.6b: Phase difference between panels 3 and 4 as a function of nondimensional frequency for the short sweep wavelength case.

360 degrees yields about 19 degrees phase shift between panels; this is the low and high frequency phase difference limit.) Mode cut on causes one irregularity in the phase difference prediction at $\omega \sim 0.9$; the other anomaly occurs near the high panel resonance frequency. Figure 3.3.6b shows a similar calculation for the short wavelength case; here additional mode cut ons (3 modes cut on between the panel resonance frequencies of $\omega = 0.5$ and 1.5) contaminate the phase difference calculation. Low and high frequency phase difference limits have changed to a larger limiting value due to the shorter external forcing wavelength. Figure 3.3.7a and 3.3.7b show panel velocity relationships for the long and short wavelength ART cases. Both plots indicate that the panel systems have matching velocity amplitudes at the ART design frequencies $\omega = 1.0$. The long wavelength case indicates that the panels reach higher velocity amplitudes around the natural frequencies than the short wavelength case.

Figures 3.3.8a and 3.3.8b show a comparison of ART tuning and the average noninteracting noise reduction results (ANNR). Recall that the ANNR is a idealized measure of the average noise reduction present in the system where only uniform panels are used, and the resulting acoustic fields do not interact, as shown in Chapter 2, Figure 2.4.5. This comparison allows the mass law and stiffness law effects associated with moving the panel resonance frequencies apart to be separated from the effects of acoustic cancellation or cutoff which are critical to optimum ART performance. In both the long and short wavelength cases, ART tuning performs better than the ANNR calculation. In the long wavelength case, between 10 dB and 25 dB of increased noise reduction is achieved. The short wavelength case, while still outperforming the ANNR result, is not as dramatic as the long wavelength case, providing an 8 dB to 12 dB noise reduction increase.

As a final comparison of ART and identical tunings, Figures 3.3.9a and 3.3.9b show a comparison of the individual pressure

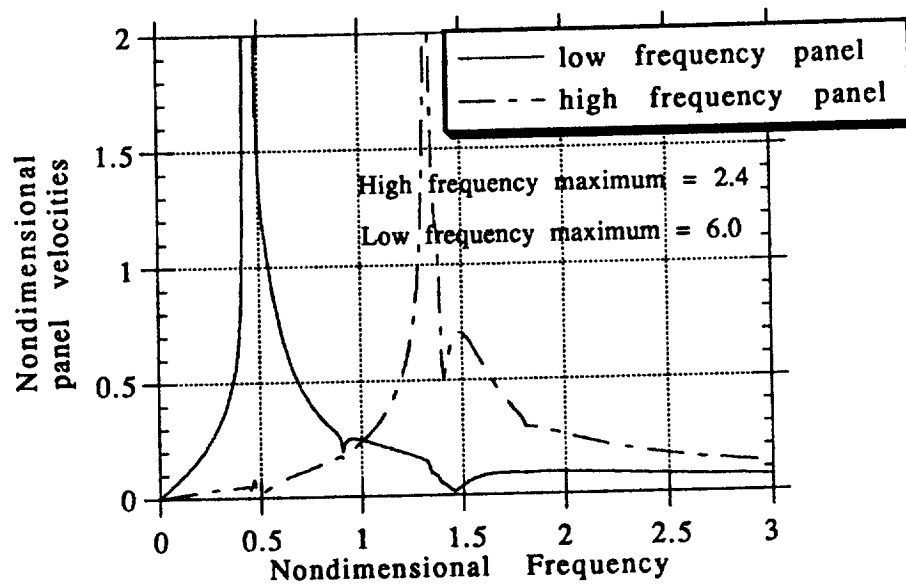


Figure 3.3.7a: Velocity relationships for panels 3 and 4 as a function of nondimensional frequency for the long sweep wavelength case.

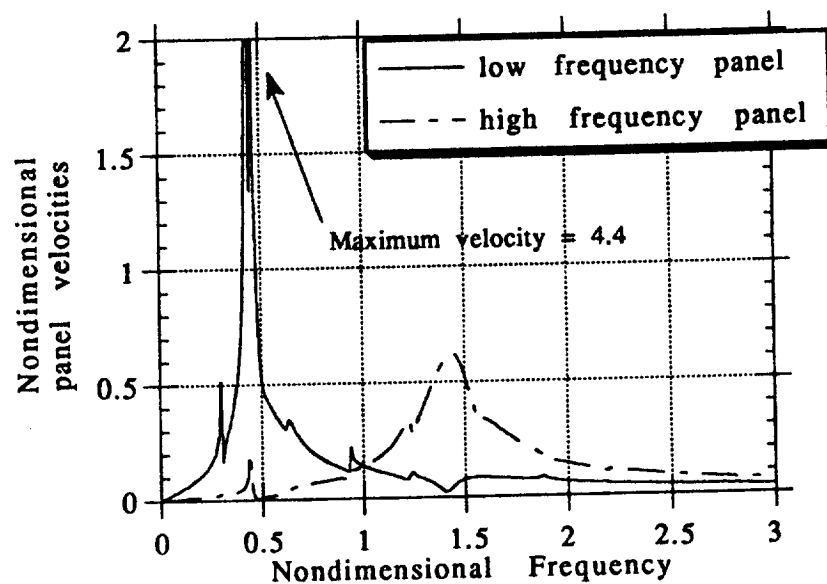


Figure 3.3.7b: Velocity relationships for panels 3 and 4 as a function of nondimensional frequency for the short sweep wavelength case.

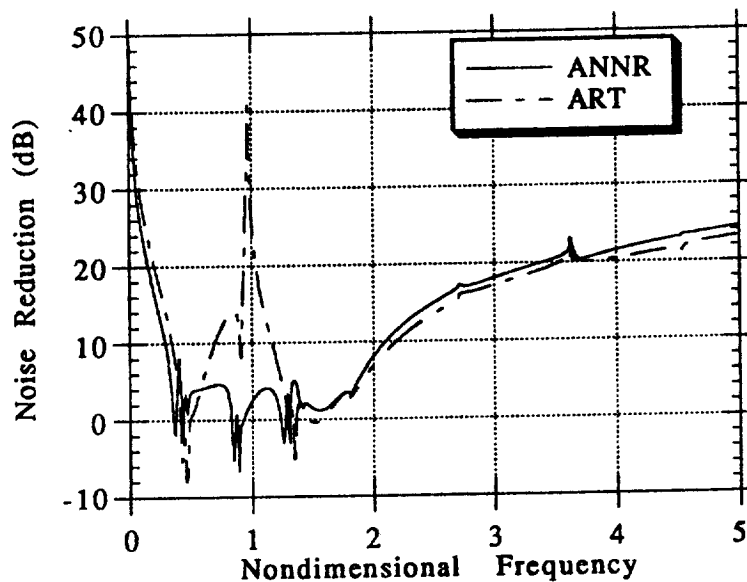


Figure 3.3.8a: Averaged noninteracting noise reduction for identical panels and two panel ART noise reduction prediction for long sweep wavelength case calculated at Location A in Figure 3.2.1.

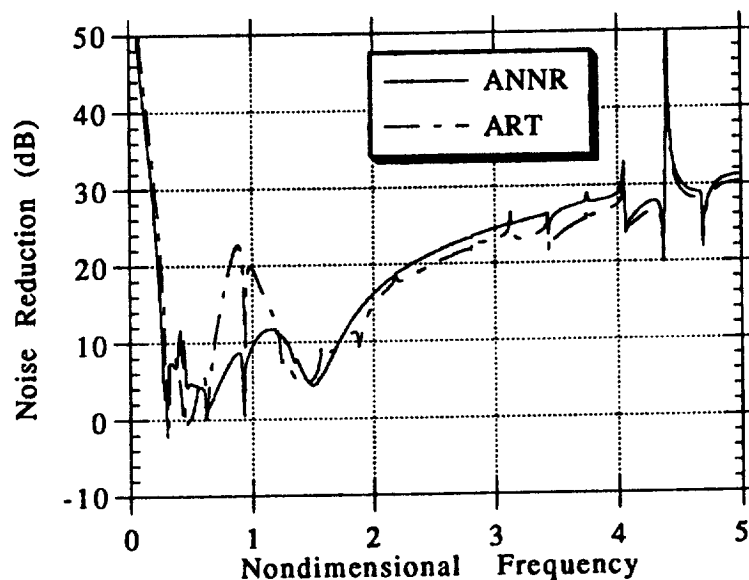


Figure 3.3.8b: Averaged noninteracting noise reduction for identical panels and two panel ART noise reduction prediction for short sweep wavelength case calculated at Location A in Figure 3.2.1.

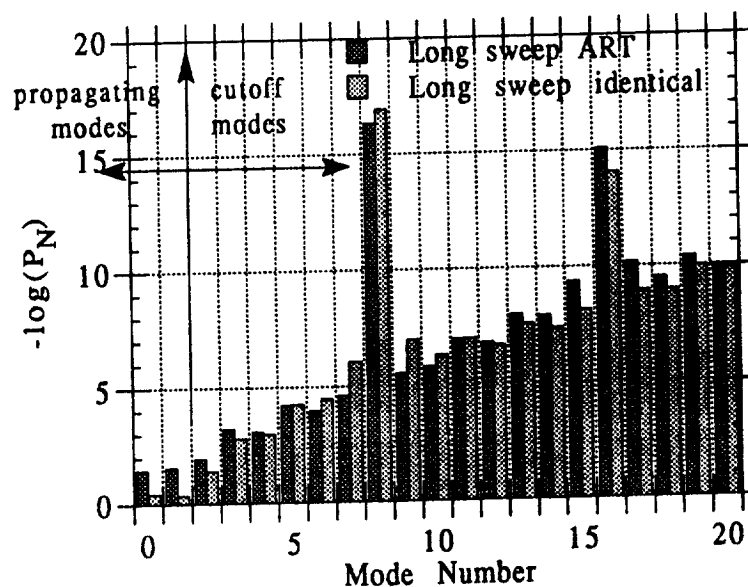


Figure 3.3.9a: Relative comparison of the first 21 modal contributions to noise reduction in the long sweep wavelength case at the ART design frequency. Note that the comparison is logarithmic.

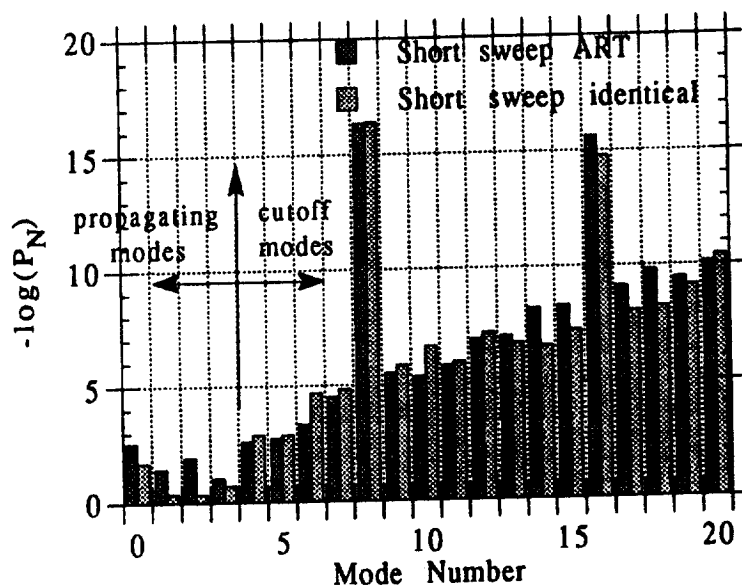


Figure 3.3.9b: Relative comparison of the first 21 modal contributions to noise reduction in the short sweep wavelength case at the ART design frequency. Note that the comparison is logarithmic.

mode coefficients for the calculation of the acoustic pressure in the duct at the ART nondimensional design frequency. Since there is a wide dynamic range of these pressure coefficients and because there is a net noise reduction across the panel barrier, the negative logarithm of the pressure coefficient results is taken. This mathematical interpretation means larger values of the modal pressure coefficients contribute more to noise reduction in the system; that is, less transmitted noise through the panel barrier occurs with larger values of the modal pressure coefficients. The following comments are made in that spirit. While the ART tuning modal pressure coefficients are not always greater than the uniform panel tuning coefficients over the range of mode numbers shown, the ART results for lower propagating modes are *always* greater than similar results for identical panels. Note that for each propagating pressure mode (as shown in Figure 3.3.9a, modes 0 and 1 for the long sweep wavelength case, and modes 0 through 3 for the short wavelength case shown in Figure 3.3.9b), the ART tuning methodology contributes to noise reduction; in some cases, this contribution is more than one order of magnitude. Also note that modes 8 and 16 have large values because these modes are integer multiples of the number of panels in the system. In general, as the mode number increases, the negative logarithm of the pressure coefficient increases more for ART panels than for identical panels, indicating that ART redirects energy into the higher, cutoff modes.

Section 3.3.4: Model Parameter Studies

A comprehensive set of parameter studies provides further insight with respect to tuning an ART panel array in the presence of an external propagating pressure field. Note that for Figures 3.3.10 through 3.3.14, noise reductions are calculated at position A as shown in Figure 3.2.1.

Figure 3.3.10a shows noise reduction calculations in the duct for three separate sets of input parameters, where the higher panel natural frequency is increased in order to increase the noise reduction bandwidth. In the long wavelength case, this is quite beneficial, since mode turn-on frequencies do not occur as often as the short wavelength case. Splitting the natural frequencies not only increases the noise reduction bandwidth, but it also increases the peak noise reduction obtained. Figure 3.3.10b shows that this procedure is still beneficial with the short sweep wavelength parameters, even in the presence of many mode turn-ons. This study suggests that when tuning an ART panel array, it is most desirable to attempt to keep mode turn-on frequencies away from the desired frequency of maximum noise reduction; however, this may not always be feasible. In general, increasing the ART noise reduction bandwidth by separating panel natural frequencies up to a difference of nondimensional frequency of 2.0 is most always beneficial. (Chapter 5 will show experimental verification of this fact.)

Figures 3.3.11a and 3.3.11b show the effect of increased panel damping on the model. As with the four panel model presented in Chapter 2, increased damping tends to increase noise reduction levels at the panel natural frequencies, as each panel in effect becomes less acoustically transparent. Since the panels are operating in a regime farther away from perfect out-of-phase behavior, absolute maximum noise reductions are less. However, the general frequency bandwidth at a given noise reduction amount remains the same, indicating the robustness of the ART

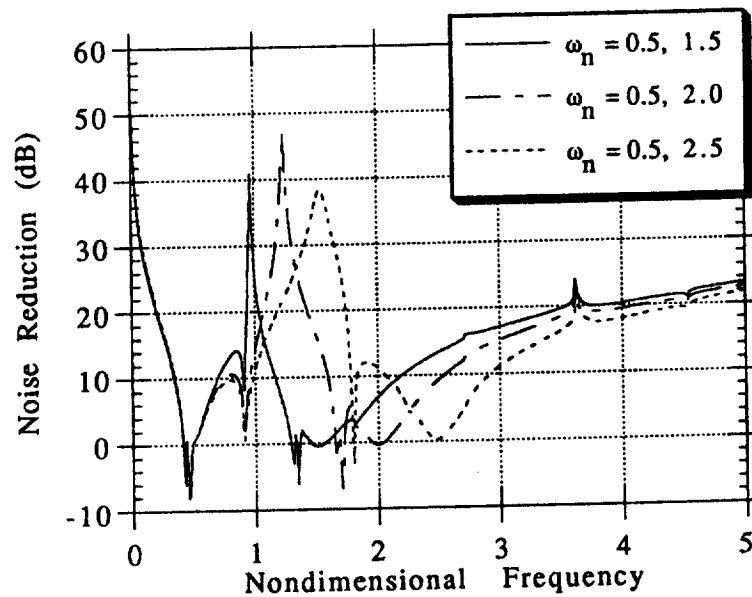


Figure 3.3.10a: Parameter studies with two panel tuning varying the higher natural frequency as indicated above to increase the noise reduction bandwidth in the long wavelength case.

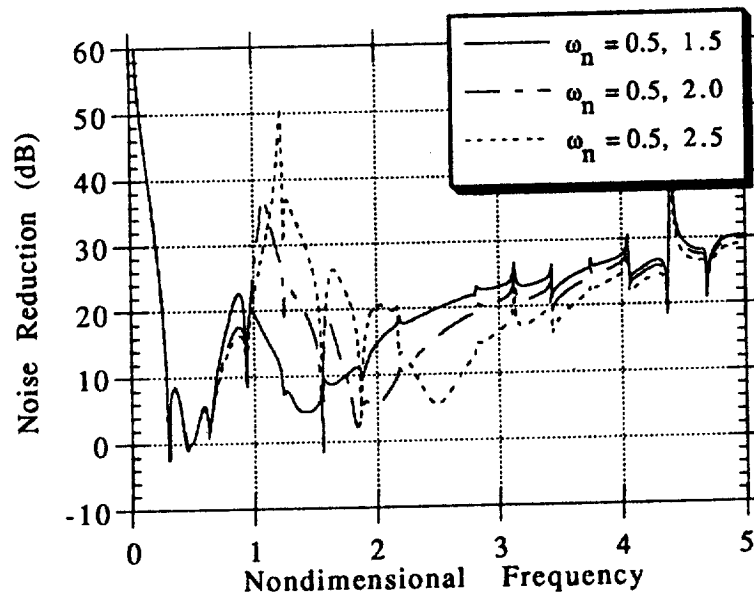


Figure 3.3.10b: Parameter studies with two panel tuning varying the higher natural frequency as indicated above to increase the noise reduction bandwidth in the short wavelength case.

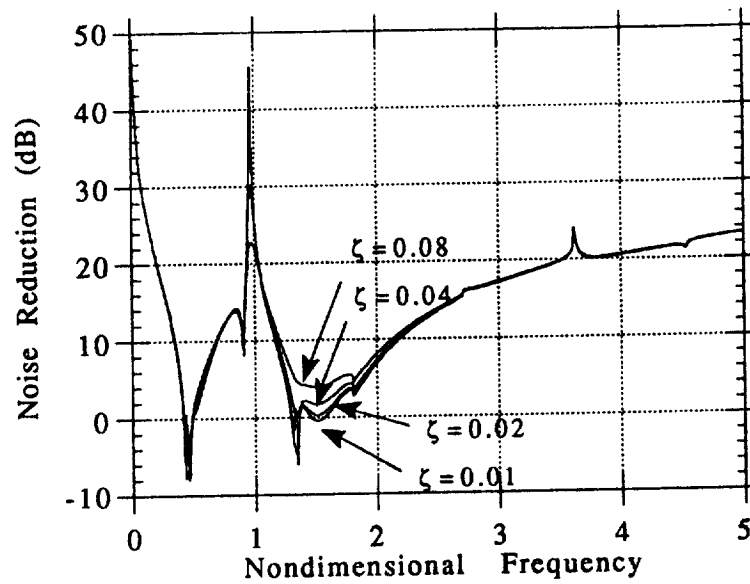


Figure 3.3.11a: Parameter studies with the two panel model varying the panel damping ratio as indicated above in the long wavelength sweep case.

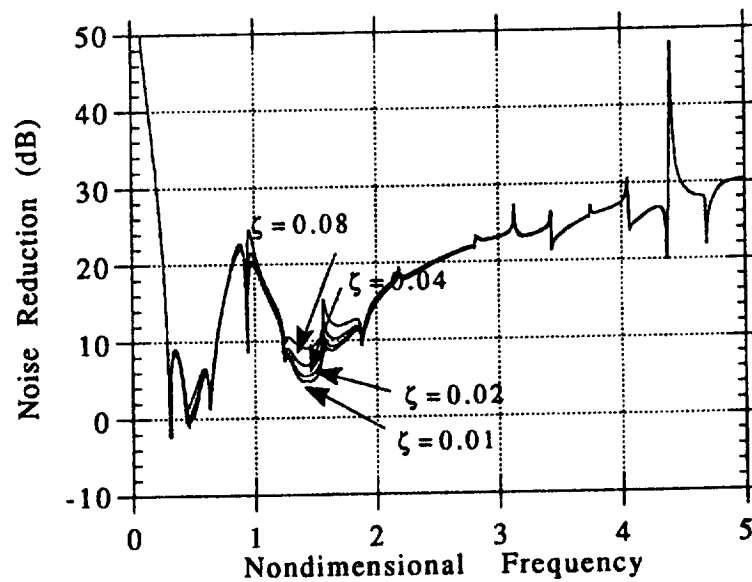


Figure 3.3.11b: Parameter studies with the two panel model varying the panel damping ratio as indicated above in the short wavelength sweep case.

tuning concept, and that ART tuning might be incorporated into other modes of noise reduction such as increased damping. Furthermore, in the short sweep wavelength parameters case, increased damping seems to play an even lesser role, indicating the tendency of the external forcing to dominate system behavior.

Figure 3.3.12a and 3.3.12b show the effect of the variation of the apparent mass loading on the ART panel array. In both the long and short wavelength cases, increasing the apparent mass loading tends to couple the panels together through the surrounding fluid such that approximate out-of-phase behavior is no longer possible. As such, maximum noise reduction and noise reduction bandwidth are simultaneously reduced. This effect is particularly noticeable in the long sweep wavelength case study, where over 25 dB of noise reduction is lost between normal air mass loading and eight times normal air mass loading. If operation of an ART panel array were necessary in a heavy fluid loading, it would become necessary to design for this loading. An alternative option might be to increase panel mass in order to maintain the apparent mass to panel mass ratio.

Figures 3.3.13a and 3.3.13b show the noise reduction predictions obtained by variation of the parameter A as denoted by Equation (3.2.17) in Section 3.2. Recall that when $A = 1$, fluid loading on only one panel side is considered, whereas when $A = 2$, fluid loading on both sides on the panel is considered. As expected, the solutions are quite similar except near panel natural frequencies. Panel velocity is the greatest around the panel natural frequency. Variation of A as shown effectively doubles the apparent mass loading, and when the panel velocities are large, this loading is most critical. Therefore, for all calculations, apparent mass loadings on both panel sides are routinely considered.

Propeller rotation direction can be controlled by the sign of the nondimensional parameter $K_e H$ (S_6 in Table 3.3.1); the default value used herein has been an upward or positive propagation

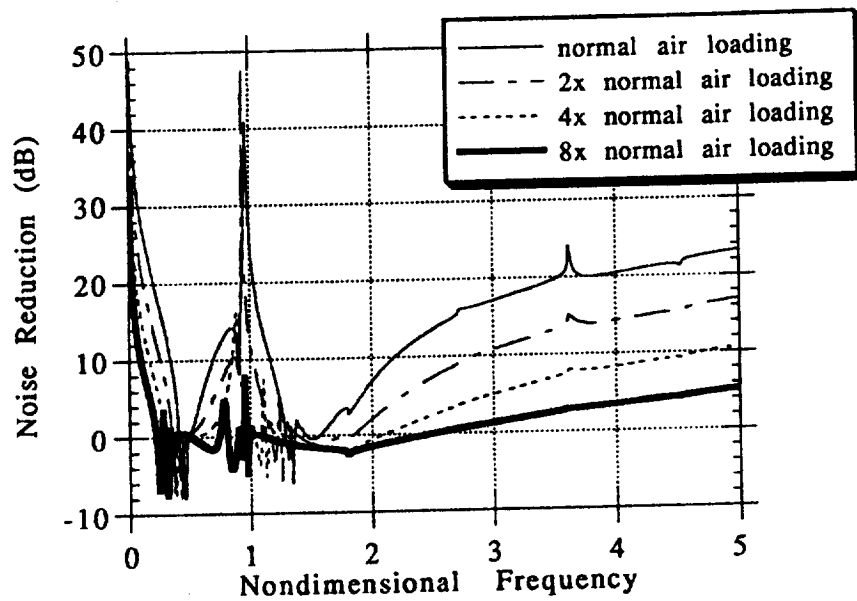


Figure 3.3.12a: Parameter studies with the two panel model varying the panel apparent mass loading as indicated above in the long wavelength case.

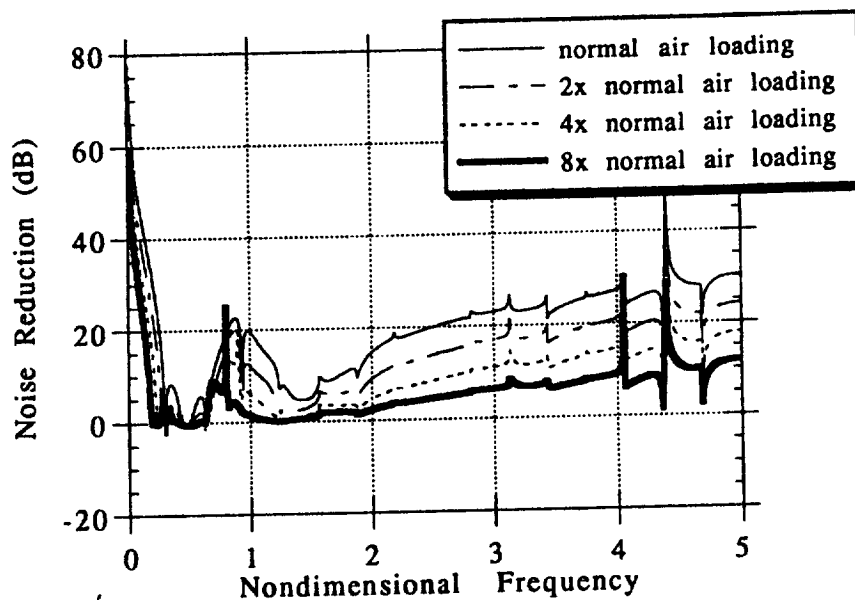


Figure 3.3.12b: Parameter studies with the two panel model varying the panel apparent mass loading as indicated above in the short wavelength case.

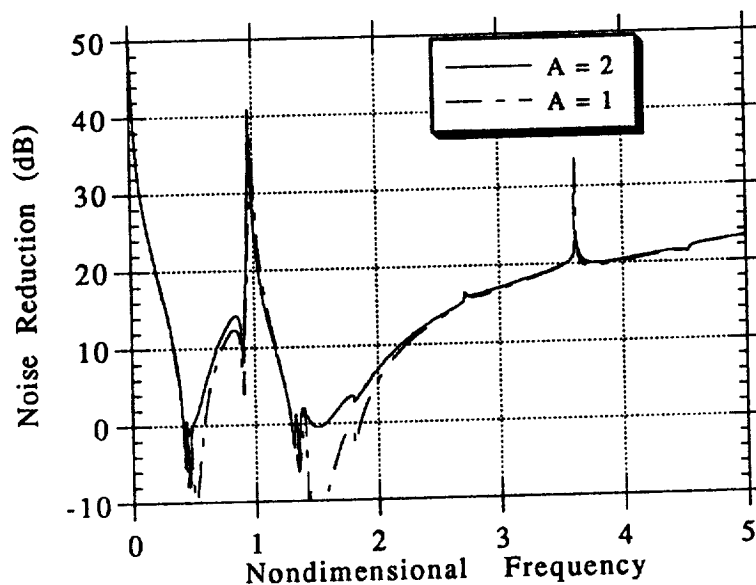


Figure 3.3.13a: Noise reduction calculation for two panel ART tuned array and long wavelength sweep parameters with $A = 1$ and $A = 2$. Noticeable difference occurs only at resonance frequencies.

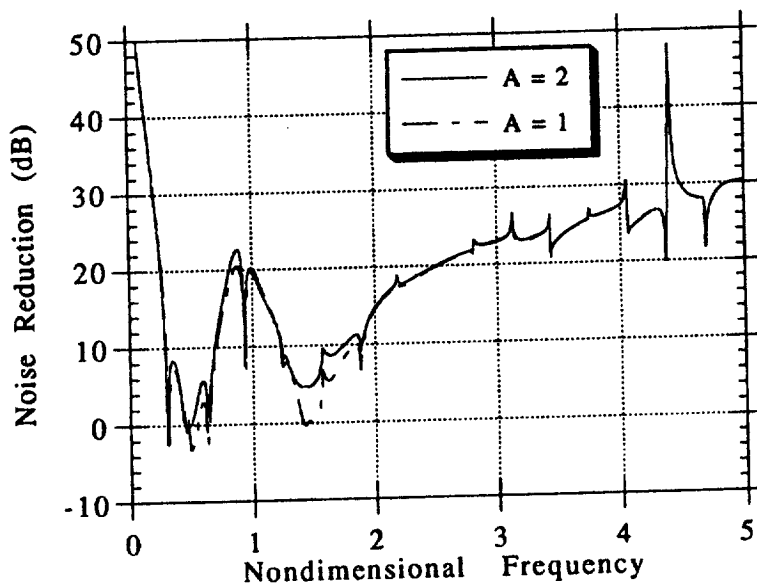


Figure 3.3.13b: Noise reduction calculation for two panel ART tuned array and short wavelength sweep parameters with $A = 1$ and $A = 2$. Noticeable difference occurs only at resonance frequencies.

direction with respect to the coordinate system shown in Figure 3.2.1. Reversal of the external sweep can be accomplished by use of negative values for the parameter $K_e H$. Figures 3.3.14a and 3.3.14b shown the dramatic effect that the propagation direction of the external forcing can have upon the noise reduction across the panel barrier with respect to a given location; again, noise reductions are calculated at Location A as shown in Figure 3.2.1. For the latter location, reverse sweep shows significant increases in noise reductions at certain frequencies. Using the long wavelength sweep parameters, as shown in Figure 3.3.14a, noise reduction is increased at higher frequencies between 3 and 8 dB. Also note slightly better noise reductions between the panel resonance frequencies. Similar results are seen in Figure 3.3.14b, representing the short external wavelength parameters. The difference in these cases might be attributed to different interactions of the panel barrier with the upper and lower duct boundaries. In the upper sweep propagation mode, the exterior propagating pressure last sees panel number 8 (referring to Figure 3.2.1), which is ART tuned to a higher natural frequency and has less mass. In the downward sweep direction, the propagating pressure last sees panel number 1, ART tuned to a low natural frequency with more mass. The different sweep directions set up different groups of oblique waves which propagate down the duct, and the increase in noise reduction can be attributed to a greater local cancellation effect. Noise reduction calculations at a point symmetrically opposite of Location A ($x = 2.0$, $z = 0.0625$) appear worse. This will be verified and discussed in the next section.

Section 3.3.5: Pressure and Noise Reduction Mapping

The solution of the governing Equations (3.2.22) yields a full acoustic solution; pressures (and therefore noise reduction levels) can be calculated at all locations within the duct knowing the panel velocities. Pressure and noise reduction mappings at one value of

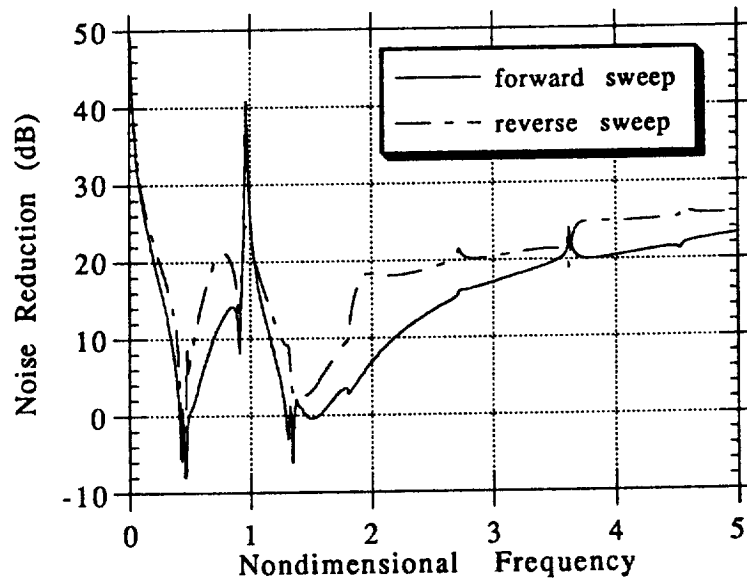


Figure 3.3.14a: Forward and reverse sweep direction noise reduction calculation for two panel ART tuning with long wavelength external sweep calculated at Location A.

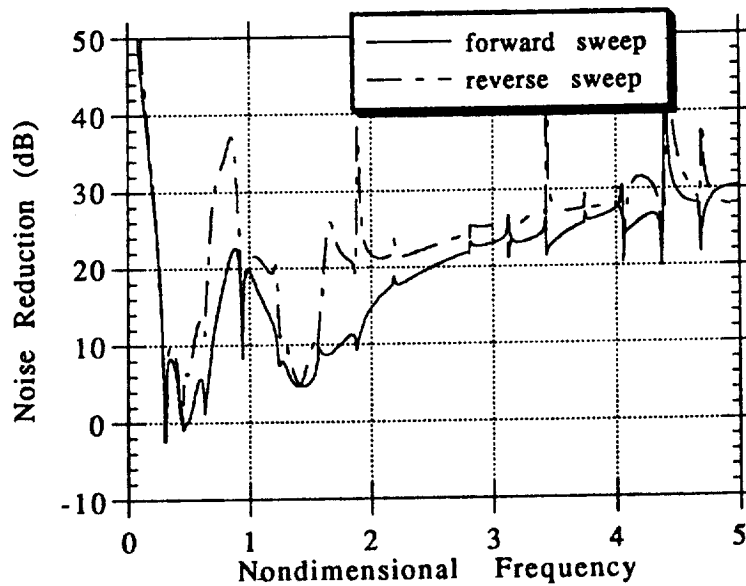


Figure 3.3.14b: Forward and reverse sweep direction noise reduction calculation for two panel ART tuning with short wavelength external sweep calculated at Location A.

frequency throughout the entire duct domain indicate the sound levels to be expected at all locations. Such calculations indicate the nature of the sound fields within the duct at a desired frequency; specifically, "hotspots" and quiet areas can be identified..

Figure 3.3.15a shows the pressure mapping in the duct at the ART frequency $\omega = 1.0$ for the long sweep wavelength parameters.. Note that the three dimensional transmitted pressure ratio plot has X location in units as nondimensionalized by panel height H, Z location in the duct (vertical position per Figure 3.2.1) on the "y" axis ($0 < z < 1$), and acoustic pressure on the "z" axis. Rather high pressure ratio values are predicted in the upper portion of the duct closest to the panel barrier in the long sweep wavelength case. The pressure ratio tends to decay to a somewhat uniform value after movement away from the panel barrier of 2-3 panel widths. The short wavelength parameters pressure mapping in Figure 3.3.15b shows the effect of more propagating modes at the ART frequency $\omega = 1.0$, where three distinct pressure peaks are observed due to the three propagating modes. Again the uppermost portion of the duct has higher transmitted pressure ratios, where noisy regimes are to be expected.

Sound mapping in decibels provides a more intuitive interpretation of the relative sound levels in the duct. Figure 3.3.16a plots noise reduction in the duct for the long sweep wavelength parameters case. When translated into decibels, the ART effect is quite dramatic; after moving a distance of 5 panel diameters away from the barrier, at least 20 dB of noise reduction has occurred. Also, the presence of only one propagating mode insures a more uniform noise reduction throughout all areas of the duct. Figure 3.3.16b predicts that the short wavelength parameters produce more variation in the noise reduction throughout the duct. Figures 3.3.16c and 3.3.16d show the same calculations without the effect of external sweep. In the long sweep wavelength case in Figure 3.3.16c, the noise reduction has approached a "tent-like" structure, appearing relatively regular in

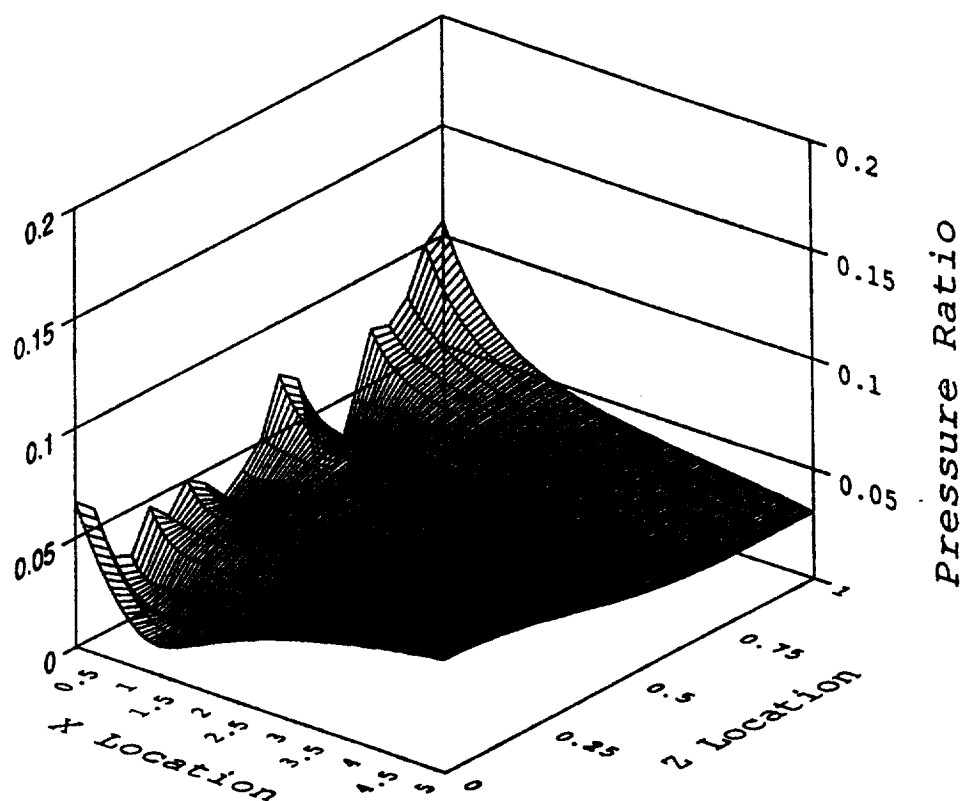


Figure 3.3.15a: Pressure map for the ART tuned panel array at the maximum ART noise reduction frequency $\omega = 1.0$ in the long sweep wavelength case.

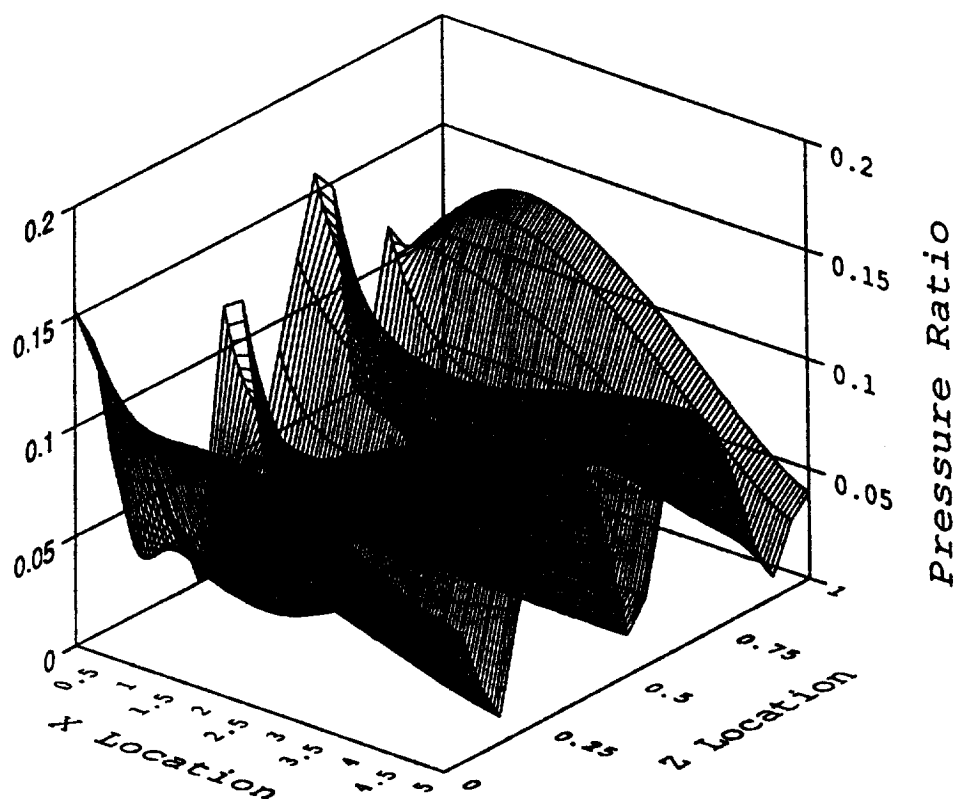


Figure 3.3.15b: Pressure map for the ART tuned panel array at the maximum ART noise reduction frequency $\omega = 1.03$ in the short sweep wavelength case.

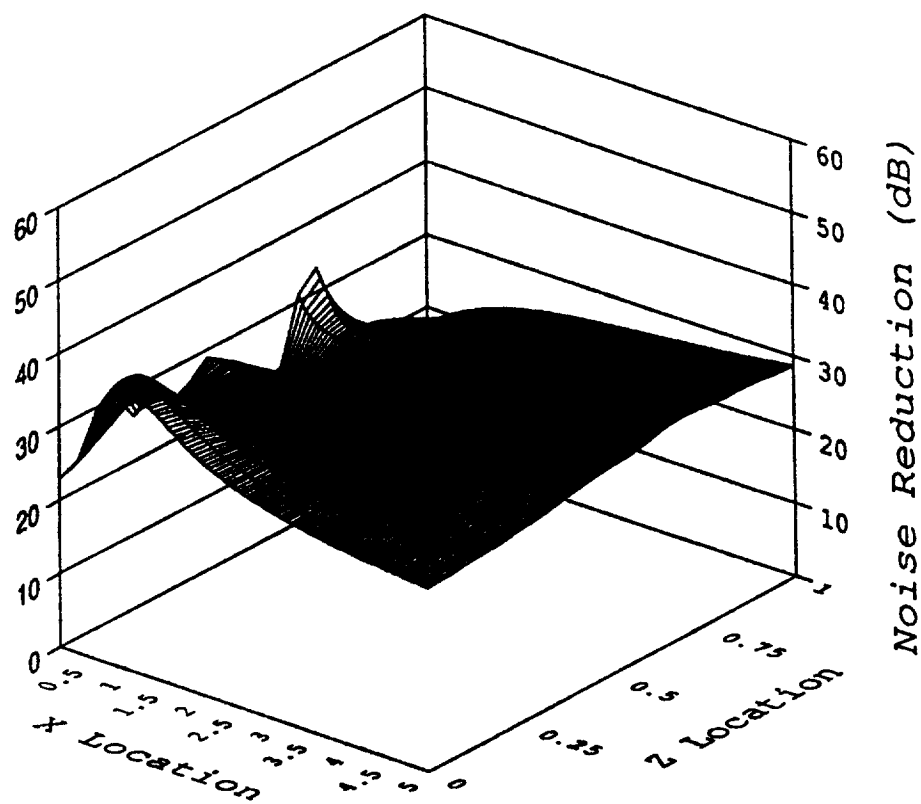


Figure 3.3.16a: Noise reduction map for the ART tuned panel array at the maximum ART noise reduction frequency $\omega = 1.0$ in the long sweep wavelength case.

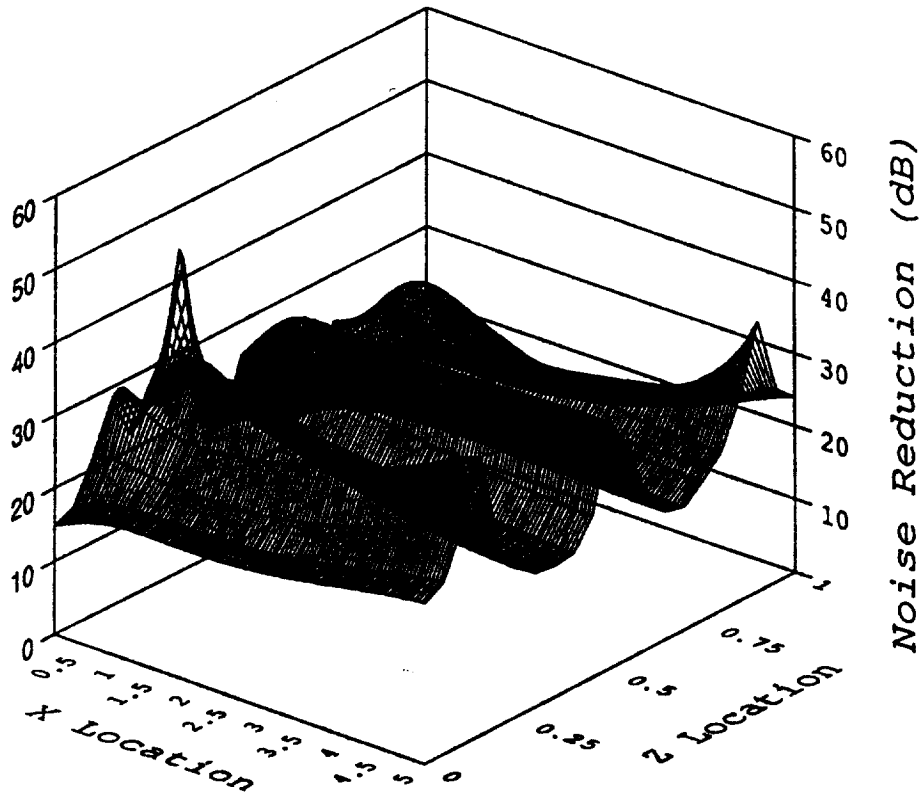


Figure 3.3.16b: Noise reduction map for the ART tuned panel array at the maximum ART noise reduction frequency $\omega = 1.03$ in the short sweep wavelength case.

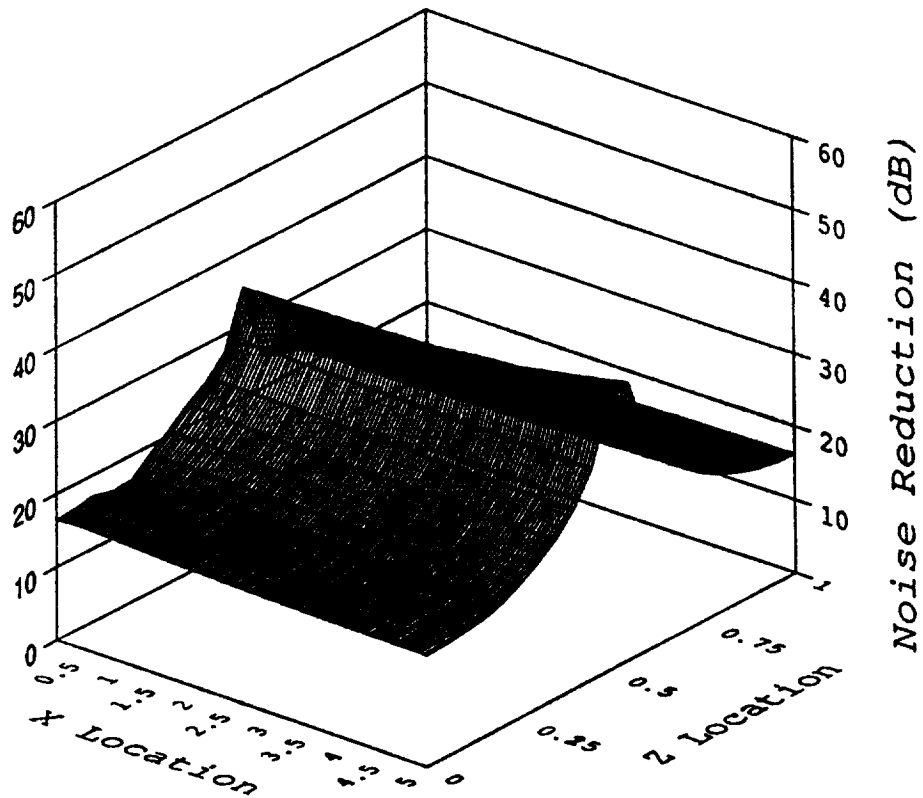


Figure 3.3.16c: Noise reduction map for the ART tuned panel array at the maximum ART noise reduction frequency $\omega = 1.0$ for the long wavelength parameters without external sweep.

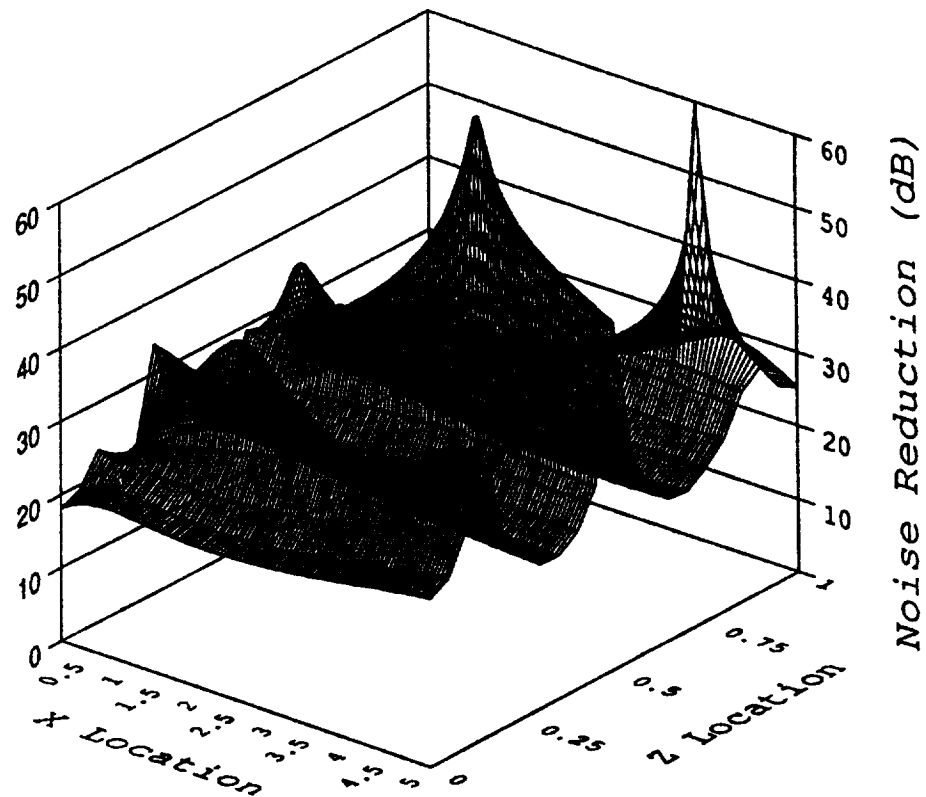


Figure 3.3.16d: Noise reduction map for the ART tuned panel array at the maximum ART noise reduction frequency $\omega = 1.03$ for the short wavelength parameters without external sweep.

construction. Figure 3.3.16d suggests again that the short wavelength parameters produce a wider variation in noise reduction throughout the duct. Some of the propagating pressures can interact to produce quite dramatic, but only locally high effectiveness in attenuating the transmitted noise. Nonetheless, the ART treatment does produce a substantially quieter interior noise level.

Figures 3.3.17a through 3.3.17d show cross sectional noise reduction calculations at the indicated panel widths downstream from the panel barrier calculated at $\omega = \omega_{ART}$. Note in these figures that noise reduction is now placed on the abscissa, and vertical location in the duct is plotted on the ordinate. In Figure 3.3.17a, the long sweep wavelength parameters produce a more regular noise reduction level moving further away from the wall. This is in contrast to the short sweep wavelength parameters shown in Figure 3.3.17b, which produce large variations across the duct. Figures 3.3.17c and 3.3.17d show the equivalent cases without the sweeping effect; in the long sweep wavelength parameters, the "tent-like" noise reduction prediction of Figure 3.3.16c is examined. Note the decay of pressure (noise reduction increase) indicated on the centerline as the calculation point moves away from the panel barrier. Also, the noise reduction calculation is not symmetrical; there is variation in the upper and lower portions of the duct due to the different boundary condition represented by panels of varying mass and natural frequency.

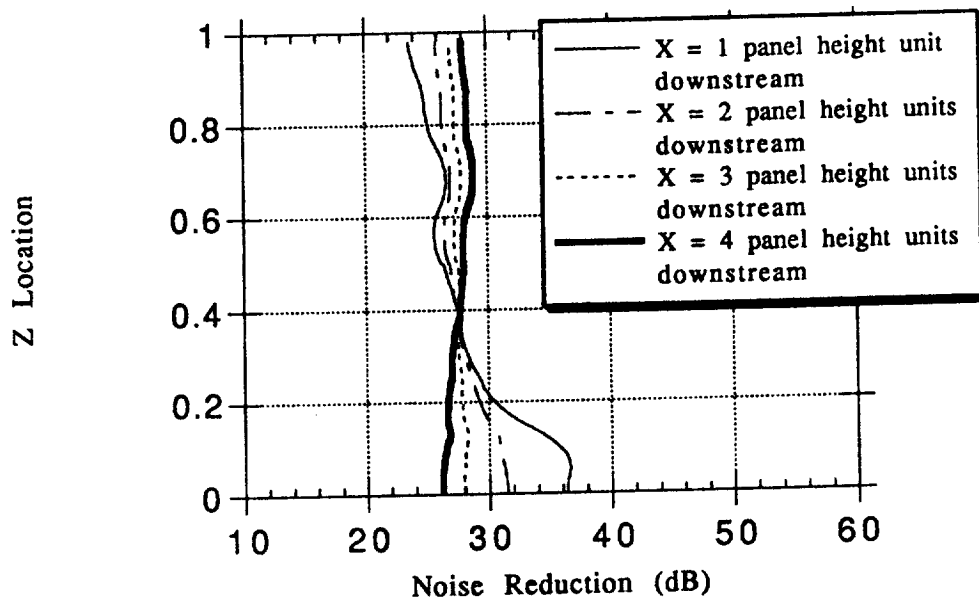


Figure 3.3.17a: Cross sectional noise reduction predictions at indicated X locations for the long wavelength sweep case.

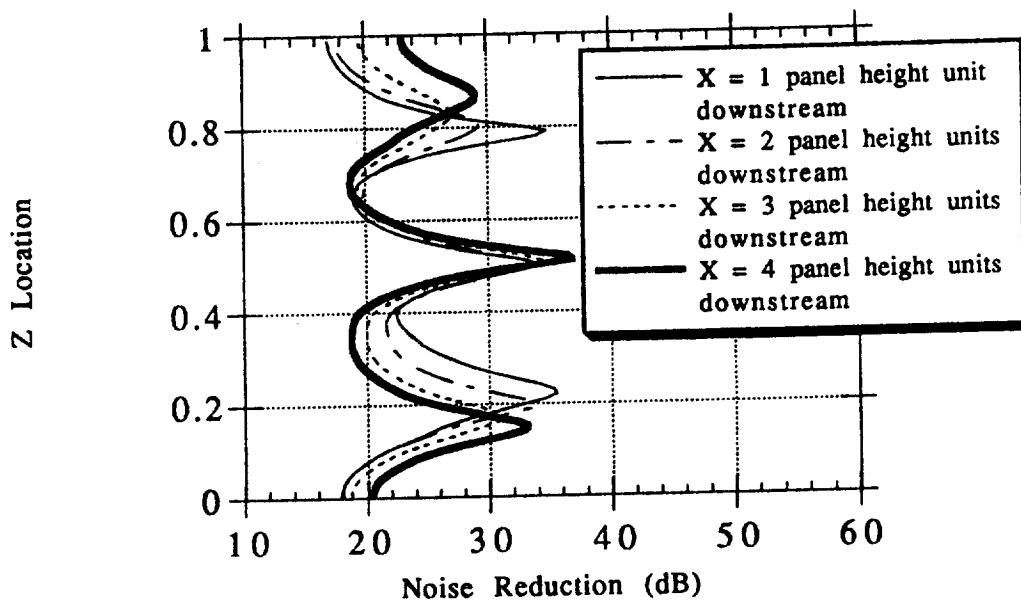


Figure 3.3.17b: Cross sectional noise reduction predictions at indicated X locations for the short wavelength sweep case.

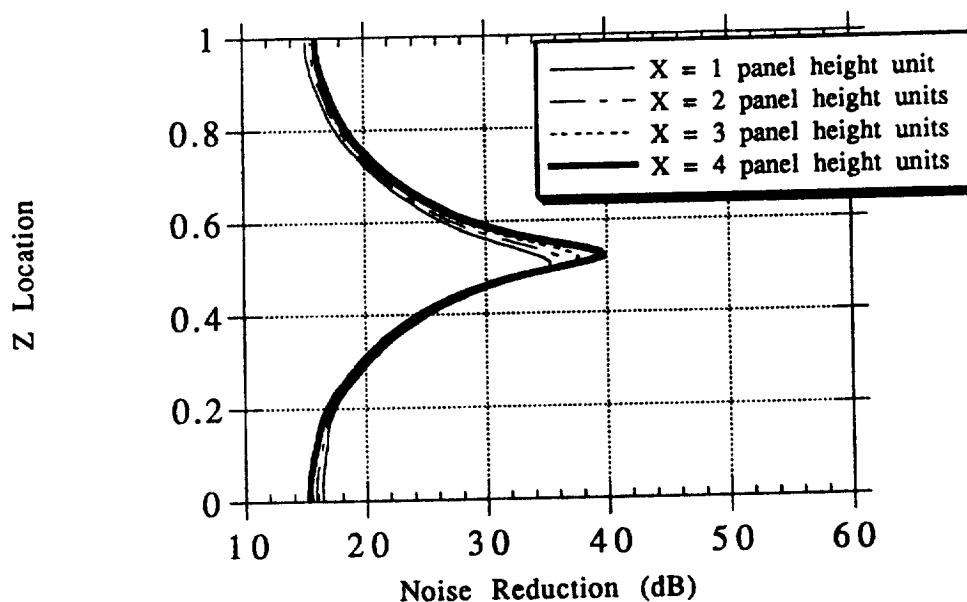


Figure 3.3.17c: Cross sectional noise reduction predictions at indicated X locations for the long wavelength sweep parameters without external sweep.

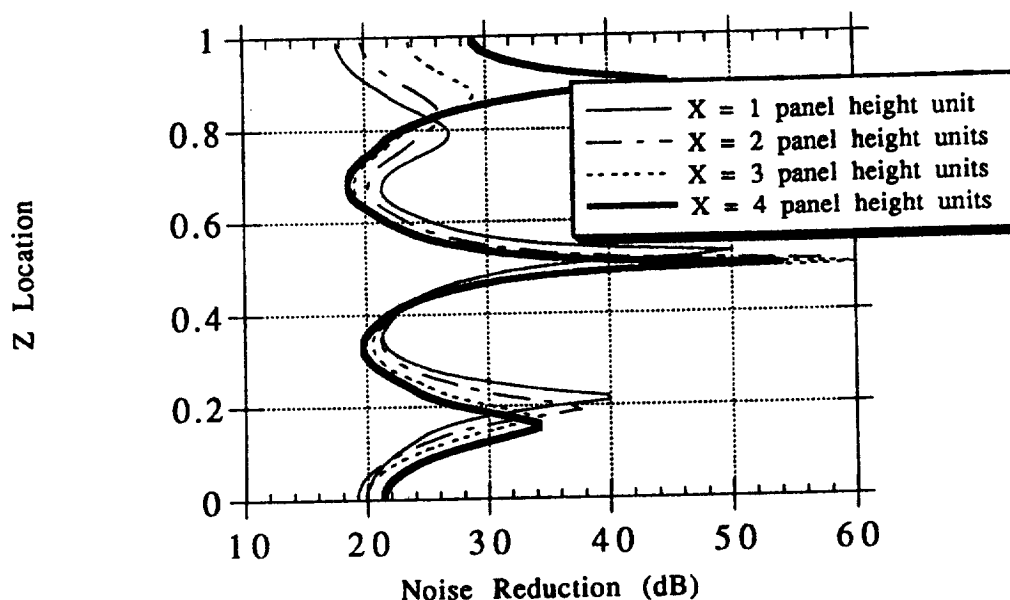


Figure 3.3.17d: Cross sectional noise reduction predictions at indicated X locations for the short wavelength sweep parameters without external sweep.

Section 3.3.6: Comparison to the Two Panel Model

Having derived a complete acoustic solution for the model presented in this chapter, a comparison to the simplified model of Chapter 2 provides additional insight into the model limitations and strengths. Figures 3.3.18a and 3.3.18b show the Chapter 3 model reduced to a panel barrier containing only two panels with no exterior pressure sweeping effect, and comparisons are made in the far field (5 duct widths away) and near field (1 panel width, or a half duct width away). The far field parameters used in the Chapter 3 model in Figure 3.3.18a shows excellent agreement with the Chapter 2 model, except around nondimensional frequency $\omega = 3.0$ where the first mode turn on occurs for the 2 panel geometry. Figure 3.3.18b calculated in the near field shows similar disagreement at the mode turn-on frequency, except that the variation is larger since the calculation point is much closer to the panel barrier. These variances between the Chapter 2 model (which assumed all higher modes decayed and only the acoustic zero mode propagated) and the Chapter 3 model are to be expected. Note that the maximum noise reduction prediction for both models in the near and far fields is quite comparable. Another interesting case is the comparison of the two panel Chapter 2 model with the full 8 panel Chapter 3 model in the near and far fields, as shown in Figure 3.3.19. Including a panel barrier with more panels creates more mode turn ons, which lower the noise reduction predictions at the ART design frequency and causes more subtle variations in the noise reduction prediction as frequency increases due to higher mode turn ons.

Section 3.3.7: Miscellaneous Results

A number of additional effects may be explored with the full acoustic solution for the external pressure sweeping model. Figures 3.3.20a and 3.3.20b show noise reduction results for a high value

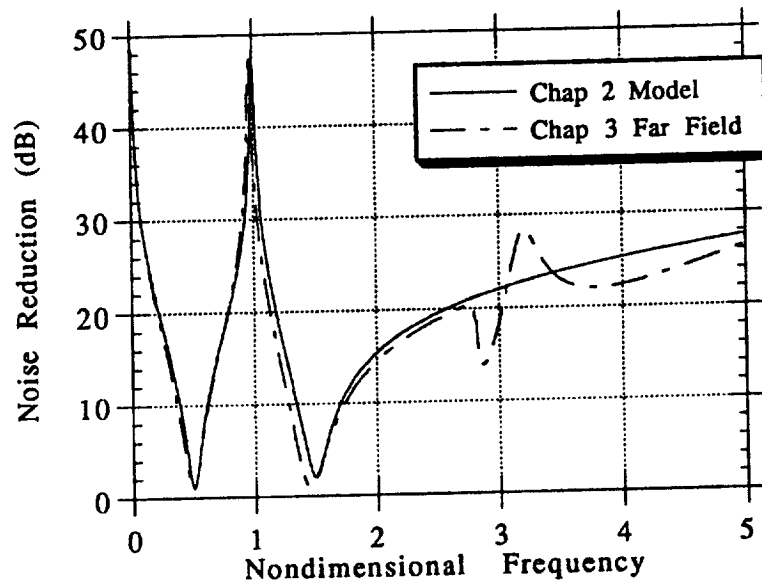


Figure 3.3.18a: Far field (5 duct widths) noise reduction predictions for the Chapter 2 model (with decay of higher modes) plotted with the Chapter 3 model including all modal contributions for the 2 panel configuration.

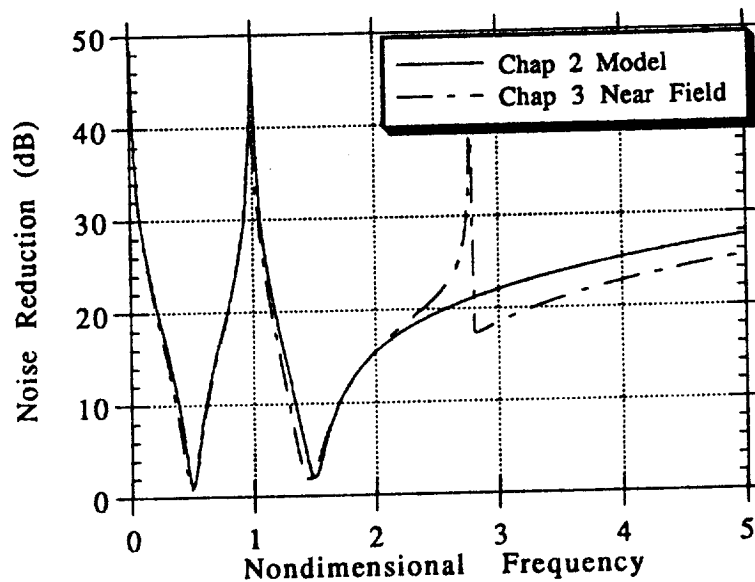


Figure 3.3.18b: Near field (1 panel width) noise reduction predictions for the Chapter 2 model (with decay of higher modes) plotted with the Chapter 3 model including all modal contributions for the 2 panel configuration.

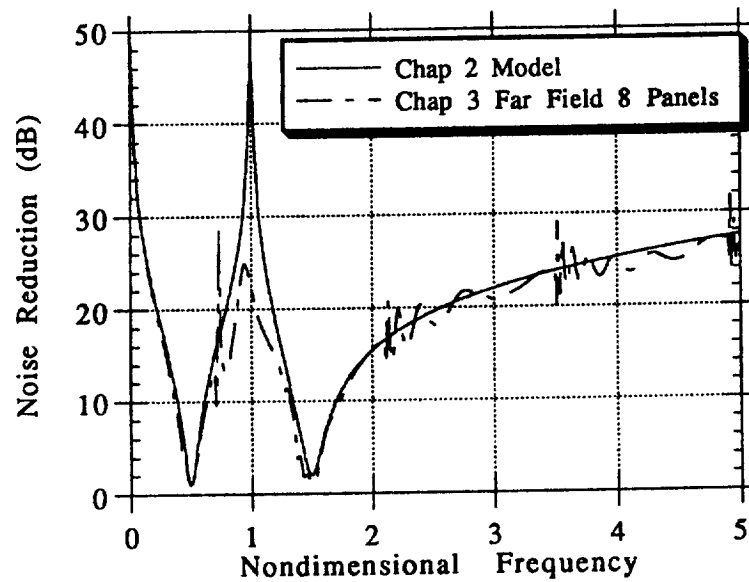


Figure 3.3.19a: Far field (5 duct widths) noise reduction predictions for the Chapter 2 model (with decay of higher modes) plotted with the Chapter 3 model including all modal contributions for the 8 panel configuration.

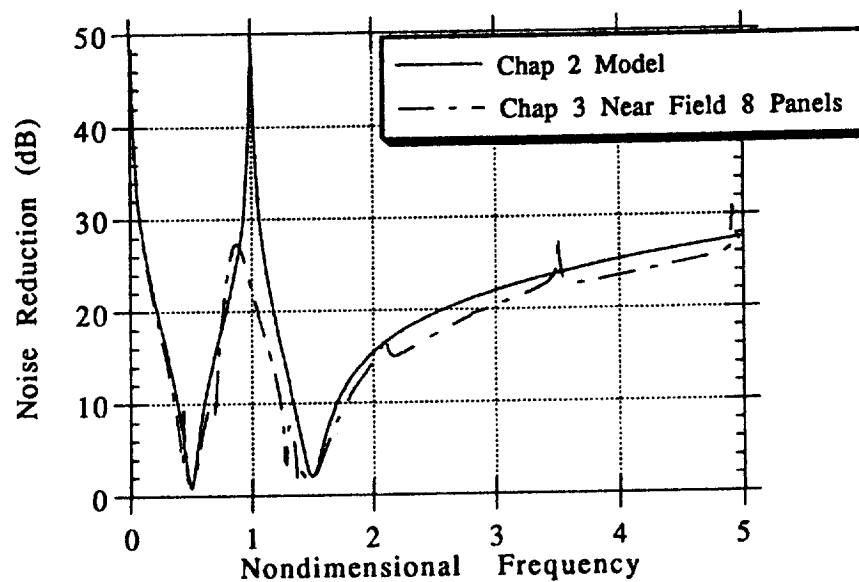


Figure 3.3.19b: Near field (1 panel width) noise reduction predictions for the Chapter 2 model (with decay of higher modes) plotted with the Chapter 3 model including all modal contributions for the 8 panel configuration.

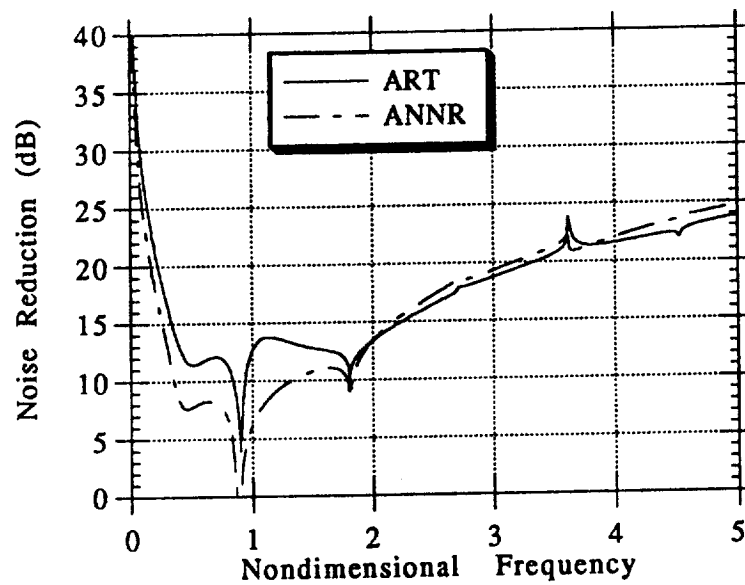


Figure 3.3.20a: High damping ratio noise reduction prediction for the long wavelength sweep case compared to the averaged noninteracting noise reduction prediction.

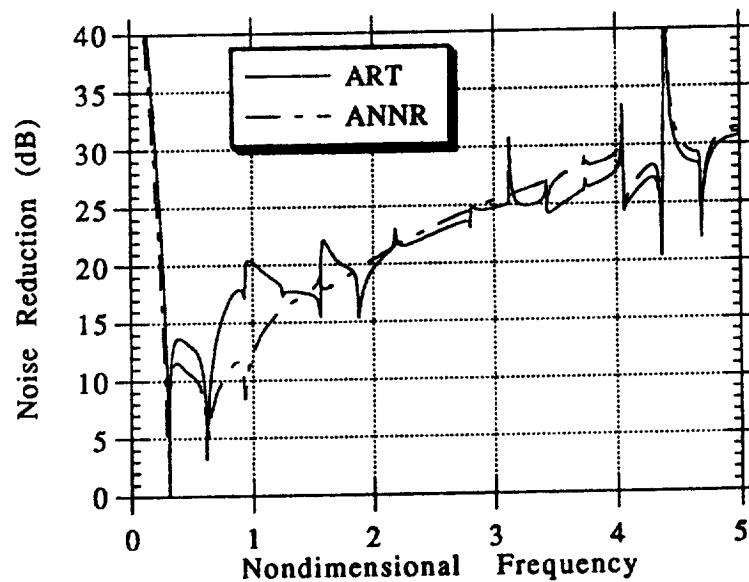


Figure 3.3.20b: High damping ratio noise reduction prediction for the short wavelength sweep case compared to the averaged noninteracting noise reduction prediction.

of panel damping ($\zeta = 0.4$) compared to the ANNR results for identical panels. Long wavelength parameter results are shown in Figure 3.3.20a; short wavelength parameter results are shown in Figure 3.3.20b. In both cases, ART performs about 5 to 7 dB better than uniform panels in the design frequency range around nondimensional frequency = 1.0. This again suggests that the ART concept might be implemented with more traditional noise reduction techniques such as increasing panel damping to achieve better quieting performance.

In practice, it is impossible to have exactly matching panel properties. Panel natural frequencies and damping ratios will always show some performance variations, although perhaps over a small margin. Figures 3.3.21a and 3.3.21b show the effect of this "detuning" on ART noise reduction, where panel mass ratios, natural frequencies, and damping ratios have been varied randomly by $\pm 10\%$ as shown in Table 3.3.3. In both the long and short wavelength cases, the ART tuning methodology is quite robust, and these tuning variations cause no negative effects. There are some additional ART noise cancellation peaks seen in Figures 3.3.21a and 3.3.21b due to the ART effect occurring between detuned parameters. For example, in Figure 3.3.21a, there is an ART peak occurring at a nondimensional frequency just above the low natural frequency panel resonance minimum. This ART peak is a result of the interaction of the panels with resonance frequencies of 0.45 and 0.55 respectively. In all other respects, the ART noise reduction performance is essentially the same as the cases where only uniform panels are used.

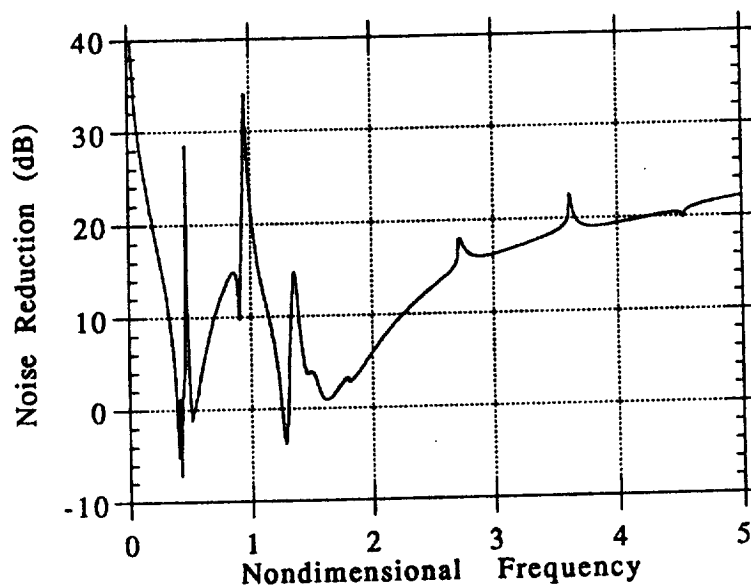


Figure 3.3.21a: Noise reduction calculation at Location A for detuned panel properties in the long wavelength sweep case.

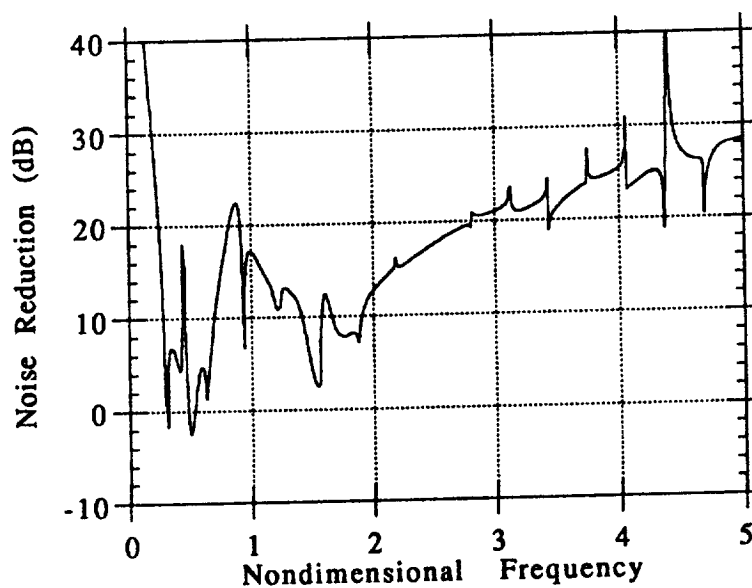


Figure 3.3.21b: Noise reduction calculation at Location A for detuned panel properties in the short wavelength sweep case.

Table 3.3.3: Panel detuned parameter values used in Figure 3.3.22.

panel #	MR_i	ω_n	ζ_i
1	0.9	0.55	0.011
2	0.603	1.35	0.011
3	1.1	0.45	0.009
4	0.737	1.65	0.009
5	1.1	0.55	0.011
6	0.737	1.35	0.009
7	0.9	0.45	0.011
8	0.603	1.65	0.009

“Off-tuning” considerations are another topic which may be explored with the Chapter 3 model. Recall that any number of panels may be used in the model, and these panels may be tuned in any manner. Occasions may arise in real structures where it will be impossible to have an even number of panels, and hence complete ART panel pairs. Figure 3.3.22 shows noise reduction predictions for a barrier with 9 panels comprising four ART tuned pairs, and one extra panel with a natural frequency of $\omega = 0.5$ placed at the uppermost portion of the panel barrier. Sweep propagation remains in the +z direction. Figure 3.3.22a shows the noise reduction predictions for the long sweep wavelength parameters, and two cases are shown at the locations indicated in the legend. These positions correspond to locations which are symmetry opposite the duct centerline at $z = 0.5$. Note that the noise reduction prediction at the lower position ($x = 2.0, z = 0.06$) shows an additional noise reduction peak. Higher frequency noise reduction is also enhanced at the lower location. Similar results may be seen in Figure 3.3.22b, where the short wavelength parameters have been employed. Figures 3.3.22c and 3.3.22d show cross sectional noise reduction predictions at $\omega_{ART} = 1.0$ for the long and short wavelength parameters cases. These figures may be directly compared to Figures 3.3.17c and 3.3.16d, which

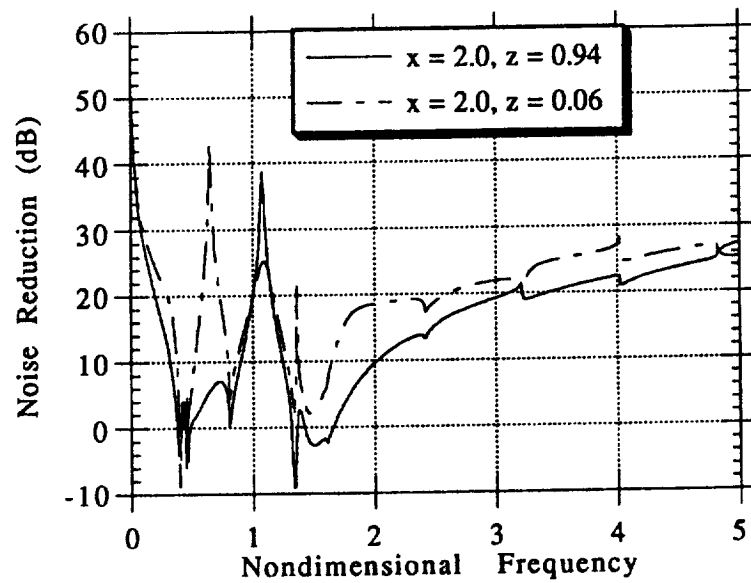


Figure 3.3.22a: Modelling a panel wall irregularity for the long sweep wavelength case.

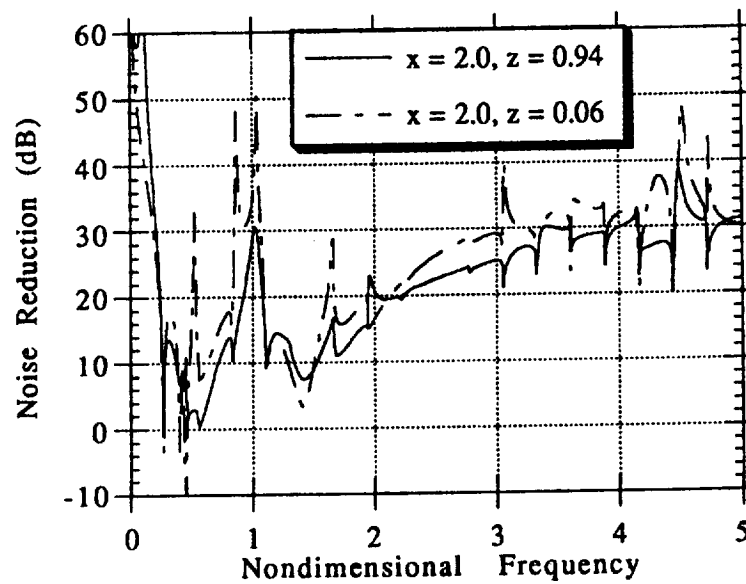


Figure 3.3.22b: Modelling a panel wall irregularity for the short sweep wavelength case.

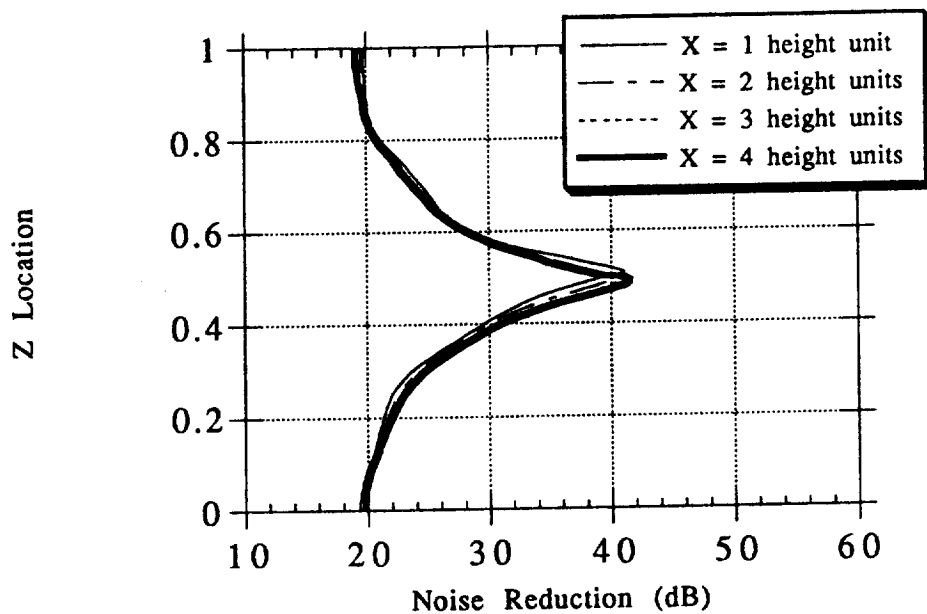


Figure 3.3.22c: Cross sectional noise reduction predictions at indicated X locations for the long wavelength sweep case with panel tuning irregularities. Calculation at $\omega_{ART}=1.0$.

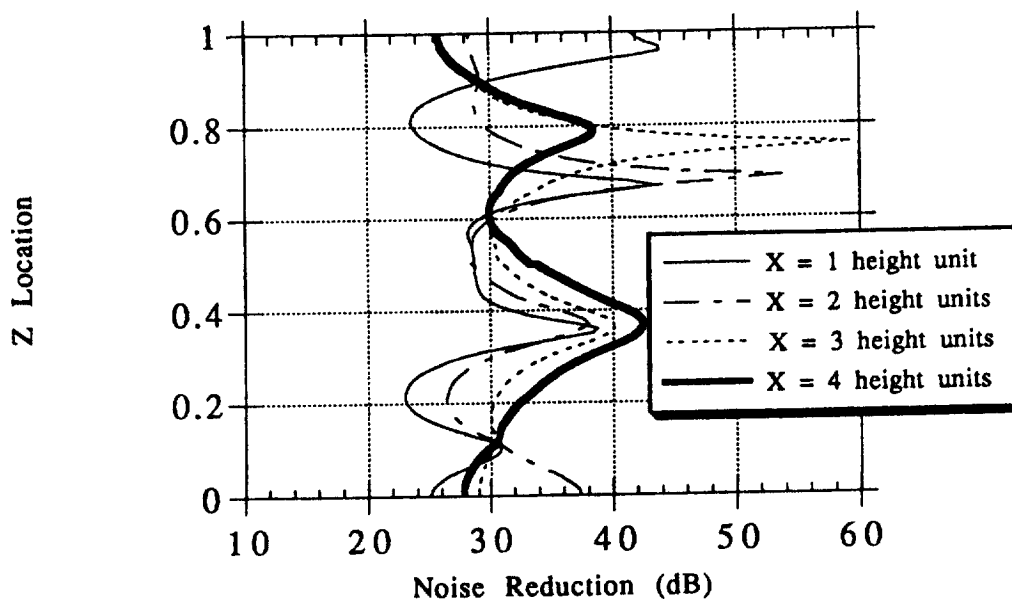


Figure 3.3.22d: Cross sectional noise reduction predictions at indicated X locations for the short wavelength sweep case with panel tuning irregularities. Calculation at $\omega_{ART}=1.0$.

show the same calculation for an even number of ART tuned pairs. In the long wavelength case (Figures 3.3.17c and Figure 3.3.22c), the use of an extra panel has increased the minimum noise reduction found in the duct by about 5 dB, and increased the maximum noise reduction by 2 dB. Slightly more impressive results may be seen in the short wavelength parameters case (Figures 3.3.17d and 3.3.22d). In the latter example, the noise reduction calculation at 4 panel widths downstream has increased by about 10 dB at some locations, although absolute maximum noise reductions have decreased slightly. This demonstrates the complex interaction of the panels in the panel barrier and the sound fields which are produced as a result of the panel motions, and implies that some noise reduction gain may be achievable by considering "off-tuning" possibilities.

Recall that the long wavelength parameters (from the aircraft quoted by Wilby and Wilby²⁴) are obtained based on a skin thickness of 0.0625". The short wavelength parameters (obtained from a study by Kuntz and Prydz²⁵) assume a skin thickness of 0.040". Figure 3.3.23 is used to compare the noise reduction predictions for the long and short sweep wavelength parameters with the two different apparent mass to panel mass ratios. Mass domination is a high frequency concept due to the $i m \omega$ component of the panel impedance formula expressed by Equation (2.2.3). As shown in Figure 3.3.23a and 3.3.23b, this extra mass is responsible for about a 5 dB increase in noise reduction at high frequencies, and about a 2-3 dB difference at the ART design frequency.

Four panel tuning is also a possibility for the model developed in this chapter. Figure 3.3.24a shows noise reduction predictions for four ART-tuned panels compared to identical panels. This long wavelength four panel ART tuning sweep case predicts increases in noise reduction of about 35, 5, and 5 dB at the three ART design frequencies of $\omega = 1.0, 2.0$, and 3.0 . This four panel tuning is not as successful in the case with the short

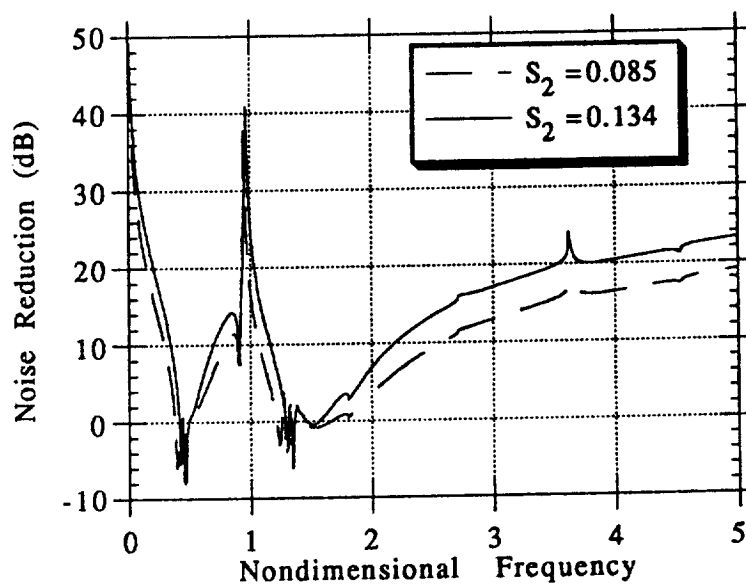


Figure 3.3.23a: Comparison of noise reduction predictions with two apparent mass loading values for the long wavelength parameters sweep case.

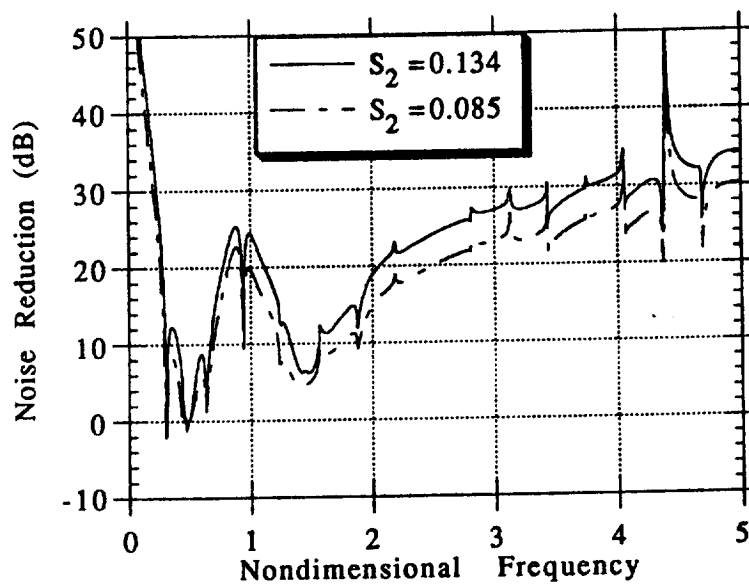


Figure 3.3.23b: Comparison of noise reduction predictions with two apparent mass loading values for the short wavelength parameters sweep case.

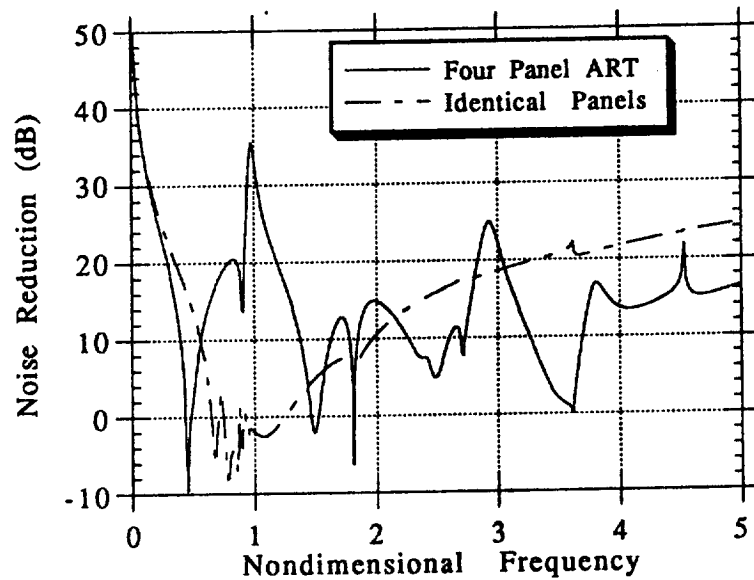


Figure 3.3.24a: Noise reduction calculation for four panel ART tuned and identical panels with long wavelength external sweep calculated at Location A in Figure 3.2.1.

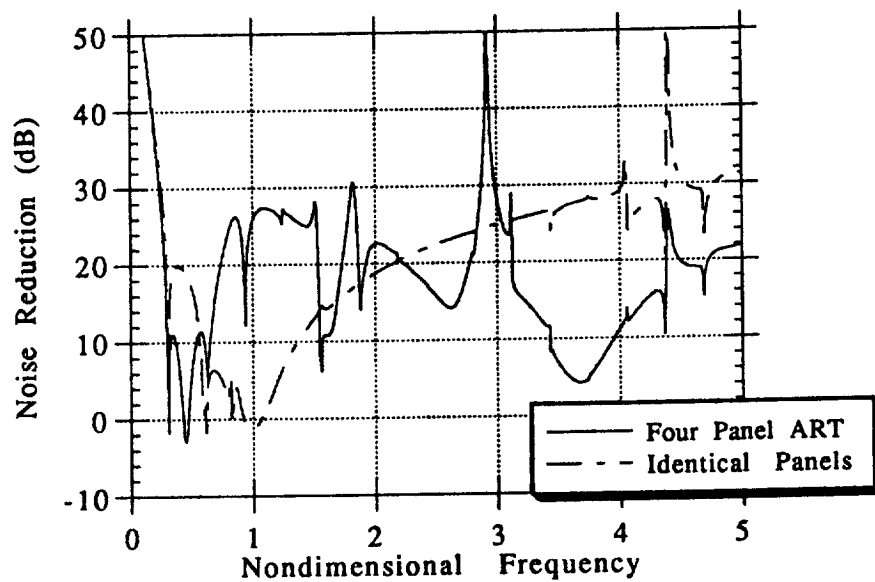


Figure 3.3.24b: Noise reduction calculation for four panel ART tuned and identical panels with short wavelength external sweep calculated at Location A in Figure 3.2.1.

wavelength parameters, however, as shown in Figure 3.3.24b, where the increases are about 25, 4, and 1 dB respectively. Recall that the short wavelength parameters are operating in a higher frequency regime, and as such, are less effective. Figures 3.3.24a and 3.3.24b show that while the ART concept can produce $N-1$ noise cancellation effects for N different panel tunings in the near field, it is inherently more effective at lower frequencies where the panel systems are more acoustically compact; as such, the two panel tuning is more worthwhile. Additionally, existing noise reduction methods tend to work better at higher frequencies and are less effective at lower frequencies. It is in the latter frequency domain where the employment of the ART technique can achieve the most dramatic results.

Chapter 4

The General ART Panel Analysis

Section 4.1: Introduction

In the analyses presented thus far, panel impedances have been represented by the familiar relation

$$Z_{mi} = R_i + i \left(M_i \omega + \frac{S_i}{\omega} \right) \quad (4.1.1)$$

This mathematical statement of the panel dynamics assumes that the panel itself is represented by a rigid flat plate section; no higher structural modes are represented here. While this representation is analytically much easier to deal with, real panels attached to a stringer-rib frame are generally held in place using rivets, and this riveting creates a panel mode shape which is "bowed" to some degree depending upon the actual boundary condition. It is necessary to investigate the effect such panel mode shapes might have on ART performance. One particularly interesting possibility is the contribution of higher structural modes to the ART process.

Section 4.2: Analysis Derivation

The most general analytic configuration is shown in Figure 4.2.1. This geometry simply includes a standard four panel array,

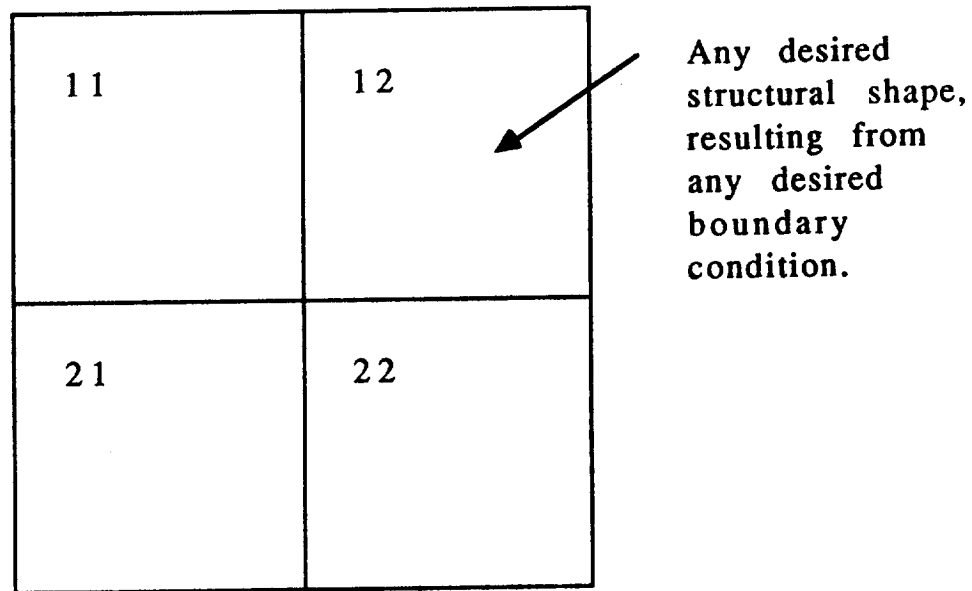


Figure 4.2.1: Configuration for ART
Real Panel Analysis

two panels on top and two panels on the bottom. Four panels for each identical panel subsystem have been chosen as a convenient number for equation derivation, but in reality, any rectangular array of panels may be considered. For the present case, panels are numbered in the standard matrix-like notation as shown. Note that no restriction has been placed on the boundary conditions of each panel. The latter assumption allows the analysis to proceed most generally, and at a later appropriate time, the boundary conditions will be chosen through specification of the appropriate structural mode shapes for the panels. The panel array is considered to be one subsystem mounted on an infinite wall composed of infinitely many panel subsystems. An anechoic termination is initially assumed beyond the wall.

To formulate the governing equations, consider panel 11 (note that this is an arbitrary choice). A general acoustic velocity function may be defined as

$$u(x,y,z,t) = \sum_i \sum_j U_{ij} \psi_{ij}(y,z) e^{i(\omega t - k_{xij}x)} \quad (4.2.1)$$

where the subscript indices i and j refer to acoustic modes, and $\psi_{ij}(y,z)$ describes the spatial dependence of an acoustic modal function. U_{ij} are the corresponding complex acoustic modal velocity amplitudes. Note that the acoustic modes are assumed harmonic in time and propagating in the $+x$ direction. Similarly, a general acoustic pressure may be expressed as

$$p(x,y,z,t) = \sum_i \sum_j P_{ij} \psi_{ij}(y,z) e^{i(\omega t - k_{xij}x)} \quad (4.2.2)$$

with P_{ij} representing the complex pressure amplitude of acoustic mode ij . Note that the relationship

$$P_{ij} = \rho_o \frac{\omega}{k_{xij}} U_{ij} \quad (4.2.3)$$

may be defined as a consequence of the x -component of the momentum equation.

For the structural problem, the wall displacement may be denoted as

$$\xi_w(y,z,t) = \sum_p \sum_q A_{pq}^{11} \phi_{pq}^{11}(y,z) e^{i\omega t} \quad (4.2.4)$$

where A_{pq}^{11} is the complex structural modal amplitude for mode pq of panel 11 and ϕ_{pq}^{11} is the individual panel shape function for mode pq of panel 11. A convention is made here that superscripts will always refer to the plate location as per Figure 4.2.1;

subscripts will always refer to either acoustic modes using i and j , or structural modes using p and q . Note that the overall wall shape function ψ and the individual panel shape function ϕ are separable functions; that is, for panel 11,

$$\phi_{pq}^{11}(y,z) = \Phi_p(y) \Phi_q(z)$$

$$\psi_{pq}^{11}(y,z) = \Psi_p(y) \Psi_q(z)$$

Differentiation of Equation (4.2.4) results in an expression for the wall velocity as

$$u_w = \frac{\partial \xi_w}{\partial t}(y,z,t) = \sum_p \sum_q i\omega A_{pq}^{11} \phi_{pq}^{11}(y,z) e^{i\omega t} \quad (4.2.5)$$

The acoustic and structural equations are linked at the panel/fluid interface, or at $x = 0$, where the acoustic velocity is equivalent to the wall velocity

$$u_{\text{acoustic}}(0,y,z,t) = u_{\text{wall}}(0,y,z,t) \quad (4.2.6)$$

This boundary condition encourages placement of Equation (4.2.1) equal to Equation (4.2.5) at $x = 0$, resulting in

$$\sum_i \sum_j U_{ij} \psi_{ij}(y,z) = \sum_p \sum_q i\omega A_{pq}^{11} \phi_{pq}^{11}(y,z) \quad (4.2.7)$$

The acoustic modes and the structural modes each form an orthogonal set with respect to themselves. However, the acoustic modes are not necessarily orthogonal to the structural modes. Application of orthogonality to Equation (4.2.7), and substituting $dS = dydx$ yields

$$\sum_i \sum_j U_{ij} \int_{S_{\text{total}}} \psi_{ij} \psi_{ij} dS_{\text{total}} = \sum_p \sum_q i\omega A_{pq}^{11} \int_{S_{11}} \psi_{rs} \phi_{pq}^{11} dS_{11} \quad (4.2.8)$$

The only modes of the left hand side of Equation (4.2.8) which survive are Ψ_{rs} . Therefore, with a change in indices,

$$U_{ij}^{11} = \frac{\sum_p \sum_q i\omega A_{pq}^{11} \int_{S_{11}} \psi_{ij} \phi_{pq}^{11} dS_{11}}{\int_{S_{\text{total}}} \psi_{ij}^2 dS_{\text{total}}} \quad (4.2.9)$$

By virtue of the momentum equation invoked to produce Equation (4.2.3), the complex acoustic pressure amplitudes may be expressed as

$$P_{ij}^{11} = \frac{\sum_p \sum_q ip\omega^2 \int_{S_{11}} \psi_{ij} \phi_{pq}^{11} dS_{11}}{k_{xij} \int_{S_{\text{total}}} \psi_{ij}^2 dS_{\text{total}}} A_{pq}^{11} \quad (4.2.10)$$

A convenient notational shorthand allows the expression of Equation (4.2.10) in a more compact form

$$P_{ij}^{11} = \sum_p \sum_q T_{ijpq}^{11} A_{pq}^{11} \quad (4.2.11)$$

where

$$T_{ijpq}^{11} = \left[\frac{ip\omega^2 \int_{S_{11}} \psi_{ij} \phi_{pq}^{11} dS_{11}}{k_{xij} \int_{S_{\text{total}}} \psi_{ij}^2 dS_{\text{total}}} \right] \quad (4.2.12)$$

Note an additional notational convention where S_p^{11} is the area of the single panel 11; its associated derivative dS_p^{11} in integral equations implies integration over the surface of panel 11. Similarly, S_{total} is the area of the entire panel array (equal to 4 times the panel width W times the panel height H); the associated derivative dS_{total} in integral equations implies integration over the entire panel assembly.

Lagrange's equations may be used to derive the equations of motion for the panel structure itself.²⁶ In general

$$M_{pq}^{11} \left[\left(A_{pq}^{11} e^{i\omega t} \right)_{tt} + 2\zeta_{pq}^{11} \omega_{npq}^{11} \left(A_{pq}^{11} e^{i\omega t} \right)_t \right] + \omega_{npq}^{11^2} \left(A_{pq}^{11} e^{i\omega t} \right) = Q_{pq}^{11} e^{i\omega t} \quad (4.2.13)$$

where M_{pq}^{11} is the generalized mass of mode pq of panel 11, ζ_{pq}^{11} is the damping ratio of mode pq of panel 11, ω_{npq}^{11} is the undamped natural frequency of mode pq of panel 11, and Q_{pq}^{11} is the sum total of all generalized forces acting on panel 11.

In particular, the generalized forces are worth further perusal. The right hand side of Equation (4.2.13) without the harmonic excitation $e^{i\omega t}$ may be expressed in general for any panel $\alpha\beta$ as

$$Q_{pq}^{\alpha\beta} = \sum_a \sum_b Q_{mpq}^{\alpha\beta,ab} + Q_E^{\alpha\beta} \quad (4.2.14)$$

where the term Q_E is the external forcing term, resulting from holding the wall fixed and observing the incident wave exhibit a hard wall reflection on panel $\alpha\beta$. The summation term is a convenient way of representing the generalized force contribution of all panels in the entire panelled system on panel $\alpha\beta$ where the analysis is focused. The notation represents the effect of the motion of mode pq of panel ab on panel $\alpha\beta$. In more general form, Equation (4.2.14) may be written for the four panel analysis configuration focusing on panel $\alpha\beta$ as

$$Q_{pq}^{\alpha\beta} = \sum_a \sum_b Q_{mpq}^{\alpha\beta,ab} + Q_E^{\alpha\beta} =$$

$$Q_{mpq}^{\alpha\beta,11} + Q_{mpq}^{\alpha\beta,12} + Q_{mpq}^{\alpha\beta,21} + Q_{mpq}^{\alpha\beta,22} + Q_E^{\alpha\beta} \quad (4.2.15)$$

Here the subscript m indicates a generalized force resulting from motion of panel ab on $\alpha\beta$. Equations (4.2.14) and (4.2.15) are a direct result of the concept of superposition applied to the panel subject to analysis.

Note that the generalized force on the right hand side of Equation (4.2.15) may be written as

$$Q_{mpq}^{\alpha\beta,ab} = \int \phi_{pq}^{\alpha\beta} p^{ab}(0,y,z) dS_p^{\alpha\beta} \quad (4.2.16)$$

$p^{ab}(0,y,z)$ may be replaced using Equation (4.2.2) as

$$p^{ab}(0,y,z) = \sum_i \sum_j P_{ij}^{ab} \psi_{ij}(y,z) dS_p^{ab} \quad (4.2.17)$$

Substitution of Equation (4.2.11) for P_{ij}^{ab} and back substitution of Equation (4.2.17) into (4.2.16) yields the generalized force on panel $\alpha\beta$ as a result of the motion of panel ab as

$$Q_{mpq}^{\alpha\beta,ab} = \int \phi_{pq}^{\alpha\beta}(y,z) \sum_i \sum_j \sum_c \sum_d T_{ijcd}^{ab} A_{cd}^{ab} \psi_{ij}(y,z) dS_p^{\alpha\beta} \quad (4.2.18)$$

Furthermore, substitution into Equation (4.2.18) yields

$$\int \phi_{pq}^{\alpha\beta} \sum_i \sum_j \psi_{ij} dS_p^{\alpha\beta} = \frac{k_{xij}}{i\rho_0\omega^2} \int \psi_{ij}^2 dS_{Total} * T_{ijpq}^{\alpha\beta} \quad (4.2.19)$$

where a panel independent quantity J_{ij} may be written as

$$J_{ij} = \frac{k_{xij}}{i\rho_0\omega^2} \int \psi_{ij}^2 dS_{\text{total}} \quad (4.2.20)$$

Therefore, the entire generalized force on $\alpha\beta$ will consist of one contribution from each panel, and may be most compactly represented as

$$\sum_a \sum_b Q_{mpq}^{\alpha\beta,ab} + Q_{Epq}^{\alpha\beta} = \sum_a \sum_b \left[\sum_c \sum_d A_{cd}^{ab} \sum_i \sum_j J_{ij} T_{ijpq}^{\alpha\beta} T_{ijcd}^{ab} + Q_{Epq}^{\alpha\beta} \right] \quad (4.2.21)$$

With the help of Equation (4.2.13) expressed in the most general form for any panel, the panel governing equations may be written as a linear system of the form

$$\sum_\alpha \sum_\beta \sum_p \sum_q \left[A_{pq}^{\alpha\beta} M_{pq}^{\alpha\beta} - \sum_a \sum_b \left[\sum_c \sum_d A_{cd}^{ab} \sum_i \sum_j J_{ij} T_{ijpq}^{\alpha\beta} T_{ijcd}^{ab} \right] \right] = Q_{Epq}^{\alpha\beta} \quad (4.2.22)$$

where $M_{pq}^{\alpha\beta}$ is the result of using Lagrange's equations to represent the panel dynamics,

$$M_{pq}^{\alpha\beta} = M_{pq}^{\alpha\beta} \left[\left(A_{pq}^{\alpha\beta} e^{i\omega t} \right)_{tt} + 2\zeta_{pq}^{\alpha\beta} \omega_{npq}^{\alpha\beta} \left(A_{pq}^{\alpha\beta} e^{i\omega t} \right)_t + \omega_{npq}^{\alpha\beta 2} \left(A_{pq}^{\alpha\beta} e^{i\omega t} \right) \right] \quad (4.2.23)$$

$Q_{Epq}^{\alpha\beta}$ is the external forcing, and the complex modal panel amplitudes $A_{pq}^{\alpha\beta}$ are the solutions to the linear system.

Expression of Equation (4.2.22) in nondimensional terms allows for the most general engineering interpretations. Note that in the combination of J_{ij} , $T_{ijpq}^{\alpha\beta}$, and T_{ijcd}^{ab} , some simplification occurs; also, the external generalized force is now stated explicitly in nondimensional terms, resulting in

$$\sum_{\alpha=1}^{yp} \sum_{\beta=1}^{zp} \sum_{p=1}^{sm} \sum_{q=1}^{sm} \left[\bar{v}_{\alpha\beta pq} - \sum_{a=1}^{yp} \sum_{b=1}^{zp} \sum_{c=1}^{sm} \sum_{d=1}^{sm} \bar{\eta}_{abcd} \alpha\beta pq = \bar{\kappa}_{\alpha\beta pq} \right] \quad (4.2.24)$$

where the nondimensional terms v , η , and κ are denoted by

$$v_{\alpha\beta pq} = \left(\frac{S_1}{S_2} \right) \bar{A}_{pq}^{\alpha\beta} \bar{M}_{pq}^{\alpha\beta} \left[\bar{\omega}_{npq}^{\alpha\beta^2} + 2i \zeta_{pq}^{\alpha\beta} \bar{\omega} \bar{\omega}_{npq}^{\alpha\beta} - \bar{\omega}^2 \right] \quad (4.2.25)$$

$$\bar{\eta}_{abcd} \alpha\beta pq = i \bar{\omega}^2 \bar{A}_{cd}^{ab} \sum_{i=0}^{am} \sum_{j=0}^{am} \bar{\phi}_{pq}^{\alpha\beta} \psi_{ij} dS_p^{\alpha\beta} \left(\frac{\omega_r}{k_{xij}} \right) \frac{\int \bar{\phi}_{pq}^{ab} \psi_{ij} dS_p^{ab}}{\int \psi_{ij}^2 dS_{total}} \quad (4.2.26)$$

$$\bar{\kappa}_{\alpha\beta pq} = \int \bar{\phi}_{pq}^{\alpha\beta} dS_p^{\alpha\beta} \quad (4.2.27)$$

Additionally, from Equation (4.2.24), yp is the number of panels in the model in the y direction (assumed to be equal to 2), zp is the number of panels in the z direction (assumed to be 2), and sm is the number of structural modes to be included in the calculation. From Equation (4.2.25), other nondimensional variables include

$$S_1 = \frac{\omega_r H}{c}$$

$$S_2 = \frac{\rho W H^2}{m_{11}}$$

where ω_r is a user-chosen reference frequency, usually set to the lowest ART cancellation frequency, H is the panel height, c is the speed of sound in air, ρ is the density of air surrounding the

panels, W is panel width, and m_{11} is the mass of panel 11 (a reference panel mass) as shown in Figure 4.2.1;

$$\overline{A}_{pq}^{\alpha\beta} \equiv \frac{\omega_r A_{pq}^{\alpha\beta} \rho c}{P_E}$$

is the complex nondimensional modal amplitude for mode pq of panel $\alpha\beta$, where P_E is the total external pressure on panel $\alpha\beta$ equal to $(2P_i - P_t)$. P_i is the incident pressure on the upstream panel side, and P_t is the transmitted pressure through the panel array. Other nondimensional relationships from Equation (4.2.25) are defined as follows:

$$\overline{M}_{pq}^{\alpha\beta} = \frac{m_{pq}^{\alpha\beta}}{m_{11}}$$

$$\overline{\omega}_{npq}^{\alpha\beta} \equiv \frac{\omega_{npq}^{\alpha\beta}}{\omega_r}$$

$$\overline{\omega} \equiv \frac{\omega}{\omega_r}$$

From Equation (4.2.26), note that am is the number of acoustic modes considered in the system. The nondimensional panel shape function is defined as

$$\overline{\phi}_{pq}^{\alpha\beta} \equiv \phi(\overline{y}, \overline{z}) \equiv \phi\left(\frac{y}{W}, \frac{z}{H}\right)$$

Note that the quantity

$$\left(\frac{\omega_r}{k_{xij}}\right)$$

is nondimensional; however, the actual form of k_{xij} cannot be determined until an appropriate choice for ψ_{ij} has been

determined; ω_r will then be used to nondimensionalize the frequency appearing in the k_{xij} .

Section 4.3: Recovering Some Familiar Results From the General Real Panel Analysis

A number of familiar example problems may be recovered from the real panel governing equations, either in dimensional form, such as Equation (4.2.22) with appropriate substitution for the elements $M^{\alpha\beta}_{pq}$, J_{ij} , $T^{\alpha\beta}_{ijpq}$, $Q_E^{\alpha\beta}_{pq}$, and Tab_{ijcd} , or in nondimensional form, such as Equations (4.2.24) through (4.2.27).

The most basic example which can be recovered is the case of a single panel in an infinite duct. After appropriate substitution, Equation (4.2.22), the general dimensional governing equation, reduces to (neglecting all summation limits temporarily)

$$\sum_{\alpha} \sum_{\beta} \sum_p \sum_q A^{\alpha\beta}_{pq} M^{\alpha\beta}_{pq} \left[\omega_{npq}^{\alpha\beta^2} + 2i \zeta^{\alpha\beta}_{pq} \omega \omega_{npq}^{\alpha\beta} - \omega^2 \right] - \sum_c \sum_d \sum_r \sum_s A^{cd}_{rs} \sum_i \sum_j \int \phi^{\alpha\beta}_{pq} \psi_{ij} dS_p^{\alpha\beta} \left(\frac{i\rho\omega^2}{k_{xij}} \right) \frac{\int \phi^{cd}_{pq} \psi_{ij} dS_p^{cd}}{\int \psi_{ij}^2 dS_{total}} = P_E \int \phi^{\alpha\beta}_{pq} dS_p^{\alpha\beta} \quad (4.3.1)$$

For a single panel in a duct, all acoustic modes except the one dimensional mode may be ignored; as such, $\psi_{ij} \rightarrow 1$ and $k_{xij} \rightarrow \omega/c$. For a flat panel, the mode shape $\phi \rightarrow 1$; all summations can be removed. From Equation (4.3.1), the ratio of the integral over dS_p^{cd} to the integral over $dS_{total} \rightarrow 1.0$ Equation (4.3.1) reduces to

$$A M \left[\omega_n^2 + 2i\zeta\omega\omega_n - \omega^2 \right] - iAWH\rho\omega c = P_E WH \quad (4.3.2)$$

Note that $i\omega A = U$, the panel velocity; also, $p_t = \rho c U$. M , the mass per unit area, may be replaced by m , the panel mass. From a fixed wall approximation, $P_E = 2P_I$. These manipulations yield

$$\frac{U}{WH} m \frac{[\omega_n^2 + 2i\zeta\omega\omega_n - \omega^2]}{i\omega} - P_t = 2P_I \quad (4.3.3)$$

The panel's mechanical impedance may be expressed in the familiar form

$$Z_m = R + i \left[m\omega - \frac{s}{\omega} \right] \quad (4.3.4)$$

where R is the mechanical damping and s is the spring constant. Also,

$$\zeta = \frac{R\omega_n}{2s} \quad (4.3.5)$$

Substitution of Equations (4.3.4) and (4.3.5) into (4.3.3) yields a familiar relationship for the ratio of transmitted to incident pressure in a duct as

$$\frac{P_t}{P_I} = \frac{2}{\frac{Z_m}{WH\rho c} - 1} \quad (4.3.6)$$

A second limit that can be recovered is the branch analysis relationship for the ART 4-panel geometry in a duct.²⁷ The branch analysis result gives the ratio of the transmitted pressure to the incident pressure across the panel barrier in a duct when only the one dimensional acoustic mode is considered. In dimensional form for an anechoic termination,

$$\frac{P_T}{P_I} = \frac{\Delta}{\Delta + \frac{2}{\rho c WH} Z_{11} Z_{12} Z_{21} Z_{22}} \quad (4.3.7)$$

where

$$\Delta = Z_{11} Z_{12} Z_{21} + Z_{11} Z_{12} Z_{22} + Z_{11} Z_{21} Z_{22} + Z_{12} Z_{21} Z_{22}$$

Note that all impedances in Equation (4.3.7) are mechanical impedances, of the form as shown in Equation (4.3.4). Again, $\psi_{ij} \rightarrow 1$, $k_{xij} \rightarrow \omega/c$, and the panel mode shape $\phi \rightarrow 1$. With respect to the dimensional governing Equation (4.3.1), summation over the panel indices $\alpha\beta$ and cd from 1 to 2 is now required. Following a similar logic as that described to derive the governing equation for a single panel in a duct, Equation (4.3.1) will reduce to a system of four nondimensional equations of the form

$$\bar{U}_{11} \left[\left(\frac{S_1}{S_2} \right) \bar{Z}_{m11} + \frac{1}{4} \right] + \frac{\bar{U}_{12}}{4} + \frac{\bar{U}_{21}}{4} + \frac{\bar{U}_{22}}{4} + \bar{P}_T = 2$$

$$\frac{\bar{U}_{11}}{4} + \bar{U}_{12} \left[\left(\frac{S_1}{S_2} \right) \bar{Z}_{m12} + \frac{1}{4} \right] + \frac{\bar{U}_{21}}{4} + \frac{\bar{U}_{22}}{4} + \bar{P}_T = 2$$

$$\frac{\bar{U}_{11}}{4} + \frac{\bar{U}_{12}}{4} + \bar{U}_{21} \left[\left(\frac{S_1}{S_2} \right) \bar{Z}_{m21} + \frac{1}{4} \right] + \frac{\bar{U}_{22}}{4} + \bar{P}_T = 2$$

$$\frac{\bar{U}_{11}}{4} + \frac{\bar{U}_{12}}{4} + \frac{\bar{U}_{21}}{4} + \bar{U}_{22} \left[\left(\frac{S_1}{S_2} \right) \bar{Z}_{m22} + \frac{1}{4} \right] + \bar{P}_T = 2$$

(4.3.8(a-d))

where nondimensional velocities are denoted by

$$\bar{U}_{ij} = \frac{U_{ij} \rho c}{P_I}$$

and nondimensional impedances are given by

$$\bar{Z}_{mij} = \overline{MR}_{ij} \bar{\omega}_{ij} \left[2\zeta_{ij} + i \left(\frac{\bar{\omega}}{\bar{\omega}_{ij}} - \frac{\bar{\omega}_{ij}}{\bar{\omega}} \right) \right]$$

Additionally, mass ratios are defined as

$$\overline{MR}_{ij} \equiv \frac{m_{ij}}{m_{11}}$$

and

$$\bar{P}_t \equiv \frac{P_t}{P_I}$$

Other relationships have been defined previously. Finally, a fifth equation expresses the fact that the resultant nondimensionalized pressure ratio is an average of all nondimensional panel velocities; that is,

$$\frac{\bar{U}_{11}}{4} + \frac{\bar{U}_{12}}{4} + \frac{\bar{U}_{21}}{4} + \frac{\bar{U}_{22}}{4} - \bar{P}_t = 0 \quad (4.3.9e)$$

With the aid of the symbolic manipulation program *Mathematica*, Equations (4.3.9) can be solved for the unknowns U_{11} , U_{12} , U_{21} , U_{22} , and P_T . In nondimensional form, P_T is the equivalent of the dimensional branch analysis relationship shown in (4.3.7)

$$\bar{P}_t = \frac{\bar{\Delta}}{\bar{\Delta} + \left(\frac{S_1}{S_2} \right) \bar{Z}_{11} \bar{Z}_{12} \bar{Z}_{21} \bar{Z}_{22}} \quad (4.3.10)$$

where

$$\bar{\Delta} = \bar{Z}_{11} \bar{Z}_{12} \bar{Z}_{21} + \bar{Z}_{11} \bar{Z}_{12} \bar{Z}_{22} + \bar{Z}_{11} \bar{Z}_{21} \bar{Z}_{22} + \bar{Z}_{12} \bar{Z}_{21} \bar{Z}_{22}$$

Section 4.4: Structural Branch Analysis

The general solution of the governing Equations (4.3.1) for the real panel analysis would formulate as described below. The solution would be carefully formulated for a general set of mode shapes; this linear system (of the generic form $[A] x = [B]$) would be sized on the order of the (number of panels) * (number of modes per panel). Numerical solution would be required to obtain the normalized modal amplitudes x , which in turn would determine the normalized panel modal velocities. The $[B]$ matrix contains expressions composed of the exterior pressure loadings integrated over the particular panel limits (where the loading is applied) with its associated mode shape.

None of the latter issues presents any real problem; the major difficulty in the exact solution to this problem is the terms resulting from the fluid loading of the higher structural mode shapes on other panel modes. The $[A]$ matrix for the system would be constructed in the same manner as the governing equations for the Chapter 2 model were formulated; that is, the diagonal terms of the matrix would contain the panel modal impedances, and all terms would contain the generalized forces. The latter forces result from modal apparent mass loadings applied to each panel modal impedance (including the panel itself) from all structural mode apparent mass contributions of each plate in the array. For the Chapter 2 models with panels represented by a rigid flat plate, this procedure was somewhat tedious but nonetheless possible. In those problems, the flat rigid panel shapes presented an obvious symmetry with respect to the apparent mass loadings (generalized forces) which could be exploited. As shown in Figure 2.2.1 for flat rigid panels, the apparent mass loading on panel 12 resulting from the motion of panel 11 is the same as the loading on panel 11 due to the motion of panel 12. Such symmetry does not exist in the general real panel problem. Figure 4.4.1 displays this concept graphically, where the top diagram shows two adjacent panels

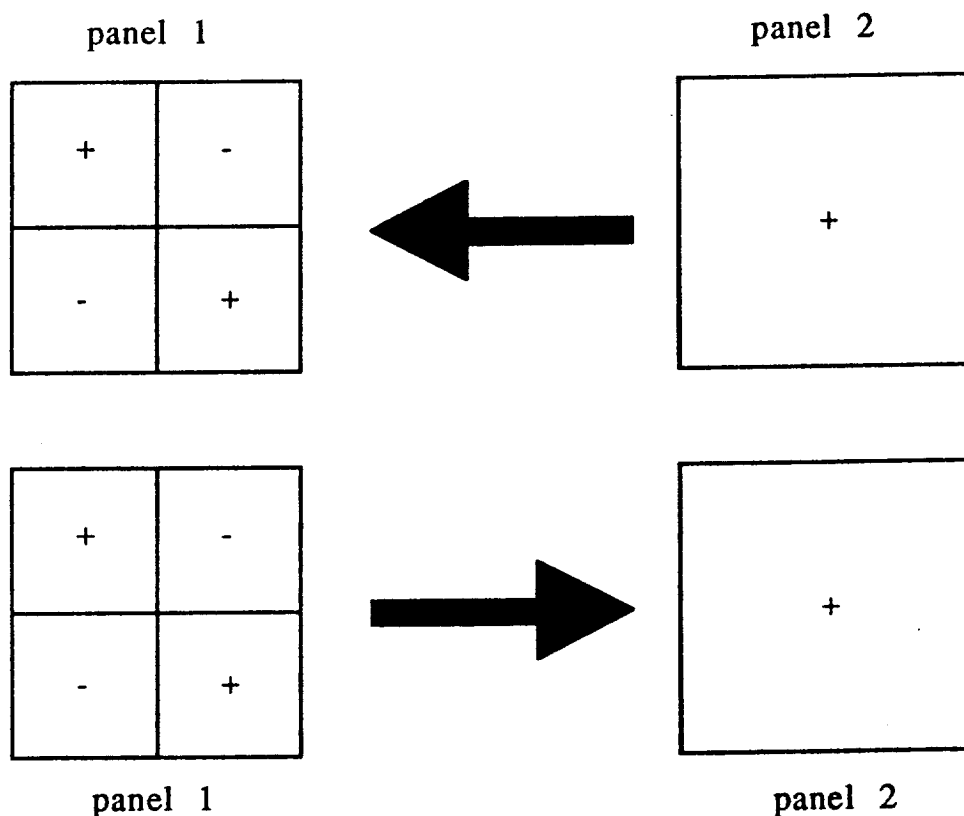


Figure 4.4.1: Dissymmetry of apparent mass modes with the inclusion of higher structural modes in the real panel analysis.

with pinned boundary conditions on all edges; panel 1 on the left has mode 22 only, while panel 2 on the right has mode 11 only. Now consider the generalized force on panel 2 mode 11 resulting from panel 1 mode 22. Looking left from panel 2, panel 1 (with mode 22) does not provide the same fluid loading as the situation shown in the lower portion of Figure 4.4.1, where the panel mode shapes are reversed. In the upper case shown in Figure 4.4.1, where upward panel deflections existed in the panel 1 mode 22 shape on the left, the lower portion of the figure shows that now downward panel deflections are present instead. Rephrased, panel 1 mode 22 does not load panel 2 mode 11 in the same manner as panel 1 mode 11 loads panel 2 mode 22. Thus symmetry cannot be exploited in the calculation of the general apparent mass

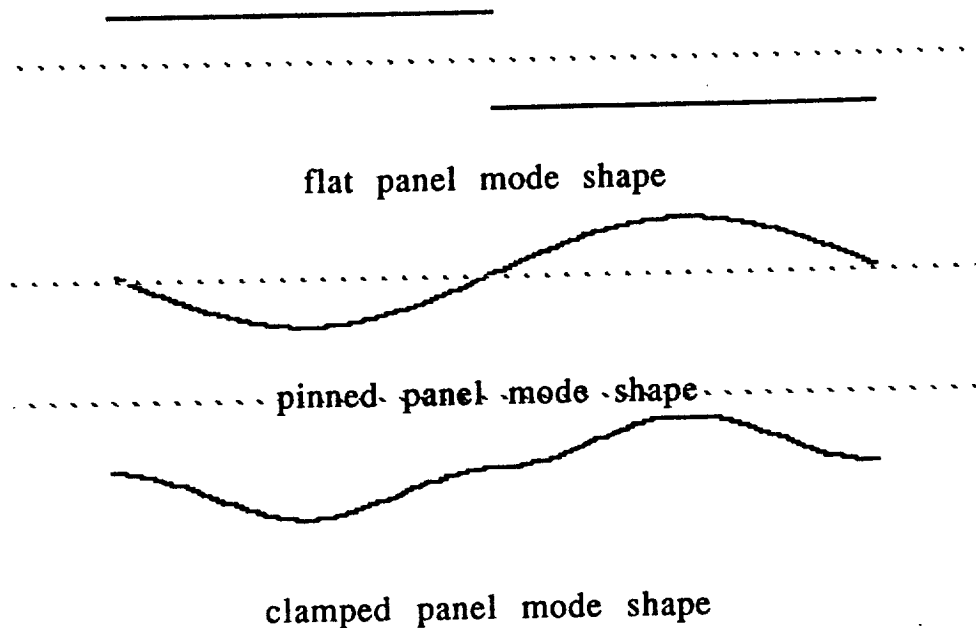


Figure 4.4.2: Qualitative apparent mass differences for flat, pinned, and clamped mode shapes.

loadings or generalized forces on the panels, and this is the major impediment to a full solution of the problem.

Another issue worthy of discussion is the general magnitude of the apparent masses for the various mode shapes which might be used. Figure 4.4.2 shows a side view of two panels with three possible mode shapes. The dotted line in each sketch represents the panel zero displacement line, and the panel mode shapes sketched represent the maximum deflected panel mode shapes which the surrounding air mass will load. The flat mode shapes shown in the top portion of Figure 4.4.2 have an idealized square displacement envelope, where much fluid is sloshed back and forth because the portions of the panels butted together in the middle are discontinuous and separate. The pinned mode shapes are piecewise continuous, as shown in the middle of Figure 4.4.2, and this overall panel displacement envelope results in less fluid sloshing back and forth between the panels. Finally, the lower portion of Figure 4.4.2 shows adjacent clamped panel sections,

where the panel displacement envelope is now totally continuous; even less mass is sloshed back and forth between the panels. The model presented in Chapter 2 used rigid flat plate mode shapes, which represents a conservative estimate of the apparent mass loading effects as described graphically in Figure 4.4.2. The Chapter 2 model indicated that while there is some effect due to the panel apparent mass loading, it is not severe unless the ratio of surrounding fluid mass to the panel mass is high. This latter parameter is S_2 as shown in Tables 2.2.1 and 3.3.1; if S_2 is less than 0.1, the apparent mass effects are not severe, and it can be predicted that the frequencies of maximum ART noise reduction will shift to only a slightly lower value due to the additional mass of the surrounding fluid in the vibrating panel-fluid system.

The branch analysis method is a reduced solution method which can be used to obtain a model which will predict the general acoustic behavior of real panels in an ART configuration. This approach will use only the one dimensional acoustic mode and as such, ignores apparent mass loading. However, it will permit an investigation of the effects of higher structural modes on ART tuning. The analysis follows a schematic identical to Figure 2.2.2, except now more branches are required to model the individual structural modes considered on each panel. A noise reduction in decibels may be described as

$$NR = -10 \log \left| \frac{P_0^B}{P_0^A} \right|^2 - 10 \log \left| \frac{P_M^B}{P_0^B} \right|^2 \quad (4.4.1)$$

where

$$\frac{P_M^B}{P_0^B} = \frac{Z_b \cos k[L - L_M] + ip_0 c \sin k[L - L_M]}{Z_b \cos kL + ip_0 c \sin kL} \quad (4.4.2)$$

Note that these quantities have been defined in Chapter 2 and carry similar meaning here. Note that Equation (4.4.2) describes the duct acoustics exclusive of the panel wall barrier (also equivalent to the branch analysis of Chapter 2). The remaining analysis portion requires the general expression of the pressure ratio P_0^B/P_0^A to include higher structural modes. Using the branch analysis procedure explained in Chapter 2, that pressure ratio may be determined as

$$\frac{P_0^B}{P_0^A} = \frac{\sum_{\alpha=1}^2 \sum_{\beta=1}^2 \sum_{p=1}^{\text{modes}} \sum_{q=1}^{\text{modes}} \frac{i\omega \left[\int \phi_{pq}^{\alpha\beta} dS_{\alpha\beta} \right]^2}{M_{pq}^{\alpha\beta}}}{\frac{S_A}{Z_0^B} + \sum_{\alpha=1}^2 \sum_{\beta=1}^2 \sum_{p=1}^{\text{modes}} \sum_{q=1}^{\text{modes}} \frac{i\omega \left[\int \phi_{pq}^{\alpha\beta} dS_{\alpha\beta} \right]^2}{M_{pq}^{\alpha\beta}}} \quad (4.4.3)$$

where

$$Z_0^B = \rho_0 c \frac{Z_b \cos kL + i\rho_0 c \sin kL}{\rho_0 c \cos kL + iZ_b \sin kL} \quad (4.4.4)$$

S_A is the overall cross sectional area of the duct, $dS_{\alpha\beta}$ corresponds to integration over the area defined by panel $\alpha\beta$. A generalized area coefficient may be described as

$$S_{pq}^{\alpha\beta} = S_{\alpha\beta} \frac{\int [\phi_{pq}^{\alpha\beta}] dS_{\alpha\beta}}{S_{\alpha\beta}} = S_{\alpha\beta} C_{\text{area}pq}^{\alpha\beta} \quad (4.4.5)$$

where $\phi_{pq}^{\alpha\beta}$ is the panel mode shape for panel $\alpha\beta$, mode pq , $S_{\alpha\beta}$ is the area of branch $\alpha\beta$, and

$$M_{pq}^{\alpha\beta} = M_{pq}^{\alpha\beta} \left[\left(A_{pq}^{\alpha\beta} e^{i\omega t} \right)_{tt} + 2\zeta_{pq}^{\alpha\beta} \omega_{npq}^{\alpha\beta} \left(A_{pq}^{\alpha\beta} e^{i\omega t} \right)_t + \omega_{npq}^{\alpha\beta^2} \left(A_{pq}^{\alpha\beta} e^{i\omega t} \right) \right] \quad (4.4.6)$$

where the usual convention follows that α and β refer to the matrix-like panel identification number (see Figure 2.2.1) and p and q index the individual panel modes. Note that α , β , p , and q again apply to the mass, natural frequency, modal amplitudes, and damping ratios of Equation (4.4.6). The generalized mass $M_{pq}^{\alpha\beta}$ in Equation (4.4.6) above may be defined as²⁸

$$M_{pq}^{\alpha\beta} = m_{pq}^{\alpha\beta} \frac{\int [\phi_{pq}^{\alpha\beta}]^2 dS_{\alpha\beta}}{S_{\alpha\beta}} \quad (4.4.7)$$

Note that nondimensionalization removes the modal amplitude coefficients shown in Equation (4.4.6) by converting them to nondimensional velocities as

$$i\bar{\omega} \bar{A}_{pq}^{\alpha\beta} = \bar{U}_{pq}^{\alpha\beta} \quad (4.4.8)$$

Using the nondimensional parameters defined earlier in this chapter and in Table 2.2.1, the results above may be expressed in nondimensional form as

$$\frac{P_0^B}{P_0^A} = \frac{\sum_{\alpha=1}^2 \sum_{\beta=1}^2 \sum_{p=1}^{\text{modes}} \sum_{q=1}^{\text{modes}} \frac{i\bar{\omega} S_2 \left[\int \bar{\phi}_{pq}^{\alpha\beta} d\bar{S}_{\alpha\beta} \right]^2}{4S_1 \bar{M}_{pq}^{\alpha\beta}}}{\frac{1}{\bar{Z}_0^B} + \sum_{\alpha=1}^2 \sum_{\beta=1}^2 \sum_{p=1}^{\text{modes}} \sum_{q=1}^{\text{modes}} \frac{i\bar{\omega} S_2 \left[\int \bar{\phi}_{pq}^{\alpha\beta} d\bar{S}_{\alpha\beta} \right]^2}{4S_1 \bar{M}_{pq}^{\alpha\beta}}} \quad (4.4.9)$$

where integrations are now calculated over nondimensional panel limits between -1 and +1. Also,

$$\overline{M}_{pq}^{\alpha\beta} = \overline{M}_{pq}^{\alpha\beta} \left[\overline{\omega}_{npq}^{\alpha\beta^2} + 2\zeta_{pq}^{\alpha\beta} \overline{\omega}_{npq}^{\alpha\beta} + \overline{\omega}^2 \right] \quad (4.4.10)$$

$$\overline{Z}_0^B = \frac{\overline{Z}_b \cos(\overline{\omega} S_1 S_4) + i \sin(\overline{\omega} S_1 S_4)}{\cos(\overline{\omega} S_1 S_4) + i \overline{Z}_b \sin(\overline{\omega} S_1 S_4)} \quad (4.4.11)$$

and

$$\frac{P_M^B}{P_0^B} = \frac{\overline{Z}_b \cos(\overline{\omega} S_1 (S_4 - S_3)) + i \sin(\overline{\omega} S_1 (S_4 - S_3))}{\overline{Z}_b \cos(\overline{\omega} S_1 S_4) + i \sin(\overline{\omega} S_1 S_4)} \quad (4.4.12)$$

Finally, the choice of panel mode shapes must be made. For flat panel mode shapes,

$$\overline{\phi} = 1$$

Pinned panel mode shapes are represented by

$$\overline{\phi}(\overline{y}, \overline{z}) = \sin(p\pi\overline{y}) * \sin(q\pi\overline{z})$$

with higher mode nondimensional resonance frequencies for simply supported square panels analytically denoted by²⁸

$$\overline{\omega}_n = \frac{m^2 + n^2}{2}$$

The presence of higher structural mode shapes for the pinned cases are added to the model in the order mode 11, mode 12, mode 22, mode 13, mode 23, and mode 33.

Clamped panel mode shapes may be represented according to Young by³⁰

$$\overline{\phi}(\overline{y}, \overline{z}) = \sum_{m=1}^p \sum_{n=1}^q A_{mn} \chi_m(\overline{y}) \chi_n(\overline{z})$$

where

$$\chi(\bar{y}) = [\cosh(\epsilon_m \bar{y}) - \cos(\epsilon_m \bar{y}) - \alpha_m (\sinh(\epsilon_m \bar{y}) - \sin(\epsilon_m \bar{y}))]$$

$$\chi(\bar{z}) = [\cosh(\epsilon_n \bar{z}) - \cos(\epsilon_n \bar{z}) - \alpha_n (\sinh(\epsilon_n \bar{z}) - \sin(\epsilon_n \bar{z}))]$$

Natural frequencies, amplitude coefficients, ϵ_m , and schematic panel mode shapes are as given in Figure 4.4.3 (reproduced from Leissa³¹). Depending on the choice of mode shapes, analytic or numerical integration is used to determine the nondimensional weighting coefficients defined as C_{area} and C_{mass} ; these are denoted as

$$C_{area}_{pq}^{\alpha\beta} = \frac{\left[\int \bar{\phi}_{pq}^{\alpha\beta} dS_{\alpha\beta} \right]}{S_{\alpha\beta}} \quad (4.4.13)$$

$$C_{mass}_{pq}^{\alpha\beta} = \frac{\left[\int \bar{\phi}_{pq}^{\alpha\beta} dS_{\alpha\beta}^2 \right]}{S_{\alpha\beta}} \quad (4.4.14)$$

It is important to note that this analysis says nothing about how many modes will be present on a given panel; that latter quantity is judiciously chosen when performing noise reduction calculations. For small panels such as those used in the analyses in Chapter 2 and 3 (aluminum panels 12" by 12"), only a few modes (and perhaps essentially only one mode!) might be present. Much larger panels might have additional modes present.

Mode	1	2	3	4	5	6
$\omega a^2 \sqrt{\frac{\rho}{D}}$	<ul style="list-style-type: none"> • 35.9866 • 35.99 	<ul style="list-style-type: none"> • 73.40 • 73.41 	<ul style="list-style-type: none"> • 108.22 • 108.27 	<ul style="list-style-type: none"> • 131.64 	<ul style="list-style-type: none"> • 132.18 • 132.25 	<ul style="list-style-type: none"> • 164.99 • 165.15
Nodal lines---						
Amplitude coefficient ^b	<ul style="list-style-type: none"> $A_{11} = 1.0000$ $A_{13} = 0.0142$ $A_{15} = 0.0020$ $A_{31} = 0.0142$ $A_{33} = -0.0031$ $A_{35} = -0.0009$ $A_{51} = 0.0020$ $A_{53} = -0.0009$ $A_{55} = -0.0004$ 	<ul style="list-style-type: none"> $A_{13} = 1.0000$ $A_{14} = 0.0101$ $A_{15} = 0.0020$ $A_{32} = 0.0406$ $A_{34} = -0.0022$ $A_{35} = -0.0007$ $A_{52} = 0.0070$ $A_{54} = -0.0011$ $A_{55} = -0.0005$ 	<ul style="list-style-type: none"> $A_{33} = 1.0000$ $A_{34} = 0.0326$ $A_{35} = 0.0073$ $A_{43} = 0.0326$ $A_{44} = -0.0019$ $A_{45} = -0.0010$ $A_{53} = 0.0073$ $A_{54} = -0.0010$ $A_{55} = -0.0006$ 	<ul style="list-style-type: none"> $A_{13} = 1.0000$ $A_{15} = 0.0085$ $A_{31} = -1.0000$ $A_{33} = -0.0141$ $A_{35} = -0.0085$ $A_{51} = 0.0141$ 	<ul style="list-style-type: none"> $A_{11} = -0.0280$ $A_{13} = 1.0000$ $A_{15} = 0.0055$ $A_{31} = 1.0000$ $A_{33} = 0.1267$ $A_{35} = 0.0118$ $A_{51} = 0.0055$ $A_{53} = 0.0118$ $A_{55} = -0.0018$ 	<ul style="list-style-type: none"> $A_{13} = -0.0406$ $A_{14} = -0.0105$ $A_{15} = -0.0017$ $A_{33} = 1.0000$ $A_{34} = 0.0560$ $A_{35} = 0.0141$ $A_{53} = 0.0238$ $A_{54} = -0.0011$ $A_{55} = -0.0009$

^a Work of Tomotika (ref. 4.30).

^b Work of Young (ref. 4.47).

^c Work of Iguchi (ref. 4.9).

Figure 4.4.3: Frequency parameters, amplitude coefficients, and schematic mode shape configurations showing modal lines for clamped modes as determined by Young (reproduced from Leissa).

Section 4.5: Structural Branch Analysis Results

Section 4.5.1: Mode Study and Comparison of ART and Identical Panels

As shown in Figure 4.4.3, Young determined mode shapes and natural frequencies for the first six modes of a clamped plate. While it is probably not feasible to expect six modes to exist on a square plate 12" by 12", the simulations were performed for all six modes for both clamped and pinned geometries to ascertain possible performance. Damping ratios ζ for all modes of all plates are set to a value of 0.01. Figure 4.5.1 through 4.5.6 show noise reduction predictions for these 6 cases. Figure 4.5.1 makes a comparison of identical and ART tuned panel noise reductions for flat (rigid) panel shapes (as predicted by the Chapter 2 branch analysis), pinned, and clamped mode shapes. The general trend here is that the greatest noise reduction is observed with clamped plates (presumably because they are stiffer); flat plates provide the least amount of noise reduction. The noise reduction predictions generally show about 3 dB noise reduction increase for pinned panels over flat rigid panels, and again about 3 dB noise reduction increase for clamped plates over pinned plates. These differences are observed at both low and high frequency limits. Thus the clamped panel appears more mass and stiffness dominated than the pinned plate, and the pinned plate is equally varied in stiffness and mass domination from the flat rigid plate. Another noticeable difference is that the ART frequency bandwidth at a constant noise reduction widens from flat to pinned to clamped plates. This widening is a typical result seen for reduced apparent mass loadings with the two panel and four panel Chapter 2 models. This noise reduction bandwidth increase results because less apparent mass is sloshed back and forth between the panels since less panel surface is moving. Fixed adjacent edges of the real panels also contribute to less apparent

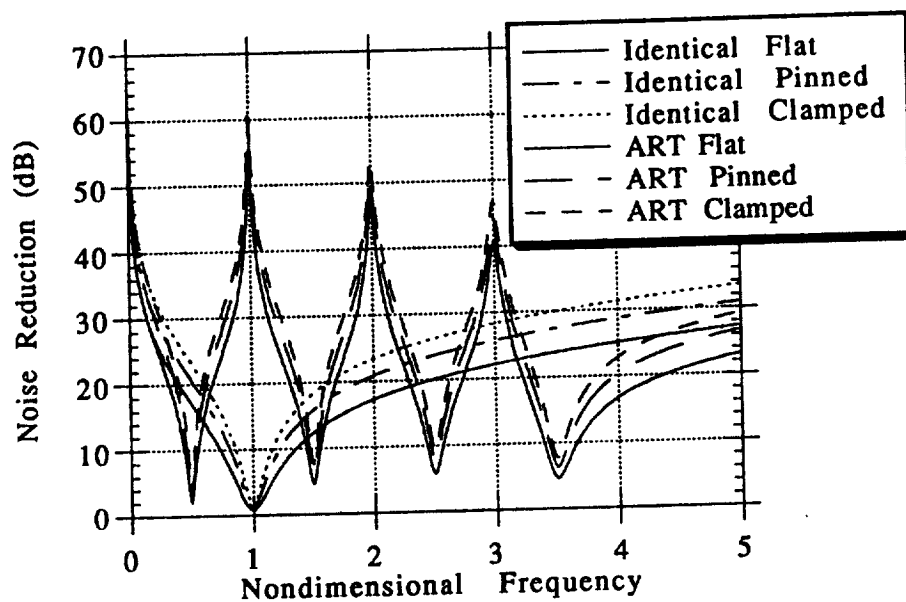


Figure 4.5.1: Noise reduction prediction for ART and identical panels using 1 structural mode and panel mode shapes as indicated.

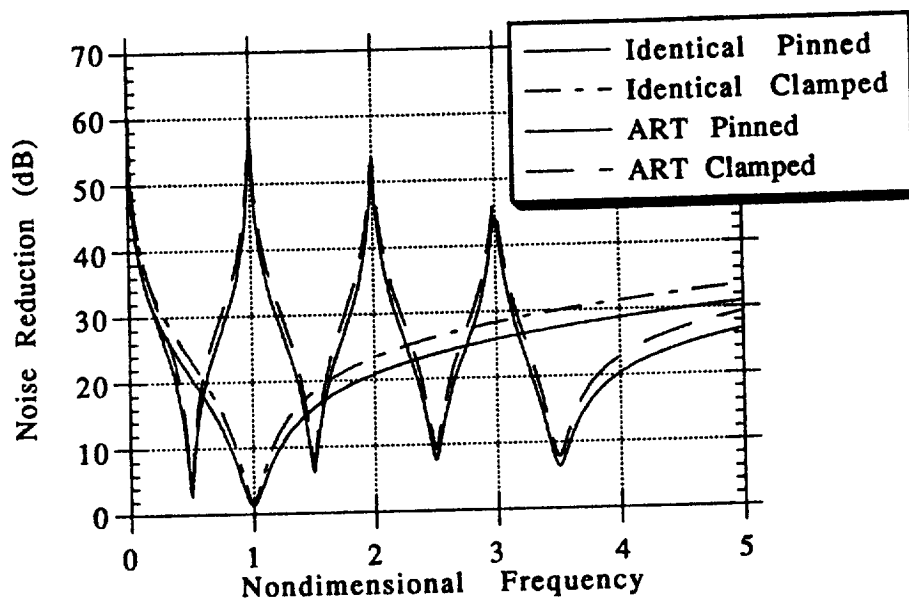


Figure 4.5.2: Noise reduction prediction for ART and identical panels using 2 structural modes and panel mode shapes as indicated.

mass sloshing as depicted graphically in Figure 4.4.2. Consequently it can be expected that the actual ART cancellation frequency will not be decreased (apparent mass loaded to reduce the ART noise reduction maximum) as much as indicated by the Chapter 2 model.

Figures 4.5.2 and 4.5.3 show noise reduction predictions for pinned and clamped panels with two and three structural modes acting. The value of the weighting coefficient C_{area} described by Equation (4.4.13) is zero for both the second and third structural modes for both clamped and pinned mode shapes, and as such these modes play no role in changing the noise reduction predictions. It is only when the fourth mode (mode 13) is added to the pinned calculation that any change is seen, and this change occurs in the identical panel calculation in Figure 4.5.4. Mode 13 has nonzero weighting coefficients, and the natural frequency is five times the mode 11 natural frequency. Thus a single plate section has effectively two resonance frequencies, and the ART effect can occur. This mode 13 natural frequency occurs at $\omega = 5.0$, and an ART cancellation is seen at $\omega \sim 4.75$. In the ART panels case, the lowest ART panel natural frequency is 0.5, and five times this frequency yields $\omega = 2.5$, which is another panel resonance frequency, so no net noise reduction effect is observed. The fourth mode for clamped plates also has a zero area weighting coefficient; no additional noise reduction contributions occur here. With the addition of the fifth mode (mode 23 for pinned and mode 5 as shown in Figure 4.4.3 for clamped), clamped panels also have higher modes playing an ART role, and additional noise reduction peaks are seen in Figure 4.5.5. The sixth structural mode (mode 33 pinned and mode 6 clamped as per Figure 4.4.3) plays no significant effect. Therefore, while it is theoretically possible to show the positive ART influence of higher structural modes for both pinned and clamped panel shapes, these ART contributions would be occurring at very high frequencies. Higher mode effects would be quite minimal, if existent at all.

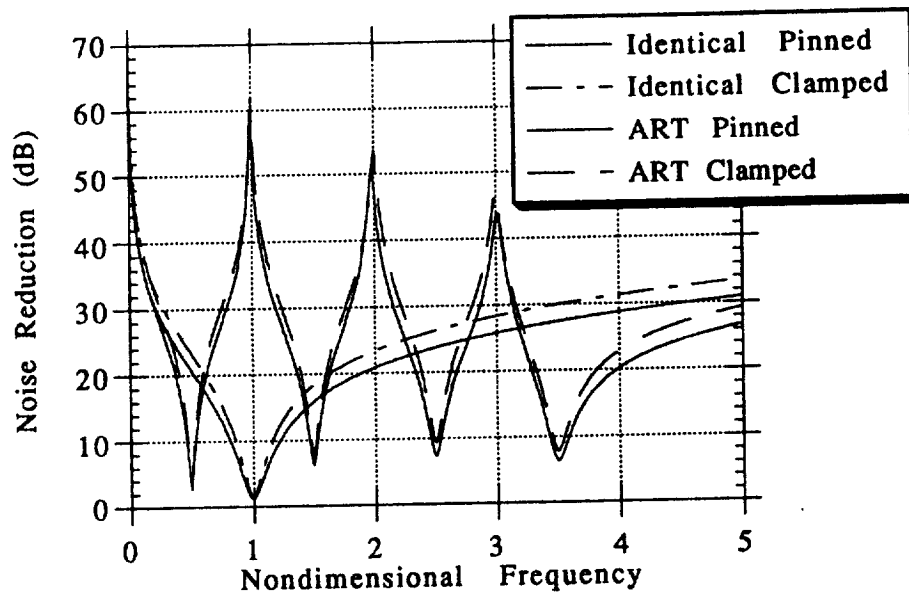


Figure 4.5.3: Noise reduction prediction for ART and identical panels using 3 structural modes and panel mode shapes as indicated.

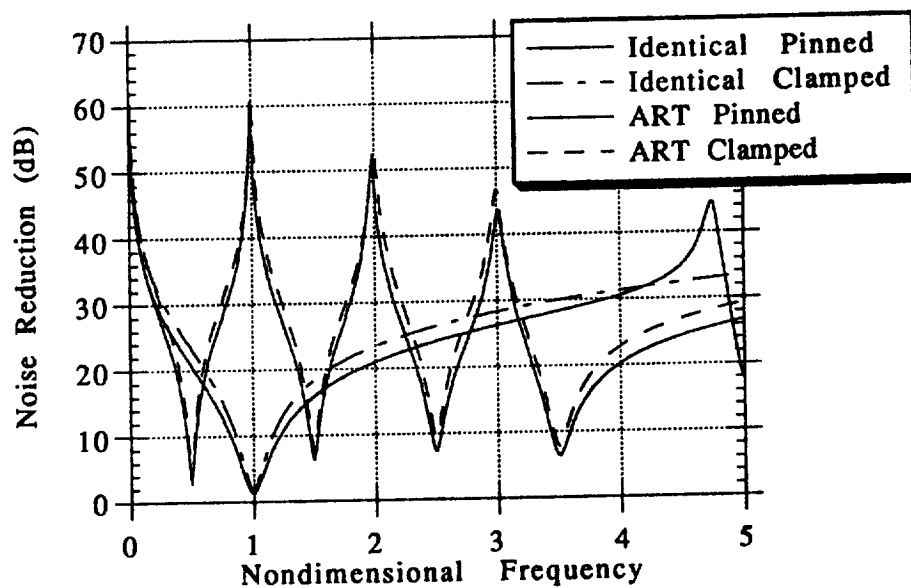


Figure 4.5.4: Noise reduction prediction for ART and identical panels using 4 structural modes and panel mode shapes as indicated.

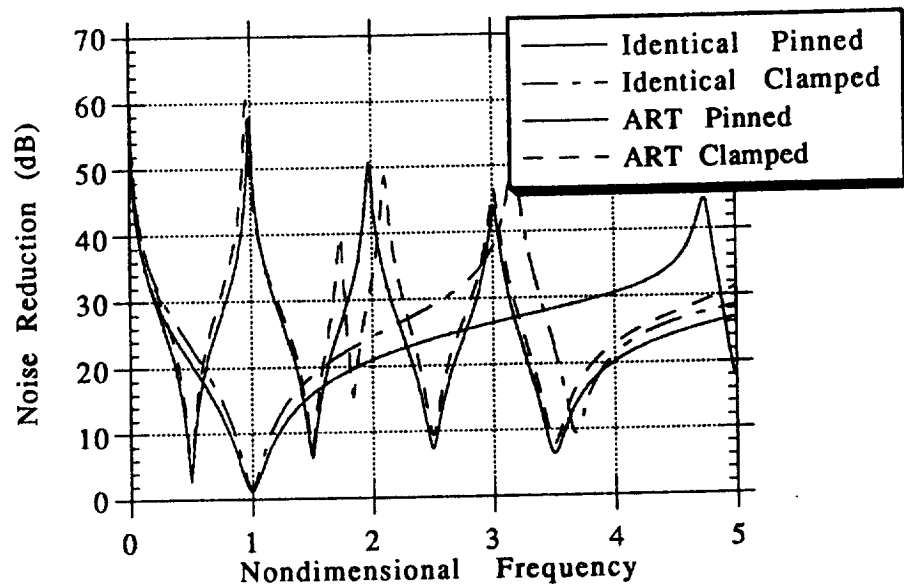


Figure 4.5.5: Noise reduction prediction for ART and identical panels using 5 structural modes and panel mode shapes as indicated.

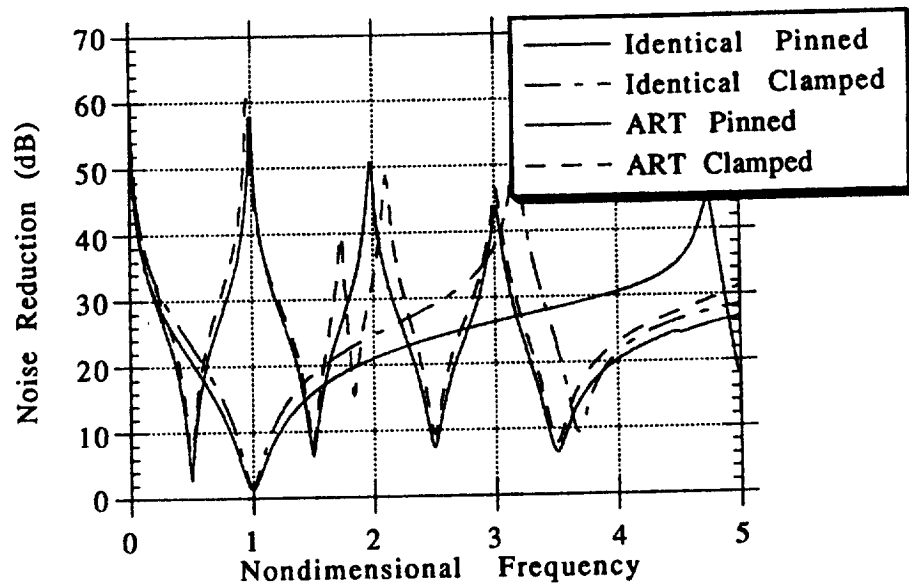


Figure 4.5.6: Noise reduction prediction for ART and identical panels using 6 structural modes and panel mode shapes as indicated.

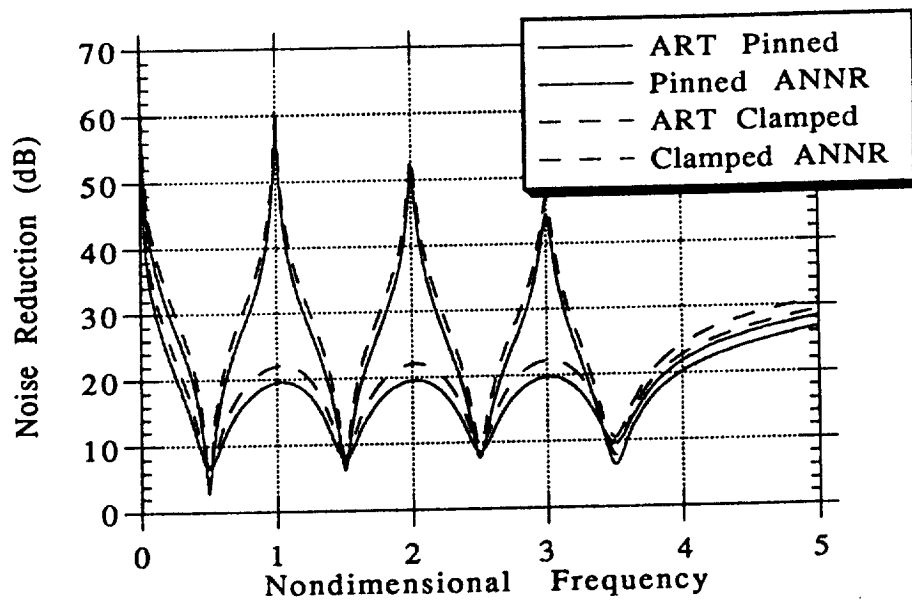


Figure 4.5.7: ANNR and ART noise reduction predictions using two structural modes and panel mode shapes as shown.

Finally, Figure 4.5.7 shows a comparison of noise reduction predictions using ART tuned pinned and clamped panel sections compared to the ANNR calculation for identical pinned and clamped panels. This prediction is very similar to previous ART and ANNR comparisons; clearly ART tuned panels are performing much better with at least a 15 to 20 dB noise reduction increase.

Section 4.5.2: Parameter Studies

Figures 4.5.8 through 4.5.11 show relative parameter study results; these results are very similar to those obtained using the Chapter 2 model. Figures 4.5.8a and 4.5.8b show a parameter study with increasing apparent mass loading for pinned and clamped mode shape panels, respectively. As reported earlier, increasing apparent mass loading by successive doubling of this

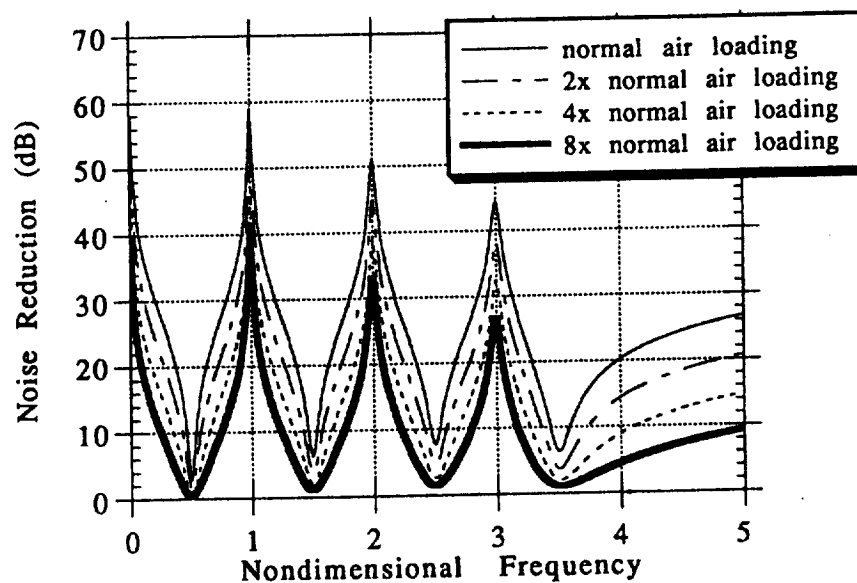


Figure 4.5.8a: Parameter studies varying the panel apparent mass loading as indicated for 1 structural mode with a pinned mode shape.

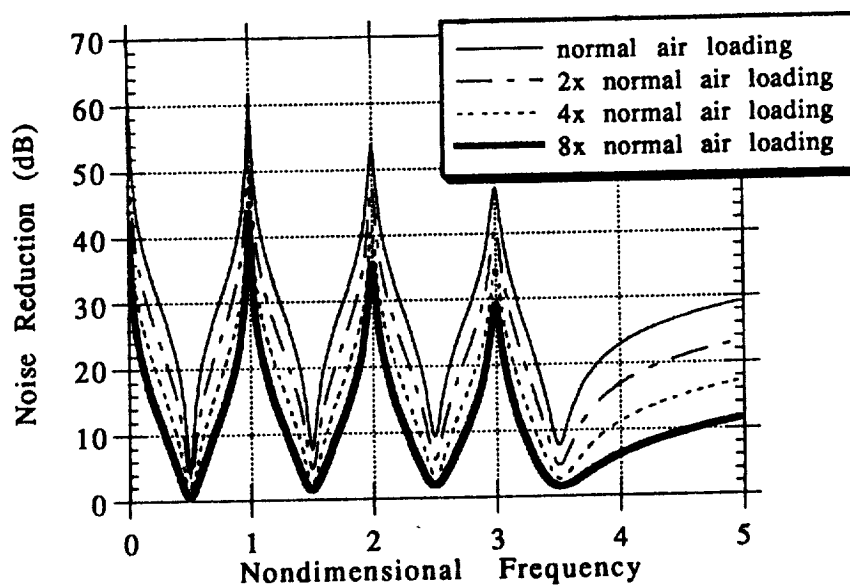


Figure 4.5.8b: Parameter studies varying the panel apparent mass loading as indicated for 1 structural mode with a clamped mode shape.

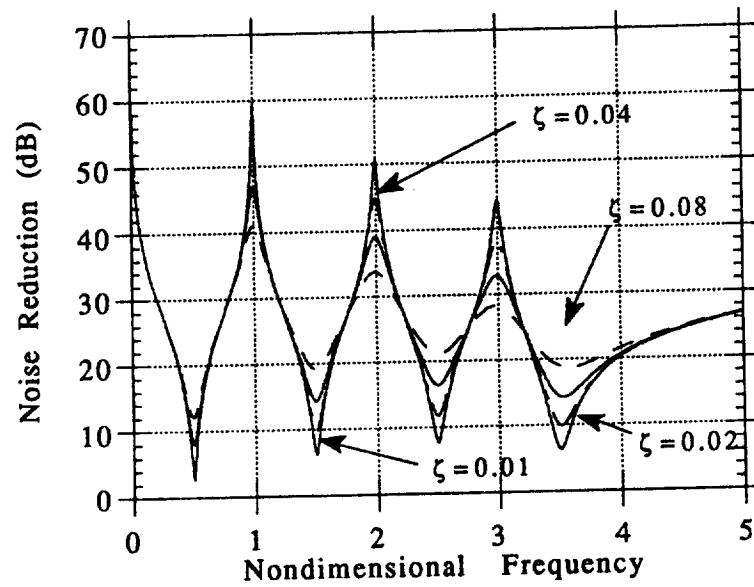


Figure 4.5.9a: Parameter studies varying the panel damping as indicated for 1 structural mode with a pinned mode shape.

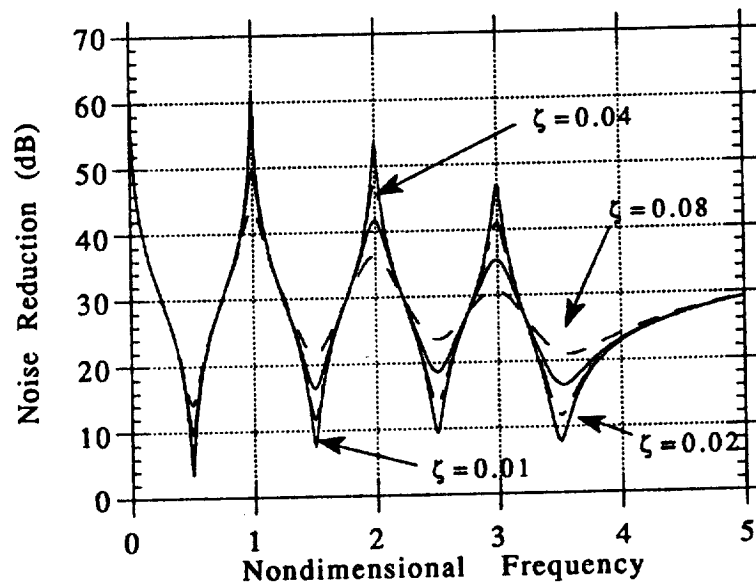


Figure 4.5.9b: Parameter studies varying the panel damping as indicated for 1 structural mode with a clamped mode shape.

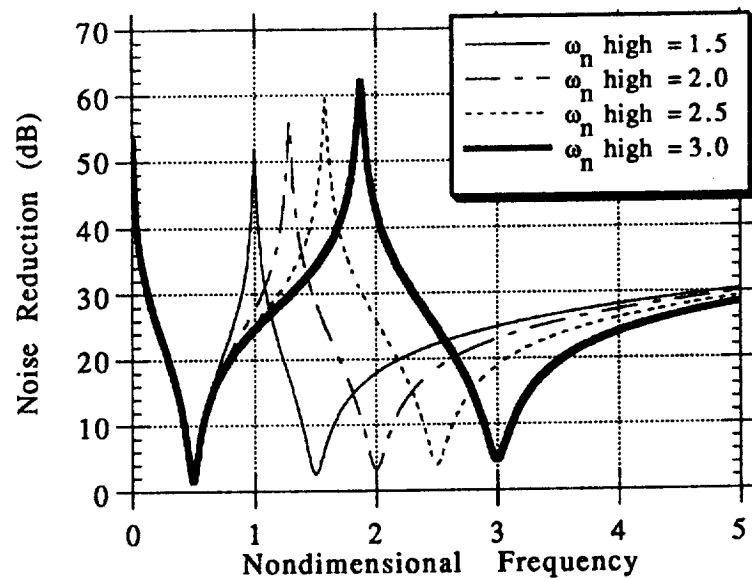


Figure 4.5.10a: Parameter studies varying the ART noise reduction bandwidth by increasing the higher panel natural frequency for 1 structural mode with a pinned mode shape.

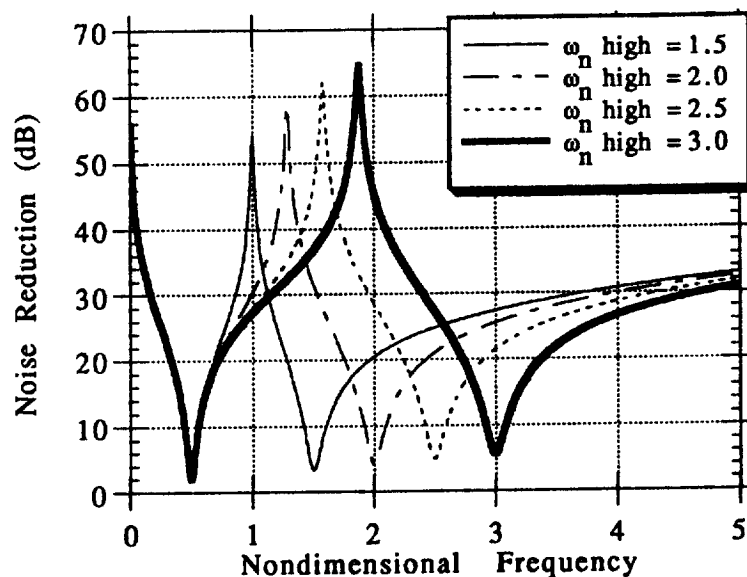


Figure 4.5.10b: Parameter studies varying the ART noise reduction bandwidth by increasing the higher panel natural frequency for 1 structural mode with a clamped mode shape.

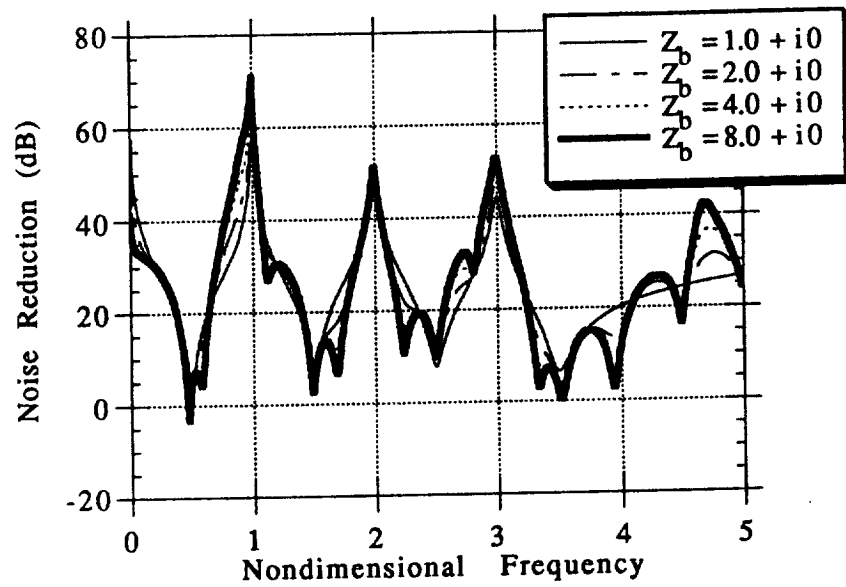


Figure 4.5.11a: Parameter studies varying duct termination impedance as indicated for 1 structural mode with a pinned mode shape.

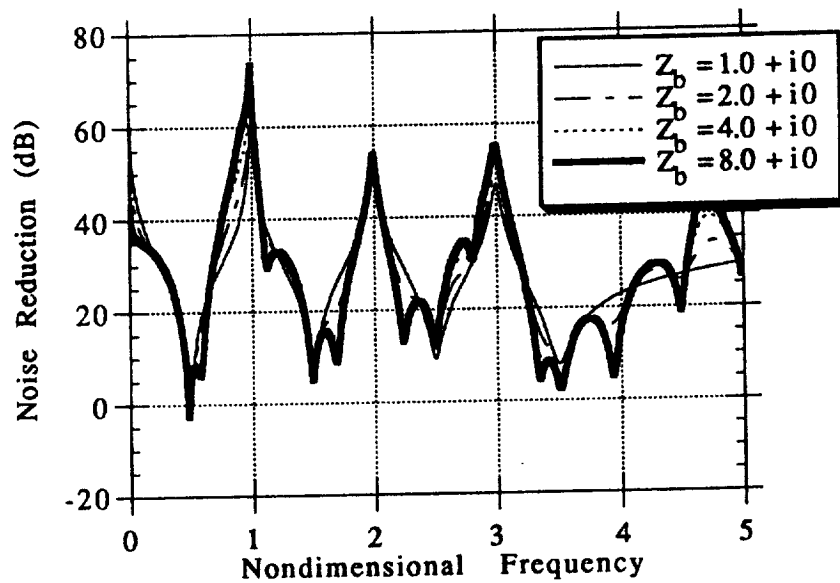


Figure 4.5.11b: Parameter studies varying duct termination impedance as indicated for 1 structural mode with a clamped mode shape.

parameter value tends to narrow the ART noise reduction bandwidth in more or less uniform amounts.

Panel damping ratios are varied as shown in Figures 4.5.9a and 4.5.9b for pinned and clamped panels, respectively. In both pinned and clamped cases, as the damping ratio is increased, noise reductions at panel natural frequencies are increased due to less acoustic transparency. Maximum noise reductions at the ART design frequencies are reduced as shown. However, the noise reduction bandwidth at about 25 dB has remained essentially constant for all damping ratios. This prediction implies that the ART concept will behave in a robust manner when applied with real panels sections.

Figures 4.5.10a and 4.5.10b show increasing ART noise reduction bandwidth by increasing the higher natural frequency panel resonance frequency as shown for pinned and clamped panels, respectively. Note also that the maximum amount of noise reduction obtained has increased as well. Increasing the higher natural frequency panel resonance frequency always provides better ART performance.

Figures 4.5.11a and 4.5.11b show variations in the duct termination impedance as indicated. As shown in Chapter 2, any termination impedance harder than $Z_b = 10 + 0i$ produces about the same noise reduction prediction. "Hardbox" frequencies again occur as predicted by Equation (2.4.4), and the ART method still provides noise reduction even with the presence of a reflected interior pressure wave from a duct termination impedance.

Chapter 5

Experimental Confirmation of the ART Concept

Section 5.1: Introduction

A series of experiments has confirmed the potential of Alternate Resonance Tuning for noise reduction applications in simple paneled structures. This chapter presents highlights of the various experiments conducted.

Section 5.2: Experimental Setup

Figure 5.2.1 shows an overall schematic of the experiment. A sound source driven by a pure tone generator or a white noise generator is coupled to a duct. A panel array test section is placed between the source-duct coupling and the downstream portion of the duct. Microphones monitor the overall sound pressure levels in decibels (dB) upstream of the panel test section (closer to the sound source) and downstream of the panel test section as shown in Figure 5.2.1. Additionally, a microphone can be placed in the center of the panel test section if the test section is a double wall configuration. Termination impedances available include anechoic and hard wall impedance values. Data shown herein considers only the anechoic termination impedance, since the ART effect is most clearly observed without the interference of a reflected wave from the downstream termination.

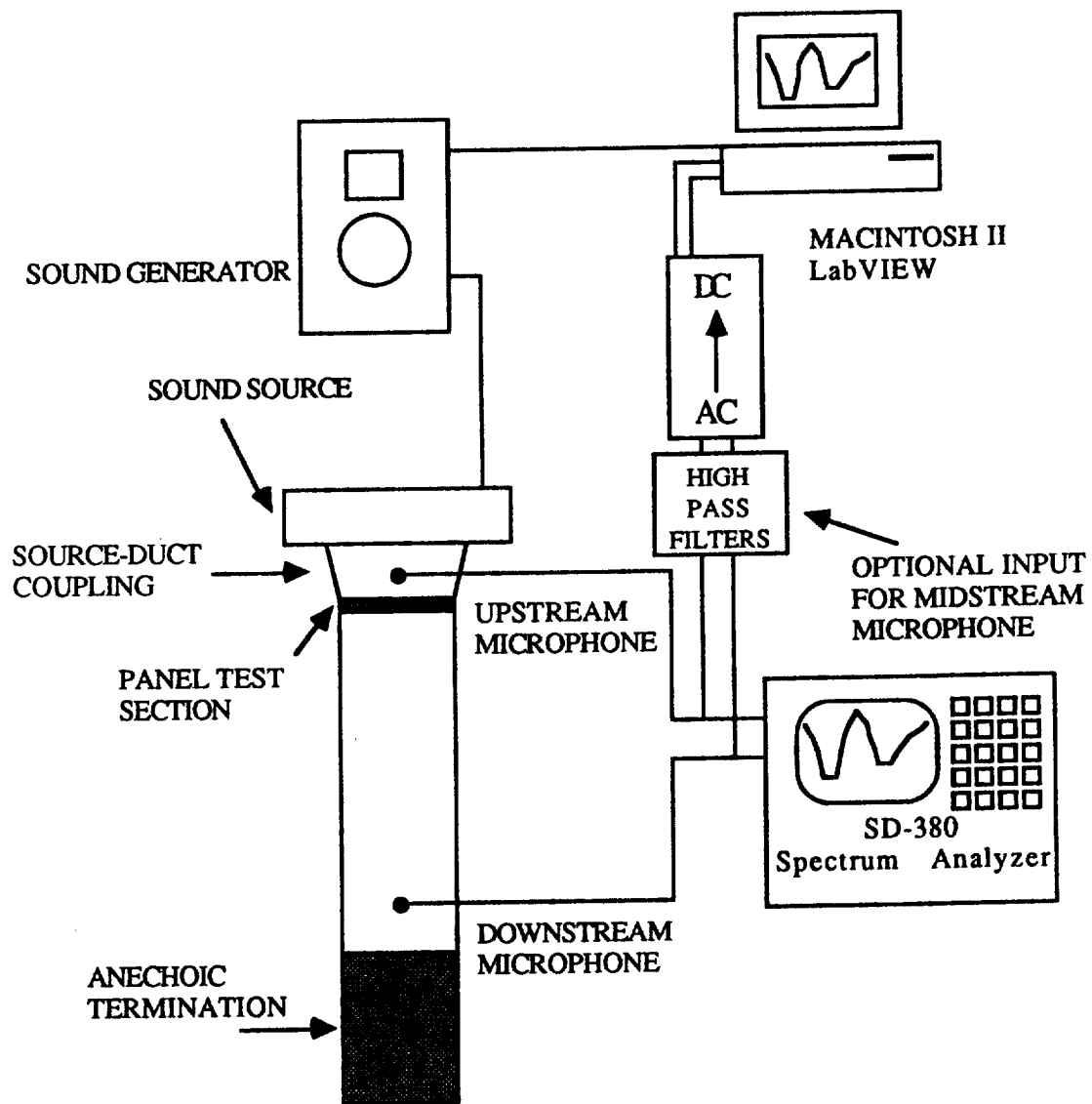


Figure 5.2.1: Overall experimental setup showing general microphone positions, test section location, and processing equipment.

Two signal processing methods are used. One setup requires the use of a white noise generator and a Scientific Atlanta SD-380 spectrum analyzer; in this mode of operation, both microphone signals are fed to the SD-380 operating in the transfer function mode to produce the noise reduction across the panel barrier. The second procedure is a modern variation on a spectrum analysis method most often used by the Bruel & Kjaer company, where a pure tone generator is mechanically driven through the frequency range of interest. Frequency is monitored directly from the pure tone generator. The microphone signals are filtered and converted to a direct current signal which is linearly proportional to sound pressure level. A Macintosh II computer then processes the signals using LabVIEW, an icon-based programming tool. LabVIEW collects the DC voltage signals in integer data form and processes them using appropriate calibration to generate frequency and sound pressure level information. A noise reduction is then calculated by differencing the upstream and downstream microphone levels. The LabVIEW software creates almost immediate graphical representation of the results; additionally, the program can write frequency information and individual microphone levels to a data file for later processing.

Panels used in the panel arrays are (with one notable exception mentioned later) passively driven audio speakers. These "panels" are low in cost and have resonance frequencies which can be easily modified with the addition of mass to the cone, lowering natural frequencies. Epoxy can also be carefully added to the suspension of the panel to raise the stiffness and increase the natural frequency. In this manner, the required separation of the natural frequencies of panels of equal size can be obtained, and the panels can be forced to work against each other acoustically according to the ART principle. The voice coil on the speakers provides a handy transducer for measuring the phase difference between the panels.

As mentioned earlier, there is one exception to the use of passively driven audio speakers as panel sections; Section 5.7 presents data obtained using real panel sections composed of Bakelite.

Section 5.3: Single Panel Wall Noise Reduction Measurements

The speakers generally used for the single panel wall experiments are 4" in diameter and have an unmodified natural frequency of about 200 Hertz. These "panels" are arranged in the duct in a number of ways as shown in Figure 5.3.1, with single panel, double panel, and four panel wall configurations possible. After modification, ART panels have resonances of approximately 100 Hertz and 300 Hertz; use of other natural frequencies will be noted as required.

Figure 5.3.2 shows noise reduction measurements for identical panels and ART tuned panels. Both panel types exhibit approximately stiffness-dominated behavior at low frequencies (well below 100 Hertz) and mass dominated behavior at high frequencies (above 400 Hertz). The identical panel results show a noise reduction minimum at the panel natural frequency of 200 Hertz. The uneven noise reduction decrease below the natural frequency and uneven noise reduction increase above the natural frequency is due to the lack of a perfectly anechoic termination. (A pure anechoic situation is quite difficult to simulate in a laboratory.) The ART tuned panels show minima at the natural frequencies of 100 and 300 Hertz; between these frequencies, a maximum noise reduction of about 24 dB is observed. The proceeding results indicate the robustness of the ART method.

The phase difference between the panels can be measured using the speaker voice coils, as shown in Figure 5.3.3. Panels are in phase at low frequencies up to the lowest panel natural frequency. Between the panel natural frequencies, a phase

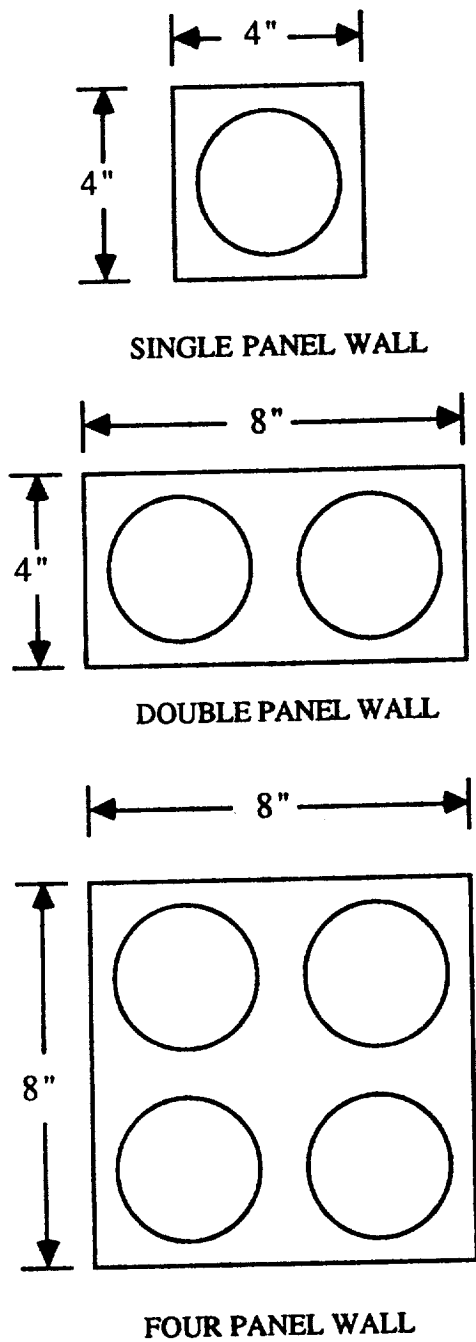


Figure 5.3.1: Single wall panel array test sections.

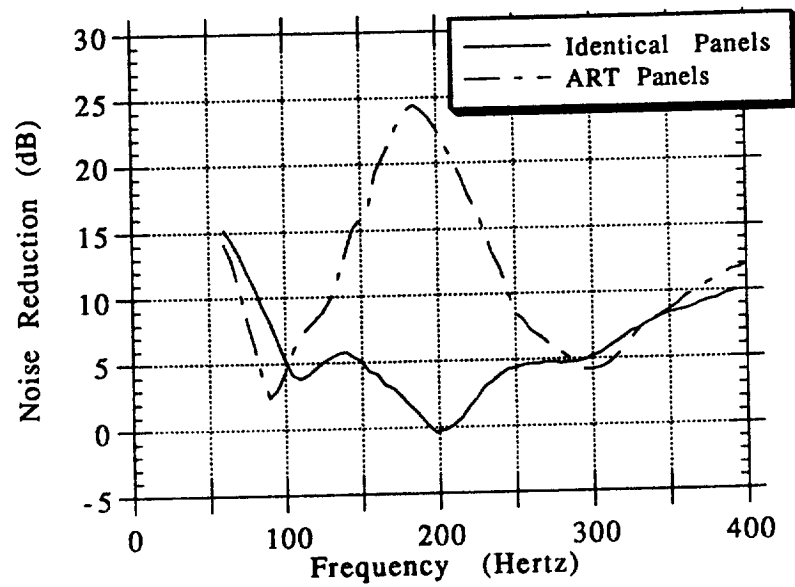


Figure 5.3.2: Experimental noise reduction measurements with two ART tuned panels and two identical panels.

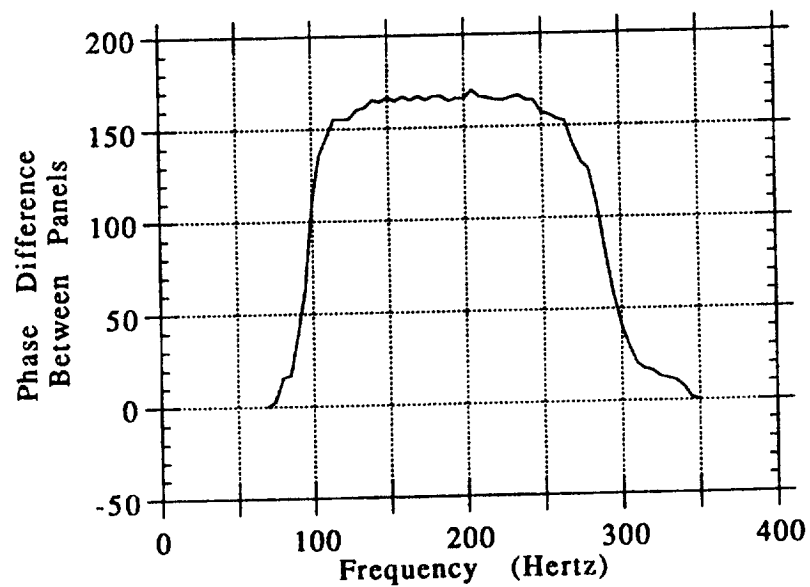


Figure 5.3.3: Measured phase difference between two ART panels used to generate ART data shown in Figure 5.3.2.

difference between panels of about 165 degrees was noted. At high frequencies, the panels are again in phase. Figures 5.3.2 and 5.3.3 demonstrate the possibility of tuning panels to achieve the ART requirements of out-of-phase behavior and approximately equal amplitude motions.

The concept of ANNR can be applied to experimental data to determine the true ART contribution to noise reduction. Figure 5.3.4 shows the two panel ART data and an ANNR calculation obtained from individual panel noise reduction data*. The ART concept effectively adds over 10 dB of noise reduction when compared to the averaged noninteracting noise reduction calculation for individual panels.

Figure 5.3.5 shows experimental noise reduction data with the two panel setup obtained by varying the higher panel natural frequency as shown. Note that increasing the frequency difference between the high natural frequency panel and the low natural frequency panel increases the noise reduction bandwidth as well as the maximum noise reduction value obtained. In general, this strategy proves advantageous from both theoretical and experimental considerations.

Four panel tuning is shown experimentally in Figure 5.3.6, where ART panel natural frequencies are arranged at about 90, 190, 280, and 410 Hertz. While these are certainly not optimum tuning frequencies, the data does indicate the possibility of tuning for more than one ART design frequency.

It is possible to verify experimentally the exponentially decaying nature of the sound field in the downstream vicinity of the panel wall using a modified impedance tube setup as shown in Figure 5.3.7. A rolling cart microphone with a long extension tube is placed through the sound source, duct coupling, and panel wall

* ANNR data is obtained by measuring noise reduction using single panels in the single panel duct. A separate noise reduction data set is then obtained for the 100 Hertz and the 300 Hertz natural frequency panels, and Equation (2.4.1) is invoked to determine the ANNR.

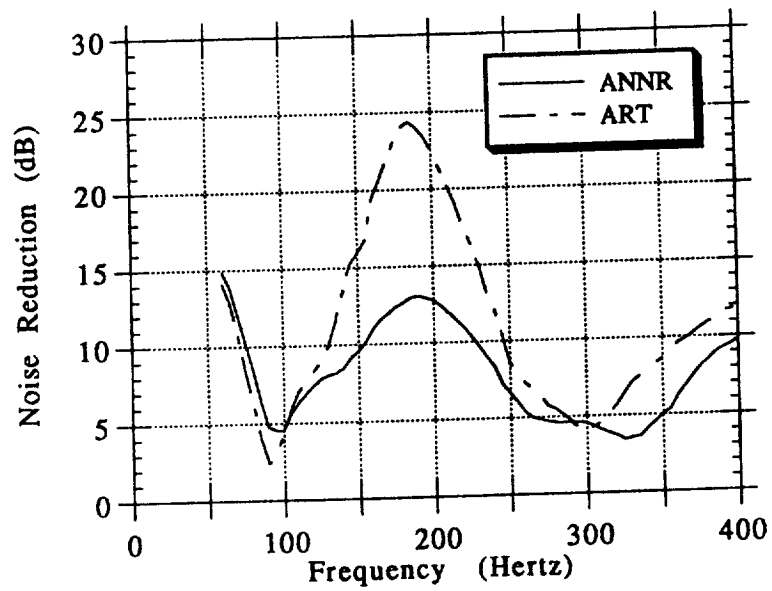


Figure 5.3.4: Two panel ART noise reduction measurement plotted with two panel ANNRR calculation.

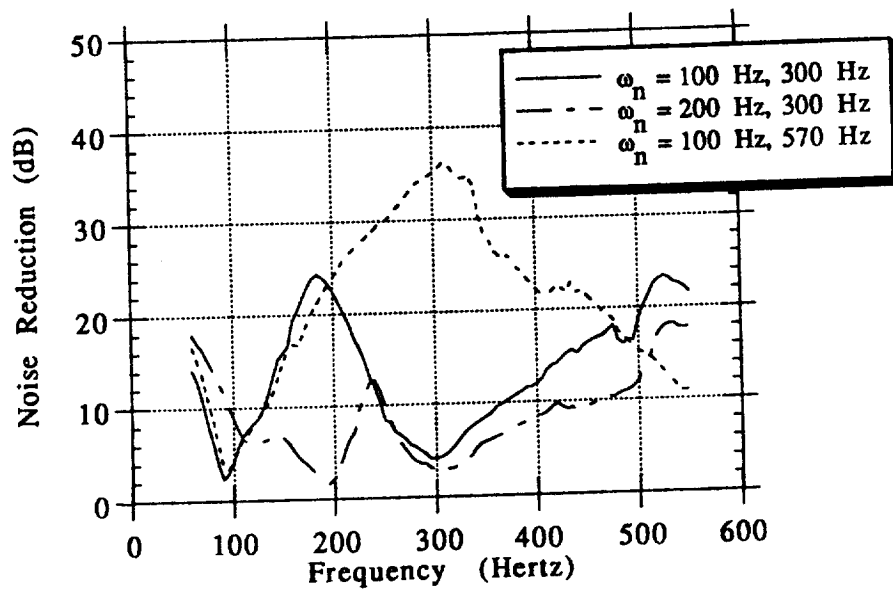


Figure 5.3.5: ART noise reduction measurements with two panel setup varying panel natural frequencies as shown.

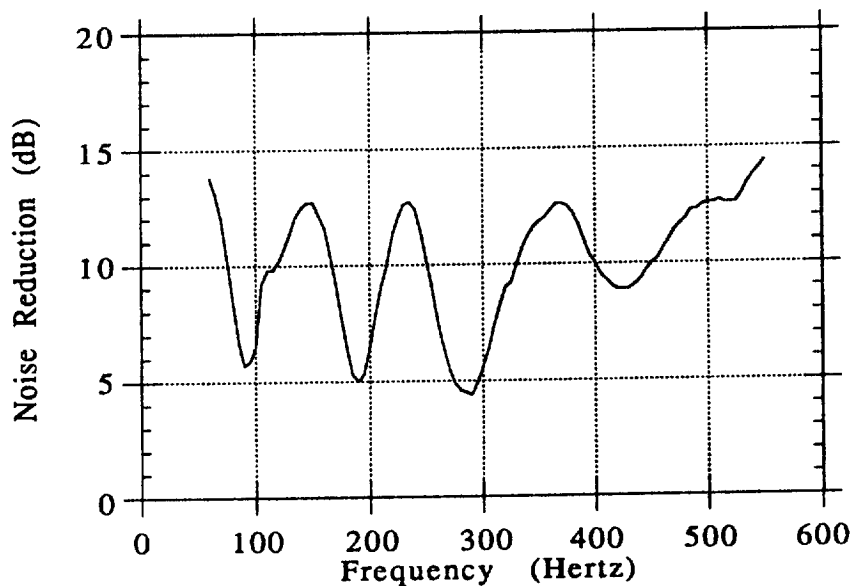


Figure 5.3.6: Four panel noise reduction measurement with panel natural frequencies at 100, 200, 300, and 400 Hertz.

at a position as shown in the panel array cross section detail in Figure 5.3.7. Note that the end of the microphone tube is supported on a rolling wheel, insuring measurement at the same vertical position in the duct. This apparatus allows the measurement of sound pressure level falloff at a given frequency at various longitudinal positions in the duct relative to the coordinate system as shown. Figure 5.3.8 displays the sound pressure level difference in decibels between the upstream microphone and the cart tube microphone plotted as a function of distance down the duct at various frequencies. Note that at the 100 Hertz frequency (lower panel resonance frequency) there is little sound level falloff; recall that at the natural frequency, a panel will appear acoustically transparent in the limit of no damping. However, at 200 Hertz (the frequency of maximum noise reduction), an 18 dB sound pressure level drop has occurred across the panel wall; an additional 6 dB of noise reduction occurs by

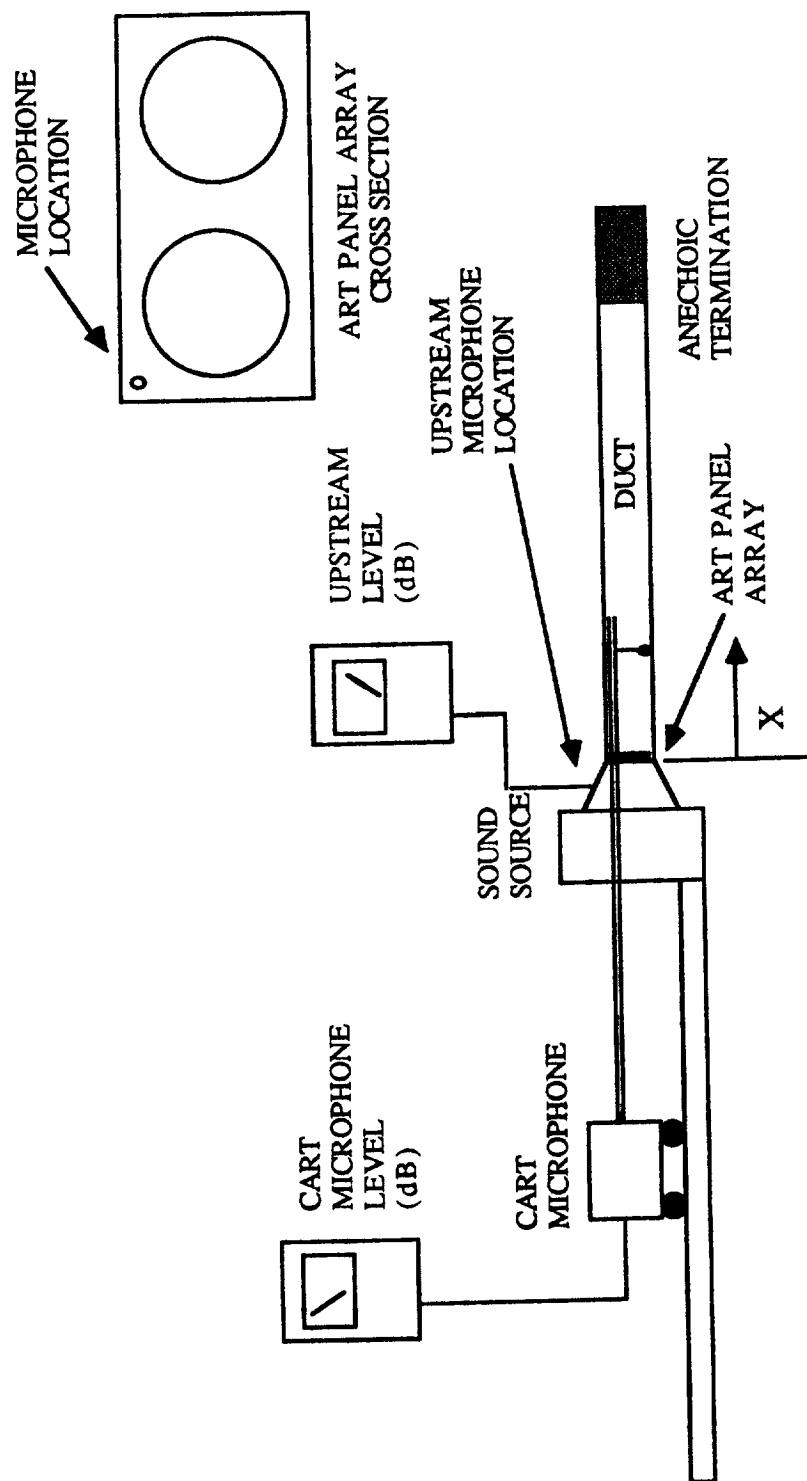


Figure 5.3.7: Experimental noise reduction falloff setup showing duct, upstream microphone, and cart microphone setup. Note coordinate system location just below ART panel array. Cross sectional view of duct at panel array shows relative microphone position in the duct.

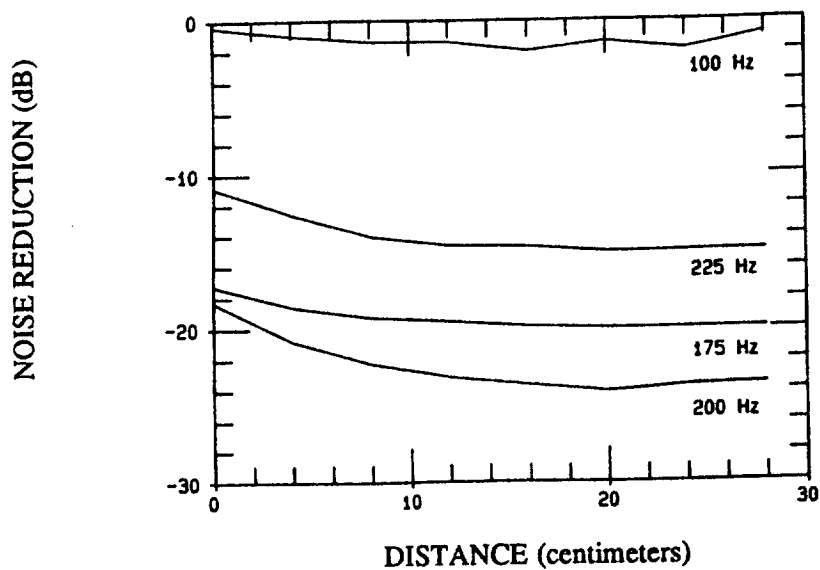


Figure 5.3.8: Difference between upstream microphone and cart microphone levels as a function of distance down the duct for the two panel ART array. Measurement is taken as shown in Figure 5.3.7.

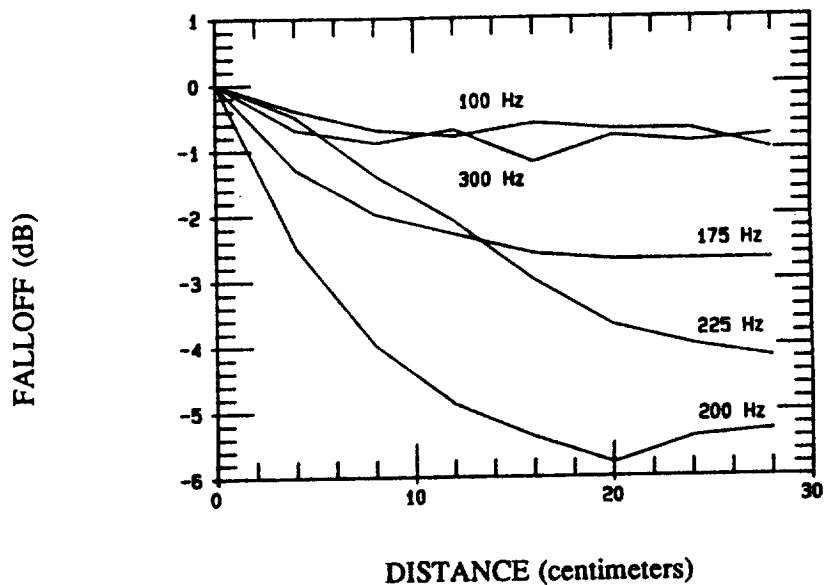


Figure 5.3.9: Falloff measured away from the panel wall array with the cart microphone. The falloff in decibels is referenced to the sound pressure level just downstream of the panel wall.

moving approximately 25 centimeters away from the panel wall. Sound pressure levels near the wall are higher; however, ART tuning has reduced them significantly. Figure 5.3.9 shows sound pressure level relative to the level just downstream of the panel array; at 200 Hertz, the exponential decay is much more evident on this scale.

Section 5.4: Double Panel Wall Noise Reduction Measurements With One Identical Wall and One ART Wall

Double wall structures are easily investigated with the test section shown in Figure 5.4.1. An upstream panel array holds two identical panels with resonance frequencies of 200 Hertz; in the downstream wall, identical or ART tuned panels may be arranged. Figure 5.4.2 shows experimental noise reduction results for identical downstream panels (meaning all four panels have resonance frequencies of 200 Hertz) and ART tuned downstream panels. Since the panel test section now contains two panels in series, the noise reduction falloff at low frequencies is about 12 dB/octave in the low frequency limit (stiffness dominated behavior). Noise reduction increase in the high frequency limit should theoretically be 12 dB/octave (mass dominated behavior). The low frequency and high frequency noise reduction results in Figure 5.4.2 show the effect of these higher order impedances. The noise reduction at the panel natural frequencies also increases because the sound must now travel through two panel arrays. ART tuning has achieved about 18 dB of additional noise reduction at 200 Hertz. Figure 5.4.3 shows the measured phase difference between the downstream panels for this same case; higher order impedances make this phase difference data appear more "rounded" than the phase difference data for the single array (Figure 5.5.3).

The effect of panel wall spacing is shown in Figure 5.4.4 for panel wall array coupling lengths of 7", 2", and 1". High frequency

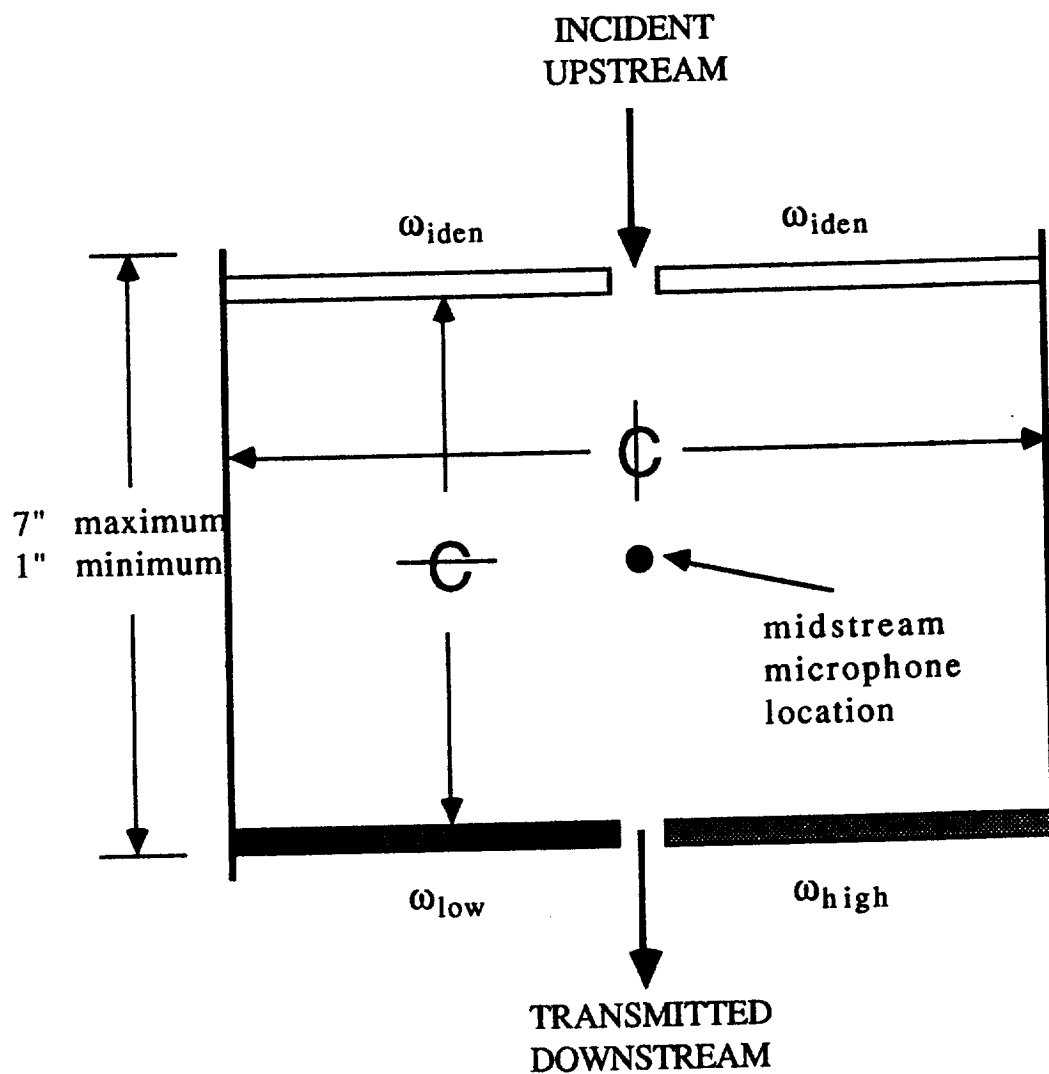


Figure 5.4.1: Top view of double wall test section with identical panels upstream and ART tuned or identical panels downstream. Midstream microphone located as shown.

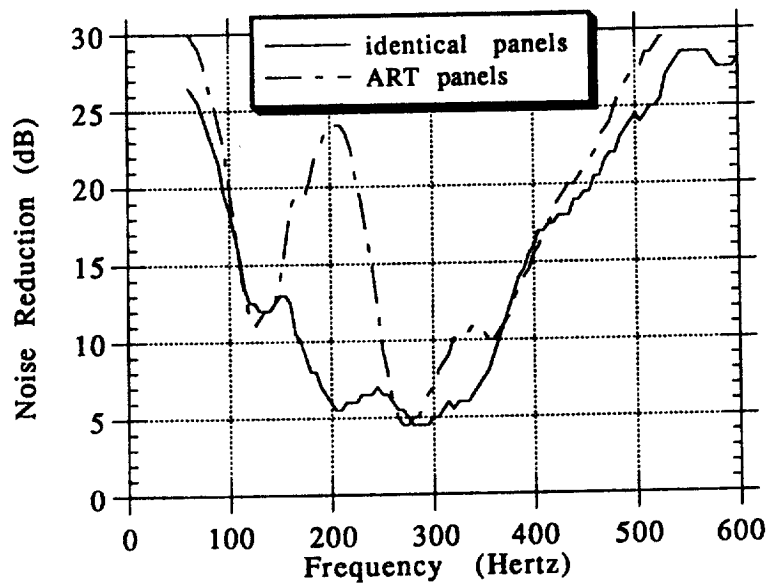


Figure 5.4.2: Experimental noise reduction measurements in the double wall setup with four identical panels and identical panels upstream and ART tuned panels downstream with the 7" coupling.

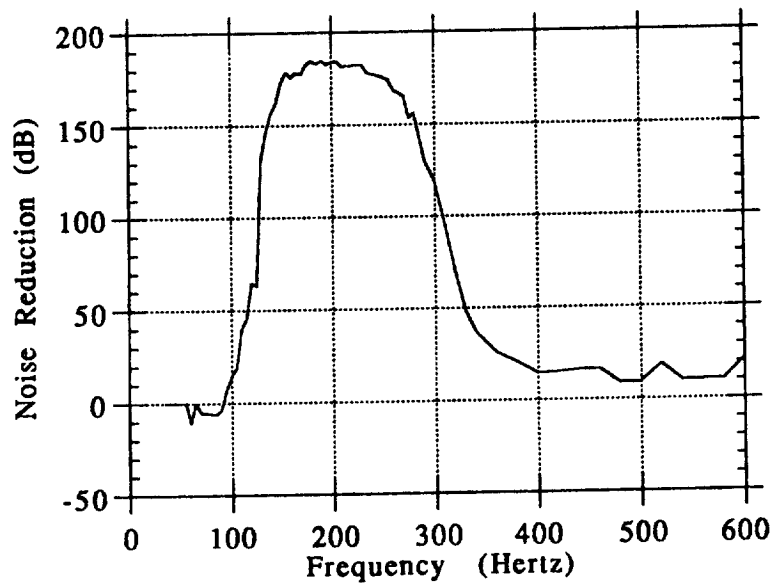


Figure 5.4.3: Phase difference between ART tuned panels used in noise reduction data shown in Figure 5.4.2.

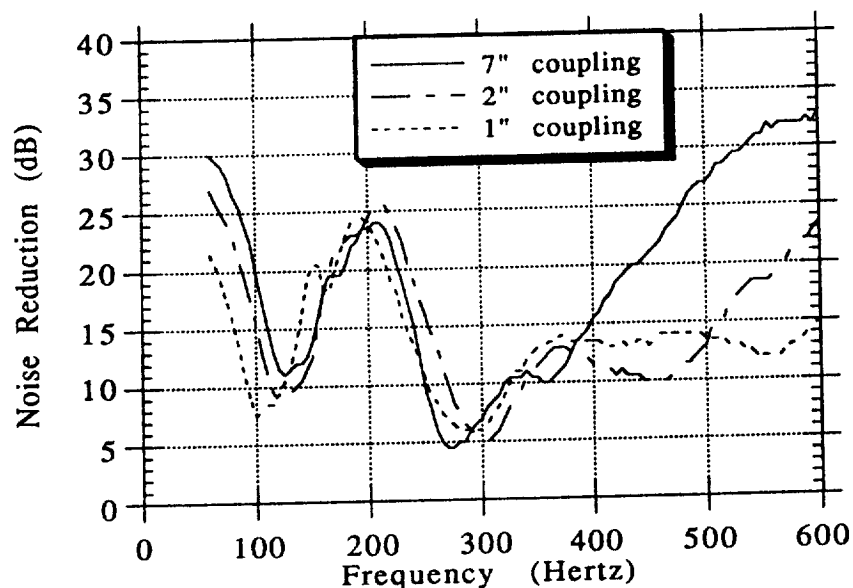


Figure 5.4.4: Noise reduction measurements for ART tuned panels downstream and identical panels upstream with coupling separation distances as shown.

data for the 7" spacing shows more noise reduction than the narrower spacings since the larger spacing has permitted the two panel arrays to behave more independently. In the ART frequency regime, the noise reduction data are not drastically different either in noise reduction bandwidth or maximum noise reduction obtained.

Section 5.5: Double Panel Wall Noise Reduction Measurements With Two ART Walls

Double wall geometries permit the investigation of noise reduction results for two sets of ART tuned panels, and Figure 5.5.1 displays the arrangement possibilities. Inline arrangement places panels of identical natural frequency on the same side of the duct; opposed arrangement places panels with the same natural frequencies on opposite sides of the panel array. The

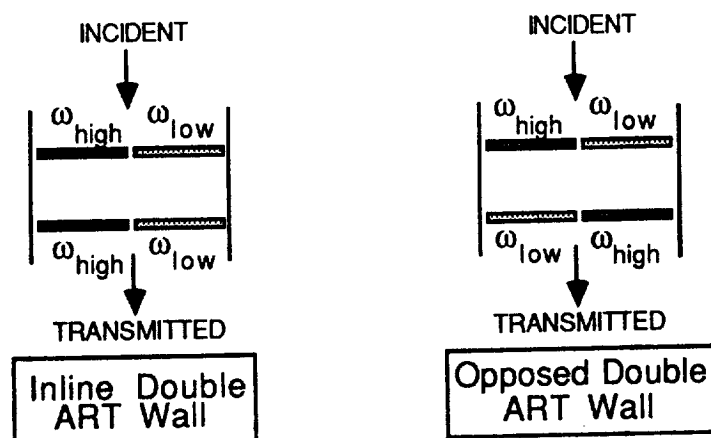


Figure 5.5.1: Double wall test sections with ART panels upstream and downstream. Note difference between inline and opposed ART configurations. Midstream microphone located as shown in Figure 5.4.1.

major physical difference here is the loading of the higher evanescent modes or surrounding fluid; inline panels slosh fluid back and forth lengthwise in the duct, whereas in the opposed geometry, panels tend to slosh fluid in a crosswise manner. Figure 5.5.2 indicates that the results are quite similar for a 7" coupling spacing except at the maximum noise reduction, where the opposed panel geometry appears about 8-10 dB better. Examination of noise reduction results in Figure 5.5.3 for inline panel arrangements at various spacings show that relatively close spacings of 1" or less behave in a similar manner; the 7" spacing shows increased noise reduction behavior. All noise reduction maxima occur at about the same frequency in Figure 5.5.3, indicating that the fluid loading on the inline panels is at least approximately constant. However, in the opposed ART panel results shown in Figure 5.5.4, successively closer spacings lower the frequency of maximum noise reduction, indicating that the panels may have an effectively higher fluid loading at closer spacings.

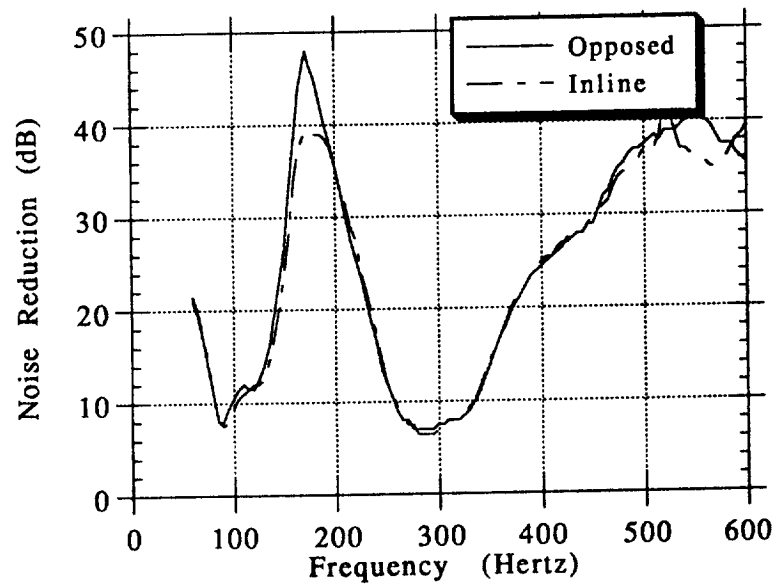


Figure 5.5.2: Experimental noise reduction measurements for inline and opposed double ART walls.

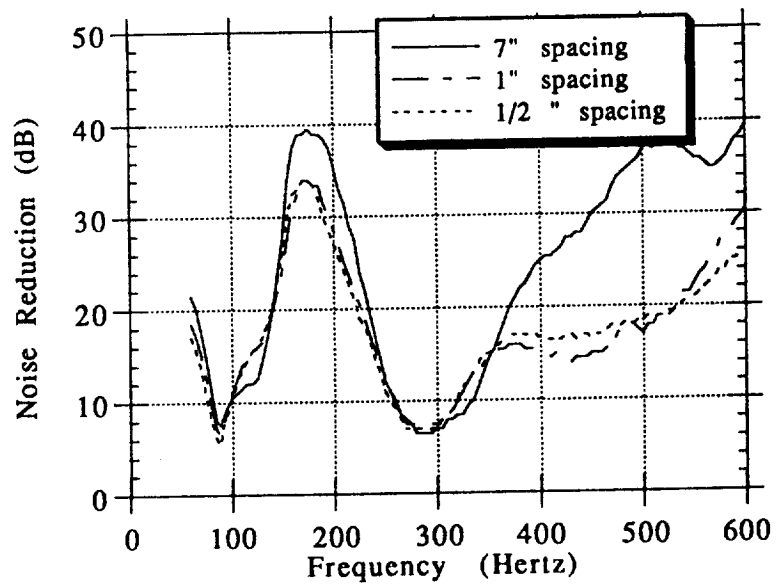


Figure 5.5.3: Experimental noise reduction results for inline double ART walls with coupler spacings as shown.

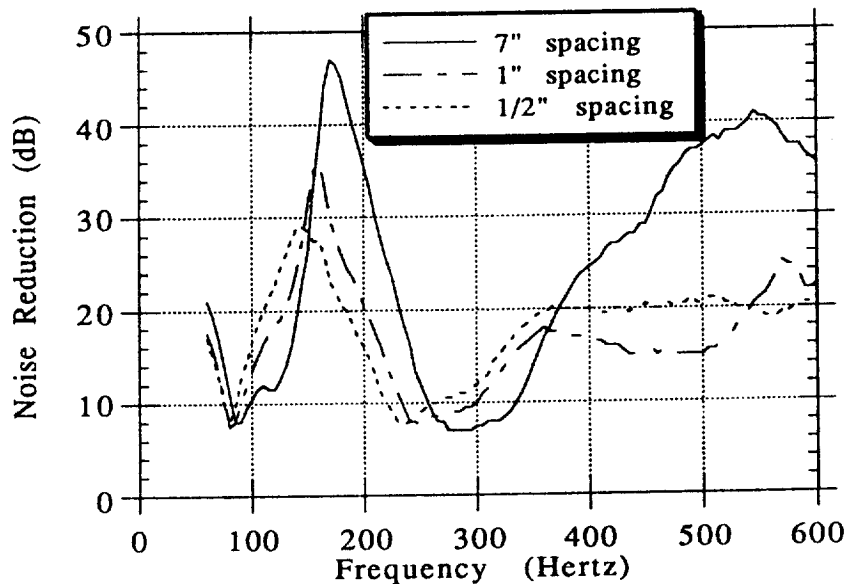


Figure 5.5.4: Experimental noise reduction results for opposed double ART walls with coupler spacings as shown.

Section 5.6: Double Panel Wall Noise Reduction Measurements With Nonuniform Panel Size

Figure 5.6.1 displays another panel arrangement possibility tested in the four panel array setup, where the double wall consists of one large upstream panel (free standing resonance frequency of 150 Hertz and 8" diameter) and four small downstream panels. Noise reduction data for identical downstream panels and ART tuned downstream panels are displayed in Figure 5.6.2, where ART tuning results in a noise reduction increase of about 22 dB over identical tunings. These results show the effect of the larger panel with a lower resonance frequency; for identical panels downstream, the large panel produces a noise reduction minimum at about 115 Hertz; for ART tuned panels, this minimum occurs at about 130 Hertz. ART panels apparently reduce the fluid loading on the larger panel; as a result,

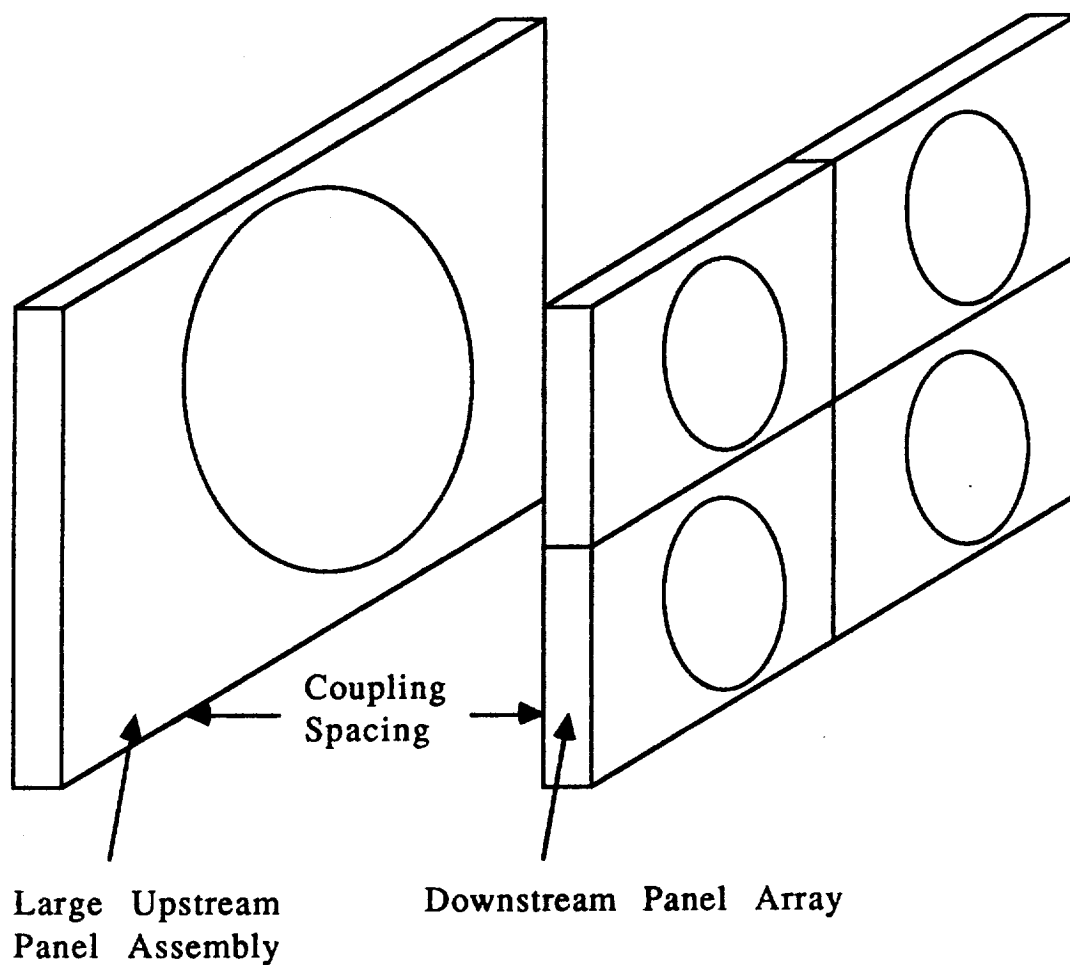


Figure 5.6.1: Double wall test section with nonuniform panel sizes. ART or identical panels are placed on downstream panel. Midstream microphone is placed on duct centerline and equidistant from each panel array.

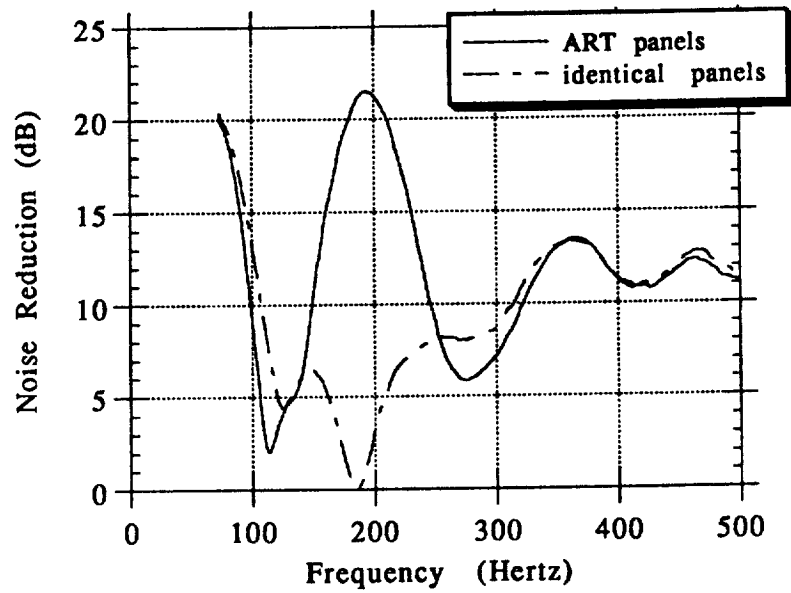


Figure 5.6.2: Experimental noise reduction comparison between uniform and ART panel arrangements for the 1" coupling.

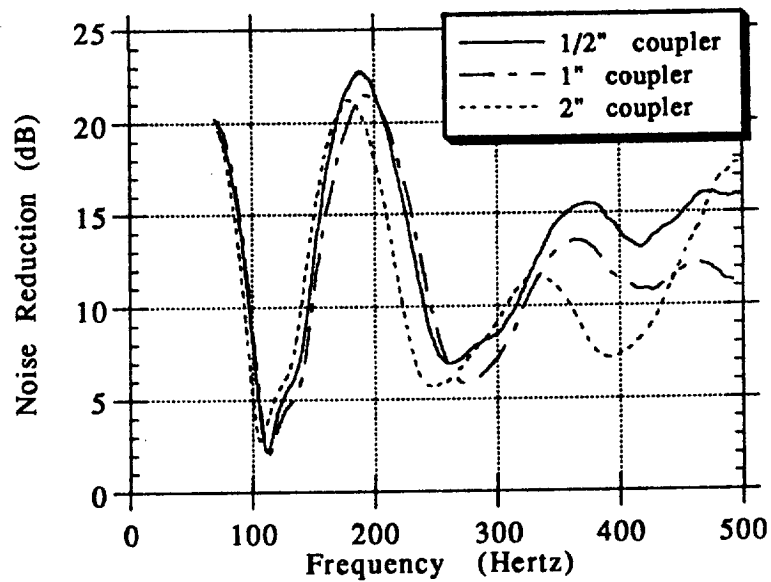


Figure 5.6.3: Noise reduction data from double wall nonuniform panel size experiments with coupling spacings as shown.

the frequency of minimum noise reduction associated with the large panel natural frequency increases from the identical to the ART panels case. Figure 5.6.3 compares ART tuning data for three coupling spacings; for the largest spacing shown (2"), the ART noise reduction peak is the narrowest; all coupling spacing data shows very similar behavior in and around the ART frequency regime. Relative maxima and minima at frequencies above 300 Hertz show the effect of coupling resonance, and the largest separation data shows a more distinct attempt to achieve mass dominated, high frequency behavior at a lower frequency.

Section 5.7: Noise Reduction Measurements With Real Panel ART Walls

Experimental results presented to this point have been obtained using passively driven speaker assemblies as panel sections. The assembly shown in Figure 5.7.1 allows the experimental investigation of the ART effect using real plates. Multiple socket head screws are used to clamp Bakelite plates (1/64" thickness) into an aluminum frame for use in the experimental apparatus shown in Figure 5.2.1. Figure 5.7.2 shows the noise reduction results for a plain panel with no modifications with a solid line. This data shows stiffness dominated, 6 dB noise reduction rolloff behavior at low frequencies. Again the irregularities in the low frequency data indicate the lack of a perfect anechoic termination. The panel natural frequency occurs at about 475 Hertz. Other small peaks in the noise reduction data are due to spurious resonances in the duct at higher frequencies.

It is useful to compare the experimental data with plate theory to determine just how predictable the panel behavior is. Panel noise reduction behavior has been observed in the laboratory to be highly dependent on the boundary conditions. For example, the data shown in Figure 5.7.2 cannot be easily

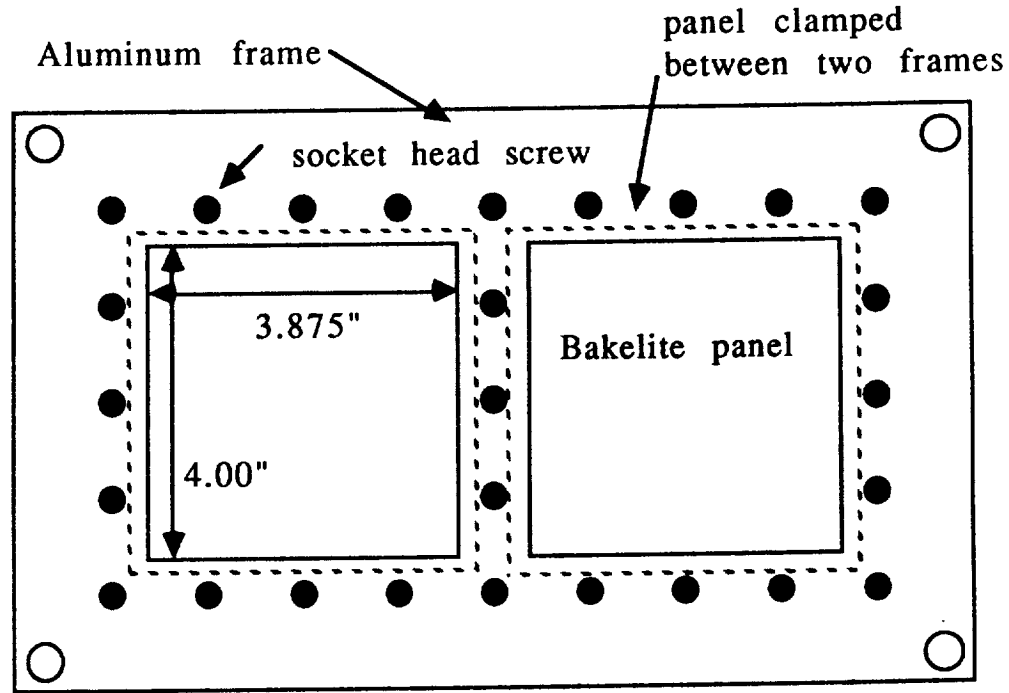


Figure 5.7.1: Plan view of real panel wall test configuration. Noise reduction measurements are made using both single panel and double panel ducts.

uplicated if the panel is not firmly attached and evenly seated in the frame. Any foreign matter interfering in the panel/frame interface can cause anomalies in the data. For the case of Figure 5.7.2, however, the comparison between theory and data is quite good. For a square plate with four clamped boundary conditions, the natural frequencies are given by³²

$$\omega_i = \frac{\lambda_i}{b^2} \sqrt{\frac{D}{m}} \quad (5.7.1)$$

where b is the length of a side of the plate. D is the flexural rigidity, denoted by

$$D = \frac{Eh^3}{1 - \nu^2} \quad (5.7.2)$$

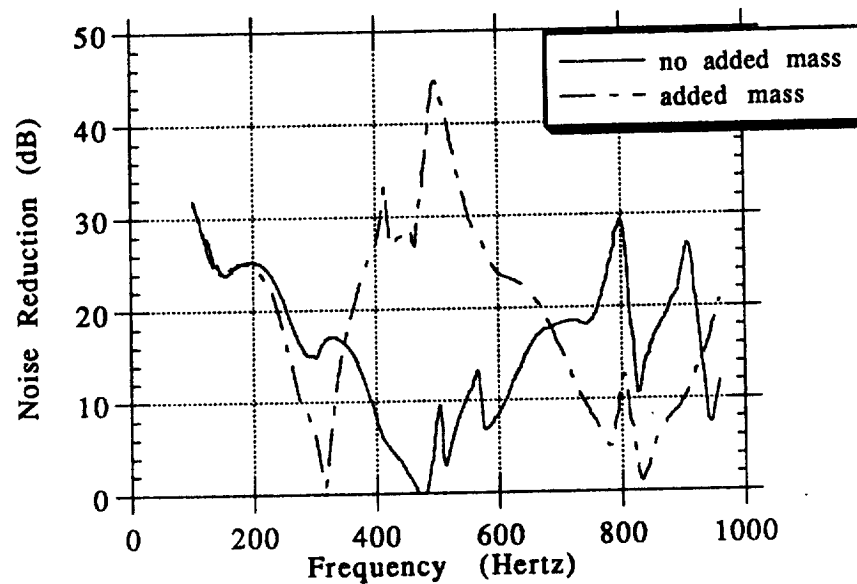


Figure 5.7.2: Experimental noise reduction measurement comparison for a single 1/64" unaltered Bakelite panel and mass-altered Bakelite panel.

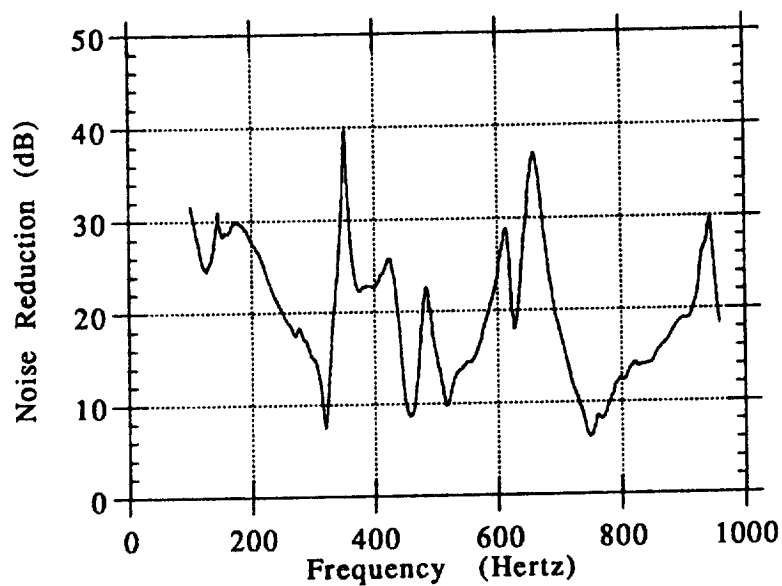


Figure 5.7.3: Experimental noise reduction measurement with two panel ART setup with unaltered 1/64" Bakelite panel and 1/64" mass-altered Bakelite panel.

where E is Young's modulus, h is the plate thickness, m is the mass per unit area of the plate, and ν is Poisson's ratio. For Bakelite, ν was assumed to be 0.3. λ_i are the solutions of the eigenvalue problem, and are shown below for the first three natural frequencies, along with other important values.

b	~4 inches
E	$0.6 - 1.0 \times 10^{10}$ Pa
m	0.516 kg/m ² for 1/64" panel
λ_1	36.0
λ_2	73.8
λ_3	109.0

Substitution of pertinent data into Equations (5.7.2) and (5.7.1) yields a first mode natural frequency of 496 Hertz, very close to the data shown in Figure 5.7.2, where a natural frequency of about 475 Hertz was indicated.

However, the addition of a point mass to the 1/64" Bakelite panel causes the panel behavior to be quite different than that which could be predicted by Equation (5.7.1). Figure 5.7.2 shows this data with a dashed line. It is curious to note the ratio of the two frequencies corresponding to the noise reduction minima; i.e.,

$$\frac{\omega_1}{\omega_2} = \frac{830}{315} \approx 2.5$$

This ratio is similar to the ratio of natural frequencies for ω_{11} and ω_{12} for a pinned plate. For a square plate with pinned boundaries on 4 sides³³,

$$\omega_{mn} = \pi^2 \left[\frac{m^2}{a^2} + \frac{n^2}{b^2} \right] \sqrt{\frac{D}{m}} \quad (5.7.3)$$

Plugging in $m=1$ and $n=1$ for ω_{11} , $m=1$ and $n=2$ for ω_{12} , a ratio of natural frequencies is calculated as

$$\frac{\omega_{12}}{\omega_{11}} = \frac{1^2 + 2^2}{1^2 + 1^2} = 2.5 \quad (5.7.4)$$

Arguably, the panel with additional mass may behave more like a pinned panel, according to plate theory equations. However, the presence of this second mode has created an amazing noise reduction between the two natural frequencies; a reduction in the transmitted noise of about 44 dB is seen at just below 500 Hertz. Recall that this is for a single panel in a single panel duct. It may therefore be possible to use higher structural mode behavior to some advantage in ART tuning a real panel. Also, the point mass placed at the center of the panel may help to enforce higher structural mode vibration.

Figure 5.7.3 shows the noise reduction data for both the 1/64" panel with no added mass and the 1/64" panel with added mass alongside each other, clamped in the two panel duct. The noise reduction minimum at 315 Hertz corresponds to the lowest natural frequency of the panel with added mass; the noise reduction minimum at 450 Hertz corresponds to the ω_{11} natural frequency of the panel with no added mass, and an ART noise reduction effect of about 40 dB is observed at 350 Hertz. Similarly, the minima at 750 Hertz (dropped about 80 Hertz from Figure 5.7.2 presumably due to fluid loading) might correspond to the ω_{12} natural frequency of the panel with added mass, and another ART noise reduction peak of 36 dB is observed at about 660 Hertz. If the panel with no added mass is actually behaving with two structural resonance frequencies, then the observed behavior shows two noise reduction minima as a result of three panel natural frequencies (two occurring from the same panel), as the ART theory has suggested.

Chapter 6

Summary and Conclusions

Section 6.1: Introduction

Existing noise reduction techniques for paneled structures have been shown to perform reasonably well at higher frequencies, but are less effective at lower frequencies, particularly if the low frequency noise problem has high forcing levels such as those found in helicopter or propeller aircraft. This research effort has focused on a new method of noise reduction for paneled structures called *Alternate Resonance Tuning*. The ART concept blocks sound transmission in a frequency band by having adjacent panels tuned to resonance frequencies alternately set above and below the frequency to be cancelled. The separation of the panel resonance frequencies causes the panels to work against each other structurally and acoustically. Ideally, adjacent panels are designed to oscillate with equal magnitude, but are nearly out of phase. The problems analyzed herein have shown the ART concept to be of potential value in the reduction of transmitted noise through paneled structures.

Section 6.2: The Four Panel Problem

The four panel problem presented in Chapter 2 analyzed a periodically repeating structure of infinite extent. The building

block for this structure is a physically two dimensional four panel subsystem (three dimensional in velocity in the panel near-field) incorporated into a duct; the panels within this subsystem can be tuned to as many as four distinct resonance frequencies, damping ratios, and masses. An acoustic branch analysis was introduced as an extremely efficient tool for predicting basic behavior of this panel system; however, the loading of the evanescent modes was neglected in this analysis. A more complete analysis of normal incidence acoustic transmission assumed pressures and velocities which satisfied the reduced three dimensional wave equation. Using a Fourier series to model periodic displacement of a single rigid panel in the subsystem, an expression was derived for an associated velocity boundary condition which matched the panel displacement. This velocity boundary condition assumed that the one dimensional acoustic mode propagated; all other modes decayed due to the cutoff effect. Using the momentum equation, a corresponding pressure solution could be obtained; this pressure solution was used to determine the forces acting on the panel. Problem symmetry and superposition could be used to obtain solutions for the case where all panels were in motion. The panel velocities then permitted the calculation of pressures and noise reductions in decibels.

Results were obtained which showed appreciable noise reductions for panel subsystems with two and four panels; the number of distinct noise reductions obtained was always one less than the number of distinct panel tunings within the subsystem. The concept of the Averaged Noninteracting Noise Reduction (ANNR) was introduced in order to calculate a true noise reduction gain due to the ART tuning. This model indicated that for typical system parameters, 10 to 30 dB of noise reduction could be obtained. Mass ratio optimization was shown to be effective in placing the maximum noise reduction frequencies at the desired values in the presence of fluid loading. A parameter study showed the effects of damping, panel fluid loading, ART bandwidth as a

function of panel natural frequencies, and variations in termination impedance; in all cases, the theory indicated that a reasonable increase in noise reduction could always be obtained by ART tuning.

Section 6.3: External Pressure Field Modeling

The purpose of this investigation was to determine the effectiveness of the ART concept under an external propagating pressure field such as that which might be associated with propeller passage by an aircraft fuselage. For this problem, a one dimensional repeating panel subsystem (two dimensional in velocity in the panel near-field) of N panels was analyzed, and all acoustic modes (both propagating and cutoff) were contained in the solution. The solution procedure used was similar to that described above for the four panel problem. A general numerical solution allowed the modeling of many effects, and a dual case study was undertaken to investigate the performance of the ART tuning method under typical limiting cases; these limiting cases included aircraft with long (low blade passage frequency) and short (high blade passage frequency) external propagating wavelengths relative to the panel size. A mode convergence study determined the appropriate number of modes to use for a converged solution.

The results obtained indicated that ART tuning yielded noise reduction increases of 10 to 25 dB relative to the ANNR calculations. An exhaustive set of parameter studies revealed some very interesting effects. Avoiding mode cut on was determined to be an important factor in obtaining the best noise reduction results. Splitting the panel natural frequencies always proved beneficial; reasonable variations in damping ratios showed the robustness of the ART tuning method. Forward and reverse sweep direction (corresponding to different rotational directions of the aircraft propeller) were found to have dramatic influence on

the noise reduction results. This acoustic solution yielded pressure and noise reduction calculations covering the entire analysis domain, and it was possible to examine variations in a given parameter over the complete model area.

A comparison was made to the model developed in Chapter 2 to determine the effect of including all acoustic modes in the solution. With the exception of some deviation around mode cut on frequencies, it was shown that the model assumptions of Chapter 2 were justifiable using the Chapter 3 model. Four panel tuning was shown to be a distinct possibility with this geometry, but in the high blade passage frequency case, the effects were less dramatic; ART tuning was determined to be most effective at low frequencies. Additional miscellaneous effects such as panel detuning (where a realistic deviation of panel properties was assumed) and off-tuning considerations (where an incomplete ART pair was present) showed that the tuning of a fluid-structure interaction such as the one modeled in Chapter 3 is indeed complex, but that the ART concept can be used to provide reasonable gains in noise reduction for such a dynamic system.

Section 6.4: The General ART Panel Analysis

The ART panel analysis presented in Chapter 4 derives the governing equations for the most general case of panel geometries. The analysis begins by assuming general acoustic velocity and pressure expressions which are related by the momentum equation. A wall displacement function expresses the panel shape in a most general way; the acoustic and structural equations are then linked at the panel/fluid interface. Lagrange's equations are used to represent the equations of motion for the panels. The generalized forces resulting from the motion of any mode of any panel on any mode of any *other* panel are then derived. The general governing equations are obtained; these equations consist principally of three components:

- > panel modal structural impedances
- > generalized forces due to the motion of a given structural mode of a given panel on another structural mode of another panel (including but not limited to the panel itself)
- > a forcing term integrated over the panel mode shape which drives the system.

The complexity of the general solution is discussed, along with the difficulties of obtaining a complete numerical and exact solution. A structural branch analysis is derived which includes the effects of higher structural modes. Clamped panels appear to be most stiff, whereas the flat rigid panel shape used in the models of Chapter 2 and 3 appears the least stiff. A panel modal study shows that while it is theoretically possible to use higher structural modes to advantage in ART tuning real panels, these modes are often occurring at higher frequencies well out of range of practical use. Given the complexity resulting from using general panel mode shapes, the simple flat and rigid plate impedance model of Chapter 2 and 3 yields conservative engineering results.

Section 6.5: Experimental Confirmation of the ART Concept

A series of experiments confirmed the potential value of Alternate Resonance Tuning and displayed the relative ease with which the phenomenon can be obtained. A general experimental setup was constructed to investigate the ART tuning method for a number of practical geometries. Single panel arrays with as many as four panels and three ART frequencies show noise reductions of 6 to 10 dB over the ANN calculations. Measured phase

differences between passively driven audio speakers indicated that an approximately out of phase situation could be obtained for much of the frequency range between panel natural frequencies.

Double wall experiments showed the possibility of using ART tuning in a multi-walled structure in numerous configurations, including nonuniform panel sizes. Real panel experiments indicated that the ART effect was not limited to simple devices such as passively driven speakers, but that legitimate panel sections could show ART noise reduction possibilities. Addition of a point mass to a Bakelite panel section "tricked" a plate into an apparent higher structural mode behavior which indicated ART cancellation potential of over 40 dB.

Section 6.6: Future Effort in Alternate Resonance Tuning

Exploration of the ART concept continues at Duke University. A panel/frame method is currently being investigated for the solution of spatially periodic wall structures such as those found in aircraft³⁴. A two-scale perturbation expansion method is used which is based on the scale separation between panel size and acoustic wavelength, and an averaging procedure is applied over a rapidly varying panel scale. A composite solution is formed which contains both a smoothed global solution and a periodic local solution that describes the details of the panel motions. Panel subsystems appear in an averaged sense in the global solution through transfer functions, obtained from the local solution for distributed frame loadings and acoustic boundary conditions. This panel/frame methodology holds great promise as a means to analyze complicated structures such as aircraft panel/frame assemblies, which appear "smeared" in a physical sense.

Other more straight forward engineering analyses such as those performed in this research effort might be applied to problems to further understanding of the ART concept and its application to engineering structures. Figure 6.6.1 shows a schematic representation of a simple model for a multi-paneled wall structure such as those found in typical aircraft applications. This model considers a plate-like outer skin attached to a vibrating frame member, an inner rigid trim liner (also attached to the frame member), and a rigid plate hung on a suspension (much like an audio speaker) located between the two walls. The trim liner or suspended plate appears to be a practical way to implement ART tuning, and since ART appears to be most effect at low frequencies, the problem could focus on a two panel model to reduce transmitted noise at one frequency only. External panel tuning on an aircraft fuselage would be impractical; as mentioned in Chapter 1, aircraft interior panels have been altered successfully in terms of mass and stiffness. Previous theoretical investigation of multi-

walled structures has encountered some difficulty in achieving the ART effect³⁵, and more investigation may reveal new and innovative ways in which the ART concept might be used to help reduce noise transmission through paneled structures.

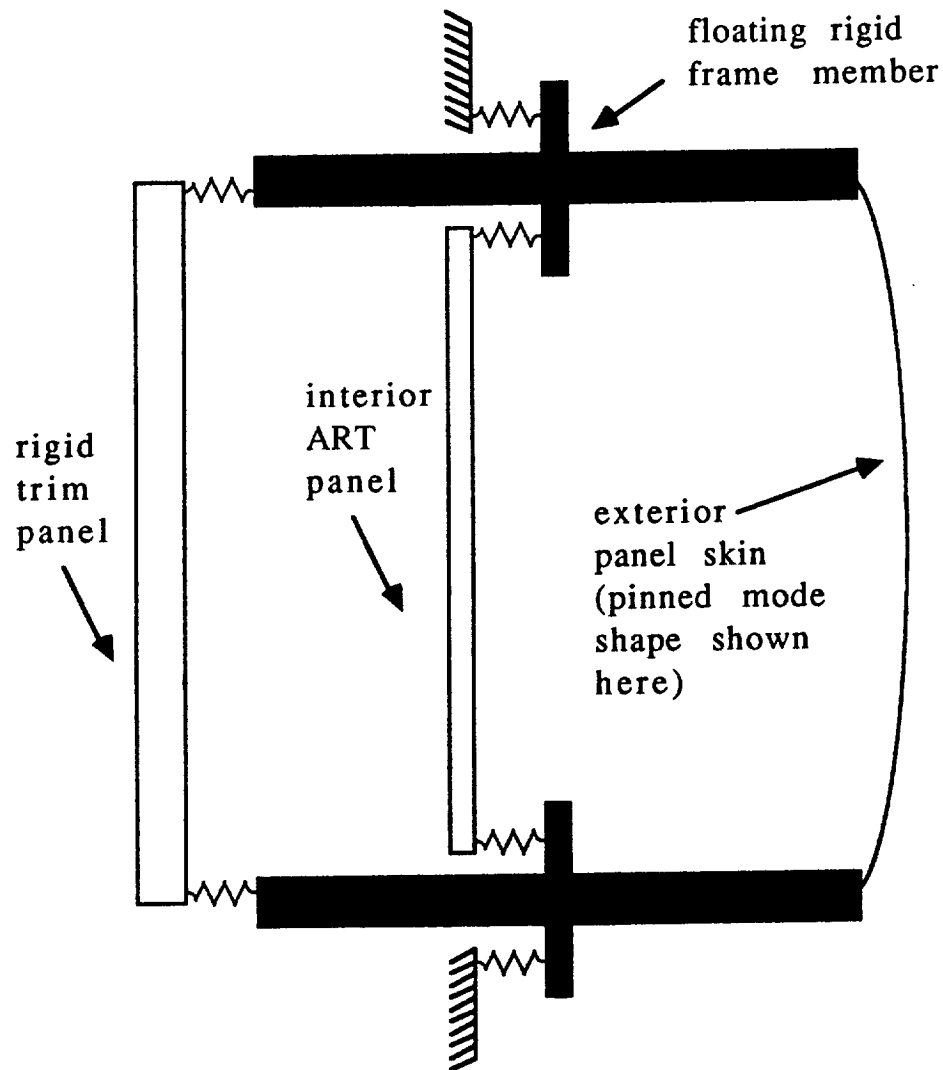


Figure 6.6.1: Multi-walled model for future investigation.

References

1. Kuntz, H. L. and Prydz, R. A., "Interior Noise in the Untreated Gulfstream II Propfan Test Assessment Aircraft," Journal of Aircraft, Vol. 27, No. 7, p. 648, July, 1990.
2. Wilby, J. F. and Wilby, E. G., "Measurements of Propeller Noise in a Light Turboprop Airplane," Journal of Aircraft, Vol. 26, No. 1, p. 42, January, 1989.
3. Knowles, K., "Importance of Broadband Noise for Advanced Turboprops," Journal of Aircraft, Vol. 24, No. 6, p. 386, June, 1987.
4. Brenter, K. S., "Prediction of Helicopter Rotor Discrete Frequency Noise for Three Scale Models," Journal of Aircraft, Vol. 25, No. 5, p. 422, May, 1988.
5. Knowles, p. 391.
6. Mixson, J. S. and Powell, C. A., "Review of Recent Research on Interior Noise of Propeller Aircraft," Journal of Aircraft, Vol. 22, No. 11, pp. 931-949, November, 1985.
7. Vaicaitis, R., Grosveld, F. W., and Mixson, J. S., "Noise Transmission Through Aircraft Panels," Journal of Aircraft, Vol. 22, No. 4, pp. 303-310, April, 1985.
8. Heitman, K. E. and Mixson, J. S., "Laboratory Study of Cabin Acoustic Treatments Installed in an Aircraft Fuselage," Journal of Aircraft, Vol. 23, No. 1, pp. 32-38, January, 1986.

9. Vaicaitis, R., and Mixson, J. S., "Theoretical Design of Acoustic Treatment for Noise Control in a Turboprop Aircraft," Journal of Aircraft, Vol. 22, No. 4, pp.318-324, April 1985.
10. SenGupta, G., "Reduction of Cabin Noise and Vibration by Intrinsic Structural Tuning," AIAA Journal, Vol. 16, No. 6, pp. 545-546, June, 1978.
11. SenGupta, G., "Reduction of Cabin Noise During Cruise Conditions by Stringer and Frame Damping," AIAA Journal, Vol. 17, No. 3, pp.229-236, March 1979.
12. SenGupta, G., "Vibration of Periodic Structures," The Shock and Vibration Digest, pp. 17-31, March 1980.
13. Kandebo, S. W., "Propfan Flight Tests Will Examine Design, Noise Issues," Aviation Week and Space Technology, pp. 36-37, January 25, 1988.
14. Prydz, R., et al., "Advanced Treatment Technology Program for Advanced Turboprop Aircraft", 3rd SAE/NASA Aircraft Interior Noise Workshop, Hampton, VA, April 11-12, 1988.
15. Silcox, R.J., Lester, H. C., and Fuller, C.R., "Sound Transmission and Active Control in Fuselage Models," 3rd SAE/NASA Aircraft Interior Noise Workshop, Hampton, VA, April 11-12, 1988.
16. Silcox, R. J., Fuller, C. R., and Lester, H. C., "Mechanisms of Active Control in Cylindrical Fuselage Structures," Proceedings of the 44th Annual Forum of the American Helicopter Society, Washington, D. C., June 16-18, 1988.

17. Bliss, D. B., "Aircraft Interior Noise Reduction By Alternate Resonance Tuning," proposal to NASA Langley Research Center, Structural Acoustics Division, Hampton, VA, September, 1986.
18. Woodward, R. P., "Measured Noise of a Scale Model High Speed Propeller at Simulated Takeoff/Approach Conditions," AIAA Paper 87-0526, January, 1987.
19. Press, W. H., Flannery, B. P., Teukolsky, S. A., and Vetterling, W. T., *Numerical Recipes*, Cambridge University Press, Cambridge, England, 1987, pp. 283-6.
20. Knowles, p. 391.
21. Pierce, A. D., *Acoustics*, Acoustical Society of America, Woodbury, New York, 1989, p. 117.
22. Mixson and Powell, p. 936.
23. Nallasamy, M., Woodward, R. P., and Groeneweg, J. F., "High-Speed Propeller Performance and Noise Predictions at Takeoff/Landing Conditions", Journal of Aircraft, Vol. 26, No. 6, p. 568, June, 1989.
24. Wilby and Wilby, p. 40.
25. Kuntz and Prydz, p. 647.
26. Dowell, E.H., et. al., *A Modern Course in Aeroelasticity*, Sijthoff and Noordhoff International Publishers, Alphen aan den Rijn, The Netherlands, 1978, p. 129.
27. D. B. Bliss and J. A. Gottwald, "Reduction of Sound Transmission Through Fuselage Walls by Alternate Resonance Tuning

(ART)", accepted for publication in the *AIAA Journal of Aircraft*, in final revision.

28. Dowell, p 138.
29. Szilard, R., *Theory and Analysis of Plates*, Prentice-Hall, Inc., Englewood Cliffs, New Jersey, 1974, p. 695.
30. Young, D., "Vibration of Rectangular Plates by the Ritz Method", Journal of Applied Mechanics, Vol. 17, No. 4, December, 1950, pp. 448-453.
31. Leissa, A. W., *Vibration of Plates*, National Aeronautics and Space Administration, U. S. Government Printing Office, Washington, D.C, 1969, p. 59-60.
32. Szilard, p. 699.
33. Ibid, p. 695.
34. Bliss, D. B., "Analysis of Sound Transmission Through Flexible Panel/Frame Walls", work in progress.
35. R. Srinivasan, "Alternate Resonance Tuning in the Two Wall Problem", Master's Thesis, Duke University, 1990.

James Allen Gottwald was born March 16, 1959 in Bethlehem, PA. Dr. Gottwald obtained a Bachelor of Science degree in Mechanical Engineering from the Massachusetts Institute of Technology in June, 1985. He obtained a Master of Science degree in Mechanical Engineering from Duke University in December, 1987, and the Doctor of Philosophy in Mechanical Engineering from Duke University in April, 1991. He is a member of the National Society of Professional Engineers, American Society of Mechanical Engineers, Acoustical Society of America, and Sigma Xi. Dr. Gottwald is currently appointed as a postdoctoral fellow at Duke University.

D.B. Bliss and J.A. Gottwald, "Reduction of Sound Transmission Through Fuselage Walls by Alternate Resonance Tuning (ART)," accepted for publication by *AIAA Journal of Aircraft*; currently in revision.

J.A. Gottwald, L.N. Virgin, and E.H. Dowell, "Experimental Mimicry of Duffing's Equation: Part I, Experimental Details and Free Vibration," accepted for publication in *Journal of Sound and Vibration*; currently in revision.

J.A. Gottwald and L.N. Virgin, "Nonlinear Mechanical Oscillator," Patent Disclosure prepared in conjunction with the Duke University Office of Technology Transfer, Durham, NC, June, 1989.

M. Zahn, Y. Ohki, J. Gottwald, K. Rhoads, and M. LaGasse, "Effects of Electrode Material on Charge Injection, Transport, Energy Storage, and Dissipation in Highly Purified Water," 1984 IEEE Symposium on Electrical Insulation, June, 1984.

M. Zahn, T. Takada, Y. Ohki, and J. Gottwald, "Charge Injection and Transport Analysis and Measurements in Highly Purified Water," 1983 Annual Report for the Conference on Electrical Insulation and Dielectric Phenomena, Buck Hill Falls, PA, October, 1983, 176-184.

